Geosciences and engineering : a publication of the University of Miskolc

1. évf. 2. sz. / 2012

Baricza Ágnes - Bajnóczi Bernadett - Tóth Mária - Szabó Csaba Deterioration of Building Ceramics by Environmental Factors - a Case Study on Zsolnai Ceramics from the Museum of Applied Arts (Budapest) 7-14

Bernáth György Identification of Fracture Zones in a Tight Gas Reservoir 15-20

Bódi Tibor Direct and Indirect Connate Water Saturation Determination Methods in the Practice of Riaes 21-26

Bódi Tibor - Tóth János The Role of Laboratory Tests in Enchanced Recovery of Conventional and Non-conventional Hydrocarbon Resources 27-32

Csuhanics Balázs - Debreczeni Ákos The Connection between Rock Wall Raveling and in Situ Rock Mass Strength - a Study on the Influencing Factors 33-38

Faitli József - Weisz Róbert Hydraulic Backfill Technology for the Closure of the Abandoned Sulfide Mine in Mátraszentimre 39-44

Fejes Zoltán - Szűcs Péter - Kompár László - Szlabóczky Pál Potential Thermal Water Exploration in the Tokaj and Szerencs Area 45-50

Federer-Kovács Gabriella Simulation of a Re-entry with Casing Drilling under HPHT Conditions 51-56

Földessy János - Németh Norbert - Gerges Anita - Kasó Attila, Jr. Reconnaissance Ore Prospecting in Northeast Hungary - in Co-operation of Academy and Company 57-62

Gyenes Gáborné - Bucsi Szabó László Geophysical Mapping of the Rudabánya Mine Waste Rock Piles and Hámor Lake 63-68

Havasi István Fight for the Third Place of the Stand - that is to Say Galileo and Compass 69-74

Havasi István - Benő Dávid Comparison of Traditional and Fuzzy Unsupervised Classification on the Basis of Vegetation Index 75-80

Horánszky Beáta Environmental Issues of CO2 Pipelines 81-86

Jarzyna, Jadwiga A. - Krakowska, Paulina I. - Puskarczyk, Edyta - Wawrzyniak-Guzi, Kamila - Bielecki, Jakub - Kwiatek, Wojciech - Gruszczyk, Michał Spatial Distribution of Petrophysical Properties on the Basis of Laboratory Results, Well Logging and Seismic Data 87-92

Kántor Tamás - Kovács Balázs Investigation of Stress Distribution during Large Scale Shearing Test 93-98

Kompár László - Szűcs Péter - Fejes Zoltán - Palcsu László - Deák József Infiltration Tests on Irrigated Agricultural Areas 99-104

Molnár József Remarks on the Problem of our Future Energy Sources 105-

	110
Móricz Ferenc - Mádai Ferenc - Walder, Ingar F. Pyrite Oxidation under Circumneutral Ph Conditions [Teljes szöveg (PDF)]	111-116
Nagy Zsolt - Pogácsás György - Juhász Györgyi - Hatalyák Péter - Milota Katalin - Csizmeg János - Laukó Ágnes - Gombos Csaba Calculation of Unconformity Related Eroded Stratal Thicknesses along the Mid-Hungarian Mobile Belt in the Danube-Tisza Interfluve Area, Hungary [Teljes szöveg (PDF)]	117-122
Ormos Tamás - Paripás Anikó Noémi Traveltime Differences in Seismic Refraction Inversion [Teljes szöveg (PDF)]	123-128
Pethő Gábor Geological Applications of the VLF Method [Teljes szöveg (PDF)]	129-136
Plooy, Andries Du - Majoros Péter - Paprika Dóra - Brand, Johan - Van Vuuren, Peter Coal Exploration for Underground Gasification (UCG) - It?s All about Planning [Teljes szöveg (PDF)]	137-142
Prakfalvi Péter From the "Palóc Karst" to the Fissure Water of Volcanic Rocks - Selections from Hydrogeology of Nógrád County, Hungary [Teljes szöveg (PDF)]	143-148
Szebényi Géza - Berta József - Hámos Gábor - Csicsák József - Szabó Richárd National Radioactive Waste Repository 2011-2012 : Construction of the First Two Disposal Galleries [Teljes szöveg (PDF)]	149-154
Tildy Péter - Prónay Zsolt - Törös Endre Seismic Tomography Measurements in the Radioactive Waste Disposal Site in Bátaapáti [Teljes szöveg (PDF)]	155-160
Turai Endre Application Possibilities of IP Method in the Fields of Environmental Protection, Ore- and Direct Hydrocarbon Exploration [Teljes szöveg (PDF)]	161-166
Turai Endre Some Field Measurement Results of IP Method [Teljes szöveg (PDF)]	167-172
Woźnicka, Urszula - Dworak, Dominik - Wiącek, Urszula - Zorski, Tomasz Neutron Well-logging Profiles in Sloped Thin Layer Formations Simulated by Monte Carlo Method [Teljes szöveg (PDF)]	173-178

Geosciences and Engineering, Vol. 1, No. 2 (2012), pp. 7–14.

DETERIORATION OF BUILDING CERAMICS BY ENVIRONMENTAL FACTORS – A CASE STUDY ON ZSOLNAY CERAMICS FROM THE MUSEUM OF APPLIED ARTS (BUDAPEST)

ÁGNES BARICZA[1]–BERNADETT BAJNÓCZI[2]–MÁRIA TÓTH[3]– CSABA SZABÓ[4]
[1]Ph.D student, Lithosphere Fluid Research Lab (LRG), Institute of Geography and Earth Sciences,Eötvös University, H-1117 Budapest, Pázmány Péter sétány 1/C, Hungary, bariczaagnes@gmail.com
[2]Ph.D, senior research fellow, Institute for Geological and Geochemical Research, Research Centre for Astronomy and Earth Sciences, Hungarian Academy of Science, H-1112 Budapest, Budaörsi u. 45, Hungary, bajnoczi@geochem.hu
[3]Research fellow, Institute for Geological and Geochemical Research, Research Centre for Astronomy and Earth Sciences, Hungarian Academy of Science, H-1112 Budapest, Budaörsi u. 45, Hungary, totyi@geochem.hu
[4]Ph.D, associate professor, Lithosphere Fluid Research Lab, Institute of Geography and Earth Sciences, Eötvös University , H-1117 Budapest, Pázmány Péter sétány 1/C, Hungary, cszabo@elte.hu

1. Introduction

Nowadays much more attention is being paid to the influence of mankind on our environment than previously. The expansion of urban conglomerations and the developing industry has resulted in an increased amount of aggressive pollutants [1]; therefore in the 21st century one of the major roles of society is to conserve its historical and cultural heritage. Pollutants from transport, heating and industry deposit on the built environment, causing its deterioration. Deterioration of natural building materials, like stone (e.g. freshwater and coarse limestone), is subject of numerous studies [e.g. 2], however few studies are designed to research the effect of air pollutants (e.g. sulfur dioxide, nitrogen oxides, soot, dust) on man-made silicate-based materials (ceramic, glaze, glass etc.). In Budapest there are many examples of historic buildings covered with glazed ceramics (e.g. the Museum of Applied Arts, Parliament, the Geological Institute and Matthias Church).

It is widely accepted that, as Tournié and Ricciardi state, "the high melting temperatures of ceramics and glasses implies that diffusion coefficients of most of the elements are too low at ambient temperature to be significant at human lifespan and these materials are often considered to be corrosion resistant" [3]. However the air pollutants derived from different sources can damage ceramics and glasses easily if these silicate-based materials are exposed for a long time to the harmful factors. The most important reactions are dissolution of ceramic, glass and glaze, material transport to the contacting meteoric water or moisture, formation of new phases on the surface of the weathered object (so-called "hydrated silica" layer) and appearance of cracks/microcracks on the surface [3].

Our purpose is to reveal the effects of air pollutants on building ceramics (glazed ceramic roof tiles and decorative items) that originating from the Museum of Applied Arts, Budapest. In order to determine the deterioration mechanisms, we have examined the phase composition and the microfabrics of the ceramic body and the glaze, and studied the depositions accumulated on the surface of the ceramics.

2. Environmental factors

Building materials (natural and man-made) are continuously exposed to environmental factors, which often cause the premature aging of the material in consequence of physical, chemical and biological degradation processes. Besides the principal gaseous pollutants such as SO_2, NO_x and CO_2, the effect of aerosols and the presence of various forms of water (e.g. meteoric water, moisture) are also important factors in deterioration. Gases easily form different acids with the contacting water (sulphuric acid, nitric acid or carbonic acid) which can corrode the building materials. Aerosol particles, dust and soot also play a significant role in the deterioration. The study of these pollutants is of paramount importance to understand the chemical mechanism of the so-called black crust appearing on the surface of the building materials. Sulphate (usually gypsum) is generally the dominant component of the black crust, and diverse particulate matters are always observed [4].

The presence of many bacteria (like the sulfur oxidizing *Acidithiobacillus thiooxidans, Acidithiobacillus caldus*) and fungi (like *Penicilium Sp.*, *Fusarium Sp.*) on the weathered surface is also frequent. These living organisms promote formation of cracks and ion dissolution from the material (Ca^{2+}, K^{+}, Mg^{2+}), thus facilitating the process of weathering [5]. In addition to the above-mentioned degradation processes, air movement and solar radiation also play a role in the weakening of the building materials, causing shorter life span and decrease of permanence.

3. Samples and methods

The Museum of Applied Arts is located in the centre of Budapest, next to one of the roads with the heaviest traffic, Üllői Street (Figure 1). Due to its location, the building is intensively exposed to air pollution and anthropogenic effects.

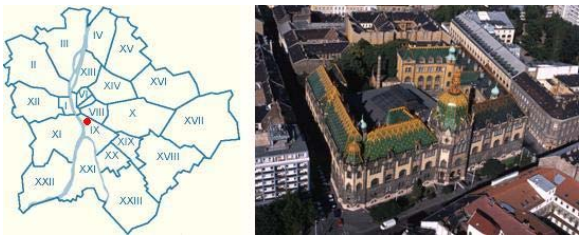

Figure 1. Schematic map of Budapest (on the left), where the red dot shows the location of the Museum of Applied Arts. Yellow and green glazed roof tiles and pyrogranite decorative items are clearly seen on the top of the investigated building (on the right)

The sampled ceramics are pyrogranite decorative objects, unglazed and glazed roof tiles. The role of the glaze layer is to decorate and protect the ceramic body. The ceramics were manufactured by one of the leading ceramic factories in Hungary, Zsolnay Porcelain Manufacturer. Since the construction of the Museum in 1896 the ceramic tiles and pyrogranite elements suffered numerous environmental and human influences therefore, the objects were damaged and from time to time had to be replaced. During sampling we collected ceramics of different ages (i.e. from different renovation periods) and with diverse glazes covered by a thick black deposition layer (Figure 2).

Figure 2. A green glazed tile from the roof of the the Museum of Applied Arts (on the left) and the studied samples of pyrogranite elements (on the right)

The mineralogical composition and texture of the ceramics was studied with a Nikon SMZ 800 stereomicroscope and Nikon E600 polarizing microscope. The phase composition of the ceramic body and the depositions accumulated on the objects was determined by X-ray diffraction analysis (XRD) with a Philips PW 1730 diffractometer. The surface of the glazed and unglazed (back) sides of some selected ceramics was studied with an Amray 1830 I/T6 scanning electron microscope (SEM). The SEM technique was also used to observe the microstructure of the ceramic body and the glaze, their interface and the alterations of the glaze, as well as the depositions on both sides of the objects. For this analysis, cross-section preparations were used.

4. Results and Discussion

Based on phase composition and microstructure, the studied ceramics can be divided into three groups (Table 1).

Table 1

Phase composition and textural characteristics of the studied ceramics

Types	**Phase composition**	**Characteristic of ceramic body/glaze**
Group 1	quartz>mullite> cristobalite, K-feldspar	ceramic body: matrix: white; grains: size max. 1 mm, white; structure: compact, few pores glaze: contains inclusions, 170–200 μm thick, lead glaze ceramic-glaze interface: sharp
Group 2	quartz> cristobalite, mullite	ceramic body: matrix: white; grains: size max. 1.5 mm, yellow; structure: porous glaze: few inclusions, 250 μm thick, lead glaze and unglazed items ceramic-glaze interface: sharp
Group 3	quartz, mullite> cristobalite, K-feldspar, plagioclase, +/–calcite	ceramic body: matrix: red, grains: size max. 0.5 mm, white; structure: porous glaze: some inclusions, 270–280 μm thick, lead glaze ceramic-glaze interface: glaze impregnated the upper 150 μm part of the ceramic body

The tiles, depending on their exposure, are covered by a grey-black deposition (contamination) layer, which firmly adheres to the surface. The deposition layer contains dust, soot and aerosols in variable quantity. Different types of spherules often appear on it, occurring on the glazed and the unglazed back sides of the tiles (Figure 3). Fe-rich, silicate spherules and spherules with complex composition, containing Si, Ca, K, Al and S, can be distinguished, which are natural or artificial in origin. We also observed artifical carbonaceous forms. The artificial spherules probably originated from fossil fuel (coal and oil) combustion [6], thus they are generated by industry and other human activities (e.g. heating).

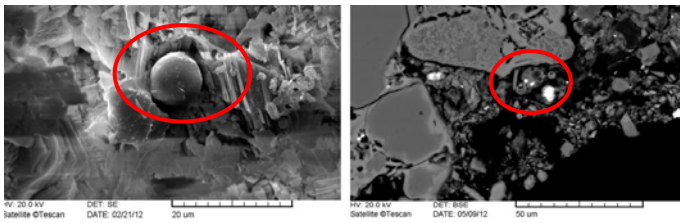

Figure 3. Scanning electron microscope pictures of natural and artificial spherules. 20 µm wide natural spherule with complex composition (Si, Fe, Ca, Al rich) in compact gypsum crust on the glazed side of a ceramic tile (on the left) (SE image) and a bright Fe-rich and several dark, carbonaceous artificial, 5-15 µm sized (in diameters) spherules in the dust layer on the unglazed (back) side of a ceramic tile (on the right) (BSE image)

Gypsum accumulates on the surface of tiles, occurring as a constituent of the deposition layer. It can be observed in different forms on the glazed and unglazed (back) sides of the ceramic tiles, depending on their exposure. On the glazed side less gypsum is present in laminar form, whereas on the unglazed, back side, where the gypsum crystals were protected from the environmental influences, dense, compact and laminar crystals also appear (Figure 4).

Gypsum generally originates from dust, which settles down and recrystallizes on the surface of tiles [2]. Another source of gypsum can be construction waste, since gypsum-containing binder is used to fix the tiles [7], or it can form by the reaction of sulphur-dioxide and carbonate.

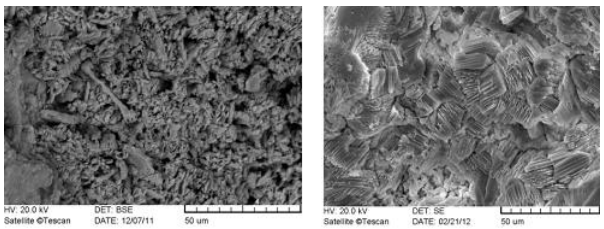

Figure 4. Dense, compact gypsum layer (on the left, BSE image) and laminar gypsum layer (on the right, SE image) on the unglazed, back side of the ceramics

We have also found traces of biological activity, which are probably residues of former microorganisms (bacteria, lichen and/or fungi) (Figure 5). These residues appear near to the cracks on the surface. In some dark deposition layer calcium oxalate (weddelite) was identified, which could have been generated by the reaction of a calcium-bearing phase and oxalic acid produced by bacteria/fungi/lichen [8]. Such organic mineral could also originate from biomineralization of microorganisms [9].

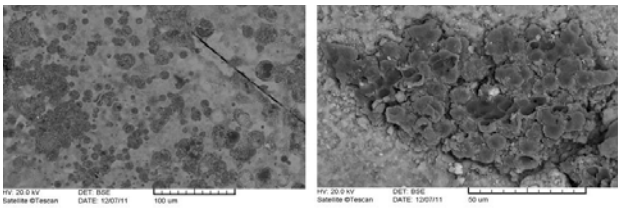

Figure 5. Residues of former organisms (bacteria/fungi/lichen) appear in "bubble-like" (on the left) and other forms (on the right) on the glazed side of the ceramics (BSE images)

The most conspicuous result of the deterioration is the appearance of a very thin weathered surface layer of glaze on some tiles of the ceramic group 2. The deposition on the weathered glaze layer shows a higher lead content than the weathered glaze itself; however both layers have lower lead content than the unweathered glaze (Figure 6).

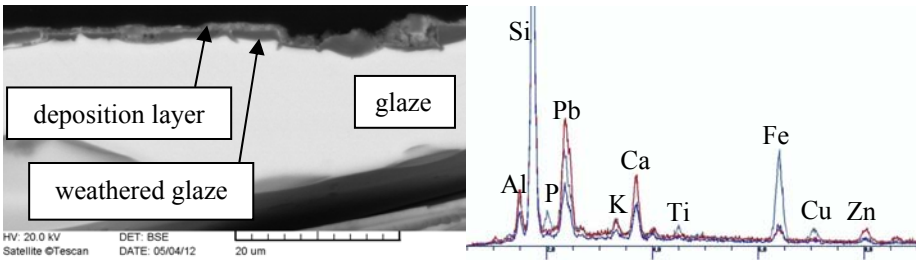

Figure 6. Cross-section of a glazed ceramic tile: the upper light grey deposition layer and the dark grey weathered glaze beneath covering the unaltered glaze (on the left). In the bottom-right corner of the BSE image a 10 μm wide crack is located in the glaze. X-ray spectra show the chemical composition of the deposition layer (grey), the weathered glaze (blue) and the unaltered glaze (red) (on the right)

One possible interpretation of the phenomenon is that lead, as one of the major components of the glaze, was dissolved, basically leached from the surface layer of the glaze by rainfall and migrated to the upper deposition layer, as Schreiner et al. observed on some corroded medieval window glass [10]. Behind this the weathered glaze is also fragmented in several places, not only on the surface but also in the glaze. Formation of cracks thus facilitates the weathering process moving toward the interior glaze (Figure 7).

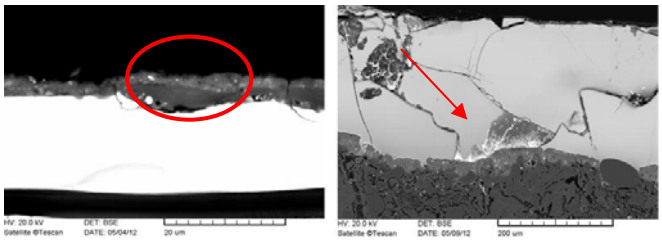

Figure 7. The weathered surface layer of glaze is fragmented (on the left) and the weathered glaze with bright precipitations rich in lead occurs along the cracks and at the ceramic-glaze interface (on the right) (BSE images)

5. Conclusion

Our purpose was to study the deterioration of Zsolnay building ceramics, mainly glazed roof tiles of the Museum of Applied Arts, Budapest. We distinguished three groups among the studied ceramics. A grey-black deposition layer was observed on the tiles, which frequently contains natural and artificial spherules. Gypsum in diverse quantity and appearance occurs on the ceramics. We identified residues of former biological activity (bacteria/lichen/fungi), confirmed also by the presence of calcium oxalate (weddelite). We demonstrated that in some tiles the glaze had started to weather. If this phenomenon continues for a long period, it will result in the deterioration of the whole glaze.

Acknowledgements

We would like to thank the Dr. Imre Takács, the director-general of the Museum of Applied Arts, for his permission to publish the results of our study, and his colleagues Gabriella Balla (art historian), Kornélia Hajtó and Katalin Csontos (restorers) for their help. We are also grateful for the help of Zsolt Bendő, Alexandra Müller, Olga Komoróczy and Miklós Csaba-Sándor in sample preparation and analysis. We would like to thank the two anonymous reviewers for their constructive criticism to improve the quality of the study.

References

[1] Fassina, V.: Air pollution in relation to stone decay. In: Lazzarini, L.–Pieper, R. (eds): The deterioration and conservation of stone: notes from the International Venetian Courses on Stone Restoration. Studies and documents in the cultural heritage, UNESCO, 1988, 16, pp. 111–181.

[2] McAlister, J. J.–Smith, B. J.–Török, Á.: Element partitioning and potential mobility within surface dusts on building in a polluted urban environment. Atmospheric Environment, 2006, 40, pp. 6780–6790.

[3] Tournié, A.–Ricciardi, P.: Glass corrosion mechanism: A multiscale analysis. Solid State Ionics, 2008, 179, pp. 2142–2154.

[4] Török, Á.: Surface strength and mineralogy of weathering crusts on limestone buildings in Budapest. Building and Environment, 2003, 38, pp. 1185–1192.

[5] Török, Á.: Deterioration-related changes in physical properties and mineralogy of limestone monuments. Engineering geology for tomorrow's cities, The 10th IAEG Congress, Nottingham, United Kingdom, 6–10 September 2006, The Geological Society of London, 2006, 297, pp. 1–7.

[6] Lefévre, R. A.–Ausset, P.: Atmospheric pollution and building materials: stone and glass. In: Siegesmund, S.–Weiss, T.–Wollbrecht, A. (eds.): Natural stone, weathering phenomena, conservation strategies and case studies. Geological Society, London, Special Publications, 2002, 205, pp. 329–345.
[7] Klemm, W., Siedel, H.: Evaluation of the origin of sulphate compounds in building stone by sulphur isotope ratio. In: Siegesmund, S.–Weiss, T.– Wollbrecht, A. (eds.): Natural stone, weathering phenomena, conservation strategies and case studies. Geological Society, London, Special Publications, 2002, 205, pp. 419–429.
[8] Schiavon, N.: Biodeterioration of calcareous and granitic building stones in urban environments. Geological Society, London, Special Publications, 2002, 205, pp. 195–205.
[9] DelMonte, M.–Sabbioni, C.–Zappia, G.: The origin of calcium oxalates on historical buildings, monuments and natural outcrops. Science of the Total Environment, 1987, 67, pp. 17–39.
[10] Schreiner, M.–Stingeder, G.–Grasserbauer, M.: Quantitative characterisation of surface layers on corroded medieval window glass with SIMS. Fresenius' Journal of Analytical Chemistry, 1984, 319, pp. 600–605.

Geosciences and Engineering, Vol. 1, No. 2 (2012), pp. 15–20

IDENTIFICATION OF FRACTURE ZONES IN A TIGHT GAS RESERVOIR

GYÖRGYBERNÁTH
Graduated Geophysicist and Geologist, H-1111 Budapest, Kende u. 14.
gyorgy.bernath@gmail.com

1. Introduction

Intensive research is going on all over the world to gain as thorough a knowledge of different unconventional hydrocarbon reservoirs as possible and to aid their modeling.One type of unconventional gas reservoirs is the tight gas reservoir. These are characterisedbyvery low permeability related to gas ($\mu_{gre\ l}$< 0.1 mD), therefore the presence of natural fractures and fracture zones, their identification and description of their orientation are essential for the development of an optimal production concept. The subject of my study was a tight gas reservoir located in a Neogenebasin of East Hungary.

Fractures and fracture zones of a reservoir can be identified with different methods and in different scales. Just like in the case of other scientific studies, it is the best way to approach the problem with different methods. In my work fracture zones of the reservoir were identified by post stack attribute analysis, examination of drilling cores and well log interpretation.

2. Overview of the applied seismic attributes

When calculating the attributes dealt with in Sections 2.1. and 2.2. I used local seismic dips. With the help of the software OpendTect so-called dip steering cubes can be produced thatcontain the inline and crossline components of a local seismic dip at a certain point. I acquired a raw dip steering cube directly from the 3D seismic by the application of "BG fast steering" algorithm. This raw cubehad to be filtered. I created differently filtered dip steering cubes like background and detailed steering cubes, according to the recommendationsof the software's user guide [1].

2.1. Most positive and most negative curvatures. In the literature a great number of curvature attributes are known [2]. From the aspect of prediction of fracture zones the most positive and the most negative curvatures are of greatest importance [3], but Gaussian curvature may also be useful [4]. If we want to examine the local shape of the surface of investigation or we are looking for flexures along faults, the joint interpretation of most positive and most negative curvatures is essential. In the latter case they appear with a high value, arranged very often in parallel bands along the faults. This is due to the characteristic shape of flexures along the faults.Positive curvature is dominant on one side of the fault (convex part of the flexure), while on the other side (concave part of the flexure) the negative curvature is dominant.

When calculating the most positive and most negative curvatures I defined in every point a geometry of 2-2 (IL-XL) step-out according to the direction of the local dips. On the 25 points marked out by the geometry a quadratic surface was fitted by the method of least squares. From the coefficients of the equation describing this surface ($g(x,y) = ax^2+by^2+cxy+dx+ey+f$) the most positive and most negative curvatures can be expressed with the help of the following formulas:

$$K_{pos} = (a+b) + \left[(a-b)^2 + c^2 \right]^{\frac{1}{2}} \tag{1}$$

$$K_{neg}\,(a+b) - \left[(a-b)^2 + c^2 \right]^{\frac{1}{2}} \tag{2}$$

It should be noted that apart from curvature attributes along classical horizons, curvatures were gained here not from the topography of an interpreted horizon but from the 3D dip steering cubes (volumetric curvature). An advantage of this method is that inaccuracies and artificial effects of interpolation appear less frequently on the maps.

2.2. Minimum similarity attribute. For attributes expressing coherence it is generally true that they are suitable for the indication of sudden changes between neighboring channel sections. They are extremely good for the detection of faults, fractured zones or boundaries related to lithological changes. There are several types of coherence attributes. The earliest (1995) and probably the best known one is the so-called coherency cube, while recently developed methods are semblance type procedures, eigen structure or variance based coherence and coherence based on the calculation of least squares [5].

The so-called similarity attribute characteristic for the coherence, used by myself,is a simple one and can be calculated quickly. Its value between two channel sections can be given by [1]:

$$sim(\underline{X},\underline{Y}) = 1 - \frac{\sqrt{\sum_{i=1}^{N} (X_i - Y_i)^2}}{\sqrt{\sum_{i=1}^{N} X_i^2} + \sqrt{\sum_{i=1}^{N} Y_i^2}} \tag{3}$$

where: sim($\underline{X}$,$\underline{Y}$) is the value of similarity between $\underline{X}$ and$\underline{Y}$ vectors containing N number of data. N can be defined by a time gate. The numerator is the Eucledean distance in the N dimension of vectors $\underline{X}$ and $\underline{Y}$, and the denominatoris the sum of the vectors' length.

I calculated similarity values in the direction of the local dips of previously counted background steering cube. By the calculation in the dip direction, sensibility of the attribute to horizontal discontinuities can be ensured. Use of a background steering cube was expedient so that the attribute should not be sensible to frequent reflection bends along faults. In order to enhance strong discontinuities I chose the minimum of the similarity values calculated between a certain point and its 9 adjacent points in the dip direction.

2.3. Spectral decomposition. Spectral decomposition of seismic channels for attribute analysis belongs to the innovations of the last decade. It is applied usually for estimation of bed thickness or stratigraphic units but it can also be suitable for identification of faults [6].

Prediction of fractures and faults by this method is based on the consideration that a seismic wave is reflected in a different way in a fractured zone: some of its components can be partially absorbed, whichcauses a characteristic trace in the reflected wave. Therefore it is expedient to examine and observe the spatial distribution of characteristic absorptions.

For the creation of a frequency spectrum of a seismic channel different DFT transforms (FFT, SWDFT) and also continuous wavelet transform (CWT) can be applied. I used the latter one in my work. Its basic principle is similar to different Fourier transforms, because

the function to be transformed is correlated with base functions, and so we gain the component in the direction of the base function. The formula defining the transformation is the following:

$$CWT(a,\tau) = \frac{1}{\sqrt{a}} \int f(t) \Psi^* \left(\frac{t-\tau}{a} \right) dt \tag{4}$$

where: $CWT(a,\tau)$ is the continuous wavelet transformed function of *f(t)*. $\Psi(t)$ is the mother wavelet, which should be localized, and $\int_{-\infty}^{\infty} \Psi(t)dt = 0$ should be true. Here, the chosen mother wavelet was the Morletwavelet, which is a harmonic wave windowed by a Gaussian function. are the base functions of the transformation, which are the compressed and shifted variants of the mother wavelet parameterized with a positive integer of τ time-shift and a real of *a*scale factor. The sign * represents the operation of complex conjugate.

I carried out the wavelet transform of the 3D seismic. Out of the gained discrete frequency components (10 Hz, 20 Hz, 30 Hz, 40 Hz, 50 Hz, 60 Hz) I found the strongest absorption lineations at 20 Hz frequency, so I choose this component for the attribute analysis.

2. Methodology and results of attribute analysis within the reservoir

Mapping of the fracture zones in the reservoir was carried out by the integrated attribute analysis of curvatures, similarity and spectral decomposition described previously. These attributes were calculated and imaged along four interpreted horizons of the reservoir. In the gained images lineations indicating fracture were marked with polylines. In my method only those lines were acceptable which were indicated by at least two of the three attributes.

In Figure 1 it is visible that the distribution of lines' directions are not randomized but arranged according to definite directions. In order to characterize orientation I calculated the azimuth values of the sections defined by the end points and nodes of the polylines, disregarding the Z coordinates.

By weighing with their own lengths I displayed the azimuth distribution of the interpreted lines in a rose diagram shown in Figure 2. Consideration of the length of sections is important because the frequency of picking nodes during the attribute analysis is a rather subjective matter. I found it expedient to develop a program in order to create an azimuth data set to be displayed in the rose diagram. This program made multiplied copies of the azimuths in a quantity proportional to their own lengths.

From the rose diagram it is obvious that the azimuth of the most characteristic strike direction is approximately 105 degrees, while that of the second one is 85 degrees. A group of lines with an azimuth of approximately 20 degrees is strongly separated from them, they are approximately perpendicular. Consequently, it can be stated that the fractures had developed because of tectonic effects.

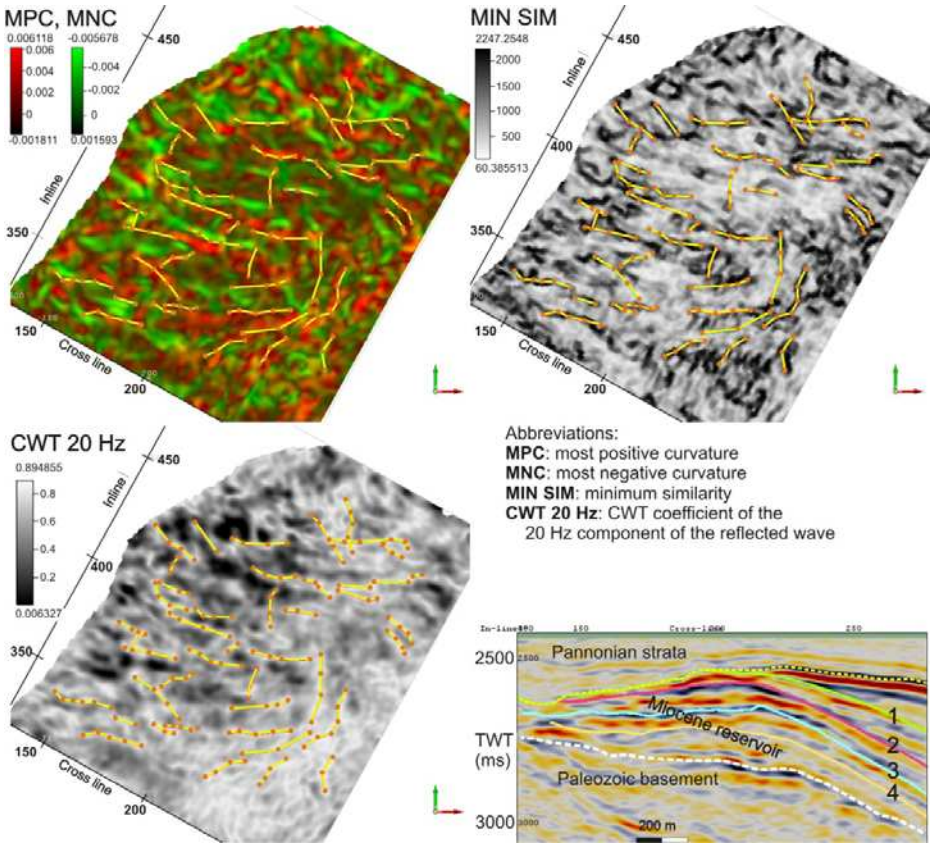

Figure 1. Seismic attribute analysis along horizon Nr. 4, within the reservoir

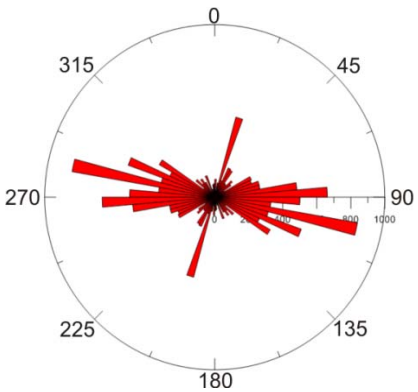

Figure 2.Rose diagram of weighed strike azimuths of the interpreted lines along horizons Nr.1, Nr.2, Nr.3 and Nr.4

3. Comparison of attribute analysis with the well logs and core data

In the second part of my studyI identified fracture intervals along boreholes. I examined macroscopicallythe cores of the compact, low porosity sandstone-argillite succession. Fractures often appeared more frequently in certain sections; steeply dipping bright sliding surfaces as well as bad core recovery rates or cores broken into small pieces referred to a fracture zone. Sometimes even fault-striae could be observed on the planes of the sliding surfaces.

For my work the following conventional well logswere available:CAL, SP, GR, RX0, Rs, Rd, CN, DEN, DTC, DTS, K, Th and U. Although none of them had been developed for fracture detection, the presence of fractures might affect the logs. The theoretical background and describing the interpretation of the logs would be far beyond the scope of this paper, but in the literature a great number of books and articles are available onthis topic, e.g. [7]. "B4" zone of "B" drilling can be seen in Figure 3. It was practical to insert the photos of the core boxes according to their measured depth next to the well logs, and in this way an integrated interpretation could be performed. Altogether 17 fracture intervals could be determined in the three boreholes of the reservoir.

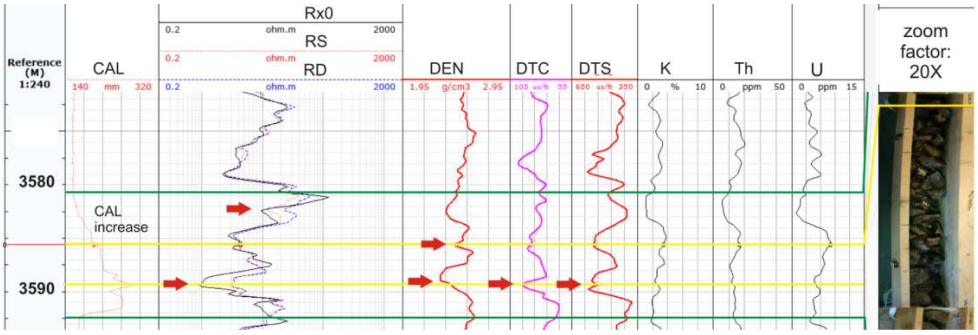

Figure 3. Determining "B4" fracture zone by well logs and drilling cores

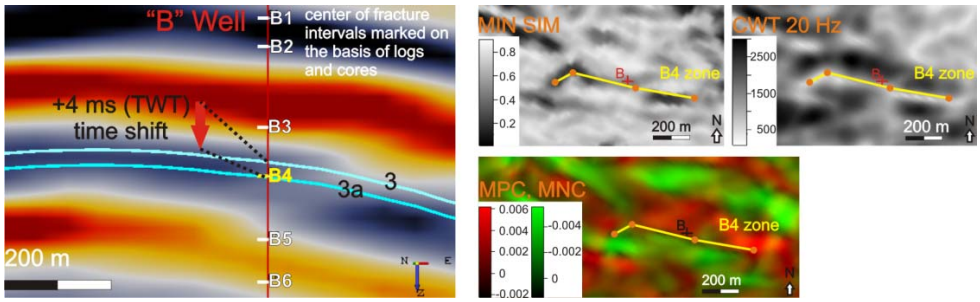

Figure 4.Confirming "B4" fracture zone by seismic attribute analysis along horizon Nr. 3a

For the joint interpretation of the wells and the seismic attributes it was necessary to tie wells to seismic with the help of a synthetic seismogram derived from acoustic and density logs. I shifted the nearest interpreted horizons to the adjacent fracture zones. Then I calculated the attributes described above. Out of the 17 fracture zones 13 could be confirmed by at least two attributes. Only in case of two zones did I find no relation with the attributes. Confirmation of the B4 zone is shown in Figure 4. For more detailed information on the study and its results, see [8].

4. Conclusions

Results show that curvature, similarity and spectral decomposition attributes were suitable for the identification of fracture zones. These attributes exploit the possibilities of 3D seismic. A great advantage of them is that they can be easily calculated. They made it possible to determine structural directions, whichcan be used in further tectonic interpretations. Although the resolution of the methods differs, they were suitable to confirm fractured depth intervals determined on the basis of logs and core examinations.

Beside the methods applied here, there are other useful ways worth trying. Image logs (FMI, BHTV) or oriented core sampling are of great help in case of interpretation along wells. Considering 3D seismic AVAZ or VVAZ analysis of pre-stack data can be a powerful tool for fracture identification. In case of post-stack analysis another possibility is to improve resolution with the help of acoustic logs, which may make even subtle faults and fracture zones visible (seismic spectral blueing).

Acknowledgements

I would like to express my thanks first of all to my thesis consultants, Dr. Balázs Kiss and PéterZahuczki, for their valuable advice and help, as well as to all thosewho assisted me during my research. I also thank MOL Plc. for providing the data sets.

References

[1] OpendTectdGB Plugins User Documentation version 4.2. dGB Earth Sciences. Copyright © 2002–2011. Available (25.08.2012): http://opendtect.org/rel/doc/User/dgb/index.htm
[2] Roberts, A.: Curvature attributes and their application to 3D interpreted horizons. First Break, 2001, 19, pp. 85–100.
[3] Chopra, S.–Marfurt, K.: Seismic Attributes for Prospect Identification and Reservoir Characterization. Tulsa, USA, 2007, pp. 73–97.
[4] Hart, B. S.–Pearson, R.–Rawling, G. C.: 3-D seismic horizon-based approaches to fracture-swarm sweet spot definition in tight-gas reservoirs. The Leading Edge, 2002,21/1, pp. 28–35.
[5] Eichkitz, C. G–Amtmann, J.–Schreilechner, M. G.: Enhanced coherence attribute imaging by structurally oriented filtering. First Break, 2012, 30/3, pp. 75–81.
[6] Neves, F.–Zahrani, M. S.–Bremkamp, S. W.: Detection of potential fractures and small faults using seismic attributes. The Leading Edge, 2004, 23, pp. 903–908.
[7] Schlumberger company: Log interpretation: Principles/Applications. Texas, USA, 1989, pp. 13-1–13-9.
[8] Bernáth, Gy.: Identification of fracture zones in a Miocene tight gas reservoir. MSc Thesis. Dept. of Geophysics and Space Sciences, Eötvös Loránd University, Budapest, 2012.

Geosciences and Engineering, Vol. 1, No. 2 (2012), pp. 21–26.

DIRECT AND INDIRECT CONNATE WATER SATURATION DETERMINATION METHODS IN THE PRACTICE OF RIAES

TIBOR BÓDI
Director, Research Institute of Applied Earth Sciences University of Miskolc,
3515 Miskolc-Egyetemváros
Pf.: 2., Hungary, bodit@afki.hu

Introduction

The recent increase in world energy demand makes it important to increase the recovery factor of the known hydrocarbon resources, and to improve the technologies making non-conventional hydrocarbons exploitable. In order to consider the economic aspects of the production of the conventional and non-conventional hydrocarbons, it is definitely required to determine amount of the in situ producible hydrocarbon (original oil/gas in place). The magnitude of the original oil/gas in place influences the economic assessment of the production methods available or being developed. It also affects investment decisions about available or newly applied technologies to a large extent.

When hydrocarbon resources are explored and developed, in order to estimate the original oil in place the so-called volumetric method is used, which, apart from the geometric extension of the resource (rock volume, pore volume), makes it necessary to determine the fluids filling the pore space. The original oil in place of the saturated oil field can be determined by the following relationship:

$$N = \frac{V\phi(1 - S_{wi})}{B_o} \quad , \tag{1}$$

where N - – original oil in place, sm^3;
V - – effective rock volume (net pay volume), m^3;
ϕ - – average porosity of reservoir rock, dimensionless;
S_{wi} - – initial or connate water saturation, dimensionless;
B_o - – oil formation volume factor, m^3/sm^3.

For conventional hydrocarbons, the minimum value of the initial water saturation is called the irreducible or connate water saturation. Connate water saturation is the amount of the water which adsorbs on the surface of the grains of the rock or on the walls of the porous pore channels (immobile with the traditional displacement methods) divided by the pore volume. For conventional hydrocarbon reservoirs, the initial water saturation is higher than or equal to the connate water saturation of the rock, so the following inequality can be written: $S_{wi} \geq S_{wc}$. It depends on the evolution circumstances whether the water saturation of the saturated oil field in our example is higher than the connate water saturation or not. For non-conventional hydrocarbon resources, the initial water saturation can be even lower than the connate water saturation.

On the basis of this, it is obvious that for the conventional hydrocarbon fields, the maximal value of the original oil in place occurs at the connate water saturation, while for non-conventional hydrocarbon fields, the connate water saturation means a good estimation

of the amount of the hydrocarbon. Thus, it can be said that in order to determine the initial water saturation and the connate water saturation, it is necessary to estimate the original oil in place.

Several methods are known from the literature to determine the saturation and the water saturation of the reservoir rocks at laboratory conditions. (i.e. the retort method, Dean-Stark distillation method, Soxhlet extraction method). All these methods assume that the tested rock sample has representative fluid saturation. However, with the traditional sampling method it is practically impossible to get a sample with representative fluid saturation. Although special sampling methods do exist (Sponge Core Barrel, Pressure core barrel), they are very expensive, and thus they are only rarely applied in industrial practice.

Considering that in most of the cases, there is no representative rock sample available, there are three methods used in the Research Institute of Applied Earth Sciences at the University of Miskolc in order to determine the connate water saturation of the rock samples. They are the following:

- Determination of connate water saturation with a rock centrifuge;
- Measuring the connate water saturation by the displacement method;
- Calculation of connate water saturation by recalculating the mercury-air capillary pressure curve for a water-air system.

The latter two methods were developed in the Research Institute of Applied Earth Sciences (RIAES)., primarily for tight, non-conventional hydrocarbon reservoir rocks.

If we have samples with representative fluid saturation, the Soxhlet extraction method is used. Here the determination methods are introduced for the connate water saturation of rock samples with non-representative water saturation.

Before the tests, the plugs are prepared for laboratory measurements by drilling, cutting cleaning and drying of the reservoir rocks. The samples are then cleaned, i.e. the drilling mud and hydrocarbon impurities are removed from them. Then they are dried in a vacuum oven until they reach a constant weight. The determination of the connate water saturation is performed on rock samples prepared in this way.

1. Determination of connate water saturation with a rock centrifuge

In the hydrocarbon industry, a frequently applied method of connate water saturation determination is obtaining the capillary pressure curve by a rock centrifuge measurement.

The theoretical background of this is the following. If the water is displaced from the 100-percent-water-saturated water wet sample with a non-wetting fluid (air, gas or oil) (drainage), and then, from the rock sample treated in this way, the oil/gas is displaced with a wetting fluid (water) (imbibition), and the displacement pressures are plotted against the water saturation of the sample, we can get capillary pressure curves like those shown in **Fig.Figure 1**. To displace the fluid from a pore channel with a radius ***r***, it must exceed the capillary pressure in the pore channel. Thus, the pressure values measured during the displacement are equal to the capillary pressure of the rock-fluid system.

In **Fig.Figure 1** it can be seen that the drainage capillary curve asymptotically approximates the connate water saturation (dashed line). This means that the further increase of the applied displacement pressure does not result in the decrease of the saturation of the wetting fluid; thus, the irreducible or connate water saturation is reached.

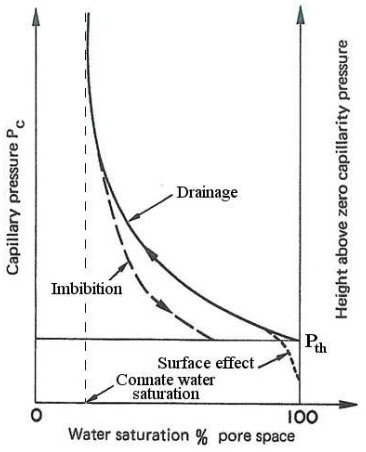

Fig.Figure 1. Capillary pressure hysteresis of porous rock

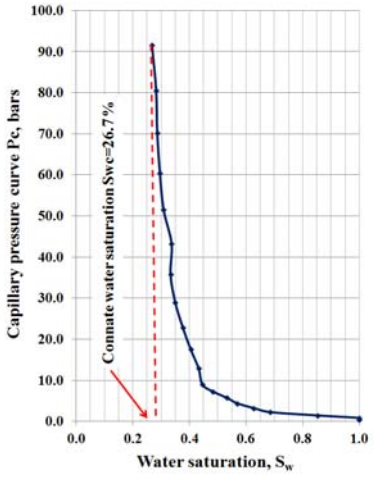

Fig.Figure 2. Capillary pressure curve (drainage) of Sample 1

Therefore, it is obvious that if the drainage capillary pressure of a tested sample is determined by a rock centrifuge, the asymptote/tangent line dragged to the curve gives the connate water saturation of the sample.

In RIAES, a CoreTest URC-628 rock centrifuge is used to determine the capillary pressure curve and the connate water saturation. The maximum rotational speed of the centrifuge is 16,500 rpm. The geometric parameters of the centrifuge ensure a maximal P_c = 100 bar reachable capillary pressure for the water-gas system. Three buckets can be placed into the rotor of the URC-628 centrifuge. Into each bucket a sample can be placed of a maximum diameter d = 1.5 inches and length l = 1-–2 inches. After the samples are saturated with water and placed in the buckets, the measurement can be started. The control program of the centrifuge keeps the rotational speed at a constant value during a previously set time interval before making the step to the next rotational speed value, until the maximum rotational speed. During the measurement, the fluid that leaves the sample is collected in collecting tubes at different rotational speed values (capillary pressure values), where the liquid level changes with this. The movement of the liquid level can be traced on a computer screen by the movement of the peaks of curves. The movement data is sent to the computer by a special camera installed on the centrifuge. By using a correctly calculated millilitre/pixel ratio (obtained from a previously performed calibration), the amount of the remaining fluid at a capillary pressure interval can be determined. Thus, the fluid saturation of the sample can also be determined.

In **Fig.Figure 2**, the centrifuge capillary pressure of a medium porosity (ϕ = 11.3%) low water permeability (k_w = 2.6 mD) Hungarian hydrocarbon reservoir sandstone sample can be seen. The connate water saturation (**$S_{w\ c}$= 26.7%**) determined from the capillary pressure curve is also shown in the figure.

2. Measuring the connate water saturation by displacement method

We place the prepared, 100-percent-water-saturated rock sample into a Hassler type core holder. To secure isolation, a mantle pressure is set that is 15-–20 bar higher than the measured pressure. Then, with a pressure control valve at the inlet of the rock sample the pressure of the nitrogen gas is gradually increased, while at the outlet, 1 bar pressure is held. At the outlet of the rock sample, a special electrode detects the start of the fluid flow, which is placed in a capillary glass tube, i.e. the pressure is measured when the non-wetting nitrogen gas penetrates the rock sample. This pressure value is considered the so-called threshold pressure.

After measuring the threshold pressure on the brine-saturated samples, the displacement is continued after the gas breakthrough until no more water production can be observed. At this point we assume that the sample plug has only connate water saturation and the other part of the pore volume of the plugs is occupied by Nitrogen. After finishing the displacement, the weight of the sample is measured. Since before the displacement the wet weight data of the plug samples were measured and their dry weights are also known, the connate water saturation of the plug samples can be calculated. The connate water saturation S_{wc} is calculated using the following equations.

$$V_p = \frac{m_{\text{wet sample}} - m_{\text{dry sample}}}{\rho_{\text{brine}}} \tag{2}$$

$$V_{w\,out} = \frac{m_{\text{wet sample}} - m_{\text{disp sample}}}{\rho_{\text{brine}}} \tag{3}$$

$$S_{wirr} = S_{wc} = \frac{V_p - V_{w\,out}}{V_p} \tag{4}$$

where ρ_{brine} - – brine density. g/cm^3;
$m_{dry\ sample}$ –- dry weight of the sample. g;
$m_{wet\ sample}$ –- wet weight of the sample ($S_w = 1$). g;
$m_{disp\ sample}$ –- weight of the sample after displacement. g;
$V_{w\,out}$ –- water volume produced from the plug sample. cm^3;
V_p –- pore volume of the plug sample. cm^3.

On a low porosity (ϕ = 7.7%), tight, extremely low absolute permeability (k_{gabs} = 0.007 mD) sandstone sample (Sample 2) from 4,095 m depth the threshold pressure (P_{th} = 73.6 bars) and the connate water saturation were determined with the introduced method. The connate water saturation was found to be S_{wc} = 67%.

3. Calculation of connate water saturation with recalculates the mercury-air capillary pressure curve for water-air system

During the mercury injection porosity measurement of the rock samples, the so-called mercury-air capillary pressure curve can be determined. In RIAES a calculation method was developed with which not only the capillary pressure of the mercury-air capillary pressure can be recalculated to an water-air system, but water saturation can also be calculated from the mercury saturation.

Thus, from the calculated capillary pressure curve for the water-air system, with the determination of the tangent and asymptote, respectively, shown in Section 1, the connate water saturation can also be determined.

Using the mercury capillary pressure curve data (air/mercury system), first the capillary pressure to water/gas system $\boldsymbol{P_{cw/g}}$ was calculated. This can be done by the following relationship:

$$p_{c\,w/g} = \frac{\sigma_{w/g}\cos\theta_{w/g}}{\sigma_{Hg/Air}\cos\theta_{Hg/air}} \cdot p_{c\,Hg/Air} \quad , \tag{5}$$

where $P_{cHg/Air}$ - – is the measured capillary pressure for mercury-air system by Pascal 140 and 440 equipment;

$\sigma_{Hg/Air}$ - – is the interfacial tension between the mercury and air (480 mN/m);

$\theta_{Hg/Air}$ - – is the contact angle between the mercury and air (141.3^o);

$\sigma_{w/g}$ –- is the interfacial tension between the water and gas at laboratory condition (70 mN/m);

$\theta_{w/g}$ –- is the contact angle between the water and gas (0^o) at laboratory condition.

After recalculating the mercury-air capillary pressure to capillary pressure valid for water-gas system, the water saturation could be calculated applying the Purcell [1] method.

Let us consider the change in saturation, ΔS, which occurs when the pressure is increased from ($\boldsymbol{P_{c1}}$.) to ($\boldsymbol{P_{c2}}$). This change in saturation is a result of liquid either entering (non-wetting liquid) or receding from (wetting liquid) all pores having capillary pressures lying between ($\boldsymbol{P_{c1}}$), and ($\boldsymbol{P_{c2}}$). All pores in this interval may be treated as if they exhibited some intermediate average capillary pressure, $\boldsymbol{(P_c)_{av}}$. If a number, ***r***, of such intervals is chosen and if **n** is the number of pores in the j^{th} interval, then we can derive the following equation:

$$\sum_{i=1}^{n_i} \frac{S_i}{(p_{ci})^2} \cong \left[\frac{\Delta S}{(p_c)^2_{av}}\right]_j = \int_{S=0}^{1} \frac{S_i}{(p_{ci})^2} \tag{6}$$

This integral may be determined by applying trapezoid rule, Simpson's rule or other numerical integration rules. With these averaging techniques, the mercury saturation could be recalculated to average mercury saturation $\boldsymbol{S_{Hgav}}$ corresponding to the average mercury capillary pressure $\boldsymbol{P_{cav}}$ that was used in the calculation of the gas-water capillary pressure curves. Then it was assumed that the water saturation $\boldsymbol{S_w}$ equals $\boldsymbol{1\text{-}S_{Hgav}}$.

Thus, the capillary pressure of water-gas system $P_{cw/g}$ was calculated along with the corresponding average water saturation S_w. These calculated data can be seen in **Fig.Figure 3** for Sample 2. In **Fig.Figure 3**, apart from the measured mercury-air capillary pressure curve and the capillary pressure curve in water-air system, the connate water saturation determined by our method is also shown. In **Fig.Figure 3** it can be noticed that the water saturation of Sample 2, which was described in Section 2, is S_{wc} = 65.89% with this calculation method.

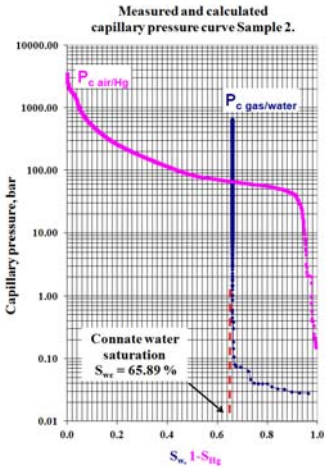

Figure 3. Measured and calculated capillary pressure curves of Sample 2

Conclusion

It can be concluded that in the Research Institute for Applied Earth Sciences, using the developed and applied methods for determining residual water saturation, the residual water saturation of rock samples can be determined with acceptable reliability considering petroleum engineering practical aspects.

The presented measurement results of Sample 2, and experience gained from our other numerous measurements on sandstone samples, show that both the direct (displacement method) and indirect (calculation from capillary pressure curve) methods are applicable in petroleum engineering practice for determining the connate water saturation.

It can be concluded that at RIAES there are a wide range of methods and technologies to determine the connate water saturation for the rock samples of both conventional and non-conventional hydrocarbon resources.

Acknowledgements

The described work was carried out as part of the TÁMOP-4.2.1.B-10/2/KONV-2010-0001 project in the framework of the New Hungarian Development Plan. The realization of this project is supported by the European Union, and co-financed by the European Social Fund.

References

[1] Purcell, W. R.: Capillary Pressures – Their Measurement Using Mercury and the Calculation of Permeability Therefrom, Petroleum Transactions, AIME, Texas, 1956.

Geosciences and Engineering, Vol. 1, No. 2 (2012), pp. 27–32.

THE ROLE OF LABORATORY TESTS IN ENHANCED RECOVERY OF CONVENTIONAL AND NON-CONVENTIONAL HYDROCARBON RESOURCES

TIBOR BÓDI[1]–JÁNOS TÓTH[2]
[1]director, Research Institute of Applied Earth Sciences,
University of Miskolc, 3515 Miskolc-Egyetemváros,
PO Box: 2., Hungary, bodit@afki.hu
[2]senior research fellow, Research Institute of Applied Earth Sciences,
University of Miskolc, 3515 Miskolc-Egyetemváros,
PO Box: 2., Hungary, toth@afki.hu

Introduction

During both the increase of the recovery factor of known oil fields and the development of producing technologies of the so-called non-conventional oil fields, several laboratory tests were performed in the past years in the Research Institute of Applied Earth Sciences of the University of Miskolc. These studies pointed out that special petrophysical laboratory measurements (pore size distribution, capillary pressure, relative permeability) and the laboratory displacement test modelling of enhanced oil recovery technologies are essential to understand the processes in the underground porous / permeable structure.

In this paper based on the laboratory tests of the past years, methods and technologies are introduced by showing measurement results as examples of special laboratory measurements (pore size distribution, displacement tests, wettability properties). Using these methods can contribute considerably to the evaluation of non-conventional hydrocarbon resources, and also to increase the recovery factor of the known hydrocarbon resources.

1. Relative permeability and relative permeability ratio functions for linearly transient flow (for displacement and phase change processes)

The initial displaced fluid saturation of a linear, cylindrical rock sample of length L, cross section A, pore volume V_p is (either oil or water) S_{ki}, and for the displacing fluid, it is S_{di}, and $S_{ki}+S_{di} = 1$. The displacement of fluid **k** can occur by fluid **d** when Δp or q_i is constant, when q_i, or Δp changes during the **displacement process** (with time t). The displacement process can be described by the following equations, which can be used for several purposes, including:

– analytical description of the displacement process,
– determining relative permeability and permeability ratios that determine the fluid exchange,
– testing the efficiency of oil displacement by water or by fluid which is not miscible with oil (like water soluble chemicals),

– reservoir engineering examination of the well draining area of oil field produced by water flooding using relationships that were written for a plane-radial flow system.

Both when Δp **= constant**, and q_i **= constant** at time intervals exceeding the moment of the breakthrough $t \geq t_a$, the linear displacement equation is valid which determines an analytical relationship between the cumulative volumes of the injected and produced volumes and can be written by the following:

$$V_i(t)/V_k = a + b\left(V_i(t)/V_p\right) \tag{1}$$

where $a = f_{kf}=1-f_{df}$, and $b = 1/(S_{dmax}-S_{di})$,

f_{kf}, f_{df} – the ratio of the displaced and the displacing fluid at the moment of the breakthrough,

S_{dmax} – maximal displacing fluid saturation, reached at infinite long displacement,

S_{di} – the initial displacing fluid saturation of the rock at the beginning of the displacement.

In case of displacement when Δp **= constant,** the change of the cumulative volume of the displacing fluid with respect to time can be written with the following relationship:

$$V_i(t) = a_2 t^{b_2} \tag{2}$$

The sum mobility of the displacing and the displaced fluids can be determined by the following relationship:

$$Y(S_{d2}) = \left(La_2 b_2^2 \left(\frac{V_p}{a_2} \right)^{\left(1-\frac{1}{b_2}\right)} \right) \Bigg/ \left(\Delta pkA(2b_2 - 1) \right) \cdot \left(\frac{V_i(t)}{V_p} \right)^{\left(1-\frac{1}{b_2}\right)} \tag{3}$$

When q_i **=** constant during the displacement, the change of the depression with respect to time for $t \geq t_a$ time intervals can be written:

$$\Delta p(t) = a_1 \left(V_i(t)/V_p\right)^{b_1} \tag{4}$$

The relationship for the sum mobility of the displacing and the displaced fluids can be written in this case with the following equation:

$$Y(S_{d2}) = \frac{q_i L}{kA(1-b_1)} \cdot 1 \Bigg/ \left[a_1 \left(\frac{V_i(t)}{V_p} \right)^{b_1} \right] \tag{5}$$

The determination of the relative permeability functions, in case of constant Δp, when μ_d and μ_k fluid viscosity values of the displaced and the displacing fluids are known, can be performed by the following procedure:

– the f_k / f_d fluid ratio can be determined from **Eq.(1**) by the following:

$$f_k = q_k/q_i = a \Big/ \left[a + b\left(V_i(t)/V_p\right) \right]^2 \quad \text{and} \quad f_d = 1 - f_k \tag{6}$$

– the parameters of the $Y(S_{d2})$ function when Δp is constant can be determined from **Eqs (1),(2),(3)**, while when q_i is constant, it can be calculated from **Eqs (1), (4), (5)**.
– the saturation of the displacing fluid at the so-called inlet section, by using **Eq. (1)**, can be determined from the following relationship in both cases:

$$S_{d2} = S_{di} + b\left(\overline{S_d} - S_{di}\right)^2 = S_{di} + b \cdot \left\{\left[\left(V_i(t)/V_p\right)\right]/\left[\left(a + b\left(V_i(t)/V_p\right)\right)\right]\right\}^2 \tag{7}$$

– thus, the relative permeability ratio can be calculated by combining the $Y(S_{d2})$ function with **Eq. (7)**:

$$k_{rd}/k_{rk} = \mu_d/\mu_k \cdot \left[a \Big/ \left(1 - \sqrt{b\left(S_{d2} - S_{di}\right)}\right)^2 - 1 \right] \tag{8}$$

– while the relative permeability of the displaced fluid by using the respective form of **Equations (1-8)** can be written by the following:

in case of constant Δp

$$k_{rk} = \frac{\mu_k L a_2 b_2^2 \left(\frac{V_p}{a_2}\right)^{\left(1-\frac{1}{b_2}\right)}}{a \Delta p k A \left(2b_2 - 1\right)} \left[1 - \sqrt{b\left(S_{d2} - S_{di}\right)}\right]^{\left(1+\frac{1}{b_2}\right)} \cdot \left[\frac{a}{b^2}\sqrt{b\left(S_{d2} - S_{di}\right)}\right]^{\left(1-\frac{1}{b_2}\right)} \tag{9}$$

in case of constant q_i

$$k_{rk} = \frac{\mu_k q_i L}{a^{(1+b_1)} k A a_1 \left(1 - b_1\right)} \left\{ \left[\left[1 - \sqrt{b\left(S_{d2} - S_{di}\right)}\right]^{(2+b_1)}\right] \Big/ \left[\sqrt{\frac{\left(S_{d2} - S_{di}\right)}{b}}\right]^{b_1} \right\} \tag{10}$$

respectively, and in both cases:

$$k_{rd} = \left(k_{rd}/k_{rk}\right) \cdot k_{rk} \tag{11}$$

Accordingly the **a** and **b** parameters of **Eq. (1)** – which is the so-called displacement equation – were determined by displacement tests, and it was completed with the parameters of **Eqs. (2)** and **(4)** – the so-called flow equations – and by knowing the basic parameters of the rock sample, by using **Eqs. (8), (9)** and **(10)**, the relative permeability of the two fluids **Eq. (10)** and their ratio **Eq. (11)** can be analytically determined.

1.1. Determination of relative permeability and relative permeability ratio functions. In **Figure 1** a rock sample can be seen whose parameters are: L = 5.67 cm, A = 11.95 cm^2, V_p = 12.79 cm^3. A displacement test was performed on it. The water permeability of the sample was k = 0.0226 D, while its initial water saturation was S_{w0} = 1. The water with $\mu_k = \mu_w$=1.04 mPa.s viscosity was displaced from the sample with $\mu_d = \mu_o$ =2.215 mPa.s viscosity oil with constant Δp = 3.5 bar depression.

The parameters of the displacement equation are: **a** = 0.552069, **b** = 1.493923, while $\mathbf{a_2}$ = 0.0263300, $\mathbf{b_2}$ = 1.036056 are the parameters of the equation which describes the change of the cumulative volume of the displacing fluid with respect to time.

Since $S_{di} = S_{oi}$ = 0, thus, $(S_{df}–S_{di}) = (S_{of}–S_{oi}) = ((1–a)^2/b = 0.1343$ and $(S_{dmax}–S_{di}) = (S_{omax}–S_{oi}) = 1/b = 0.6694$; therefore, the relative permeability ratio and relative permeability function can be determined in the interval between these two saturation values.

The relative permeability ratio can be determined from the $k_{rd}/k_{rk} = k_{ro}/k_{rw} = 2.215/1.04\cdot(0.552069/(1-(1.493923\cdot(S_o-S_{oi}))^{0.5})^2-1)$ equation (**Figure 1**), while $k_{rk} = k_{rw} = 0.3744875\cdot(1-(1.493923\cdot(S_o-S_{oi}))^{0.5})^{1.9652}\ (0.247364\cdot(1.493923\cdot(S_o-S_{oi}))^{0.5})^{0.0348}$ equation for relative permeability for water and the $k_{rd} = k_{ro} = (k_{ro}/k_{rw})k_{rw}$ the relationships for calculating the relative permeability of water and oil were used, respectively (**Figure 2**).

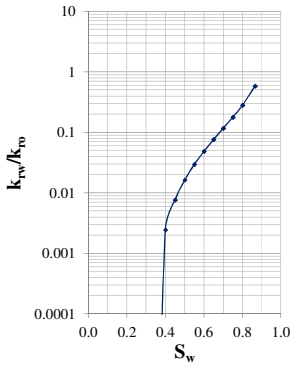

Figure 1

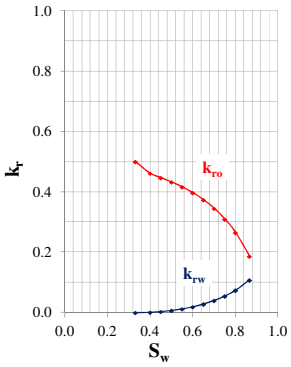

Figure 2

1.2. Displacement of oil with water and other fluids which are not miscible with oil (e.g. water soluble chemicals); evaluation of the efficiency of the displacement. In **Figure 3**, the displacement function of the slug type surfactant-polymer oil displacement (2 V_p) is shown with the preceding 1 V_p water displacement and the 1 V_p following water injection, while in **Figure 4** the respective excess displacement efficiency (related to the water displacement) function is plotted (the final result is $\Delta E_D = 0.2243$ on the tested sample). In **Figure 5** the relative permeability curves for water-oil and tenside+polimer-oil systems can be seen too.

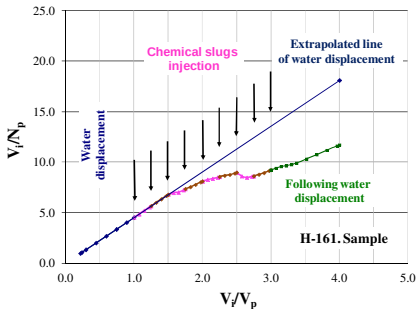

Figure 3

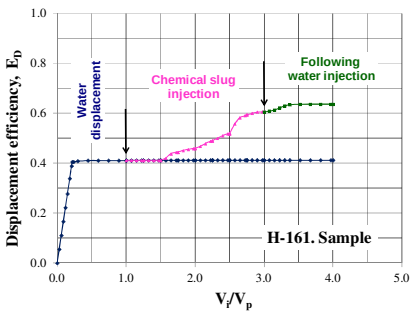

Figure 4

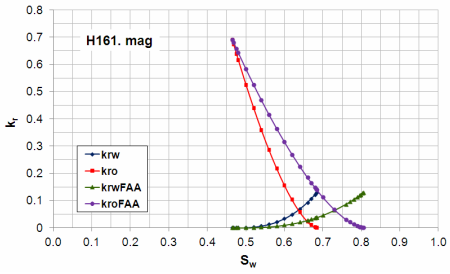

Figure 5

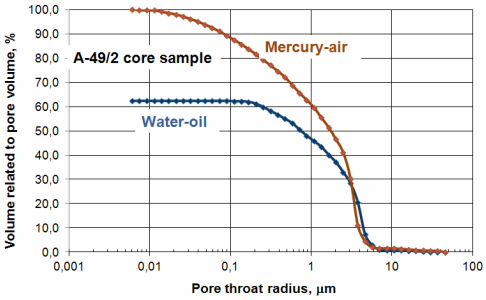

Figure 6

1.3. Passing through capillary pressure with excess oil recovery. The efficiency of the surfactant-polymer type oil displacement (a very special EOR technology) depends on whether the hydraulic pressure gradient of the displacement is high enough to exceed the capillary pressure gradient at the pore throat or not, when a decreased interfacial tension of reservoir condition water/oil phases occurs at a certain pore distribution in the reservoir rock. The successful study of the problem is shown here with the data of a laboratory surfactant-polymer slug type displacement test.

From the basic **Eq. (12)**, the capillary pressure gradient can be calculated by knowing the water/oil interfacial tension at the pore throat exit:

$$\frac{dP_{cow}}{dl} = -\frac{2\sigma_{ow}\cos\theta}{r^2}\frac{dr}{dl} \tag{12}$$

where r is the radius of the pore throat, dr/dl is the change of radius along the length at the pore throat exit, σ_{ow} is oil / water interfacial tension, and θ is the contact angle.

During the displacement tests, a hydraulic differential pressure (depression) Δp is applied along the whole length (L) of the rock assembly to move the fluids (oil and displacing fluid), thus, the following approximation can be assumed: $\Delta p/L \sim dp/dL$. Thus if the condition

$$\frac{dp}{dL} \geq \frac{dP_{cow}}{dl} \tag{13}$$

occurs, the surfactant-polymer slug type oil displacement will be efficient. On the other hand, the pore throats in sandstone-type reservoir rocks are of different radii, what means a difficulty to some extent, but their whole distribution can be given by converting measurement data for air/mercury capillary pressure to a water/oil system (see **Figure 6**).

It is a correct assumption that the oil can be displaced first from the largest pores, then from the smaller ones; thus, by knowing the data of the rock sample and taking the pore throat size distribution (**Figure 6**) into account, the capillary pressure distribution and hydraulic pressure gradient distribution can be plotted in **Figures 7–8** at $\sigma_{ow} = 0.5$ and $\sigma_{ow} =$

0.1 mN/m and at three different values of dr/dl=0.0001-0.0005-0.0010 as the function of the water saturation.

As can be seen clearly in **Figures 7–8**, at σ_{ow} = 0.5 mN/m interfacial tension, the hydraulic pressure gradient is not high enough to move the oil droplets at the following water injection, independently from the ***dr/dl*** parameter; therefore, no more oil can be produced during the process. On the contrary, at σ_{ow} = 0.1 mN/m oil/water interfacial tension (**Figure 8**), the hydraulic pressure gradient remains higher than the capillary pressure gradient throughout the whole displacement; thus, excess oil can be constantly produced.

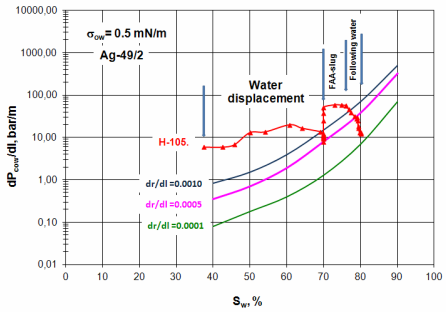

Figure 7

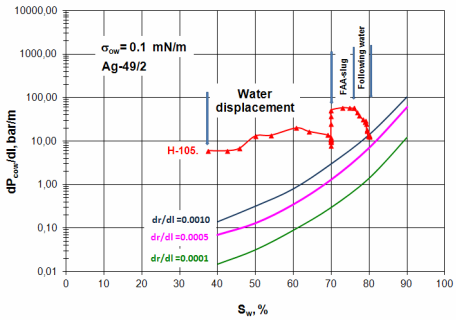

Figure 8

On the basis of these results (**Figures 7–8**) it can be assumed that the σ_{ow} interfacial tension is near 0.1 mN/m, since oil can be produced during the following water injection as well.

Summary

Taking the reviewed methods and described examples into account, it is obvious that the evaluation of the recovery factor of the conventional hydrocarbon fields, along with the increase of the oil production, make comprehensive laboratory tests necessary. The aim of performing these tests is to obtain detailed information regarding the relationships between the properties of the reservoir rock and the properties of the fluids, and to clarify the flow processes taking place in the reservoir.

Acknowledgements

The described work was carried out as part of the TÁMOP-4.2.1.B-10/2/KONV-2010-0001 project in the framework of the New Hungarian Development Plan. The realization of this project is supported by the European Union, and co-financed by the European Social Fund.

Geosciences and Engineering, Vol. 1, No. 2 (2012), pp. 33–38.

THE CONNECTION BETWEEN ROCK WALL RAVELING AND IN SITU ROCK MASS STRENGTH – A STUDY ON THE INFLUENCING FACTORS

BALÁZS CSUHANICS[1]–ÁKOS DEBRECZENI[2]
[1]assistant research fellow, University of Miskolc,
Institute of Mining and Geotechnical Engineering,
H-3515 Miskolc-Egyetemváros, bgtcsub@uni-miskolc.hu
[2]associate professor, University of Miskolc,
Institute of Mining and Geotechnical Engineering,
H-3515 Miskolc-Egyetemváros, bgtda@uni-miskolc.hu

Abstract

Definition of the stability characteristics through the strength of jointed rock masses is an important and challenging task in rock mechanics. The existing methods of rock mass classification systems use specific factors; therefore, the proper designation of these methods are important for appropriate rock wall design in open pit mining.

Besides joint sets and cleavage, which have a well-known influence on in-situ rock mass strength, this paper focuses on the factors influencing ravelling by means of in situ observations and laboratory tests.

The aim during the research was to identify the most important influencing parameters and to examine the possibility of the introduction of an in situ measurable parameter as an analytical tool.

1. Introduction

When we think of opencast mining, designers should give detailed consideration to the rock mass, with the mining methods employed and tailored to the specific geological conditions found on site. In order to define interactions between the specific geological conditions and the different environmental acting factors the following parameters are used commonly: intact rock strength, rock mass quality indicators such as RQD (Rock Quality Designation), joint distance and groundwater condition, as well as geological survey techniques and analyses based on the in situ morphology and structural characterization of the rock material.

We examined during our observations and laboratory measurements the parameters influencing slope raveling, focusing on limestone rock walls of a chosen quarry. Previous studies focused on the prediction of raveling using empirical design and rock mass classification systems which rely on e experience and judgment of the engineer. It was concluded that "analytical techniques for prediction are non-effective" and "no analytical tools are available for this task" [1].

The aim during the research was to identify the most influential parameters and to examine the possibility of the introduction of an in situ measurable parameter as an analytical tool.

1.1. Study area. The selected study area was the quarry of Mexikóvölgy, which produces limestone (Figure 1). Blasting is typically used by miners to loosen stone for quarrying. The mine is situated between 300 and 600 m above sea level over an area of 1.23 km^2. The

slope faces have an average dip between 75° and 85° at the observed area. The average height of slopes is 14 to 16 m. The elevation of the observed mining area is between 330 m and 345 m.

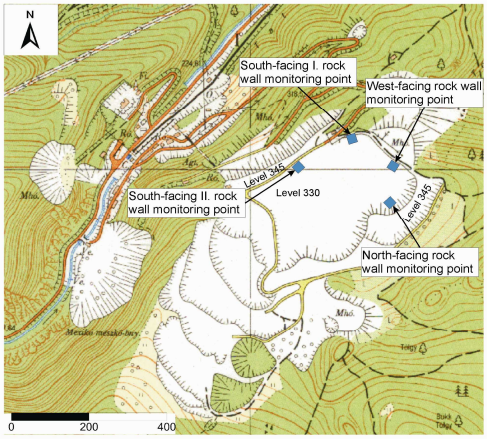

Figure 1. Map overlooking the Mexikóvölgy quarry

1.2. Geology. The rock material of the quarry is heavily fractured, grey Triassic limestone with well-developed cleavage and white-yellow calcite veins. The rock material belongs to the Bükkfennsík Limestone Formation. The dolomite content of the formation is minimal, it is represented as a few pelitic dissolution residuals. Clay-red clay cavity fillings are significant. Typical accessory vein minerals are gypsum, calcite, manganese oxides, marcasite, pyrite and iron-oxides.

2. Materials and methods

2.1. Site selection criteria and sampling methods. The observation period lasted for two months, starting on 5 March 2012. The observed rock walls were selected according to their cleavage characteristics, the homogenous and heterogeneous properties of the rock material and their orientations. Furthermore, the selected rock walls had to be located at least 50 meters away from blasting operations and should not have been disturbed for at least a year. The collection of the rock fragments was the crucial part during the exploration work.

Since ravelling causes small rock falls, we could use plastic sheets as artificial sampling areas. Six heavy-duty plastic sheets with an area of 6x20 m^2 were used to collect the rock fragments. In accordance with the average 15 m height of slopes and the 5 m length of each sheet parallel with the rock wall, it follows that the area we could sample was 6x75 m^2.

Another aspect was to select monitoring points where the crests of the slopes were clear of rock fragments, because not only the fractured material of the rock walls and the interbedding clay could ravel but also the loose rock previously deposited on the crest of the slopes. Three main monitoring zones were specified on the level of 330 m, underneath of south, north and west-facing rock walls.

The monitoring zone beneath the south-facing rock wall was divided into two different locations 100 m from each other. South-facing 1 represented a heavily fissured zone filled

with clay. The sampling zone of south-facing 2 represented a fissured rock zone without any clay interbeddings. We used one sheet for each of these monitoring zones. The west-facing zone, called 'sugar hill' by the miners, and the sampling zone beneath the north-facing wall represented the dominant fissure sets perpendicular and nearly parallel to the plane of the rock walls. Some of these fissures are filled with fine-grained rock debris or clay. Table 1 reports the summary statistics of the dry weights of the collected rock material in grams.

Table 1

Summary statistics of the collected rock fragments

Sampling points	Quantity [pieces]	Dry weight [g]					
		Average	Median	Std. deviation	Min	Max	Sum
south-facing 1	9	264.85	125.6	306.68	22.27	811.98	2383.64
south-facing 2	10	134.28	120.5	110.64	13.08	315.99	1342.84
west-facing	12	1889.29	689.69	2281.63	23.53	6531.8	22671.4
north-facing	11	4290.88	987.6	7989.55	117.95	27172.9	47199.7
Total	*42*	*1752.32*	*327.64*	*4454.82*	*13.08*	*27172.9*	*73597.6*

2.2. Temperature conditions during the observation period. The study area, because of its location, has a subalpine climate. As regards the temperature, the research period enabled us to study the effect of daily freeze-thaw cycles on the rock mass. We measured negative temperatures ten times during the evenings in March and four times in the evenings of April.

Weathering of material and expansion and contraction associated with freeze-thaw cycles are the principle causes of raveling [2]. "Freeze-thaw conditions loosen once solid rock from quarry high walls. Spring generally causes an increase of raveling activity at open cast mines, especially quarries. Diurnal freezing and thawing penetrate to centimetre-to-decimetre scale depths, producing rock debris mainly of pebble size or smaller on rock slopes"[3].

2.3. Precipitation conditions during the observation. When measuring started, a dry period had lasted for weeks. There was no rainfall in March, which was unusual as regards this early spring season. In April the total precipitation was 31 mm.

2.4. Orientations of the rock walls. The importance of orientation of the observed rock walls arises from the different solar radiation and wind-load exposure. The prevailing wind direction of the area is from the northeast and southwest, according to the direction of the valley the quarry is located in. For the sake of simplification, we took into consideration only the prevailing wind direction and we assumed that the rock wall temperature was determined by air temperature.

2.5. Rock quality designation index (RQD). The Rock Quality Designation index was developed to provide a quantitative estimate of rock mass quality from drill core logs. In 1976, Priest and Hudson found that an estimate of RQD could be obtained from joint spacing measurements made on an exposure by using

$$\mathrm{RQD}\ [\%] = 100 \cdot e^{-0{,}1\lambda}\ (0{,}1\lambda + 1)$$

where λ is the total joint frequency [joints/m] [4].

During the field works λ was measured only horizontally at approximately 2.0 m height from the toe of the slope. Table 2 shows the average joint frequency of 1.0 m and the calculated RQD.

Table 2

Rock quality classification according to RQD [5]

Sampling points	Length of the scan line [m]	$\overline{\lambda}$	RQD [%]	Rock quality classification*
south-facing 1	1.85	26.5	25.8	*Very poor/Poor*
south-facing 2	3	12.33	65.1	*Fair*
west-facing	7	11.4	68	*Fair*
north-facing	6	22.3	35	*Poor*

2.6. Laboratory strength tests. We carried out 21 uniaxial compressive tests and 24 indirect or Brazilian tensile strength tests (Table 3). The uniaxial compression tests were complemented with longitudinal deformation measuring in order to determine Young's elastic modulus (also in Table 3). Relevant reference of the ISRM (International Society for Rock Mechanics) contains the regulation of stress tests of the rocks [6, 7], thus they are not detailed here.

Table 3

Summary statistics of uniaxial compressive strength tests

Sampling points	***Quantity [pieces]***	***Unaxial compressive strength [MPa]***				
		Average	***Median***	***Std. deviation***	***Min***	***Max***
south-facing 1	5	160.66	168.26	22.24	133.39	187.17
south-facing 2	4	137.33	143.14	28.98	99.18	163.85
west-facing	4	140.95	138.54	17.34	124.41	162.30
north-facing	8	127.01	115.95	22.44	103.37	161.05
Sampling points	***Quantity [pieces]***	***Young modulus [GPa]***				
		Average	***Median***	***Std. deviation***	***Min***	***Max***
south-facing 1	5	43.83	38.57	16.78	24.59	69.37
south-facing 2	4	35.23	34.60	3.06	32.26	39.44
west-facing	4	38.33	38.98	4.07	33.17	42.21
north-facing	8	35.44	36.86	5.13	26.66	40.90
Sampling points	***Quantity [pieces]***	***Brazilian tensile strength [MPa]***				
		Average	***Median***	***Std. deviation***	***Min***	***Max***
south-facing 1	5	7.68	7.98	0.98	6.04	8.61
south-facing 2	5	6.30	6.12	1.40	4.59	8.48
west-facing	5	7.26	8.12	2.12	3.67	9.06
north-facing	9	7.94	7.94	1.90	5.08	10.59

3. Results and discussion

3.1. Comparison of fallen weight trends with rock mass quality indicator and intact rock strength parameters. We found that the characterising RQD based on the relations using total joint frequency is not consistent with the amount of crumbled rock fragments. The basis for this observation is that, although we took heavily jointed rock mass into consideration, the faults, fissure sets and joints directionality are unfavourable for the rock falling.

The trend of the amount of crumbled rock fragments shows a relatively weak relationship with the characterising uniaxial compressive strength as well as with the Young's elastic modulus. We observed that fractures influenced the strength parameters measured in the laboratory, due to sigmoidal tension gashes present in the structure of rock

samples. This phenomenon can be explained by the influence of the volume of a specimen on this mechanical behaviour, the so-called size effect. The trend of the amount of crumbled rock fragments shows a relationship with the tendency of tensile strength. This result may refer to the presence of veinlets and microfissure sets, although more testing is required to confirm the correlation.

3.2. Stereographic projections of the structural elements in the observation area. Stereograms were made by plotting measurements of the fault planes, striae and systematic joint sets at the areas of the four monitoring points (Figure 2). It can be concluded that the results fitted the characterising Neogene stress field of the mountain rim. The cleavage dipping to north-northeast forms steep fissures with smooth surfaces, frequently filled with calcite. This system is traceable over a long distance, and the planes were often transformed to faults [8].

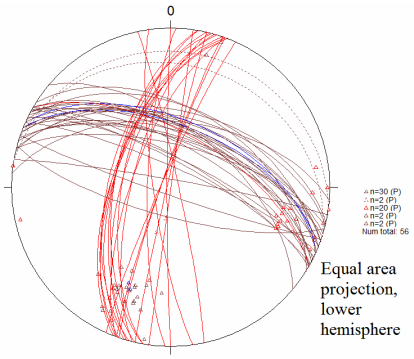

Figure 2. Stereoplot of structural orientation data from south-facing 2 monitoring point

3.3. Comparison of fallen weight trends. To compare the different weight populations, we used the Kruskal-Wallis test as a multiple-sample comparison. It tests whether the sample medians are significantly different. Since the P-value = 0.000159, less than 0.05, there is a statistically significant difference amongst the medians at the 95.0% confidence level, therefore statistically there is no connection between the four weight populations. As a consequence, these statistically different weight trends could be connected to different environmental, e.g. climatic, acting factors.

We used linear regression analysis to find connections between weight populations and the populations of climatic factors. We calculated with weight populations as the dependent variables, while temperature differences, precipitation values and maximal wind speed values were used as independent variables. Temperature differences mean the absolute values of the differences between the maximum and minimum temperatures of the observation periods. The R-Squared statistic indicates a relatively strong relationship between the variables of south-facing 1 weight population and precipitation, a moderately strong relationship for south-facing 2 and west-facing weight populations and precipitation, and a relatively weak relationship for north-facing weight population and precipitation.

P-values in the ANOVA tables show a statistically significant relationship between south-facing 1 weight population and precipitation and between west-facing weight population and precipitation.

4. Conclusion

The aim of the research was to identify factors that influence the raveling of rock blocks and fragments at steep rock walls of a strong rock mass with disturbed structure. We carried out our observations in a limestone quarry near Miskolc, Hungary. Directivity of cleavage and foliation shown with stereographic projections, joint sets of the rock walls, laboratory strength parameters, daily temperature fluctuations, precipitation and maximal daily wind velocity were taken into account during the research of factors influencing the amount of ravelling.

To sum up, it can be concluded that if the directivity of cleavage and joint sets correspond and the cleavage dipping is less than the angle of the rock slope, more significant weights of rock fragments could be observed on the sheets. There were not enough data to find connections between poor rock quality according to RQD and the weight populations of the crumbled rock fragments; further measurements are needed. Diurnal freeze/thaw cycles, precipitation and significant wind pressure have an influence on the amount of the raveled rock fragments.

It is important to emphasize that the mass data of rock fragments collected by the sheets should be taken into account as trends, not as specific values. If we would like to adopt this trend as a factor which involves the influencing factors mentioned above, then further measurements are needed.

Acknowledgements

This research was carried out as a part of the TAMOP-4.2.1.B-10/2/KONV-2010-0001 project with support by the European Union, co-financed by the European Social Fund.
The research project would not have been possible without the support of Mr. Ottó Csordás, the manager of the Mexikóvölgy limestone quarry.

References

[1] Maerz, N. H.: Highway Rock Cut Stability Assessment in Rock Masses Not Conducive to Stability Calculations Proc. 51st Ann. Highway Geology Symposium, Seattle, Washington, Aug. 29–Sep. 1, 2000, pp. 249-259.
[2] Girard, J. M.: Assessing and Monitoring Open Pit Mine Highwalls, 2001, http://www.cdc.gov/niosh/mining/pubs/pdfs/aamop.pdf
[3] Matsuoka, N. et al.: The role of diurnal annual and millennial freeze-thaw cycles in controlling alpine slope instability Permafrost – 7th Int. Conf. (Proceedings), 1998, Yellowknife (Canada), Collection Nordicana No. 55.
[4] Priest, S. D.–Hudson, J. A.: Estimation of discontinuity spacing and trace length using scan line surveys. Int. J. Rock Mech. Min. Sci and Geomech., 1976, Vol. 18, pp. 183–197.
[5] Deere, D. U.: "Rock quality designation (RQD) after twenty years", U.S. Army Corps of Engineers Contract Report GL-89-1, 1989, Waterways Experiment Station, Vicksburg, MS (67).
[6] Bieniawski, Z. T.–Franklin, J. A. et al.: Suggested Methods for Determining the Uniaxial Compressive Strength and Deformation of Rock Materials. International Journal of Rock Mechanics and Mining Sciences & Geomechanics Abstracts, 1979, Vol. 16, No. 2, pp. 135–140.
[7] Bieniawski, Z. T.–Hawkes, I.: Suggested Methods for Determining Tensile Srength of Rock Materials. Int. J. of Rock Mechanics and Mining Sciences & Geomechanics Abstracts, 1978, Vol. 15, No. 3, pp. 99–103
[8] Németh N.: Structural features of the eastern part of the Southeastern Bükk Mountains. PhD dissertation, University of Miskolc, 2005, p. 117.

Geosciences and Engineering, Vol. 1, No. 2 (2012), pp. 39–44.

HYDRAULIC BACKFILL TECHNOLOGY FOR THE CLOSURE OF THE ABANDONED SULFIDE MINE IN MÁTRASZENTIMRE

J. FAITLI[1]–R. WEISZ[2]
[1]Associate professor, Head of Institute, Miskolci Egyetem,
Nyersanyag-előkészítési és Környezeti Eljárástechnikai Intézet
3515 Miskolc-Egyetemváros. ejtfaitj@uni-miskolc.hu
[2]Project Leader, Geo-Faber Zrt.
7633 Pécs, Esztergár u. 19. robert.weisz@freemail.hu

1. Introduction

The Mátraszentimre underground base-metal mine is found 100 km east of Budapest, in the Mátra Mountains near the town of Gyöngyös. The mine used to produce about 100-150 kt of low grade Pb-Zn ore, annually. The total ore production of the mine was 3.6 Mt, with 33 kt Pb and 102 kt Zn metal content. In 1985 ore production was halted. The most hazardous environmental effect of the mine – during operation and after the temporary closure – has been the effluent acidic mine water. For a long time the effluent mine water has been treated with lime additives. Final closing of the mine requires backfilling of most of the open mine cavities, because the present high concentration of pyrite causes the Acid Rock Drainage (ARD) process. So far extensive research has been carried out by many companies and institutes [1–7]. Utilization of Hungarian fly ashes from different dumpsites was investigated by Csőke et al. [3] and Mucsi et al. [4]. Pozzolanic activity of fly ash from Mátra Power Station was examined in order to develop a new hydraulic binder with the addition of lime. As results of the different examinations it had been decided that the backfilling material should be lignite fly ash from the tailings pond of the nearby Mátra Power Plant.

The decided target volumetric concentration of the designed fly ash – water dense slurry was 35%, with the addition of 3 mass % of powder form lime, compared to the dry mass of the fly ash. The process engineering design of the hydraulic backfilling technology was carried out by the Institute of Raw Materials Preparation and Environmental Process Engineering, and the mechanical design and the construction was carried out by the GeoFaber Zrt. The system had been constructed, and after industrial size test experiments, the backfilling of the mine has begun. This paper reports on the above-mentioned hydraulic backfilling technology.

2. Determination of the pressure loss

In 1996 the Mátra Power Plant was forced by the Hungarian Authorities to improve their dilute slurry fly ash pipeline system, because of the environmental impact of the deposited dilute slurry. The Institute of Raw Materials Preparation and Environmental Process Engineering carried out the previous experiments, and the Tarján–Faitli: fine suspension-coarse mixture flow model was introduced [8–10]. The hydraulic transport system, with 50% by mass (about 34% by volume) transport concentration was designed based on this model. Since then, this pipeline has been in operation and now this is the

backfilling material source for the Mátraszentimre project. In the power plant, different fly ashes and slag are generated in the different dust separator and heat exchange process units. The original pipeline system was designed for the so-called R4 mixture (5% ECO, 20% Ljungström, 67% electrofilter and 8% slag by mass). Figure 1 shows a pressure loss curve chart for the designed 1:1 by mass, solid–liquid R4 fly ash–slag and water dense slurry. It was the final result of the 1996-98 research.

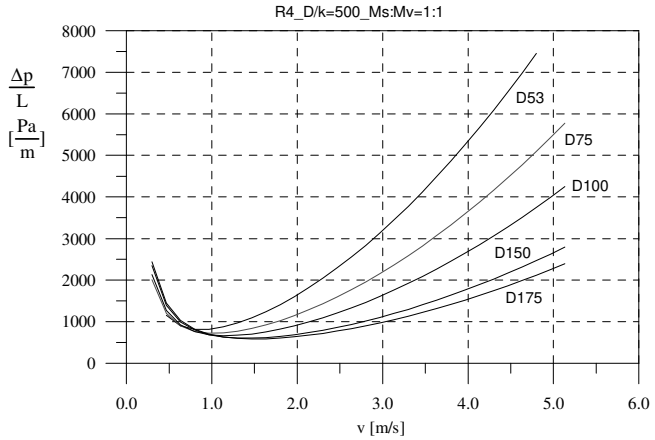

Figure 1. Calculated pressure loss curves (Δp/L – v) of fly ash–slag water mixtures of the Mátra Power Plant. Parameter: pipe diameter
(Research report 1998.)

In the last 4-5 years, during the fundamental research before the design of the backfill technology, the physical characteristics of the recent outflow of the Mátra fly ash pipeline were tested extensively. Regarding the particle size distribution, particle density and rheological properties of the water mixtures of the <160 μm fly ash suspensions (typically Bingham Plastics), the parameters are quite similar. The pressure loss could be calculated by the fine suspension-coarse mixture flow model, developed in 1998 with the application of the measured material data.

3. Concentration setting

The fly ash is transported from the tailings pond in Gyöngyös to Mátraszentimre by truck. This fly ash is wet, it contains lots of water. The hydraulic transport and particularly the backfilling require a precise concentration setting (designed as 35% by volume). This means that the amount of the excess (washing) water has to be precisely determined. The question is how to measure the moisture content of the raw fly ash. The laboratory standard method of drying at 105°C in a heat chamber is too time consuming. A quick and simple physical method was needed to measure the coarse moisture content. One possible solution might be an electric conductivity sensor, such as the TRIME [11] sensor, to measure the volumetric moisture of porous materials. The fly ash load of a truck is a three-phase disperse system, there are solids, water and air in it, and therefore the bulk density must be

known for the calculation of the dry mass of the fly ash. The measurement of the bulk density is even more difficult than the measurement of the volumetric moisture, because if the material is manipulated (a sample is taken) the bulk density changes. A simple physical method was developed with a glass volume column and a weight balance. The developed method is applicable if the particle density of the solid is known. The particle density of the fly ash can be measured by a picnometer. The particle density of the outflow fly ash of the Mátra pipeline (typically 2100 kg/m^3) has been tested over a long time and has been found to be quite stable. Of course it is tested regularly.

A sample is taken into the glass column and the weight of the wet raw sample is measured. Then a known mass of excess water is poured into the column, into the raw sample. After some mixing, the air has to be removed, and now the mass and the volume of the solid-liquid slurry can be measured. From this data, the mass of the fly ash and the coarse water moisture of the load of the truck can be calculated. If the mass of the solid and the water is known, the amount of the necessary washing water can be calculated and the exact concentration can be set.

4. The hydraulic backfilling technology

The hydraulic backfill technology in its present form is the result of long-term experimental development; some other previous versions were tested as well. The most important part of the hydraulic backfill technology is the mixing system. A schematic drawing of this system is shown in Figure 2.

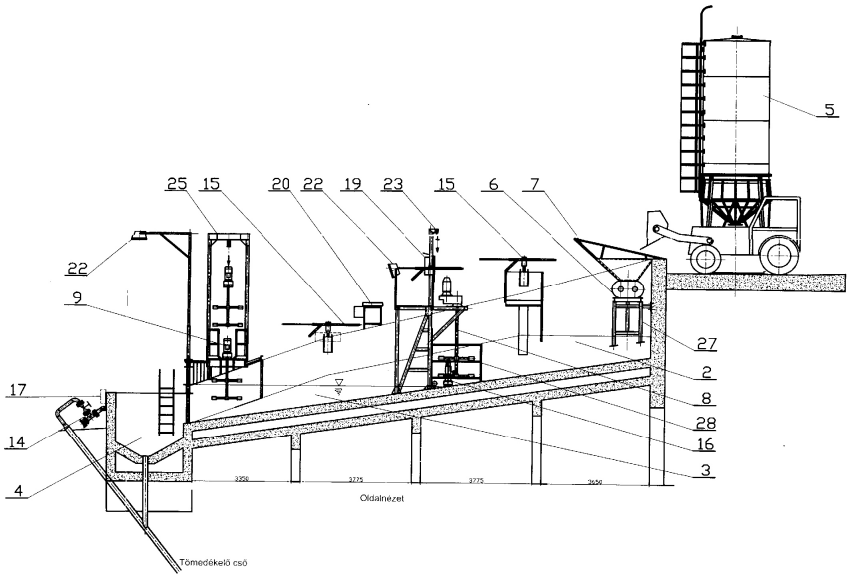

2. first mixing pool; 3. second mixing pool; 4. last pool with pipeline input; 5. lime silos; 6–27. fly ash breaker; 7. sieve; 8., 9–28. mixer; 14–17. washing water valve; 15–19. water jets; 16. slurry pumps

Figure 2. Schematic of the mixing system

The raw fly ash coming from the tailings pond by truck is deposited in the mine yard. The lime (CaO) additive is temporarily stored in two lime silos. The water used for washing the fly ash is mine water, pumped temporarily into water tanks. A wheel loader with a 1 m^3 bucket is used to load the raw fly ash into the sieve and the breaker. The installation of a disintegrator was necessary, because the aggregated fly ash has to be broken. The disintegrated fly ash moves into the first mixing pool. Washing of the fly ash is solved by high speed water jets; there are three installed water guns here. The washed fly ash slurry flows to the bottom of the mixing pool, where two rotating mixing blades are installed. Generally the determined quantity of washing water is not enough to suspend all of the loaded fly ash and previous experiments showed that the material has to be mixed and worked by the impeller of a pump as well. Well-mixed slurry behaves differently in the pipe, settles differently and the final settlement (backfill) will be different. Therefore, two submersible slurry pumps were installed. These pumps hang on cranes; the position of them can be easily set. In this way the mixing pumps can be positioned in a given concentration layer and good mixing can be performed even after the washing water has run out.

Previous experiments showed that 3% by mass lime has to be added. Lime is necessary for the adequate strength and hydraulic conductivity of the backfilled material. Lime is stored in two silos. In the bottom of the silos, there is a valve and a feeding chamber. From the feeding chamber compressed air transports the lime into a steel pipe, where a water jet pump is installed. The mixed lime suspension is fed into the first mixing pool next to the mixing blades.

When mixing of a batch (about 56 tons) is completed, the mixture is allowed to flow into the second mixing pool by opening the sluice. There are two mixing pools installed, because continuous backfilling was planned. While the mixed batch from the second pool is allowed to flow into the pipeline, the preparation of the next batch is being carried out in the first pool. The mixed fly ash from the second pool can go through another sluice into the last (third) pool. In the bottom of this pool there is the input of the backfilling pipeline (150 mm inner diameter) with a valve. After a 40 m long inclined pipe section, there is a vertical pipe section in the main mine shaft followed by a horizontal section. Depending on which level and which stope of the mine is being backfilled, the total height of the pipeline might be 320 m, and the total pipe length might be 1000 m.

After backfilling, the slurry pipeline must be washed. For this reason a separate water washing system was installed. Through the valve, the washing water can lead into the pipeline. Another important point about washing is that the quantity of the washing water going into the backfilled stope has to be minimized. For this reason the deepest point of the pipeline lies near the mine shaft, before the horizontal pipe section. From this deepest point the washing water can be discharged through another valve into the mine dewatering plant under the shaft. In this way the washing water in the pipeline (quite a large amount) does not go to the backfilled area. The above description clearly shows that this hydraulic backfilling technology requires sophisticated operation. The operation of valves and other equipment should be coordinated, and this requires a good communication system among the different working places.

5. Operational tests

At the time of writing this paper, the described hydraulic backfilling technology is in normal operation. So far about 2,000 tons of fly ash has been backfilled. This technology is the result of long-term experimental development; many operational tests were performed. In this paper two interesting things are pointed out:

The mixing system described in Section 4 was designed for semi-continuous backfilling; we stated that the flow of one mixed batch and preparation of the next batch is carried out at the same time. However, the operation has showed that the mixing of one batch (about 56 tons) of fly ash slurry in the first pool requires about 30-50 minutes, and this mixed slurry goes through the pipeline in about 5-6 minutes. The flow rate in the pipeline cannot be controlled; it is determined mainly by the geodetic height and the length of the actual pipeline. Therefore, the two parts of the system cannot be synchronized; continuous backfilling cannot be performed in this way. Backfilling can be performed periodically, but the pipeline has to be cleaned after each mixing and backfilling cycle. With good coordination and with the above-mentioned deepest point valve the quantity of washing water getting into the backfilling has to be minimized.

The other experience described here is about the pressure loss of the system. During normal operation, the main parameters of the hydraulic transport system are known. The pressure loss of a given operation is known as well. The pressure loss is equal to the hydrostatic pressure of the slurry of a height between the inflow and outflow. The hydrostatic pressure of the air can be neglected. The main parameters of a given backfilling setup were as follows: geodetic height 290 m; total pipe length 870 m; quantity of filled slurry 56 t, 40.4 m^3; density of slurry 1385 kg/m^3; and time of run in the pipe 6 min. The calculated values are: hydrostatic pressure (39.4 bar), flow rate (404 m^3/hour), average flow velocity (6.35 m/s) and the specific pressure loss (4528 Pa/m).

One remark has to be made about the flow velocity: the 6.35 m/s value is extremely high. The typical working flow velocity of drinking water pipelines is 1 m/s, because pipe wear is minimized. Pump driven fly ash hydraulic transport pipelines are generally operated near the minimum point (energy minimum) of the pressure drop curve and it is typically around 2 m/s. Larger dredging pipelines are generally operated around 4 m/s. Another remark is about the pressure loss. The measured specific pressure loss of the system is 4528 Pa/m and if we look at Figure 1 in the 150 mm pipe and extrapolate the specific pressure loss for the 6.35 m/s velocity the result is pretty much the same. The pressure loss chart in Figure 1 was made in 1998 for the Mátra pipeline by the Tarján–Faitli fine suspension-coarse mixture flow model. In the recent backfilling process the fly ash from the same power plant is used and the same concentration is set so it is a very good result. During factory-like operation the parameters are recorded and this database serves for the calibration of the model. In this way the material parameters can be determined. After some time, when the lower levels of the mine have been backfilled, the geodetic height, the driving force will be lower. The question is if the slurry will go through the long horizontal pipe section if the height is lower. From the model this can be calculated. If the height is known, the pressure loss is known. The flow velocity can be calculated in a reverse and iterative manner. If this flow velocity is higher than the deposition velocity limit, the slurry will go through. If not, a slurry pump will have to be installed.

6. Conclusions

In 1985 the Mátraszentimre underground sulfide mine was closed and only the vertical mine shaft was backfilled. Because the mine stopes remained open, the ARD process resulted acidic water outflow. Some 10 years ago the work on the final mine closure was started, and so far about 2000 tons of fly ash have been backfilled in the reopened mine. The installed hydraulic backfilling technology was result of a long time experimental developing process. The Tarján–Faitli: fine suspension-coarse mixture flow model was developed in 1998 based on the examination on the Mátra Power Plant fly ash. This model well fits on the measured data on the Mátraszentimre hydraulic backfilling pipeline.

Acknowledgements

The described work was carried out as part of the TÁMOP 4.2.1.B 10/2/KONV 2010/0001 project in the framework of the New Hungarian Development Plan. The realization of this project is supported by the European Union, co-financed by the European Social Fund.

References

[1] Debreczeni, Á.–Gombkötő, I.–Meggyes, T.: Slurry handling, treatment and transport techniques, including dewatering and paste technologies. In: T Meggyes, K E Roehl, D Dixon-Hardy (eds.) Tailings Management Facilities. London, 2008, pp. 203–261.
[2] Bokányi, L.–Varga, T.–Mádai-Üveges, V.–Paulovics, J.: Bioprocessing research in Institute of Raw Materials Preparation and Environmental Processing. Miskolc, Biotecnology&Metals 2nd International Conference, Kosice, Slovakia, 2011, p. 5–8.
[3] Csőke, B.–Mucsi, G.–Opoczky, L.–Gável, V.: Modifying the hydraulic activity of power station fly ash by grinding. Cement International No. 6/2007. Vol. 5, pp. 86–93.
[4] Mucsi, G.–Csőke, B.–Gál, A.–Szabó, M.: Mechanical activation of lignite fly ash and brown coal fly ash and their use as constituents in binders. Cement International, No. 4/2009 Vol. 7, pp. 76–85.
[5] Sivakugan, N.–Rankine, R. M.–Rankine, K. J.–Rankine, K. S.: Geotechnical considerations in mine backfilling in Australia. Journal of Cleaner Production 14 (2006) pp. 1168–1175.
[6] Wang, X.–Zhao, B.–Zhang, C.–Zhang, Q.: Paste-like self-flowing transportation backfilling technology based on coal gangue. Mining Science and Technology 19 (2009) pp. 0137–0143.
[7] Kuganathan K., 2001 Mine backfilling, backfill drainage and bulkhead construction – a safety first approach. Australia's mining monthly February, pp. 58–64.
[8] Tarján, I.–Faitli, J.: The Distinction of the Fine Suspension Flow from the Coarse Mixture Flow by Measuring of the Pressure Loss on a Horizontal Pipe. HYDROMECHANISATION 10, International Conference, Zakopane, Poland, 1998, pp.185–194.
[9] Faitli, J.: Design of transport of particulate materials by fluid flow in pipelines Part 1: Experimental equipment and model. Építőanyag, 63. évf. 1. szám, 2011, pp. 10–15.
[10] Faitli, J.: Design of transport of particulate materials by fluid flow in pipelines Part 2: Calculation of the pressure loss. Építőanyag, 64. évf. 1–2. szám, 2012, pp. 2–7.
[11] http://www.imko.de/en/products/soilmoisture/soil-moisture-sensors/trimepico32

Geosciences and Engineering, Vol. 1, No. 2 (2012), pp. 45–50.

POTENTIAL THERMAL WATER EXPLORATION IN THE TOKAJ AND SZERENCS AREA

ZOLTÁN FEJES[1]–PÉTER SZŰCS[2]–LÁSZLÓ KOMPÁR[3]–PÁL SZLABÓCZKY[4]
[1]Pre-PhD student; Department of Hydrogeology and Engineering Geology;
3515 Miskolc, University of Miskolc;
fzolee14@gmail.com
[2]Head of department, professor; MTA–ME Research Group pf Geoengineering,
Department of Hydrogeology and Eng. Geology;
3515 Miskolc, University of Miskolc;
hgszucs@uni-miskolc.hu
[3]PhD student; MTA–ME Research Group of Geoengineering,
Department of Hydrogeology and Engineering Geology;
3515 Miskolc, University of Miskolc;
hgkompar@uni-miskolc.hu
[4]Geoengineer (retired); 3515 Miskolc, University of Miskolc;
fzolee14@gmail.com

1. Introduction

The area around Szerencs lies in the border of many landscape contacts, so it is characterised by morphological diversity. The city of Tokaj lies on the southern part of the Tokaj Mountains. The region lies between the Bodrog River and the Nagy Kopasz Hill, built up from andesite, and is therefore a geologically complex unit. Both sides of Nagy Kopasz Hill are volcano tectonically and geomorphologically structured lines.

In the paper mainly Szerencs and Tokaj will be analyzed within their administrative boundaries, but also the wider environment will be mentioned. The area is bordered by Abaújdevecser to the north, Nyíregyháza to the east, Tiszaújváros to the south and Szikszó to the west (Figure 1).

In the wider environment hundreds of wells and geological exploration drilling units have been installed. The 74 wells in which effluent water is over 20°C provide the main information for thermal water research. We collected many parameters of the wells (code, EOV coordinates, depth, temperature, filtering etc.). From these data we made the basic database. The major lukewarm and hot water wells are illustrated in Figure 1.

From the wider environment we located a narrower area, where we made detailed research for Szerencs and Tokaj. This area is bordered by Tállya to the north, Prügy to the south, Mád to the east and Megyaszó to the west. On this map we marked the preliminary results of geophysical investigations, including the structural and the tectonic lines.

Szerencs and Tokaj are in a hydrogeologically disadvantageous environment. In spite of this fact, we attempt to mark the places with hot water potential, which can be used for long-term hot water supply.

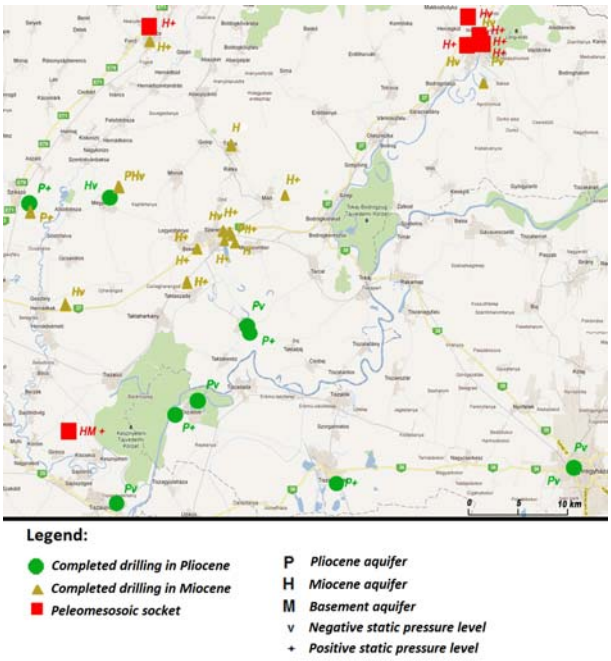

Figure 1. Map of the regional area with the warm and hot water wells

2. Geomorphological characterization of the Szerencs area

We have wide knowledge from the geological documentation, but precise depth parameters of the basement are insufficient. The depth and the material of the basement have not yet been identified (Table 1).

The tectonic and structure lines of the basement maps are approximately parallel [2–6], [11]. The lines of three basement maps from the six we used coincide, and this line lies next to Szerencs in North-South direction. This line is probably the Hernád tectonic line, from which transverse fractures may permit hot water updraft.

Table 1

Suspected materials of the basement under Szerencs

Year	Author(s)	Material of basement
1967	Viktor Dank, József Fülöp	Trias
1987	József Fülöp, Viktor Dank	Unknown material
1989	K. Brezsnyánszky, J. Haas	Unknown material
1990	Viktor Dank, József Fülöp	Unknown material
1990	János Tanács, R. Lászlóné	Unknown material
2010	János Haas	Unknown material

Different rocktypes are formed due to the updrafting solutes: hydrothermal quartz, geyserite and sweetwater quartz [8]. These rocktypes imply to postvolcanic activity. Mád and Szerencs are bounded by two faultlines: North-Southern and the East-Western direction. is the faultlines intersect at Aranka Mountain. On higher levels the peaks are covered with hydrothermal quartz, while the valleys are covered with sweetwater quartz [1], [7].

We measured the potential temperature values of the depth from the effluent water's temperature to fill in the missing geothermal data of the depth. From this we defined the geothermal gradient, which is 7.1°C/100 m, which we then used as a constant in this area.

3. Summary of geothermal research activity in Szerencs

In Szerencs's surroundings there is a North-Eastern hydrothermal zone. It can be seen on the surface: Fekete Hill – Aranka Mountain – Árpád Mountain to the North and also to the South at the Bocskai church (Figure 2). Further to the South it tends to the deep and can only be traced in the drills' stratigraphical lines. The filtering of the transversing drills through the hydrothermal quartz is on this layer, because of its high permeability. (Table 2).

Table 2

Comparison of warm water anomalies in wells of Szerencs

Well name	**Sign**	**Static water level** ***[maB]***	**Outlet temp.** ***[°C]***	**Yield** ***[l/min]***
Bakery	K-43	99.8	20	270
Chocolate factory-III	**Cs-III**	**102**	**25**	**1,500**
Motel Fridez	K-60	100	24.8	1,300

The Chocolate factory drill (Cs-III) has the highest static water level, effluent temperature and yield. With these conditions we can assume in the depth there is a plentiful yield of warm water from the aquifer layer, due to the drainage capacity of the hydrothermal quartz's zone.

Approaching the centre of the Taktaköz Basin the hydrothermal quartz formation's dip increases, so the temperature of the water increases. The tectonic breccia is intersected by disaggregated hydrothermal quartz and fractured siliceous rhyolitic tuff at a depth of approximately 220–230 m. Water with a temperature of approximately 28 °C can potentially be found at this depth. If we assume 0.5 °C /100 m updraft cooling, the fissure's temperature is still around at least 26.5 °C. When further geophysical experiments show the hydrothermal quartz's continuation to the depth (around 360 m at the periphery border), the base temperature may be about 39 °C. In this case the effluent water's temperature is around 37 °C. Surface investigations should be carried out in Vince Tanya (a dairy farm) to the south of Szerencs, in the area of Mád and Ond.

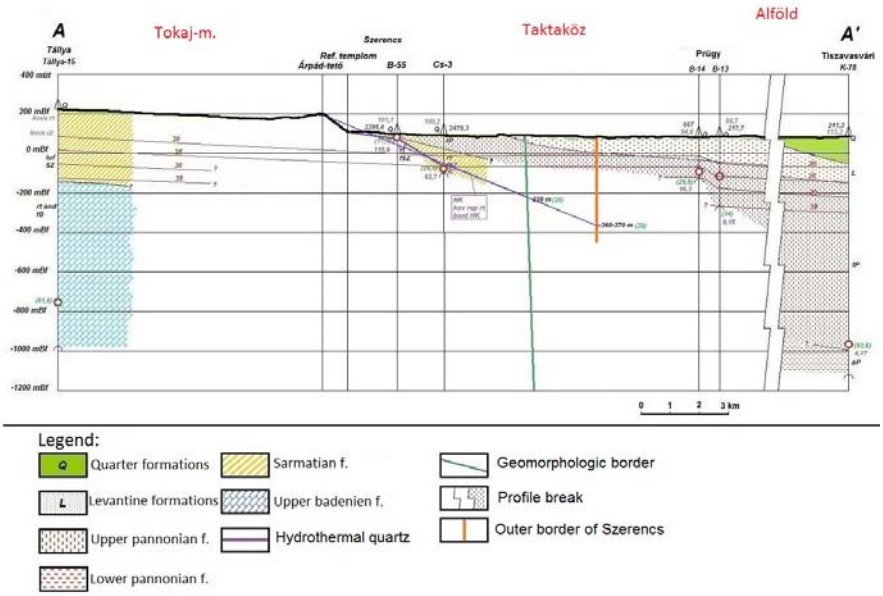

Figure 2. North-South hydrogeological profile

4. Geomorphological characterization of the Tokaj research area

In the environment of Tokaj there are many shallow drillings and wells, but these only tell us the near-surface geological structure and hydrogeological conditions. Withou deep drillings, we do not have enough knowledge about the deeper layers. As far as thermal water research is concerned, only the environment of the Sárospatak–Végardó Spa has been sufficiently examined, due to kaolin mining, uranium exploration and subsequent spa well drillings [9].

In Table III we can see the most likely rock material of the basement under Tokaj and its estimated depth according to several studies [2–6], [11].

Table 3

Material and depth of basement under Tokaj

Year	Author(s)	Material of basement	Depth
1967	Viktor Dank, József Fülöp	Supposed Perm	–1500 m
1987	József Fülöp, Viktor Dank	Unknown basement	–900 m
1989	K. Brezsnyánszky, J. Haas	Unknown basement	–1000 m
1990	Viktor Dank, József Fülöp	Unknown basement	–900 m
1990	János Takács, R. Lászlóné	Badenien formations	–900 m
2010	János Haas	Unknown basement	–900 m

As can be seen from the table, our knowledge about the consistency of the basement and is depth is uncertain. On the southern part of the Tokaj Mountains there is an andesitic

volcano-tectonic line and along this volcanic material erupted onto upper Tortonian and lower Sarmatian formations. After the end of volcanic periods huge tensile stresses affected the solidified lava. On the edges of the mountain the taper volcanic matter became less resistant to the emerging tension, thus it was cut and dropped, made the pair of structural lines [10] (Figure 3).

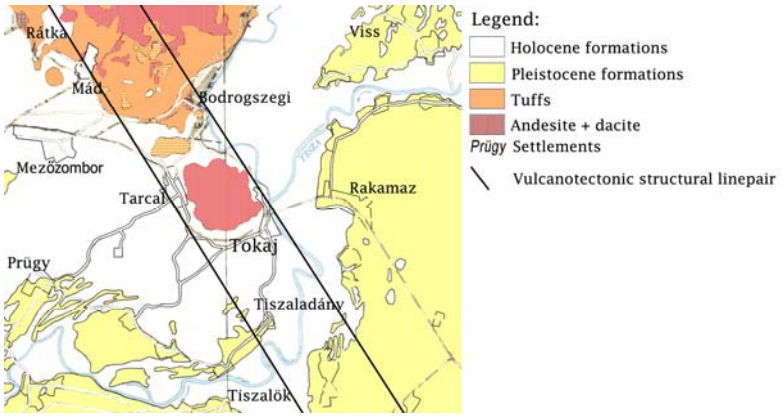

Figure 3. Pair of structural lines of Tokaj

A more detailed picture of the previously shown structural lines can be seen in Figure 4. It shows the depth's geological structure between the geothermal well at the Tokaj synagogue and the well in Viss settlement. Drilling into the structural line at sufficient depth results in inflowing hot water. Further geophysical experiments are needed to define the precise location and depth.

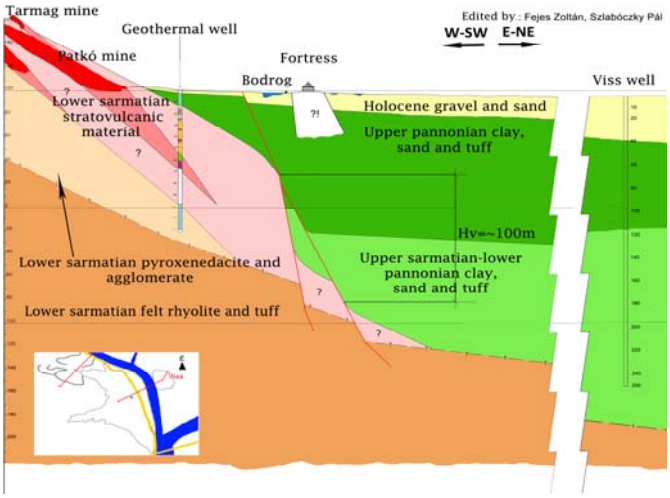

Figure 4. Conceptual hydrogeological profile

5. Conclusion

Recently the hot water supply of Szerencs and Tokaj has become more important. We used the previous research results, a thermal well database and the complex geology of the area for our exploration. In this territory the hot water providing basement is at a great depth, so it cannot be a target of thermal water research.

The highest chance of hot water updraft is in the occurrences of structural lines and layers formed by the post-volcanic activities that can be found in this area. To clarify these locations, further geophysical experiments are required in this region.

Acknowledgements

The described work was carried out as part of the TÁMOP-4.2.2/B-10/1-2010-0001 project in the framework of the New Hungarian Development Plan. The realization of this project is supported by the European Union, and co-financed by the European Social Fund.

References

[1] Boczán, B.–Franyó, F.–Frits, I.–Láng, S.–Lodvay, L.–Pantó, G.–Rónai, A.–Stefanovics, P.: Magyarázó Magyarország 200000-es földtani térképsorozatához (M34XXXIV) Sátoraljaújhely. Budapest, Műszaki Kvk., 1966.
[2] Brezsnyánszky, K.–Haas, J.: Subface geological map of the pre-tertiary basin,1989.
[3] Dank, V.–Fülöp, J.: Geological map of the palezoic and Mesozoic basement of Hungary, 1967.
[4] Dank, V., Fülöp, J.: Tectonic map of Hungary, 1990.
[5] Fülöp, J., Dank, V.: Geological map of Hungary without Cenozoic, 1987.
[6] Haas, J.: Pre-Cenozoic geological map of Hungary, 2010.
[7] Miklós, G.: Langyosvízbeszerzési lehetőségek Szerencs térségében. Miskolc, Geokomplex Kft., 2003.
[8] Pinczés, Z.–Konecsny K.: Szerencs természetföldrajza, 2006. http://www.sulinet.hu/oroksegtar/data/telepulesek_ertekei/Szerencs/konyv/002_szerenc_tmesztfoldrajza.htm
[9] Szűcs, P.–Ritter, Gy.: Sárospatak–Végardó Termálfürdő hévízkútjainak hidrodinamikai modellezése. In: A Kárpát-medence Ásványvizei. V. Nemzetközi Tudományos Konferencia. Románia, Csíkszereda, Konferencia kiadvány, pp. 1–10, 2008.
[10] Szűcs, P.–Fejes, Z.–Szlabóczky, P.: Hévízkutatás Szerencs és Tokaj környezetében, In: A Kárpát-medence ásványvizei. IX. Nemzetközi tudományos konferencia. Románia, Herkules-fürdő, Konferencia kiadvány, pp. 13–24, 2012.
[11] Tanács, J.–Rálisch, L.: Worm-eye map of the Cenozoic formations of Hungary, 1990.

Geosciences and Engineering, Vol. 1, No. 2 (2012), pp. 51–56.

SIMULATION OF A RE-ENTRY WITH CASING DRILLING UNDER HPHT CONDITIONS

GABRIELLA FEDERER-KOVÁCS
associate research scientist
Research Institute of Applied Earth Sciences, University of Miskolc
3515 Miskolc-Egyetemváros, federer@afki.hu

1. Introduction

Due to the ongoing depletion of available hydrocarbon reserves, the petroleum and oil industry is impelled to explore more daring depths and complex geological formations recently. This study aims at providing information about hydraulics and the importance of mud selection when drilling into unusual depths and formation structures, particularly in high temperature high pressure (HTHP) conditions.

HTHP wells are defined as follows [1]: the "undisturbed" bottomhole temperature is higher than 300° F (149 °C) and/or the pore pressure exceeds 0.8 psi/ft.

Since most HTHP wells contain condensates or gas under extreme pressure and temperature, special attention should be paid to planning the casing process. The following factors should be considered when planning the casing tube of a HTHP well [1]:

- the $13^{3/8}$" casing tube should be able to yield annular temperature effects.
- the $9^{5/8}$"section should not be inclined by high temperature.
- the $9^{5/8}$" and 7" sections should resist CO_2 and H_2S effects, while their nominal values are expected to be lower (due to the temperature effect).

However, despite all the precautions and proper geo-technical planning, unanticipated problems may arise, so the application of non-conventional methods may be necessary to make a well productive.

Published data show that deepening of an existing well requires half the cost of drilling a new well [2]. Drilling with casing might further reduce costs.

By simulating the sidetracking operation of a HTHP ultra deep well, this study aims to demonstrate the hydraulics and formation damage deriving from extreme conditions.

2. Problems arising

Due to the high value of the geothermal gradient, which this region is well-known for, the deep-level underground temperature is very high in Hungary. This causes the production fluid (formation fluid) in the casing to heat up the fluid entrapped between the production and the intermediate casing columns. As a result of thermal expansion, pressure will grow in the annular space between the two respective casings. If the fluid or the pressure is not released on a regular base, overpressure will occur. It may exceed the critical value defined for the pipe, which leads to its deformation or the collapse.

3. Re-entry examples

When simulating new methods, it is important to ascertain that there is a need for the modeled solution. Considering this fact, I gathered examples where this application has been used.

3.1. The Texas re-entries [2]. Re-entries usually target partially depleted reservoirs with an anticipated pressure lower than 7,000 psi. The respective wells have a 5 or $5^{1/2}$" production casing with a premium connection that provided a second barrier in case of a leak. The drilling-with-casing(DWC) connection selected for the re-entries was a $2^{7/8}$" RTS 6 which has been used successfully as both work string and production tubing in south – Texas wells.

In this typical re-entry, the existing production equipment was recovered to the point of casting failure. A whipstock was set and a window was cut in the 5" or $5^{1/2}$" casing. A modified drilling assembly was used for DWC and work underbalanced. Using a $3^{3/8}$" or $4^{1/8}$" drill bit makes it possible to drill the entire interval (500 ft–1,800 ft) without tripping. A back pressure valve was installed in the bit sub, and a landing nipple was run above the bottomhole assembly, so that an additional back-pressure valve could be run on wireline as backup. A watermelon mill was used for cutting the window and elongating it.

The (casing) drillstring was not centralised and was rotated during cementing. The BHA was shortened to 100 ft. A surface stripper was used to divert the well returns and hold pressure while making connections to minimise inflow from underbalanced zones.

The first three re-entries DWC can be considered representative of the entire program and demonstrate the advantages of underbalanced drilling with casing. One case, Well D, is described in detail in this study as a sample model for the following simulation experiments.

Well D was the first new well where underbalanced (UB) DWC was used. After setting a $7^{5/8}$" liner, drilling continued with reduced mud weight (from 17 to 15 lbm/gal) until a zone of unexpectedly high pressure was reached. At total depth, the mud weight was increased to 16 lbm/gal, but complete returns were lost in one of the upper zones, and the fluid level dropped 2,600 ft. The openhole was squeezed with LCM cement. Normally, at this point a $5^{1/2}$" drilling liner would be run across the depleted zones; instead, an attempt was made to ream out the cement squeeze with the production casing and cement it at total depth. A rotating head was installed and a $6^{1/2}$" PDC bit and conventional double-valve float collar were run on $3^{1/2}$", 12.7 lbm/ft, L80 casing with a premium connection. The mud weight was reduced to 15 lbm/gal. Gas inflow was handled by a rotating head and a large gas separator. The cemented section was drilled out in 24 hours; then a mandrel hanger was positioned above the casing bowl, with the string rotated while cementing. The $3^{1/2}$" casing was finally cemented with full returns.

3.2. Kuwait [3]. In the Kuwait region in 2004, a 22,094 ft exploration well was the second deepest, to target, through the perforation of Paleozoic and Trias strata, the exploration of hydrocarbon reserves at 18,500 to 21,500 ft. The re-perforation of the well was completed underbalanced, with a $3^{1/2}$" drillstring at 16,260 ft. The results of these completed projects are taken as a basis for the hydraulic data discussed. Since DWC is potentially applicable in Hungary in the future, it is reasonable to use in-place temperature and pressure data for

modeling the potential outcomes. Considering these data, a 12,000 ft depth level was assumed for the sidetrack simulation and associated calculations presented in this paper.

4. Formation properties

Ultra deep wells are unique not only regarding depth, but also other characteristics like special properties of the targeted formation. While drilling these wells, one or more production zones have to be penetrated to reach the targeted sedimental stratum. In Hungary, the respective average storage temperature is 200–250 °C (390–490° F) and the average storage pressure is approximately 10,000 psi (700 bar). Besides HT and HP, low porosity and permeability rates of the targeted zone can cause complications.

5. Simulating hydraulic conditions during re-entry

Due to high surface pressure and HTHP conditions, the re-entry of ultra deep wells is challenging. Since special drilling operations have to be executed under harsh conditions, uncertainties are involved in both the testing and the implementation of these projects.

Expected difficulties and issues to consider include: [3]

- high pressure and, high temperature of the well
- wall thickness of the casing and cement tubes separating the targeted formation
- extraordinary diameter of production casing
- careful selection of the drilling mud, with respect to formation properties.

Deepening and sidetracking usually target partially depleted reservoirs (for reasons of recovery). Less frequently, such operations are performed to eliminate failures resulting from casing damage or a defective cement column.

In the case of sidetracking, it is advisable to conduct wireline logging in order to detect potential damage to the casting and/or cement column and determine the exact depth. After placing a whipstock above the potential defect or at the planned depth of sidetracking, a window is cut in the 7" casing. A $4^{1/2}$" tube is selected for casing drilling, equipped with a PDC bit and 6" underreamer and a bottomhole motor. The back pressure valve is installed in the bit sub, and the landing nipple is run above the bottomhole assembly. A watermelon drill is necessary for cutting the window. In an optimal case, this assembly makes it possible to drill a 500- 1,800 ft section (~150 to 550 m) without tripping.

Sidetracking with the specified casing size is often combined with underbalanced drilling, basically in order to reduce losses. A critical point of practice is the control of formation pressure, where static and dynamic fluid pressures are used to maintain sidewall stability. If the fluid pressure is too high, the differential pressure between pore pressure and fracture pressure will drastically fall, which in an extreme case might lead to total fluid loss. Bottomhole pressure during circulating is determined as the sum of hydrostatic pressure and annular pressure loss.[4] This is called total pressure or dynamic pressure.

$$p_{din} = p_h + \Delta p_a \tag{1}$$

$$\rho_e * g * h = p_h + \Delta p_a \tag{2}$$

$$ECD = \frac{p_h \Delta_{p_a}}{g * h} \tag{3}$$

where ρ_e is equivalent circulating density and h is depth.

Hydrostatic pressure is defined by average mud density and cutting concentration in the annulus. DWC makes it possible to attain a good cutting carry index even at lower flow rates.

$$p_h = g * (\rho_m * (1 - C_v) + \rho_c * C_v) * h \tag{4}$$

where ρ_c is cutting density and C_v is the concentration of annular cutting.

Annular pressure loss depends on sidewall geometry, flow regime and rotated casing and drillstring dynamics.

In addition to the fact that well geometry differs significantly for a sidetracked well and for a conventionally drilled one, other irregularities are also considered in this paper. Due to the (joint) effect of smaller annular diameter and increased annular pressure losses, the equivalent circulating density (ECD) will be higher when drilling-with-casing is conducted. This might turn an otherwise underbalanced state/assembly overbalanced while flushing.

Let us assume that the simulated well section is drilled with 1.8 SG (15 lbm/gal) mud, supposing that this weight is enough to balance formation pressure at 12,000 to 13,800 ft (3,660 m to 4,200 m) under static conditions/in static position. The Drilling Formulas™ Excel table is used for the calculations. Tables 1 and 2 show comparative data for rotary and casing drilling under the assumed circumstances.

Perhaps one of the most relevant parameters concerning drilling at this depth and casing size is proper cutting transport. This is given by the cutting carry index calculated as below:

$$CCI = \frac{K * v_a MW}{4 * 10^5} \tag{5}$$

where K is the power law constant (consistency factor), V_a is annular velocity (ft/min) and MW is mud weight (lbm/gal)

$$K = 511^{1-n} * (PV + YP) \tag{6}$$

$$n = 3,322 * \log \frac{(2PV + YP)}{(PV + YP)} \tag{7}$$

where n is the flow behavior index, PV is plastic viscosity and YP is yield point.

In case the cutting carry index is ≥ 0.5, it denotes inappropriate cutting transport. Transport is considered good if the value is between 0.5 and 1. If it exceeds 1, cutting transport is considered excellent.

Accordingly, a value of optimal cutting carry index has been considered for the calculations. As seen, drilling-with-casing allows lower flow rates to obtain this optimal value. Due to irregular/complex hole geometry, however, annular pressure loss will be still higher (than normal). As a result, ECD is also higher.

Proper cutting carry and minimal and maximal flow rates specified for the given bottomhole assembly will limit the pump rate. However, it is important to minimise the damage made to the formation and to avoid potential mud loss.

6. Formation damage effects

If properly cemented and perforated, a 400–500 m long section could be enough to actuate production from the given well. Assuming optimal conditions and drilling without tripping, attention should be paid to the selection of mud weight. Besides avoiding

unanticipated problems, the careful selection of mud weight should ensure that the potential production zone, characterized by low permeability and low porosity, will not be contaminated so that formation damage will not cause a problem when starting production.

Table 1

Well Data

	Rotary drilling	**Casing Drilling**	
Well depth (ft)	13,800		13,800
Casing size (in)	7		7
Casing shoe depth (ft)	12,000		12,000
Bit size (in)	6		6
Drill pipe (in)	3.5	Casing (in)	4.5
Drill Collar (in)	4 3/4		–
Length of drill collar (m)	183		–
Bottomhole assembly (m)	30		30
	–	Drilling Motor	3.5
Mud properties			
Mud weight (kg/m^3)	1,800		1,800
Plastic viscosity (cP)	15		15
YP (Pa)	10		10
Cutting properties			
Cutting density (kg/l)	2,600		2,600
Cutting size (mm)	19.05		19.05

Table 2

Comparison of circulation properties when cutting carry index is equal

	Rotary drilling	**Casing drilling**
Pump rate (liter/min)	**460**	**300**
ECD (kg/m3)	**1,820**	**1,840**
Static bottom hole pressure (bar)	**760**	**760**
Dynamic bottom hole pressure (bar)	**770**	**773**
Annular pressure loss (bar)	**10**	**13**
Cuttings velocity (m/min)	**23**	**23**
Annular velocity (m/min)	**38**	**38**
Cutting carry index	**0.87**	**0.87**

Most mud contains weighting additives. However, differential pressure might allow these substances to enter in the formation and destroy it. Common types of destruction are a negative effect on relative permeability, too high capillary pressure and particle migration. All have negative effects on actuating production. In case re-entry is planned a relatively high-cost technique it is worth considering that formation damage would cause extra costs.

Proposed solutions: (1) mud and mud cake analyses, (2) underbalancing, (3) decreasing ECD: by decreasing plastic viscosity and yield point a practically acceptable small amount of bottom-hole pressure decrement can be obtained [5].

Among the listed solutions, underbalancing is proved effective by the published data. Therefore, we propose the application of this technique to the simulated well data published in this paper. The results obtained are summarised in Table 3.

Table 3

Circulation properties underbalanced

	Casing drilling	
Pump rate (liter/min)	**300**	**460**
MW (kg/m^3)	**1,680**	**1,680**
ECD (kg/m^3)	**1,700**	**1,750**
Static bottom hole pressure (bar)	**706**	**706**
Dynamic bottom hole pressure (bar)	**720**	**734**
Annular pressure loss (bar)	**13.4**	**28**
Cuttings velocity (m/min)	**23**	**41**
Annular velocity (m/min)	**40**	**57**
Cutting carry index	**0.85**	**1.23**

7. Conclusions

If a re-entry is necessary in extra deep HPHT wells, such exist even in Hungary, we frequently meet with unpredictable conditions where the benefits of casing drilling can be advantageous. Although using this technique causes elevated ECD and therefore damage the formations that may have already been problematic to produce.

For this reason calculations were made to find a solution for cases where the reservoir characteristics require casing drilling but the hydraulic conditions does not allow to drill with regularly calculated balancing mud parameters. Calculations results indicate that using a low mud weight compared to formation pressure (which means underbalanced condition) can be a solution for re-entry under the above mentioned hydraulic conditions.

Acknowledgement

The described work was carried out as part of the Tlution for cases where the reservoir characteristics require casing drilling Development Plan. The realisation of this project is supported by the European Union, co-financed by the European Social Fund.

References

[1] Rabia, H.: Oilwell Drilling Engineering-Mud Engineering and Rig Hydraulics.
[2] Gordon, D.–Billa, R.–Weissman, M.: Underbalanced Drilling With Casing in South Texas, JPT March, 2004, p. 55.
[3] Al-Bader, H.–Zaid Al-Salali,Y.–Duggiral, V. S.: Successful Discovery of Light Oil from an Unsuccessful Paleozoic Well Through Re-entry-A Case Study of HPHT Well SPE 147247
[4] Diaz, H.–Miska, S.: "Modeling of ECD in Casing Drilling Operations and Comparison with Experimental and Field Data" , University of Tulsa, 2004. IADC/SPE 87149
[5] Federer, G.: Evaluation of well hydraulics in relation with casing drilling, Freiberger Forschungsforum, 16. 18. Juni 2004.

Geosciences and Engineering, Vol. 1, No. 2 (2012), pp. 57–62.

RECONNAISSANCE ORE PROSPECTING IN NORTHEAST HUNGARY – IN CO-OPERATION OF ACADEMY AND COMPANY

JÁNOS FÖLDESSY[1]–NORBERT NÉMETH[1]–ANITA GERGES[2]–ATTILA KASÓ, JR.[2]
[1]Institute of Mineralogy and Geology, University of Miskolc,
H 3515 Miskolc-Egyetemváros, email: foldfj@uni-miskolc.hu
[2]Rotaqua KFT, 7673 Kővágószőlős, hrsz 222/2

1. Introduction

The northeastern region of Hungary has rich exploration potential for base metals. Active involvement in mineral exploration is an efficient tool to teach earth sciences to engineering students. The Institute of Mineralogy and Geology of the University of Miskolc entered into scientific cooperation with Rotaqua Ltd. in 2006 in starting exploration programs in the region. The results of this work by now: a great number of theses, student projects and research programs, not only from the University of Miskolc, but also from Eötvös Loránd University in Budapest. These are now summarised briefly by this review.

2. Western Mátra

The largest Pb-Zn mine in Hungary, Gyöngyösoroszi has been closed since 1986. The ore forms a sub-vertical array of veins, which can be traced several km in length and up to 4 m in width. The ore bodies were followed down to 350 m depth from the surface. The old sealed drifts of the Mátraszentimre and Gyöngyösoroszi Pb-Zn mines have been reopened recently to backfill the abandoned stopes and drifts. The project has been coupled with exploration of greater depths. The geological model is based on seismic profiles made by the ELGI Geophysical Institute, which indicated the possible presence of five hidden sub-volcanic intrusives in shallow position [1]. Pecsenye [2] has processed four sets of surface geochemical sampling data and correlated the geochemical anomalies with the revised geological information. The geochemical anomalies showed good coincidence with the assumed hidden intrusive centres. Stream sediment geochemical anomalies were also checked and evaluated near Parádsasvár by Gaburi [3]. Csuhanics [4] has carried out an environmental geochemical survey with a view to assessing the impact of Cd anomalies derived from the abandoned, non-reclaimed sulphide ore dumps in Parádsasvár. Students have participated in a comprehensive rock chip sampling program in the re-opened main haulage drift of the Gyöngyösoroszi mine at the +400 m a.s. level. The program aimed at revealing alteration and enrichment halos in the surroundings of the ore veins. In the study several penetrating sub-volcanic dikes were identified which were previously considered to be lava flows. No substantial enrichment halo was detected in the vicinity of the ore vein intersections. A pronounced potassic alteration zone had already been mapped on the surface earlier [5]. This was also identified in the underground sections, characteristically linked to the northern parts, near Mátraszentimre. Subsequently a vertical hydro-geological monitoring drill-hole was further deepened to 400 m for exploration, and the top alteration zone of a shallow diorite-porphyry intrusive body has been reached in one of the centres

forecast by the seismic survey. The geochemical assay data of the drill-core samples were evaluated and successfully correlated with the main haulage drift samples [6]–[7]. The cores have also been tested by using systematic laboratory acoustic measurements [8], providing evidence of different petrophysical properties between the fresh unaltered andesites and those of the alteration halo. Sulfide enrichment was restricted to the immediate vicinity of intersections of known ore veins. In contrast the Mátraszentimre vein samples have shown extensive alteration in both the mineralized zone and its surrounding exhibiting dispersed low-grade gold enrichment halo. Paprika [9] carried out fluid inclusion microscopy of the same set of samples and gave paleo-thermometry and salinity data from the lithologies of the main-haulage level. In the final summary evaluation [10] it is assumed that two temporally separated stages of ore mineralization are found superimposed in the area. The older one (Gyöngyösoroszi central vein system) is in uplifted position, where the lower portions of the hydrothermal system are exposed. The younger system postdates and hydrothermally affects the rocks belonging to the Tar Dacite Tuff horizon, and represents the higher epithermal portion of a hydrothermal system with signs of HS type gold mineralization.

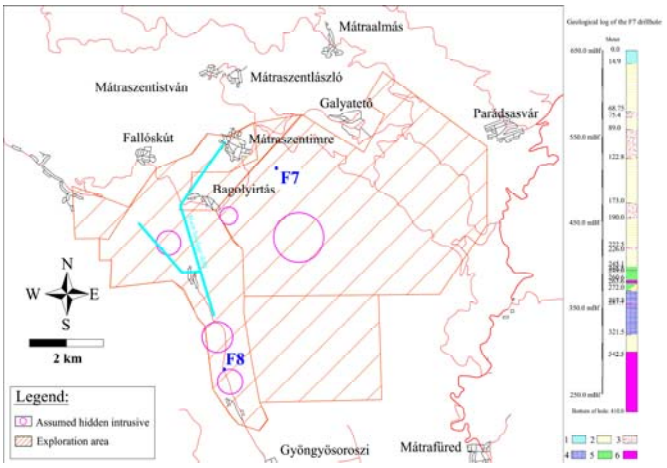

Figure 1. Western Mátra exploration blocks projected on the assumed hidden intrusive centres. The F7 drillhole log shows intersection of the cupola zone of a hidden intrusive body (modified from [7])

3. Rudabánya

Rudabánya was the largest iron ore mine in Hungary until the 1980s. Its comprehensive geological characterisation was given by Pantó [11]. The iron ore-bodies formed by metasomatic processes in Triassic limestones and dolomites, and subsequently fractured, deformed during the later structural deformations related to repeated overthrusts and to the displacement activity along the Darnó Zone. The explorations of the Rotaqua were aimed at localising the ore-bodies of the scarcely known lead and copper mineralization. The historic drill-holes, underground geology, geological profiles were interpreted and built into an integrated 3D geological model by Majoros [12]. Field explorations started with

reambulation mapping, surface sampling and soil and rock chip geochemistry [13]. Soil sample assays outlined several multi-element soil anomalies also in areas untouched by previous mining. The statistical analysis of these data was carried out by Boros [14]. Kemény [15] studied carbonate metasomatism, which was the main ore forming process of the iron ores. He defined a complex successive alteration of limestone to dolomite and siderite and vice versa. Bodor [16][17] is working on the lithological characteristics of the siliciclastic rocks of the zone, with special focus of early stage siderite ore indications hosted by these rocks. Several details of the ore genesis are still unknown, but an early stage Lower Triassic sedimentary exhalative Pb-Zn-Ba deposit is now distinguished and separately interpreted from the already known later-stage Pb-Cu-Ba ores [13][18]. The optical study supporting this distinction was carried out in cooperation with the University of Oviedo by Kupi [19]. Mineralogical evidence of similar Pb-Zn mineralization in the nearby Martonyi ore occurrence has been given by Boros [20]. The silver-bearing phases were in the focus of the research done by Lukács [21]. She verified the presence of pyrargirite (Ag-Sb sulphide) in the sulphide enrichment zone. Other minerals, like Cu-amalgams in native copper or cuprite, were also found by Kupi [22]–[23]. The lignite resources have been studied with a new resource estimation of the overlying lignite seams by Kazai [24]. The project brought advancements in the methodology of exploration, too. The drilling works encountered serious initial problems due to the extreme fracturing of rocks. This has largely been eliminated by the use of Geobor triple-tube drilling. The method was compared to conventional techniques by Kasó [25]. Field detection techniques to reveal the presence of mercury in soils were tested and reported by Lux [26].

The century-long iron ore mining has left significant environmental legacies. The proposed new mining stage will also produce impacts. The different ore and waste dumps were sampled and volumetrically assessed by Tóth [27]. The hydrological properties of the lake formed in the central largest open pit were monitored and its water quality tested by Németh [28] and Balázs [27].

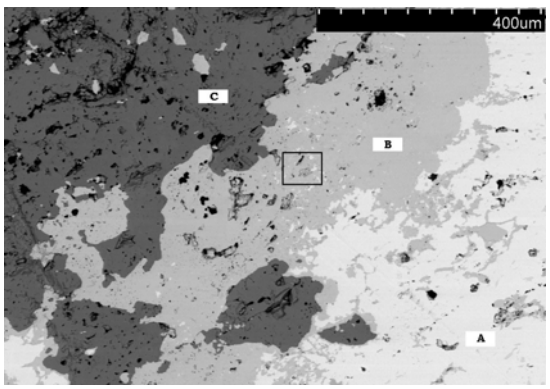

Figure 2. Backscattered scanning electron microprobe image of an ore sample from Rudabánya, baritic rim facies of the siderite. Sample RbLA003, A: galena, B: cerussite, C: barite [21]

4. Cserehát

Near Irota earlier uranium ore prospecting works have shown the presence of sulphide enrichment in Paleozoic metamorphic rocks [30]. The works re-started in 2010, with the reambulation of the previous exploration information and outcrop mapping. By reviewing the historic drillcores, an intensive hydrothermal alteration halo has been revealed. This has been followed by the re-interpretation of the underlying deep magnetic anomaly, using high sensitivity ground magnetic gradient mapping. Its interpretation was carried out by Czeglédi [31], who has worked out a high-resolution 3D anomaly model of the possible source rock-mass. The explorations are still under way.

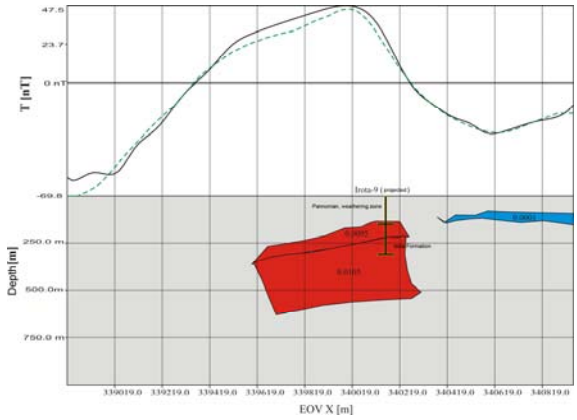

Figure 3. Interpretation of ground-magnetic measurements at Irota (at the Irota-9 dirllhole); bodies of enhanced susceptibility used in the model result in the fitted curve along a surveyed section [31]

5. Conclusions

Early-stage explorations require a great deal of data collection, transformation and preparation work, frequently beyond the possibilities of industrial companies. The capabilities of universities may give a substantial added value to exploration programs.

Participation in industrial projects offers the opportunity to students to solve real exploration problems, which are seldom provided by academic coursework. During these programs nine studies on the undergraduate level and 16 studies on graduate level were prepared, some of them published, providing a multi-faceted impression about the nature, depth and volume of works in mineral explorations.

Acknowledgements

Rotaqua Ltd. has kindly given permission to access and publish proprietary company information and provided a great number of summer internships for our students.

A great number of industrial consultants and university lecturers have helped students to prepare high-quality theses and project reports. Their time and effort is gratefully acknowledged here.

The review was prepared as part of the TÁMOP-4.2.1.B–10/2/KONV–2010–0001 project in the framework of the New Hungarian Development Plan. The realization of this project is supported by the European Union, co-financed by the European Social Fund.

References

[1] Schönviszky, L.–György, L.–Szalay I.: Jelentés a Középső- és Nyugat-Mátra 1985. évi geofizikai előkutatásáról. I. kötet. Gravitációs és szeizmikus előkutatás a Zagyva-árokban, nagyfrekvenciás reflexiós mérések a Mátrában. MBFH Archive, AD-613. 1986.
[2] Pecsenye, P.: A felszíni geokémiai mintavételek adatainak összefoglaló értékelése a Közép- és Nyugat-Mátrában. Unpubl. Dipl. Thesis, Univ. Miskolc, 2010.
[3] Gaburi, I.: Ásványtani és geokémiai vizsgálatok a parádsasvári ércesedés területén. Unpubl. Dipl. Thesis, Univ. Miskolc, 2010.
[4] Csuhanics, B.: Environmental geochemical investigations of the Parádsasvár polymetallic mineralization (Mátra Mts, Hungary). Unpubl. Dipl. Thesis, Univ. Miskolc, 2010.
[5] Varga, Gy.–Csillagné, Terplánszky, E.–Félegyházi, Zs.: A Mátra hegység földtana. MÁFI Évkönyv, 1975, 57/1.
[6] Czeglédi, B.: Vulkáni képződmények és hidrotermális elváltozások geokémiai jellemzése a gyöngyösoroszi altáró mintavételezése alapján. Unpubl. Student Research Society study, Univ. Miskolc, 2009.
[7] Czeglédi, B.: Az F-7 fúrás földtani rétegsorának vizsgálata és értelmezése. Unpubl. B.Sc. Thesis, Univ. Miskolc, 2010.
[8] Holló, D.: Dinamikus rugalmassági állandók meghatározása a Nyugat-Mátrában mélyített F-7 jelű víz- és érckutató fúrás magmintáin. Unpubl. Student Research Society study, Univ. Miskolc, 2011.
[9] Paprika, D.: Kőzetátalakulási és ércképződési folyamatok a gyöngyösoroszi altáró szelvényén. Unpubl. M.Sc. Thesis, Eötvös Loránd Univ., Budapest, 2010.
[10] Földessy, J.–Gerges, A.–Kasó, A. jr.: Előrehaladási jelentés „Közép-Mátra" kutatási jog területére. Rotaqua Ltd. manuscript, 2011.
[11] Pantó, G.: A rudabányai vasércvonulat földtani felépítése. Yearbook of the Hungarian Geological Institute, 1956, 44/2, 329–637.
[12] Majoros, P.–Földessy, J.: Bányászattól a kutatásig – Egyszerű térinformatikai eszközök alkalmazása rudabányai kutatási területen. In: Lóki J.–Demeter G. (szerk.): Az elmélet és gyakorlat találkozása a térinformatikában. 2010, p. 443.
[13] Földessy, J.–Németh N.–Gerges, A.: A rudabányai színesfém-ércesedés újrakutatásának előzetes földtani eredményei [Preliminary results of the re-exploration of the Rudabánya base metal ore deposit]. – Földtani Közlöny, 2010, 140/3, pp. 281–292.
[14] Boros, A.: A felszíni geokémiai mintavételek adatainak összefoglaló értékelése Rudabánya körzetében. Unpubl. Dipl. Thesis, Univ. Miskolc, 2010.
[15] Kemény, B.: Karbonátos kőzet-átalakulások a rudabányai vasérces összletben. Unpubl. Dipl. Thesis, Eötvös Loránd Univ., Budapest, 2009.
[16] Bodor, S.: A rudabányai alsó-triász sziliciklasztos képződmények vizsgálatának eredményei. University of Miskolc, Doktoranduszok fóruma conference volume, 2011, pp. 20–23.
[17] Bodor, S.–Földessy, J.: Petrological and geochemical study of the Lower Triassic siliciclastic succession of the Rudabánya ore deposit (NE Hungary). Acta Mineralogica-Petrographica, Abstract Series 7: 20. 2012.
[18] Németh, N.–Földessy, J.–Kupi, L.–Zajzon, N.–Zelenka, T.: Zn-Pb mineralization in Rudabánya (Hungary): a recognized new deposit type. Acta Mineralogica-Petrographica, Abstract Series 7: 94., 2012.
[19] Kupi, L.: Paragenetikai vizsgálatok a rudabányai színesfémércesedésben transzparens- és opakoptikai megfigyelések alapján. Unpubl. company report, Miskolc, 2011.

[20] Boros, G.: A Martonyi vasérc-színesérc-előfordulás földtani újraértékelése. Unpubl. Dipl. Thesis, Univ. Miskolc, 2011.
[21] Lukács, A.: Silver bearing sulphides in the Rudabánya ore mineralization. – Unpubl. Dipl. Thesis, Univ. Miskolc, 2008.
[22] Kupi, L.–Szakáll, S.–Zajzon, N.–Kristály, F.–Fehér, B.: Copper-amalgams from the Rudabánya base metal mineralization, NE Hungary. Acta Mineralogica-Petrographica, Abstract Series 6: 430., 2010.
[23] Zajzon, N.–Szentpéteri, K.–Fehér, B.–Szakáll, S.–Kupi, L.–Barkóczy P.: New data on Cu-amalgams, kolymite and belendorffite from Rudabánya, Hungary. Acta Mineralogica-Petrographica, Abstract Series 7: 160., 2012.
[24] Kazai, L.: Rudabányai lignit előfordulás ásványvagyon becslése. Unpubl. B.Sc. Thesis, Univ. Miskolc, 2011.
[25] Kasó A. jr.: A Rudabányai-hegység T-11-es kutatófúrás rétegsorának vizsgálata és értelmezése. Unpubl. B.Sc. Thesis, Univ. Miskolc, 2011.
[26] Lux, M.: A higany terepi kimutatási módszerei és eloszlási törvényszerűségei Rudabányán. Unpubl. Student Research Society study, Univ. Miskolc, 2008.
[27] Tóth, P.: A rudabányai érces meddőhányók haszonanyag tartalma, új vagyonbecslése. Unpubl. B.Sc. Thesis, Univ. Miskolc, 2008.
[28] Németh, Á.–Kovács, B.: A rudabányai bányató hidrológiai és hidrogeológiai viszonyainak vizsgálata. Unpubl. company report, Miskolc, 2011.
[29] Balázs, I.: Rudabányai bányató hidrológiai és vízkémiai viszonyai. Unpubl. B.Sc. Thesis, Univ. Miskolc, 2011.
[30] Csáki, F.: A Csereháti-dombvidék paleozoos képződményeinek komplex földtani vizsgálata. PhD dissertation, Eötvös Loránd Univ. Budapest, 1976, p. 111.
[31] Czeglédi, B.: Mágneses mérések a Csereháton, egy érctest múltbeli kialakulásának nyomozása. Unpubl. Student Research Society study, Univ. Miskolc, 2011.

Geosciences and Engineering, Vol. 1, No. 2 (2012), pp. 63–68.

GEOPHYSICAL MAPPING OF THE RUDABÁNYA MINE WASTE ROCK PILES AND HÁMOR LAKE

GÁBORNÉ GYENES[1]–LÁSZLÓ BUCSI SZABÓ[1–2]

[1]Háromkő Ltd., 3519, Esze Tamás u. 1/A

[1]gyenes.gaborne@gmail.com, [2]bucsil@t-online.hu

1. Introduction

Ore and mineral mining at Rudabánya dates back to ancient times. Initially, sulphide ores and materials of surface oxidation zone were utilized. Later carbonate iron ore was produced here, with additional silver, copper and lead ores. Large-scale iron ore mining began in 1880 and lasted for a century. During the mining activity, millions of tonnes of waste rock material were deposited on the surface near the villages of Rudabánya and Felsőtelekes. Because of technological developments and new ideas the material of the spoil tips – iron oxides and remaining sulphides, barite – can be utilised. Due to Háromkő's previous successful investigations on the Toka-Creek region [1] and refuse damp near Miskolc [2], the company was requested to take part in the project of "Rudabánya Ore Occurrences Research Development Program for Geological Studies". The task was: general geological mapping of the area and identifying the site boundary and the inner structure on the heaps. The four areas are the following: Rudabánya No. 1. heap – a "Baritmix" landfill and three areas near Felsőtelekes. The area No. 1 and no. 3 were studied in detail and only exploratory measurements were performed on other two heaps.

Considering the extent of fields and quality of materials in the subsurface we combined four geophysical surveying methods: multielectrode profiling, VES sounding, IP sounding, total magnetic field and gradient measurements and GPR. These methods have been successfully applied abroad [3, 4].

During the processing of data measured we determined near-surface resistivity distribution of multi-electrode section and the real resistivity distribution from the VES data as well. From the IP data the types of contamination were determined. The earliest IP sounding, Turai interpreted corrected electric conductivity [5] was introduced for the mapping of contamination. Measuring the total magnetic field and magnetic gradient were successful.

As a second example of geophysical mapping, we briefly discuss the resistivity profiling of Hámor Lake. A floating Schlumberger array probe was used on Lake Hámor's water surfaces and sonar measurement with so-called "fish radar" was utilised within the project of "Diagnostic and Research Work of Miskolc's Endangered Karst Aquifer".

2. Measurements and interpretation

Vertical electrical soundings, and multielectrode measurements were carried out with Hungarian Diapir-10 instrument made by ELGI, using traditional Schlumberger array, $AB_{max.}$= 200 m supply electrode distance reaching a penetration depth of approx. 40 m-s. For the profiling 5-5-5 m-s… Wenner-arrangement was used along a 160 m line. VES curves were processed, then calculated by Marquardt 1D inversion, and the multielectrode

profiling's data were evaluated by Res2D inversion. This way real specific resistivity sections were made and finally interpreted as (geological) sections.

Magnetic field mapping was performed with a G-856 GEOMETRICS Proton Precession Magnetometer.

As for the GPR; on the ground surface a GSSI instrument with 100 MHz and 270 MHz antennae (Radan-6 software) was used, and in the water LOWRANCE LMS-240 sonar.

Large quantities of measurements were taken in the first area (No. 1.) which is waste rock full of dry ferromagnetic material, next to the ore-dressing factory. Figure 1 shows the resistivity section based on the VES data. Close to the surface among points RB101-102, 103-104 and 105-107 one can observe a high anomaly zone with 200–1000 ohm-meters. The result suggests a dry and solid material. Between points RB102 and 104 there is a landfill of looser structure. At a depth between 8 and 10 m-s the material of the heap changes into a reactive material. The anomalous IP data interpreted at the RB101 and 104 points reflects on a strong oxidation-reduction zone with good electrical conductivity; simply put, it is a highly polluted area. Between RB 103 to 105 points under the depth of 20 meters a large imbedding with high resistivity can be seen. This resistive anomaly is not due to the waste rock, it is believed to be the limestone basement.

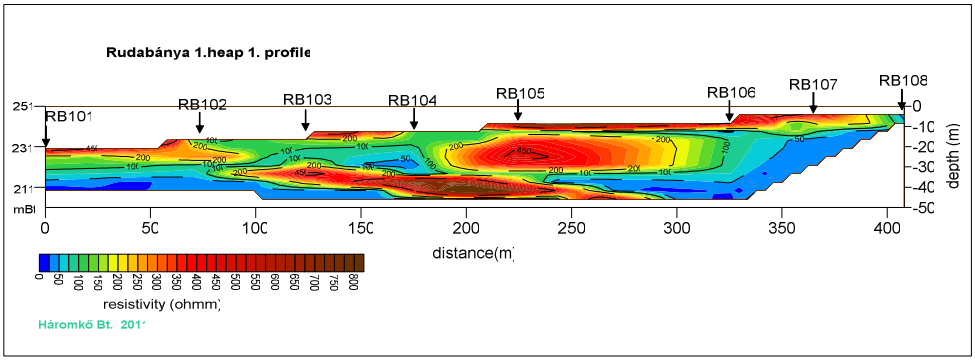

Figure 1. Resistivity section

Figure 2 shows the results of IP measurements –for two stations of the first profile. Surprisingly at several points high values appeared. This type of pollution is substantial in terms of the metal and redox-polarization. Induced polarization is a very useful geophysical method in general, and especially in the detection of environmental contamination.

Figure 3 presents a magnetic profile measured along a profile parallel to the first geoelectric profile. This part of the magnetic field indicates a very high level, a 2000–3000 nT surplus to the natural background. At the same place this zone is very heavily polluted as is shown by the IP measurements: metallic and electrochemical polarizations are assumed and the reactive material relates to a ferromagnetic metal content.

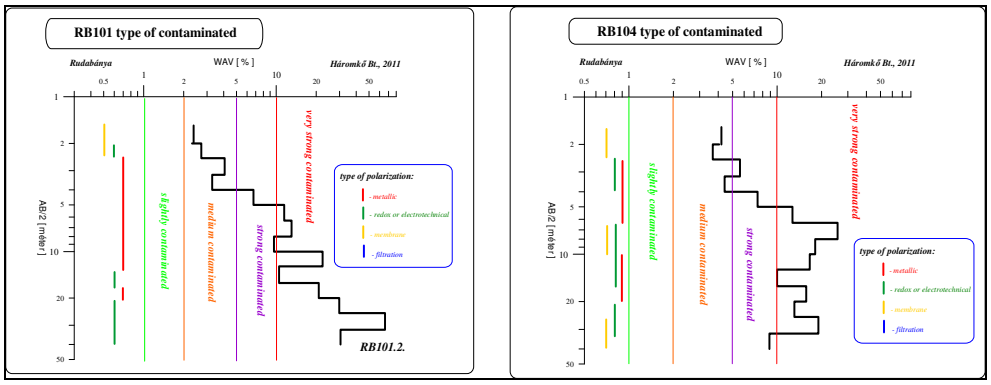

Figure 2. Type of polarization and contamination

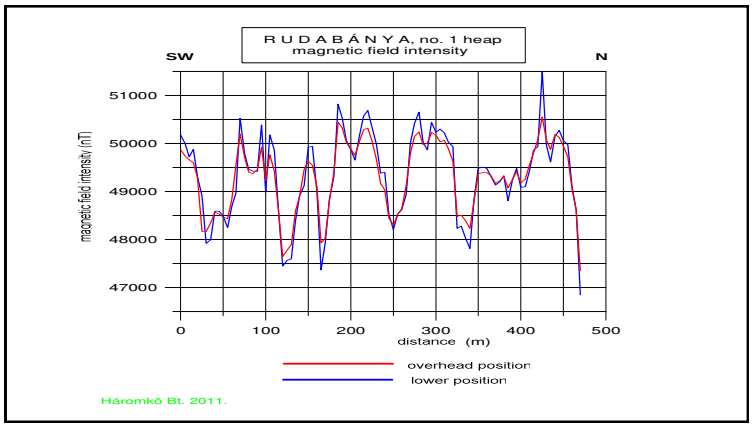

Figure 3. Magnetic profile

In the next example Figure 4 describes measurements on the Felsőtelekes No. 3 heap: the geoeletric section No.1 is parallel to the multielectrode and the IP profile. This profile started with a "virgin site" on a meadow surface. Low resistivity can be observed in the vicinity of the FT101 point on the western part of the profile, due to the clay sediments. FT103 measuring point is displayed in the ore material landfill. According to the calculated data of point FT 104 there are 10 meters of dry and solid spoil material. At the end of the section of the FT108 point there is the high – greater than 500 ohm-meters – resistivity. This is partly due to a concrete spot on the surface, but it is mainly the result of the underlying Triassic bedrock. Between FT103 and FT106 points below the massive spoil there are low resistivity Pannonian sediment layers. In the course of IP measurements a highly contaminated zone was detected in which both redox and metal polarization occures. The pollution is not only in the upper part, we detected it at the depth of 10 meters as well.

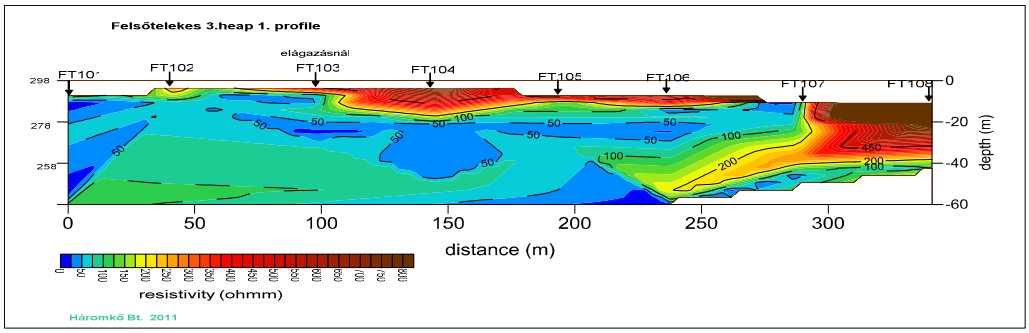

Figure 4. Resistivity section

Figure 5 is a multielectrode section where you can see that the first part of the section does not contain reactive material; however, between 80m and 320m the resistivity of the spoil mass is more than 200 ohm-meters on the surface and beneath to the depth of 7–9 m.

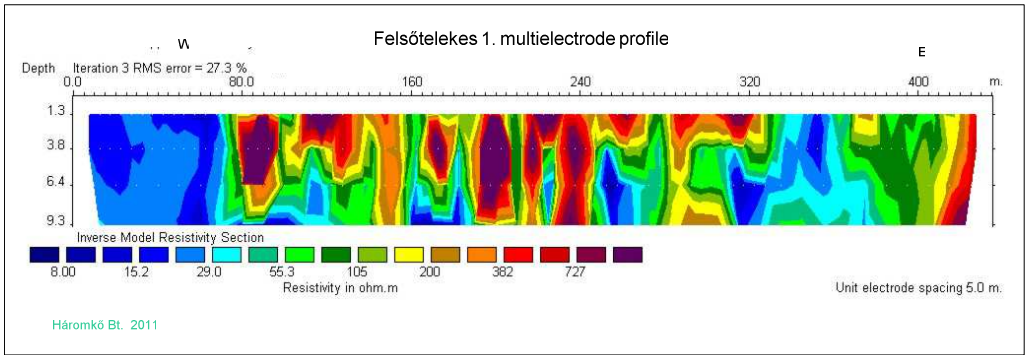

Figure 5. Multielectrode section at Felsőtelekes

3. The Lake Hámor hydro-physical measurements

Resistivity surveys were carried out to characterize the lake sediment in order to determine the sludge (mud) thickness and the bottom of the basement, performed with a 100 metre long floating probe (made by A. Madarasi). The radar measurements were continuously performed during towing (measuring the depth, time, temperature and coordinates).

During water radar measurements sonic wave packets are reflected from the solid basement, thus we could identify the depth of the substrate and we also could obtain a relief of the bottom of the lake. The difference in physical terms of the two methods allows us to separate the loose muddy part from the substrate based on the discrepancy of measured data. The mud is not the first reflective layer but behaves like a more resistive substratum than the water. This fact allows us to determine the sediment thickness. Figure. 6 presents the sediment thickness distribution. The sediment becomes thicker near the shore (a few metres only), in the south-eastern part sometimes the thickness is about 6–8 m.

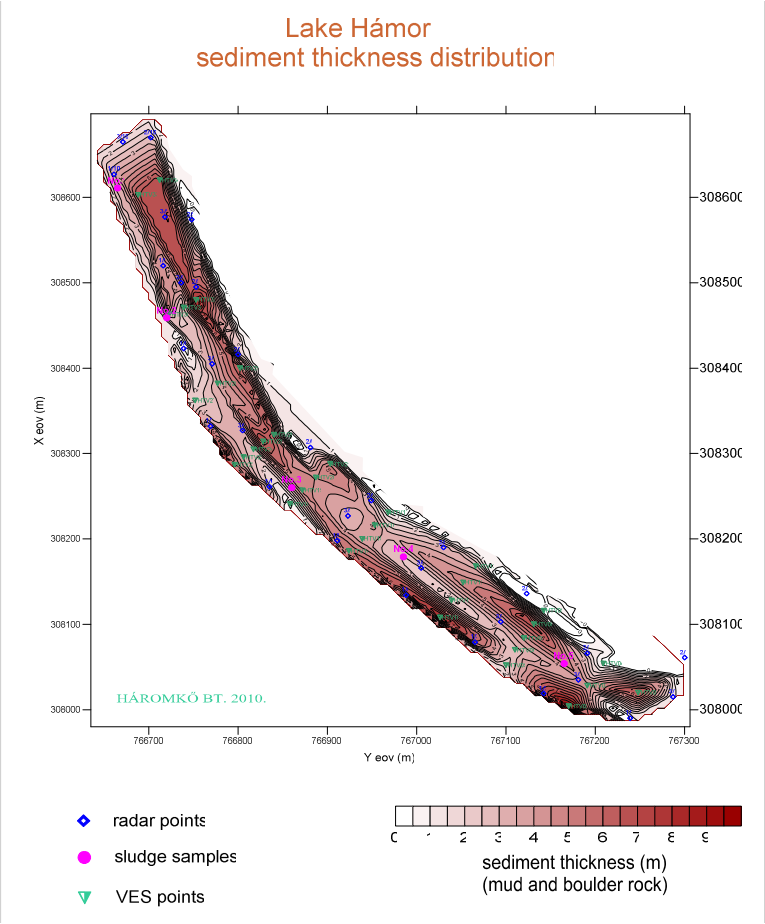

Figure 6. Sediment thickness at Lake Hámor

4. Conclusions

Based on the geophysical measurements described here we were able to provide information on the boundary of mining waste heaps, theirs inner structure/stratification and in some cases the types of deeper layers.

IP sounding clearly indicates the polluted zones and allows us to estimate the kinds of pollutants. Geophysical mapping techniques were also used to provide estimates of sediment depth in a small lake and a relief map of the lake bottom.

Acknowledgement

The described work was carried out as part of the project: Rudabánya Ore Occurrences Research Development Program for Geological Studies" (identification number GOP-1.1.2-08/1-2008-0002 - Economic Development Operational Programme) and the project of "Diagnostic and Research Work of Miskolc's Endangered Karst Aquifer" (identification number KEOP-2.2.3/A-2008-0012- Environment and Energy Operational Programme).

References

[1] Bucsi Szabó, L.: Geophysical and hydro-physical measurements for the detailed environmental assessment of TOKA-Creek, Gyongyosoroszi-Mine AMD, and there watershed, 2006 Háromkő Ltd. Miskolc.
[2] Gyenes Gáborné–Bucsi Szabó, L.: Geophysical measurements on the Mexikóvölgy refuse damp near Miskolc city, 2011 Háromkő Ltd, Miskolc
[3] Godfrey, K. A.: "Monitoring for hazardous waste leaks." Civil Engineering 1987, vol.57, pp. 48–49.
[4] Campos, D.–Choteau, M.–Aubertin, M.–Bussière, B.: Using Geophysical Methods to Image the Internal Structure of Mine Waste Rock Piles, Department-CGM, Ecole Polytecnnique de Montreal, 2002, Canada.
[5] Turai E,: IP Data processing results using TAU-transformation to determine time-constant spectra, Geophysical Transactions 2004, Vol. 44: (No. 3–4.) pp. 301–312.

Geosciences and Engineering, Vol. 1, No. 2 (2012), pp. 69–74.

FIGHT FOR THE THIRD PLACE OF THE STAND – THAT IS TO SAY GALILEO AND COMPASS

ISTVÁN HAVASI
Associate Professor, Department Head,
Department of Geodesy and Mine Surveying, University of Miskolc,
3532 Miskolc-Egyetemváros, gbmhi@gold.uni-miskolc.hu

1. Introduction

Today it can be stated undoubtedly that ***satellite navigation*** has become an integral part of everyday life. It is known that the basis of this is provided by satellite fundamental systems. The two most developed representatives of these are the American ***NAVSTAR GPS*** and the Soviet-Russian ***GLONASS***. In the fight for market positions of satellite navigation – in addition to the afore-mentioned determinant systems – further competitors joined in, and they also appeared with their plans for implementing fundamental systems. One of these was the European ***Galileo***, the development of which has slowed down recently; the other one was the Chinese ***Compass*** (***Beidou-2, B-2***), the investigation of which means another purpose of my study. We can say that the implementation of the Chinese satellite fundamental system has been dynamic recently. We can often read newer and newer launches of navigation satellites; it was one reason of our topic selection aiming at Compass. The other reason was that Hungarian literature pays relatively little attention to Compass, so this part of my article is intended for completion.

2. Characteristics of Galileo satellite fundamental system

Galileo is the first global satellite positioning and navigation system to be developed by the ***E***uropean ***U***nion (***EU***) and the ***E***uropean ***S***pace ***A***gency (***ESA***) for ***special civil purposes*** in the form of a joint venture. A modern, future, second generation system will be reviewed now where the process of implementation has not been fulfilled yet.

The space segment of Galileo is planned to consist of 30 satellites deployed in three Mean Earth Orbits. The inclination of orbital planes to the Equator is 56º, and there will be 9 satellites and a spare one in each plane (Figure 1). This satellite constellation will provide better coverage on locations of higher geographical latitude – such as in the northern part of Europe – than it is realized with American GPS satellites today. The mean rotation altitude of satellites is 23,616 km; the orbital periodic time is 14 hours; their weight is 650 kg and their life expectancy will reach 12 years. On board of each satellite two atomic clocks will provide the required frequency etalon. One of them will be a rubidium clock, while the other one will be a hydrogen maser clock. These clocks are produced in Europe and are being tested on board of the first pilot satellites. The Galileo system time will be adjusted to the International Atomic Time. Galileo satellites will transmit ten different signals on the following four L-band frequencies: 1176.45 MHz, 1207.14 MHz, 1278.75 MHz and 1572.42 MHz. As it can be seen, the frequencies of two Galileo signals are equal to the L1 and L5 frequencies in American GPS system (the L5 signal is connected to only new F type

satellites). The service provided by Galileo signals can be divided into two levels: basic level and selective availability. The basic level is intended to be free here as well, similarly to the American GPS, but the system operators promise more reliable service for general user applications. To use the other value-added commercial and professional level, naturally, it will be fee-paying, and available only to authorized users.

The ground service infrastructure of Galileo system and its sub-system of monitor stations (30–40) will be widened with an integrity-monitoring infrastructure separated from the afore-mentioned sub-system. The main tasks of the subsystem of monitor stations will be to observe the satellite constellation continuously – that is, to determine each satellite's orbit – to provide time synchronization and to produce navigation messages. All of these are provided by establishing and operating 15 automatic monitor stations, a control centre and 4 telemetric stations. An independent monitoring system consisting of a European integrity centre and 3 radio stations will be responsible for system integrity. Integrity capability of the system is a key issue for navigation applications.

The most important element of the user system is the receiver itself. Galileo will be compatible with the American GPS system. When designing Galileo receivers, combined receivers came into consideration to enable all the three fundamental systems to receive the transmitted signals. It also means that new processing programmes will be needed as well. Because of competition it is also not difficult to predict that the modernization process of each operating fundamental system will lead to increasing demand for receivers, including combined receivers – a trend which has been confirmed by the market in recent years.

In addition to the applications that are well known among users, a number of value-added services will be offered by Galileo. As it was mentioned earlier, application fields will cover, among others, traffic (road, rail, aviation, maritime) and the transport of goods; energetics; telecommunications; agriculture; fishing; environmental protection; the construction industry; recreation activities; national defence; civil defence; tasks related to safety and private defence and finally, such kind of special fields as mining.

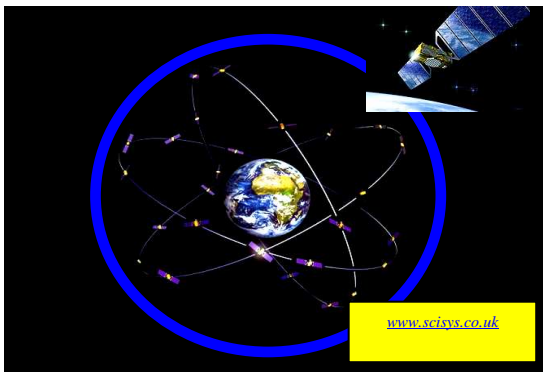

Figure 1. Galileo satellite configuration

As far as the present situation connected to the development of Galileo is concerned, let us mention some matters. With reference to this system, it is well known that it is in ***Initial Test Operation Phase***. The tasks in this phase are to model the designed orbit; to form

navigation message and to test the on-board clocks. The two test satellites launched until now to perform these tasks are ***GIOVE-A*** and ***GIOVE-B***. A brief life story and the mission of the test satellites are as follows:

- In the morning of ***December 28, 2005*** the first test satellite, ***GIOVE-A*** was launched successfully according to schedule with a Soyuz-Fregat booster, and put into its final orbit. Thus GIOVE-A started its planned mission. The mission of this satellite is to test Galileo navigation signals and both on-board rubidium atomic clocks. A further task of this satellite is to examine the radiation along its space orbit, the height of which is 23,258 km and whose inclination is 56º to the Equator.
- On ***April 27, 2008*** – with a significant delay compared to the scheduled time – the Russians put ***GIOVE-B*** in orbit. The primary task of this satellite is to test frequency etalons, the passive hydrogen maser clock which can provide more precise positioning and is designed for installation in the final satellites.

(Both test satellites have been withdrawn from service this summer. According to officials their missions were performed.)

Launches of further satellites giving already real service were delayed significantly due to recent economic problems. Then, on April 21, 2011 the first two "true" Galileo satellites were put in orbit with a Soyuz booster from Kourou Launch Centre, French Guiana. Launch of the next two satellites is expected in September this year. The satellite sub-system of Galileo includes 4 satellites; two test and functional ones. By 2018 the officials would like to operate 18 satellites. The configuration of 30 satellites they would like to realize by 2019. By the end of 2011 about 3 billion Euros were spent on Galileo system, from which 560 million was used for developing and 2.4 billion for establishing costs. Between 2014 and 2020 further 7.5 billion Euros are intended for the European satellite global positioning system. The separate cost items cover the implementation of Galileo; its operation and EGNOS as well. The Fucino Control Centre near Rome received the first navigation signals at the beginning of 2012.

It was considered as a significant step forward, however, that the Septentrio Company developed the first Galileo receiver card. The Belgian Septentrio is an active participant in the Galileo program, and this company runs several research and development projects continuously at Galileo Joint Undertaking (GJU) and European Satellite Agency (ESA). According to this Septentrio will be able to offer the best Galileo receivers in commercial circulation very soon.

The Galileo concession company, led by Alcatel Espace, agreed with the EU about the most important ground locations of this system. As a result of this agreement the Centre of Concession Owner will be planned in Toulouse (France), however the Operation Centre will be established in London (United Kingdom). The ***C***onstellation ***C***ontrol ***C***entre (***CCC***) and one of the ***P***erformance ***E***valuation ***C***entres (***PEC***) will be built in ***Germany***. The other PEC and the ***M***ission ***C***ontrol ***C***entre (***MCC***) will be established in Italy. In Spain, an essential establishment, a Second Control Centre will be developed for critical applications being important from the aspect of life and property safety such as commercial shipping and public aviation). When ***primary control centres*** (CCC, MCC) are operated in perfect order this station will be the venue for further education of the staffs of MCC and CCC and for testing new hardware, software and processes.

3. Compass global navigational satellite fundamental system

In the middle of the first decade of the 21st century China started to develop a new second-generation satellite positioning system that is designed to be realized first in regional form (China and its region), then in global form (extended for the Earth). The name of this system is COMPASS, which is the name used here from now on, although an accepted practice is to term COMPASS Beidou-2 (B-2). COMPASS is a system under development which cannot be considered an extension of the available B-1 at all.

According to the plans the future fundamental system would consist of ***35*** satellites, from which ***5*** rotate in geostationary orbit (hereafter GEO); ***3*** in inclined geostationary orbit (IGSO) and ***27*** (***3x9***) in a so-called Middle-Earth Orbit /hereafter MEO/ (Figure 2). Each launch was executed from ***X***ichang ***S***atellite ***L***aunch ***C***entre (***XSLC***), (Figure 3). The MEO satellites move in orbits having an altitude of about 21,000 km and an inclination of 55 degrees. Their rotation time is 12 hours. The ***first herald*** of COMPASS system was a MEO satellite. The task of this satellite was to validate and test the frequencies of Compass signals. This launch was symbolic at the same time because it became unambiguous that since that time the Asian country has been working for implementing an own global system which is independent from its rivals.

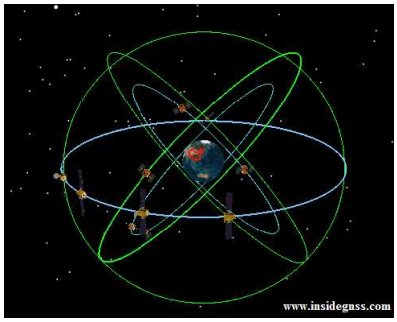

Figure 2. Compass configuration

Figure 3. Launch of a Compass satellite

The new Compass satellites – in contrast to Beidou-1 satellites (S-band) – send L-band signals. Beidou-2 – following the American GPS, European Galileo and Russian GLONASS – introduced such kind of signal structure which applies frequencies near to the afore-listed navigation fundamental systems or are identical with them completely in case of the implementing ***regional system***.

The Chinese Compass global navigation system will offer its users 10 services (on the basis of common signal structure of phases 2 and 3); among them 5 will be free (open), and 5 will be restricted (official). Each service is based on 8 carrier phases, and ***two-kinds of modulation techniques*** are used. One of them is the so-called ***Q***uad ***P***hase ***S***kip ***K***eying (***QPSK***, phase 2, end of 2012); the other one will be the ***B***inary ***O***ffset ***C***arrier (***BOC***). By 2020 (phase 3), when, the full global system is expected to be implemented, Beidou signals – applying mainly the ***BOC modulation technique*** – will approach further to the American GPS and European Galileo.

The first two satellites of Beidou-2 were followed by two additional GEO ones (B2-G1 and B2-G3), and on July 31, 2010 the Chinese also successfully launched the fifth, and at the same time the first IGSO satellite (B2-IG1). In 2010 a further GEO (B2-G4) and an IGSO satellite joined the satellite constellation of this system.

According to Chinese officials the ***basic function*** of Compass navigation system was realized with the launch of the eighth satellite (B2-IG3) on April 04, 2011. Together with the previous five satellites (3 GEO and 3 IGSO), the ***basic configuration*** of this system was implemented, which (after finishing tests) will enable the system to meet navigation demands in the greatest part of China.

The tenth Chinese navigation satellite (B2-IG5) was put in orbit on December 1, 2011 with an HM-3A booster from Xichang. Even at the end of December Chinese officials announced the official test run of B-2, and a document (protocol) introducing the navigation signals of this system accurately came to light (***BNSS ICD***). It describes the ***regional service system*** (implementation by 2012), which will be developed as a global one by 2020. The nominal satellite sub-system of BNSS regional system covers 5 GEO and 9 non-GEO satellites, the latter group of which includes 5 IGSO and 4 MEO satellites.

This year (on February 24, 2012) the Chinese first put in orbit the fifth GEO satellite in geostationary orbit, then on April 29, 2012 two MEO satellites were launched with a single LM-3B booster. So the present satellite configuration is as follows: ***4 GEO***; ***5 IGSO*** and ***3 MEO***. This year three further spacecraft launches are expected.

After all this information, let us survey in Table I what the actual Compass satellite constellation is like.

Table 1

Satellites of Beidou-2 system (08. 2012)

BEIDOU-2 (COMPASS)	***1.***	B2-M1	13. 04. 2007.	MEO	test
	2.	B2-G2	14. 04. 2009.	GEO	drifting
	3.	**B2-G1**	16. 01. 2010.	GEO	usable
	4.	B2-G3	01. 06. 2010.	GEO	usable
	5.	**B2-IG1**	31. 07. 2010.	IGSO	usable
	6.	B2-G4	31. 10. 2010.	GEO	usable
	7.	B2-IG2	17. 12. 2010.	IGSO	usable
	8.	B2-IG3	09. 04. 2011.	IGSO	usable
	9.	B2-IG4	26. 07. 2011.	IGSO	usable
	10.	B2-IG5	01. 12. 2011.	IGSO	usable
	11.	B2-G5	24. 02. ***2012***.	GEO	usable
	12.	**B2-M3**	29. 04. ***2012***.	MEO	usable
	13.	**B2-M4**	29. 04. ***2012***.	MEO	usable

As for Beidou-2 satellites they are more robust than their predecessors were. Their designed life is about 8 years.

The ***first phase of COMPASS*** (the ***Chinese regional system***), which would consist of 14 satellites, is planned to be finished by 2012, and with it they intend to service the potential users of the Pacific Ocean region. Afterwards, according to the plans, they would develop the afore-mentioned global CNSS (Chinese Navigation Satellite System) system. It will mean total operation capacity. The cost of this system can be estimated at 62 billion US dollars. Hundreds of Chinese companies already deal with producing satellite receivers and

specialize in GNSS services. At present the ***contribution of China to satellite-based services*** amounts about ***25%***.

By the autumn of 2012 B-2 tests are expected to be finished. The accuracy of the regional development phase carried out this way will improve for 5–10 m. With B1+GPS L1 signals an accuracy of 5 m might be obtained (about 12,000 receivers till now); moreover by means of combined application of B1/B2 and GPS L1/L2 signals an absolute positional accuracy of about 2 m can also be guaranteed.

The CNSS system (***5 GEO***, ***3 IGSO*** and ***27 MEO*** satellites) will be fully similar to the afore-mentioned other fundamental system in a sense that the so-called one-way range measurement is used for determining the position of a ground receiver. The expected accuracy of autonomous surveying is about 10 m; the accuracy of time measurement is 10^{-8} seconds with synchronized clocks. It is free. Applying surveys of a ground-based augmentation system positioning accuracy with real time corrections might improve for 1 m. The second level (licensed) will cover the military and authority demands where, considering the previous data, much higher accuracy, communication facilities and system-status are provided.

5. Conclusions

The purpose of our study was to introduce the features of Galileo and Compass and their actual status. As for ***Galileo*** it turned out that its predicted development – because of mainly financial reasons – slowed down significantly. The ***plans referring to the near future are promising,*** from which we hope for accelerated implementation of the satellite sub-system.

We know that realization of ***Compass*** is one of the main objectives of Chinese national strategy. Considering its state of development it is ***in the third place*** among the fundamental systems, surpassing the European Galileo system discussed here previously. I think that the ***future of Compass*** seems to be ***bright*** now.

Acknowledgement

"The described work was carried out as part of the ***TÁMOP-4.2.1.B-10/2/KONV–2010-0001 project*** in the framework of the New Hungarian Development Plan. The realization of this project is supported by the European Union, co-financed by the European Social Fund."

References

[1] Frey, S.: Short articles on the astrological news portal called 'Space World', e.g. Expanding Beidou (2012); Chinese satellites, navigation and mapping (2011.)

[2] Havasi, I.–Mezei, L.: Compass (Beidou-2) Chinese global navigation satellite fundamental system – development, state of affairs and future, Hungarian Journal of Mining and Metallurgy, 2012/1 pp. 12–17.

[3] Havasi, I.: GLONASS and Galileo, state of affairs and future. 43rd Conference on Mine surveying, Proceeding, Dobogókő, Hungary, 2004.
http://www.beidou.gov.cn; http://www.sinodefence.com
http://www.globalsecurity.org; http://www.nasaspacefight.com
http://wwwen.wikipedia.org; http://www.gpsworld.com
http://www.insidegnss.com; http://europa.eu.int/comm/energy_transport/en/gal_en.html

Geosciences and Engineering, Vol. 1, No. 2 (2012), pp. 81–86.

ENVIRONMENTAL ISSUES OF CO_2 PIPELINES

BEÁTA HORÁNSZKY
assistant lecturer, Miskolci Egyetem, Kőolaj és Földgáz Intézet,
3515 Miskolc-Egyetemváros
bea.horanszky@uni-miskolc.hu

1. Introduction

One means in the struggle against climate change is the reduction of greenhouse gas (GHG) emissions. The emitted GHG's contain CO_2 (carbon dioxide) up to 80% so the reduction of this element can lead to notable results. One way for this procedure is to separate CO_2 from flue gas at source points of high emission (which are usually power plants), and then allocate it to a subterranean level in different kind of formations by carbon capture and storage (CCS) technology. The separation site and the geological storage site are not at the same place, so there is a need for CO_2 to be transported by pipeline.

A long-term plan of the European Union (EU) is the construction of a CO_2 pipeline structure, similar to the one used in natural gas transportation. According to the plans, by 2050 this pipeline system will reach Hungary as well.

Important questions arise in connection with environmental protection when considering the construction and operation of the pipelines. The author attempts to summarise the issues to be considered.

2. The CCS chain

In 2009 the high rate of emission of CO_2 meant 29 billion tonnes. About half of this enormous amount consisted of emissions from thermal- and electric energy producers, the traffic sector and public consumption, and this is similar in the present as well. The two latter sectors are made up of numerous, even several millions of emitters, while power plants and other energy industry settlements have fewer source points. A significant part of the great amount of CO_2, produced at these resource points can be detached from flue gas by different types of technological methods. The "accessible" quantity of CO_2 was more than 1,300 million tonnes in the EU-27 and 15 million tonnes in Hungary in 2009 [1].

The first step of the technological chain at sites of energy producers and other energy industry actors is the separation of the nascent CO_2 from fuel gas. Among separation processes we differentiate pre-combustion, post-combustion and oxy-fuel technological separation.

Transportation is also an important task in the CO_2 chain, which can take place by an appropriate pipeline structure or by tanker. Specialists of the hydrocarbon industry have gained diverse experience in connection with this important task, since enhanced oil recovery (EOR) technologies. The first pipelines of the type were established in the 1970s in the USA; in Hungary a line to serve the oil production of Budafa was installed in 1972. The length of the CO_2 pipelines nowadays in the USA is nearly 6,000 km, while in Europe

the total length is less than 500 km. The separated CO_2 can be stored underground in appropriate geological forms so as to decrease the emissions load of the energy industry. Different storage formations are: deep saline reservoirs, unrecoverable coal seams and depleted oil and gas fields.

2. The CO_2 pipeline system in the EU

On 11 March 2011 the European Commission released a communiqué titled "A roadmap for moving to a competitive low carbon economy in 2050" that marked out the path to an economy with lower CO_2 emissions. The EU considers present CCS technology as only a temporary solution, but considers it to be an important area that should be regulated and whose pilot projects should be financed, too [2].

Table 1

Active CCS CO_2 pipelines in the EU [3]

Name	County	Amount of CO_2 (Mt/y)	Length (km)	Diameter (mm)	Pressure (bar)	Start of operation
Sleipner	Norway	1	160	n/a	n/a	1996
Snøhvit	Norway	0.7	153	200 (8")	100	2006
Lacq	France	0.06	27	n/a	n/a	2010

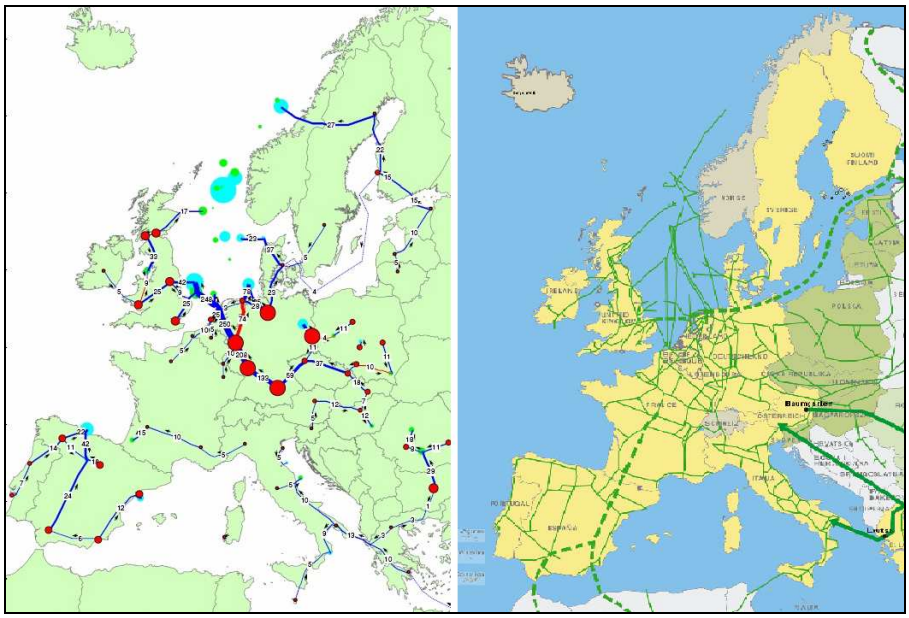

Figure 1. The planned CO_2 network system by 2050 [5] and the natural gas network system in 2010[8]

Three CCS projects are presently in operation in Europe (Table 1), a Norwegian pipeline is under construction, and three projects (two Norwegian and one Dutch) were cancelled (due to the economic crisis, probably). Several projects across the continent are in the planning stages and several theoretical project locations are under consideration [1].

According to a study of JRC [4], the research institute of the European Commission, the EU will spend 25 billion Euros on the construction of a 2,005-km-long CO_2 pipeline until 2020 and by 2050 a so-called European CO_2 pipeline network is to be established, which means a pipeline of more than 20,000 km at a cost of 28.9 billion euro. The pipeline network to be built may be similar to the gas transportation network spanning the EU (Figure 1). Pipelines would connect source points of high emission to places of storage that are mostly within marine-located formations (e.g. distressed hydrocarbon fields).

4. Environmental effects of CO_2

Naturally, environmental effects of the transported material, and the protection of the pipeline's environment are notable points of view when considering the establishment and operation of CO_2 pipeline as an element of CCS technology.

3.1 Characteristics of CO_2 [5]

CO_2 is a languid type of gas, which exists in the air at a low proportion (at 0.039% static pressure), is non-combustible, and is heavier than the air (1.98 kg/m$^{3)}$. It can be easily liquefied (at room temperature, at a 35 bar load), but strongly evaporates at normal static pressure, while detracting heat from its environment. At this point a solid snow-like material arises, the so-called dry ice (often used as cryogenic media).

CO_2 forms a light acid with water – carbonic acid – so it weakly dissolves in water.

3.2 Effects on the human body [5]

Naturally existing CO_2 in the air does not have any effect on human health, but if the cubic capacity percent of CO_2 in the air is 5%, it can cause dizziness, headache and nausea. In high concentration it attacks the respiratory centre and affects the metabolic process of the blood. At an increasing concentration of CO_2, the oxygen concentration of the air drops and at a 16% oxygen proportion asphyxia can occur.

3.3. Effects on the eco-system

CO_2 pipelines functioning nowadays go through areas of low population density, so the CO_2 that blows out from the pipe affects mainly the flora and fauna. Above the necessary concentration, CO_2 can be dangerous to plants, but in some cases it can act positively, up to 20–30%.

When CO_2 gets into groundwater there is an acid reaction and in some disadvantageous cases it releases chemical elements from rocks, so it can change the composition of groundwater and the stability of rocks.

It can also happen that marine pipelines malfunction and the filtering gas mixes with marine water. An acid reaction occurs here as well, with the degree of the negative effects

strongly depending on the pH value. The creatures most seriously affected are those which are immovable and cannot leave the area polluted by CO_2.

5. Construction, operation and environmental protection of pipelines

Specialists of the hydrocarbon industry have gained diverse experiences in connection with this important task, since EOR technologies apply CO_2 in rock-oil exploitation, and pipelines are used for transported to the site of exploitation.

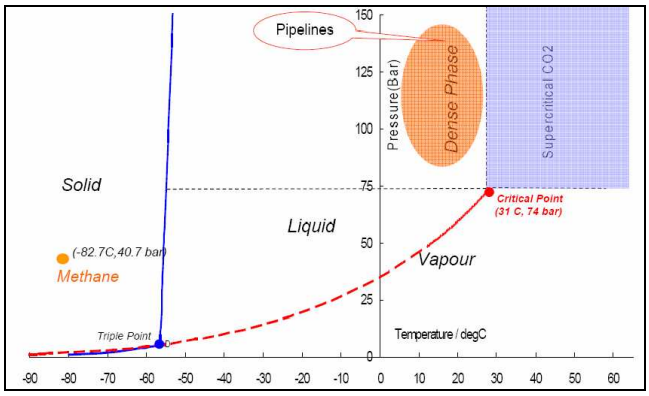

Figure 2. Properties of CO_2 [6]

The path of the pipelines should be carefully chosen considering the right of way (ROW). It is important to take into account that CO_2 is denser than air, so when lying down the pipeline path, it is necessary to consider the possibility of an accidental outflow that could be dangerous to the environment.

In pipelines, which can run several hundreds of kilometres (the longest one in the USA is 800 km) CO_2 should be at a high pressure – more than 100 bars – so as not to let its liquid aggregate rise to a temperature of more than 31°C (see Figure 2).

Due to the applied high pressure it is very important to keep the area safe. The security area can extend from 10 m up to even 24 m in Hungary [7].

Before implementing a project an environmental impact study is carried out to investigate the environmental effects of the construction and operation of the pipeline.

Pipeline construction can have effects on:

- *The cleanness of air*: pipelines are constructed fractionally, so effects do not occur organically in the pathway. During the laying of the barrel and the extrusion, CO_2 pollution can be notable. Earth moving equipment and the exhaust fumes of transporters vehicles can temporarily increase dust and air pollution (CO, NO_x, etc.) at the construction site.
- *The soil, groundwater, subterranean water*: earth moving equipment should be in impeccable condition and well-serviced, and during their operation it is necessary to ensure that no fuel or dangerous chemicals contact the soil and surface water. The extent of accidental pollution should be immediately limited.

- *Flora and Fauna*: strict care should be taken of species living in the vicinity of the construction area, especially those under protection. For example a temporary restriction can be applied for the nesting period of a protected bird species.
- *Noise pollution:* during the operation of the transporters and the earth moving equipment it can temporarily occur.
- *Managing Waste:* waste produced should be taken away.

According to the categorisation above, effects during operation can be:

- *The cleanness of air*: the appropriate operation of the pipelines does not inferewith air quality, except for emissions from the compressors. Typically, , the quantity of CO_2 emitted in the air when pipeline damage occurs is not significant if pipeline monitoring is constant and block values are applied.
- *The soil, groundwater, subterranean water*: when the pipeline is operating appropriately it does not have any negative effect. When it is damaged, the emitted CO_2 can change the pH value of the soil and can make it acid. Also, heat reduction can cause freezing.
- *Flora and Fauna*: operation does not have any danger if the path is well-cleaned.
- *Noise pollution:* During the operation only the noise caused by the compressors can result in this pollution.
- *Managing Waste:* no waste is produced during operation, but waste from maintenance (e.g. oily rags, waste oil, etc.) should be taken away, and communal waste should be managed by the general regulations.

6. Conclusions

One of the main goals of the EU is the creation of an economy with lower CO_2 emissions, by which climate change and global warming can hopefully be significantly decreased, even if it cannot be turned back. CCS technology, which is at an initial status for the present, can serve this aim. Only a few projects operate presently in Europe but the EU plans to finance more for the collection of experience.

There have been several pieces of information collected about CO_2 transportation, the middle element of the technological chain, thanks to application of EOR technology, and to continuous build-up and development of the natural gas pipeline network that has been taking place for decades.

The environmental regulations of planned European CO_2 pipeline network would be based on these experiences, according to the previously described effects.

Acknowledgements

The article was carried out as part of the TÁMOP-4.2.1.B-10/2/KONV-2010-0001 project in the framework of the New Hungarian Development Plan. The realisation of this project is supported by the European Union, co-financed by the European Social Fund.

References

[1] Database of European Environmental Agency http://www.eea.europa.eu/data-and-maps (2012. 07. 20.)
[2] European Commission. A Roadmap for moving to a competitive low carbon economy in 2050 COM, 2011, 112. http://eur-lex.europa.eu/LexUriServ/LexUriServ.do?uri=COM:2011:0112:FIN:EN:PDF
[3] Bellona Environmental CCS Team: A világ CCS projektjei, 2011. november http://bellona.org/ccs/uploads/media/CCS_projects_Nov2011.xlsx
[4] Morbee, J.–Serpa, J.–Tzimas, E.: The evolution of the extent and then investment requirements of a trans-European CO_2 transport network. 2010, JRC Scientific and Technical Reports http://publications.jrc.ec.europa.eu/repository/bitstream/111111111/15100/1/ldna24565enn.pdf
[5] Berecz, E.: Kémia műszakiaknak, Tankönykiadó, Budapest, 1991, pp. 393–394.
[6] Seevam, P. J.: Transporting the Next Generation CO_2 for Carbon, Capture and Storage, Proceedings of IPC2008 International Pipeline Conference, Calgary, 2009.
[7] 79/2005. (X.11) GKM rendelet, a szénhidrogén szállítóvezetékek biztonsági követelményeiről és a Szénhidrogén Szállítóvezetékek Biztonsági Szabályzata közzétételéről.

Geosciences and Engineering, Vol. 1, No. 2 (2012), pp. 87–92.

SPATIAL DISTRIBUTION OF PETROPHYSICAL PROPERTIES ON THE BASIS OF LABORATORY RESULTS, WELL LOGGING AND SEISMIC DATA

JADWIGA A. JARZYNA[1]–PAULINA I. KRAKOWSKA[1]–EDYTA PUSKARCZYK[1]–
KAMILA WAWRZYNIAK-GUZ[1]–JAKUB BIELECKI[2]–
WOJCIECH M. KWIATEK[3]–MICHAŁ GRUSZCZYK[4]

[1]AGH University of Science and Technology, Faculty of Geology Geophysics and Environment Protection, Department of Geophysics, al. Mickiewicza 30, 30-059 Krakow, Poland,
[2]National Centre for Nuclear Research, Swierk, ul. A. Soltana 7, 05-400 Otwock, Poland;
[3]H. Niewodniczański Institute of Nuclear Physics Polish Academy of Sciences (IFJ PAN), ul. Radzikowskiego 152, 31-342 Krakow, Poland,
[4]GEOFIZYKA Krakow, ul. Lukasiewicza 3, 31-429 Krakow, Poland
e-mail addresses: jarzyna@uci.agh.edu.pl; paulina.krakowska@gmail.com; puskarczyk@geol.agh.edu.pl; wawrzyniak@geol.agh.edu.pl; jakub.bielecki@ncbj.gov.pl; wojciech.kwiatek@ifj.edu.pl; michal.gruszczyk@gk.com.pl

1. Introduction

The Miocene formation in the Polish Carpathian Foredeep is still the subject of prospecting works due to many gas fields discovered there in the long period from the 19th century up to now [1]. The Sarmatian sandy-shaly thin-bedded formation in gas fields from this region was selected for tests of proposed methodology as rocks being potential hydrocarbon and water reservoirs.

Mutual relationships between rock properties determined using methods based on different physical phenomena and measured in various scale (micro- in laboratory, mezzo- and macro- *in situ*) were the basis for petrophysical three- dimensional analysis. Rock models – important for proper petrophysical parameters determination – were the result of modeling of mineral composition, volume and type of media filling pore space (combining data from various sources and of different scale). Input parameters for simulations were obtained from laboratory measurements on rock plugs and comprehensive interpretation of well logging. The X-ray computed microtomography (μCT) is a new non-destructive technique for visualization of three dimensional rock structures basing on variations in X-rays absorption. Prototype μCT equipment (IFJ PAN) provided structural data of fine spatial resolution (about 4 μm). Basing on μCT data simulations of the fluid dynamics in the void space of porous media was carried out. The Lattice Boltzmann method was used in order to predict the hydraulic permeability of the media. Mercury porosimetry provided us with data on the volume of porous space and its geometry (distribution of predominating pore diameters and specific surface of porous space). Nuclear Magnetic Resonance laboratory spectroscopy delivered information on total porosity with division into clay bound water, capillary water and movable water or hydrocarbons. Mineralogical investigations (roentgen analysis) and results of well logging interpretation were the basis for construction of the mineral composition of rock formation. The spatial distribution of petrophysical properties was realised on the basis of combination of seismic attributes calculated in the vicinity of wells with attributes calculated in the same way as seismic ones for the acoustic full wavetrains. Reservoir and elastic properties were included in properties distribution calculations to gain information on the fluid flow ability of the rock.

2. Geological setting

3D seismic survey T-C-Z in the middle part of the Polish Carpathian Foredeep was selected as the study subject [1, 2]. Four wells (C2, C3, C5k and M1) are sited in the western part of the project. The goal of the seismic industry standard processing and interpretation was recognition of the Miocene siliciclastic formation as a potential gas reservoir. In the presented study the Sarmatian sandy-shaly thin-bedded formation in the depth between 900 and 3500 m was the subject of special core and well logging analyses and advanced processing of seismic data.

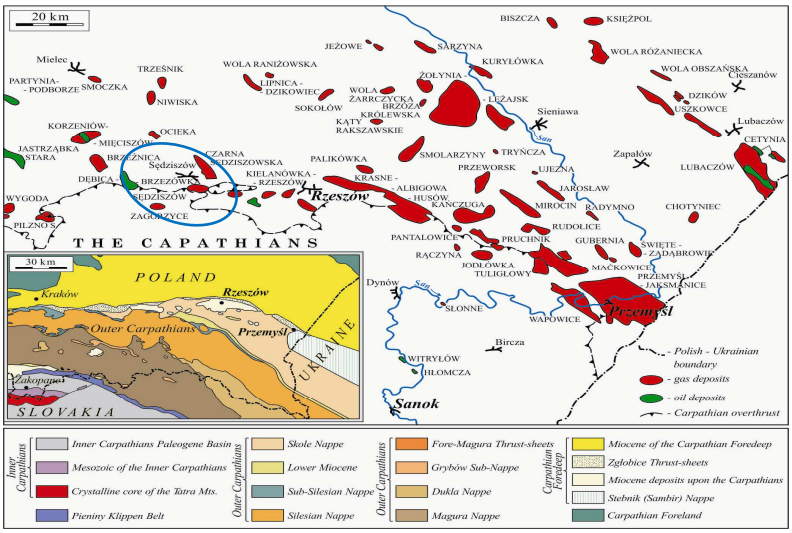

Figure 1. Location of the study (blue ellipse) area on the background of the Polish Carpathian Foredeep (after [1, 2])

3. Data set

Industry seismic data and well logging results were of good quality to be a proper basis for non-standard analyses. Seismic acquisition was done by GEOFIZYKA Krakow in 2006 and 2007 in the Vibroseis system for POGC Co., Warsaw, Poland [3]. Attributes were calculated both on the basis of the pre-stack (AVO) seismic data and on the final data after migration.

Well log data comprised the following results: natural gamma ray intensity, GR, neutron porosity, NPHI, acoustic transit interval time, DT, bulk density, RHOB, photoelectric absorption index, Pe, resistivity logs – ILD, ILM and HRAI, and caliper, CAL. Also, results of the comprehensive interpretation were included: total porosity, PHI, volumes of sandstone, VSAND, volume of shale, VSH, water saturation, SW and permeability K. Acoustic full waveforms were available in all wells.

A few dozen lab results of porosity and permeability were at our disposal, but in the C2, C3 and C5k wells only single data were dispersed in the Sarmatian depth section. In Well M1 25 samples were gathered in the Miocene interval (1065.5–1699.65 m). Standard

lab measurements comprised: total porosity, specific density, bulk density, permeability, resistivity, radioactivity – volume of K, U, Th. Laboratory NMR results and mercury porosimetry outcomes and micro-CT images and other μ-CT digital data were also available. Roentgen mineralogical analyses were done only on samples from two wells: C5k and M1, but data from two wells S34 and S33k, sited closely to south-western part of the study area, were additionally included into analyses.

3. Relationships between rock properties

Mutual relationships between petrophysical properties from various sources are the basis for rock model construction [4]. Different values of the parameters obtained from different methods provide additional information due to the physical basis of selected measurements. Results obtained for rock samples in Well C5k are presented in Table I. There are distinct differences observed in porosity values. The large differences visible in permeability are explained on the basis of methods of calculation of the parameter.

Table 1

Results of laboratory measurements and well logging interpretation

	VSAND	VSH	PHI	Por_{NMR}	FFI	$Por_{\mu CT}$	Por_{Hg}	Ra	Ts	K	$K_{\mu CT}$
	[%]	[%]	[%]	[%]	[%]	[%]	[%]	[mm]	[m^2/g]	[mD]	[mD]
9023	35	61	3.78	18.06	10.11	14.76	8.85	0.1799	1.967	0.064	24
9025	33	63	4.23	12.82	6.73	11.27	0.03	0.1129	0.12	0.095	3.5
9026	38	56	6.10	13.09	7.03	1.76	4.55	0.1355	1.343	0.705	3.5
9087	56	34	10.4	19.48	16.41	20.33	8.61	0.2410	1.429	7.02	175
9088	45	50	5.86	13.10	4.90	12.41	4.23	0.0246	6.891	0.52	8.5
9090	50	40	10.1	19.26	14.77	20.79	6.01	0.0751	3.203	5.39	52

VSAND, VSH – volume of sandstone and shale, respectively; PHI – total porosity, Por NMR – total porosity from NMR, FFI – movable water from NMR, Por μ-CT-porosity from microtomography, Por Hg – porosity from mercury porosimetry, Ra – radius of pores, Ts – specific surface, K- permeability from well logging interpretation, K μ-CT – permeability from microtomography

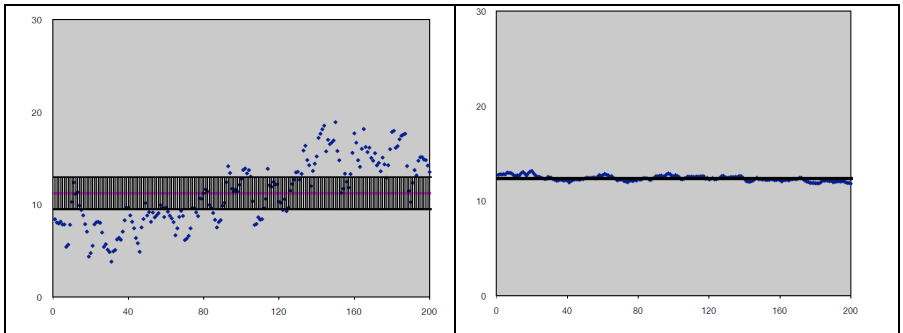

Sample – 9025 Por μ-CT (average) = 11.27%, Stand. Dev. = 3.62% VSAND =32% , VSH=64%	Sample – 9088 Por μ-CT (average) = 12.41%, Stand. Dev. = 0.28% VSAND=45% , VSH=40%

Figure 2. Porosity from μ-CT method; C5k well; left sample is heterogeneous, right one is homogeneous; vertical axis- porosity, horizontal axis – scan number

Two examples of porosity results from the microtomography method illustrate the influence of heterogeneity of the rock (Figure 2). Total porosity, Por μ-CT, is similar in both samples. The increased volume of clay in Sample 9025 justifies changes in results.

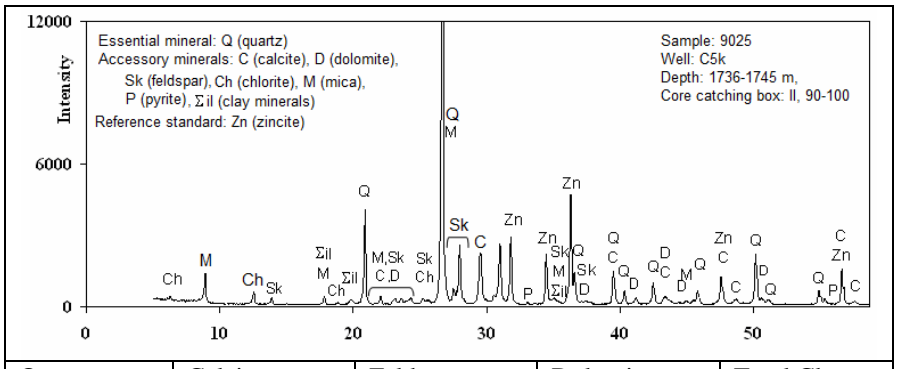

Quartz	Calcite	Feldspar	Dolomite	Total Clay
49 %	17 %	9 %	11 %	14 %

Figure 3. Results of the roentgen analysis of Sample 9025, Well C5k

Results of the roentgen analysis were used for determination of element (mineral) content in the rock sample (Figure 3). They were compared with data obtained from well logging interpretation. Dispersion of data observed in Figure 4 reflects the difficulties in depth matching of well logging and laboratory data and the influence of vertical resolution of well logs.

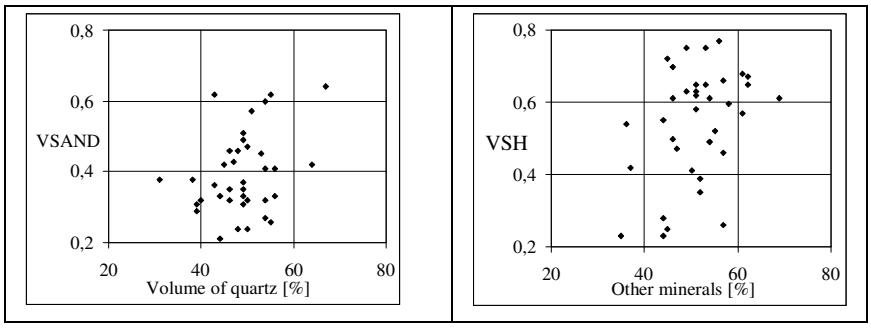

Figure 4. Comparison of mineralogical analysis results made on the basis of roentgen measurements and well logging interpretation

Histograms of sandstone volume in sandy-shaly rock formation and the volume of quartz from roentgen analysis are compared to illustrate unavoidable differences resulting from point rock samples in laboratory analyses and averaged values of parameters determined from well logging interpretation due to the defined radius of investigation and vertical resolution of log devices.

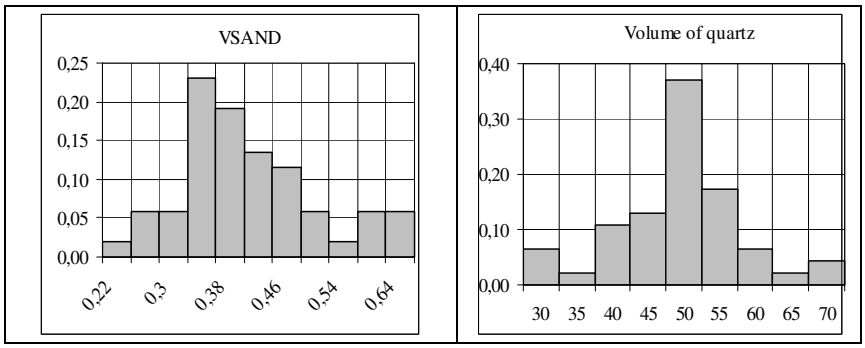

Figure 5. Histograms of volume of sandstone, VSAND and volume of quartz

3. Acoustic full waveforms and seismic attributes

Wide list of seismic attributes were calculated from seismic traces located in the vicinity of wells. Among other attributes, results of spectral decomposition for specific frequencies (sd10Hz, sd25Hz, sd40Hz, sd60Hz, and avgFr_sd60Hz) and integral

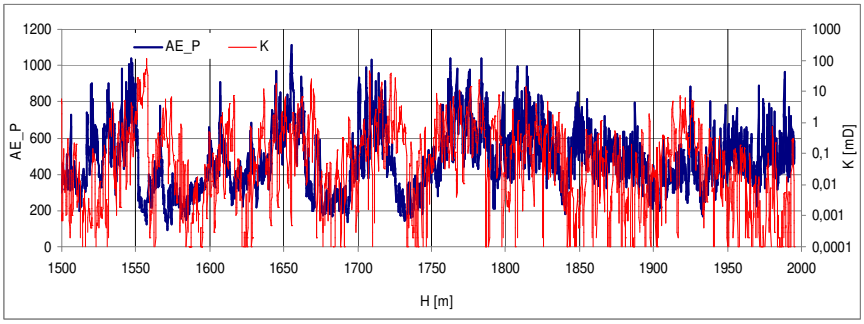

Figure 6. Attribute of amplitude envelope of P-wave from acoustic full waveform, AE_P, and permeability from well logging, K, vs. depth; Well C2

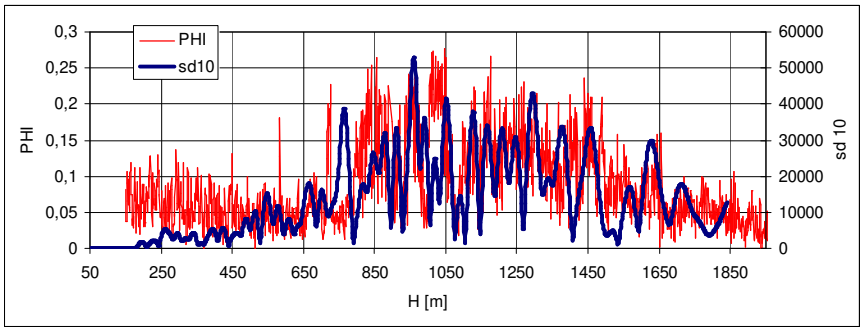

Figure 7. Seismic attribute, sd10Hz, and total porosity, PHI, vs. depth; Well M1

(calculated from impedance section) were used [5]. Instantaneous attributes such as amplitude envelope, AE_P, instantaneous phase and instantaneous frequency, were calculated on the basis of acoustic full waveforms for the P-, S- and Stoneley-wave packets using seismic software. Selected plots of attributes vs. depth are presented to reveal mutual relationships between petrophysical properties of gas sandy-shaly reservoira (Figures 6 and 7).

4. Conclusions

A model of the reservoir rock should be constructed on the basis of all available data. Wide-ranging analysis of laboratory results is the source of information which cannot be obtained in other way. Improvement of mutual relationships between petrophysical parameters from measurements made on different scales (micro- in the laboratory, mezzo- in well logging *in situ*, and macro- in seismic *in situ*) is necessary to obtain the basis for rock model construction. Combining laboratory results and well logging results with seismic data is a way of upscaling data and of making the spatial distribution of petrophysical properties. Elastic properties as a basis of seismic method and acoustic method are the platform of data junction from various methods.

Acknowledgments

This research was done in the frame of the scientific project No. NN 307 294439 (2010-2013) financed by Ministry of Science and Higher Education, Poland. The authors thank the Polish Oil and Gas Company Co., Warsaw, Poland, for the data. Standard laboratory measurements were done in the Oil and Gas Institute, Krakow. Porosimetry results were obtained from AutoPore equipment at AGH UST. Microtomography results were obtained at the H. Niewodniczanski Institute of Nuclear Physics Polish Academy of Sciences, Krakow. Seismic survey and interpretation and measurements and interpretation of well logging were done by GEOFIZYKA Krakow.

References

[1] Karnkowski, P.: Oil and Gas Deposits in Poland. Geosynoptics Society “GEOS”, Cracow, Poland, 1999, pp. 197.
[2] Oszczypko N.: Development of the Polish sector of the Carpathian Foredeep. Prz. Geol., 2006, 54: 396–403 (in Polish, abstract in English).
[3] Syrek-Moryc, C.: 3D seismic survey Trzciana-Cierpisz-Zaczernie as a cause of renaissance of exploratory works in Miocene deposits and its mesopalaeozoic substratum in the middle part of the Carpathian Foredeep. Proceedings of the Geopetrol 2008 Conference, Zakopane, September, 2008, pp. 87–95 (in Polish, abstract in English).
[4] Jarzyna J. A.–Krakowska P. I.–Puskarczyk E.–Wawrzyniak-Guz K.–Semyrka R.–Bielecki J.–Kwiatek W. M.: Reservoir rocks – digital models and petrophysical analysis of clastic rocks. Proceedings of the Geopetrol 2012 Conference, Zakopane, 2012 (in Polish, abstract in English).
[5] Wawrzyniak-Guz K.–Gruszczyk M.: Attributes of acoustic full waveforms and seismic attributes for determination of petrophysical properties of sandy-shaly formations. Proceedings of the Geopetrol 2012 Conference, Zakopane. (in Polish, abstract in English).

Geosciences and Engineering, Vol. 1, No. 2 (2012), pp. 93–98.

INVESTIGATION OF STRESS DISTRIBUTION DURING LARGE SCALE SHEARING TEST

TAMÁS KÁNTOR[1]–BALÁZS KOVÁCS[1]
[1]Department of Hydrogeology and Engineering Geology;
3515 Miskolc, University of Miskolc,
tamas.kantor@gmail.com
kovacs.balazs@gama-geo.hu

1. Introduction

In 2007 a great developing process began at the University of Miskolc. The Geotechnical Soil Testing Laboratory – part of Faculty of Earth Science and Engineering – started to build a large-scale shearing machine. The goal was to build a modular machine with various functions for geotechnical science. The main ways that we determined were the possibilities to the traditional direct shear tests with different box sizes, the ability to perform tribologic investigations (e.g., between geosynthetic materials and soil or waste) and enough space to build in innovated technologies, for example pressure sensors. The large size could help us to make investigations at a wider range of loads and make tests with larger grain size as well.

In this study we represent an innovative solution to the direct shearing tests. The paper focuses on two main parts: the first is the new large scale shearing machine with a flexible control system, and the second is the creation of a special measurement protocol to determine accurately the stress distribution in a large shear sample during testing.

2. Large scale shearing machine

The main difference between the traditional and innovated equipment is the size. Usually the samples used for shearing measurements are square-shaped 100 mm x 100 mm x 20 mm or rounded with 100 mm diameter. Our large shear box's dimensions are 400 mm x 400 mm x up to 300 mm, but we may also apply a shearing box of 700 mm x 700 mm x 700 mm (Figure 1). The normal load may rise up to 22 tons. These dimensions provide the abilities to carry out investigations on larger samples and reduce the distortions of mechanical parts of the equipment [2].

Figure 1. Large scale shearing machine (University of Miskolc)

2.1. Stress distribution in shear samples. The effect of sample height is one of the most problematic issues. The vertical load is applied through the loading plate on top of the sample, but this load produces not only normal but horizontal stresses also on the soil body (Figure 2). The normal stresses cause horizontal forces at the side wall of the shear-box, which results in some frictional forces. These frictional forces are proportional to the unknown normal stresses and surfaces. The normal force and naturally also the normal stresses decrease due to the frictional force, so the measured cohesions will be different from the real values (Figure 3).Due to this fact we can never know exactly the normal stress at the shearing plane.

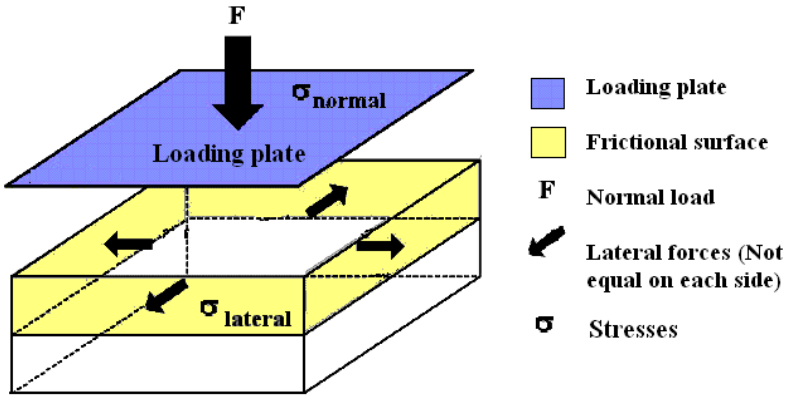

Figure 2. Scheme of surfaces and stresses causing side wall friction

To reduce this error two options are available:

- we have to reduce the surface of friction with reduction of sample height
- we have to measure or estimate the ratio of normal vs. lateral stresses [3].

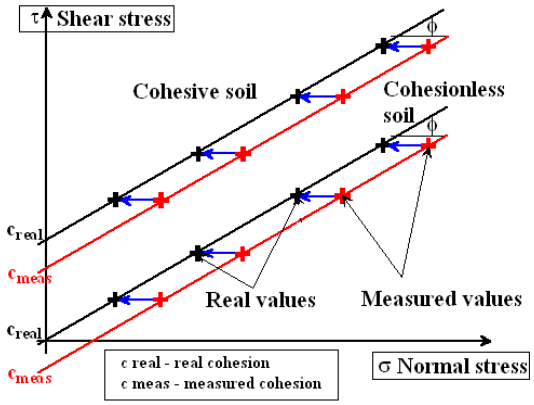

Figure 3. Theory of effect of friction on wall to the cohesion

2.2. Reducing of sample height. To reduce the frictional surface we can reduce the sample height in the shear-box. With height reduction (thinner samples) we can be sure that the normal stress due to applied load is close to that calculated ($\sigma_n = F/A$). This measurement results are closer to linear on σ-τ plane (Figure 4). Unfortunately the mentioned frictional error causes the reduction of "apparent" cohesion values, since during the measurement's evaluation we consider a higher normal stress than actually occurs.

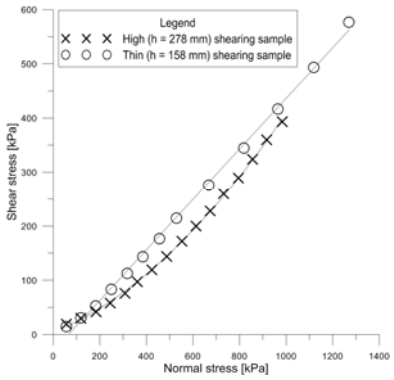

Figure 4. Effect of sample height reduction on Coulomb failure lines during shear tests

This can lead also to the measurement of "negative cohesion" in cohesionless soils (see Figure 3). In the case thatside wall friction force is not constant, an alteration in internal friction can also occur. Since parallel to the increase of the lateral forces there is also a decrease of contact surface due to soil compaction, the result of the two opposite procedures may cause either the increase or the decrease of the determined angle.

2.3. Measuring of stresses on the boundary. To measure the normal vs. lateral stresses function there are several ways. It is possible to build sensors into the side wall of the shearing-box, which can be one of the solutions. A sensoric measuring system was developed at University of Miskolc, Department of Earth Science and Engineering in 2011.

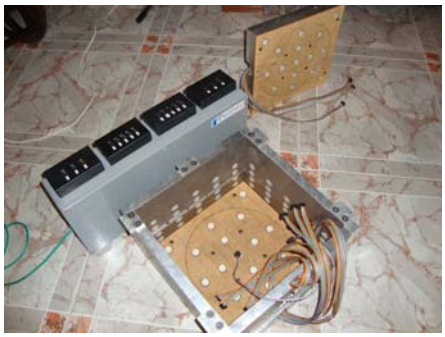

Figure 5. Parts of sensoric measuring system

This is an optional part of the large-scale shearing machine that makes possible to measure the stresses on the whole surface of shearing sample. The system consists of 82 pressure sensors (Figure 5). The measuring range of the stress sensors is 0 to 800 kPa. This means that the highest load we can apply on the surface (A = 1225 cm^2) is approx 10–12 tons due to the energy dissipation inside the soil sample body. This load range is high enough to simulate a number of processes that could occur in geotechnical practice.

In Figure 6 we can see a stress distribution map for a shear sample that is made from acrylate. This test was carried out in the early 1990s in Miskolc and the aim was to determine the stress zones in shear samples by optical techniques [4]. The investigation showed us that the stress distribution in the sample body is not homogeneous and a variety of effects deform it. The isobars help us to see the different stress zones.

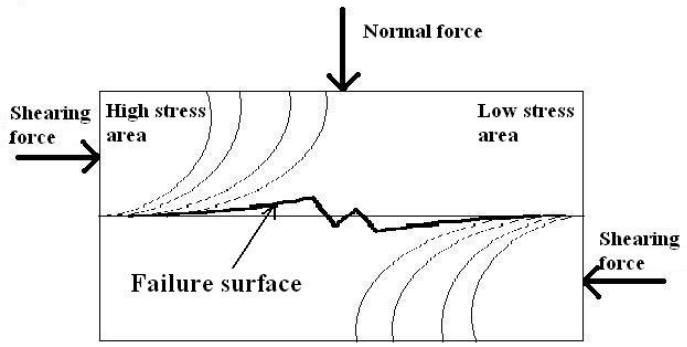

Figure 6. Stress distribution in a shear sample (reconstruction by authors)

Our research group aimed at a similar investigation. Thanks to the sensoric development on the large-scale shearing machine we could start the investigation. The measurement protocol was a traditional one, starting with a consolidation phase while the investigated soil compacted and next a shearing phase with horizontal movements.

The material used was a sandy agricultural soil in dry conditions. It comes from the investigation way of the Geotechnical Soil Testing Laboratory. We characterised loose agricultural soil with traditional geotechnical methods in laboratory, semi-laboratory and field situations.

Compaction behaviour of different soils mostly depends on its granulometry and moisture content level.. The sandy soil has an optional consolidation behaviour because if it is dry (w% = 1–2% m/m) we can reach the 80% of consolidation degree in a short time (a couple of minutes).

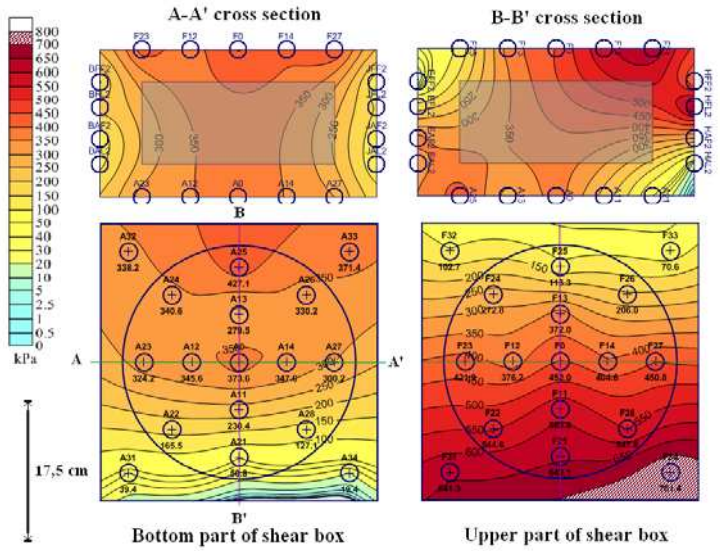

Figure 7. Stress distribution in large scale shear sample (pressure sensors)

Figure 7 summarises the results of a shearing test in an isobaric map. If we compare it with Figure 6 we can find significant similarities. The compaction zones are in the same places and the characteristics are the same. That means the stress zones that were measured in an acrylate sample are similar in grainy materials.

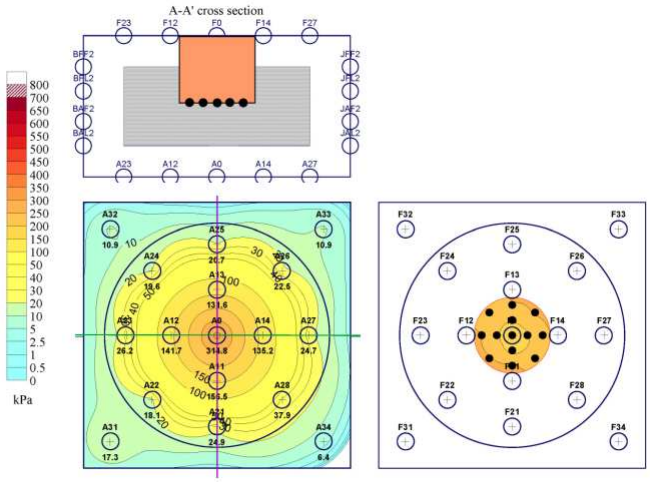

Figure 8. Stress distribution in an intender test (pressure sensors)

Another investigation was carried out with the sensoric system. It was an intender test, meaning that a rigid element was pushed into a pre-consolidated soil sample. The results provide a lot of information about the stress distribution (Figure 8). As we can see, the stress is not homogeneous on the contact surface of intender and soil [5]. Previous tests confirmed this behaviour; the root of causes come from the friction effects on the cylinder wall. These results could be useful in geotechnical piling technologies or bridge piers.

3. Conclusions

In the aspect of sample height we could say the following: as thin a sample as possible is to be used to reduce side wall friction or to make lateral stress measurements possible in the shearing box. In case the sample height is reduced too much, the boundary conditions at the top and bottom of the sample disturbs the processes inside the sample, therefore we have to find a compromise. In case of approx. 10 cm sample height at the highest vertical loads measurement results were already of acceptable side wall friction but without problems of effect of top and bottom are plates. The comparison of the stresses on several side-walls and the distribution character of stresses on the bottom plane give information on the initial homogeneity of the sample, which is a key issue due to the fact of skewing measurement results by such irregular errors.

Although a homogenous stress field is considered as an approximation there are large differences both inside the investigated sample and on the boundaries. It is not possible to measure the stress distribution inside the sample, but the measured values on the boundaries present a coherent picture of stress distribution that makes the estimation of in-sample stresses more accurate.

The measured parameters can be used as input parameters of further numerical simulations for soil characterisation that makes possible the control of determined constitutive law parameters. The measurement of real time distribution of stresses allows us to determine the character of energy dissipation that helps us to determine the transient geotechnical parameters. The determination of lateral vs. normal stresses gives an option to characterise the plastic Poisson ratio and its change during the compaction procedure.

Acknowledgements

The described work was carried out as part of the TÁMOP-4.2.1.B-10/2/KONV-2010-0001 project in the framework of the New Hungarian Development Plan. The realization of this project is supported by the European Union, and co-financed by the European Social Fund.

References

[1] Kézdi Á.: Talajmechanika I. Tankönyvkiadó, Budapest, 1972.
[2] Kántor T.–Kovács B.: Laza, (konszolidálatlan) talajok nyíróvizsgálatai nagyméretű nyíróberendezéssel. Mérnökgeológia Kőzetmechanika 2010, Budapest, Mérnökgeológiai-Kőzetmechanikai Kiskönyvtár Vol. 8, pp. 113–122.
[3] Kántor T.–Kovács B.: Developing of an innovative large-scale shearing machine and conclusions of first measurements. Geotechnical Engineering: New Horizons, Rotterdam, 2011, pp. 267–272.
[4] Szabó I.–Kovács B.–Czinege L.: Korszerű nyírószilárdságvizsgáló berendezések a Hidrogeológia-Mérnökgeológiai Tanszéken. Geotechnika konferencia kiadványa, Ráckeve, 1992, p.72.
[5] Kriston S.–T. Kántor–Czinkota I.: The evolution of stress field in loose, agricultural soils. 8th Alps-Adria Sci. Workshop, Neum (Bosnia-Herzegovina), April 27–May 2, 2009.

Geosciences and Engineering, Vol. 1, No. 2 (2012), pp. 99–104.

INFILTRATION TESTS ON IRRIGATED AGRICULTURAL AREAS

LÁSZLÓ KOMPÁR[1], PÉTER SZŰCS[2], ZOLTÁN FEJES[3],
LÁSZLÓ PALCSU[4], JÓZSEF DEÁK[5]
[1]PhD student;MTA-ME Research Group of Geoengineering,
Department of Hydrogeology and Engineering Geology;
3515 Miskolc, University of Miskolc; hgkompar@uni-miskolc.hu
[2] Head of department, professor; MTA-ME Research Group of Geoengineering, Department of Hydrogeology and Engineering Geology; 3515 Miskolc, University of Miskolc; hgszucs@uni-miskolc.hu
[3] Pre-PhD student; Department of Hydrogeology and Engineering Geology;
3515 Miskolc, University of Miskolc; fzolee14@gmail.com
[4] Head of departement; Institute of Nuclear Research of the Hungarian Academy of Sciences;
18/C Bem tér 4026 Debrecen; palcsu@atomki.hu
[5] Managing director, GWIS Ltd; 45 Alkotmány u. 2120 Dunakeszi; deak47jozsef@gmail.com

1. Introduction

The Duna-Tisza ridge is one of the largest recharge areas in Europe. There is an international project, which is coordinated by the International Atomic Energy Agency (IAEA) to investigate the natural groundwater recharge at some test sites in Europe. In Hungary a special research group carries out this interesting research program at two sampling sites named Méntelek and Kecskemét Szv II. The aim of the research is to build flow and transport models for the sample sites, which are based and calibrated on tritium isotope measurements in order to derive local recharge values. In earlier papers the research work at Méntelek has been presented [1]; we showed our model simulations and the results. Now in this work another test site, which was irrigated for agricultural purposes earlier, has been investigated close to Kecskemét.

2. Materials and method

^{3}H is the radioactive isotope of hydrogen. The only difference between the ^{3}H and the hydrogen is the number of the neutrons. Tritium is formed in the upper atmosphere during – β decay. It has a half life of 12.4 years, during which tritium decays to ^{3}He.

The main aspects of selection of sample area were the followings:

- on the site there was sewage disposal for at least 5 years,
- the site was used for agriculture ,
- the sites must be on the Hungarian Great Plain,
- the depth and the quality of the groundwater must be suitable to model the movement of sewage components.

The choice was based on these parameters, so for a test site Kecskemét was chosen [2]. Kecskemét can be found near Méntelek in the Duna-Tisza ridge [Méntelek was the base of the previous studies (Figure 1)]. The test site in Méntelek operates just for research; only a meteorological station works on the site. This test site in Kecskemét was installed in 1944 for research purposes on an agricultural area. At that time there was a plan to join the

Danube and the Tisza rivers through a canal. At the station in Méntelek the decreasing of groundwater level would have been monitored, but this plan was never realised.

The wells in Kecskemét were installed in loess and sand bedrock on the Duna-Tisza ridge. This area has a moderately warm and arid climate. The average annual precipitation was about 550 mm/year in the last 70 years. The soils of the site were investigated before the study began. The test site is physiologically heterogeneous; there are several soil types on the area [3].

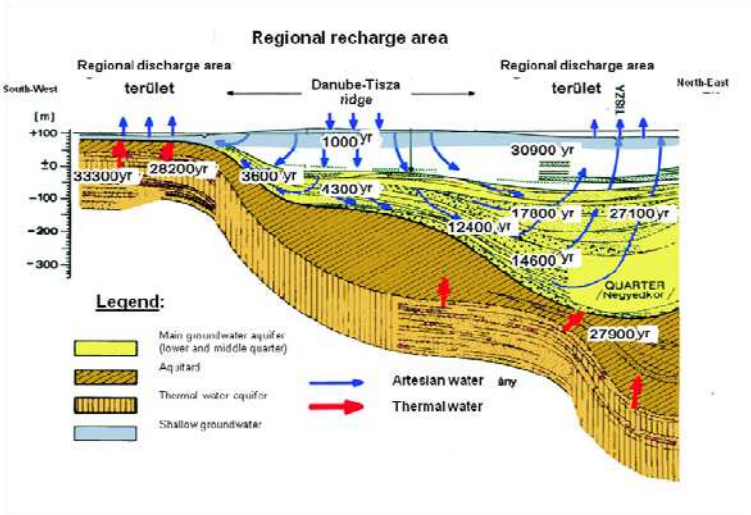

Figure 1. The Duna-Tisza ridge is the main recharge area of Hungary

The test site, as in Méntelek, is a typical recharge area. The groundwater flow is nearly vertical. This is the reason for its selection as a test site. The tritium profile was measured in 2001 at 6 different depths under the surface from groundwater, because at that time 6 wells were drilled (Figure 2). A numerical transport model was created covering the period between 1951 and 2010, like for Méntelek. The tritium content of the Hungarian precipitation was estimated for this period using precipitation data since 1972, wine samples of 1960 to 1977 and GNIP data of Vienna and Ottawa.

The framework of the model is the same as in the model of Méntelek: a column model was built, which works with just vertical flow involving recharge. The hydrodynamic model is similar to the other model; while the groundwater level is different, the geological parameters are the same. These geological parameters were determined from the boreholes from 2001.

Figure 2. The 6 wells near Kecskemét

MODFLOW is a U.S. Geological Survey modular finite-difference flow model. This computer code can solve the groundwater flow equation. The governing partial differential equation solved numerically in MODFLOW is given in the following form:

$$\frac{\partial}{\partial x}\left(K_{xx}\frac{\partial h}{\partial x}\right)+\frac{\partial}{\partial y}\left(K_{yy}\frac{\partial h}{\partial y}\right)+\frac{\partial}{\partial z}\left(K_{zz}\frac{\partial h}{\partial z}\right)+W=S_S\frac{\partial h}{\partial t}$$

where K_{xx}, K_{yy}, and K_{zz} are the values of the hydraulic conductivity along the x, y and z coordinate axes (L/T), h is the hydraulic head (L), W is the volumetric flux per unit volume representing the sources and sinks of groundwater, for which the negative values mean extractions while the positive values mean injections (T^{-1}), S_S is the specific storage of the investigated aquifer (L^{-1}), and t is time (T). This program is widely used throughout the world by hydrogeologists to simulate the flow of groundwater through aquifers. The code is a free software, written in the FORTRAN language, and can be compiled and run on the DOS, Windows, or UNIX operating systems. Since its original development in the early 1980s [4], the USGS have released four major versions of this code, and it is now considered to be the de facto standard industrial code among groundwater specialists for aquifer simulation. Currently there are many actively developed commercial and non-commercial graphical user interfaces for MODFLOW.

Commercial MODFLOW programs are typically used by governments and consultants for practical applications of MODFLOW to real-world groundwater problems. The applied PMWIN-Pro may be considered as a professional commercial version of MODFLOW. A three-dimensional flow model considering 44 layers was implemented with the help of the MODFLOW-2000 module in the current project work. This model was used to characterise

the nearly vertical groundwater flow of the investigated area in Kecskemét, which is a main recharge region on the Hungarian Great Plain. The required input data for the flow model were readily available from an earlier geological and hydrogeological prospecting activity.

Besides the flow model, a transport model was also built to investigate tritium concentration distribution under the surface due to the groundwater recharge from precipitation. The tritium transport movement investigations were carried out in the field-study by the module MT3DMS, where MT3D means Modular 3-dimensional transport model, and MS means the multi-species structure to model several components simultaneously. MT3DMS has a comprehensive set of options and capabilities for simulating the advection, dispersion, diffusion, radioactive decay and chemical reactions of contaminants in groundwater flow systems under general hydrogeologic conditions. MT3DMS was developed for use with any finite-difference flow model such as MODFLOW, and is based on the assumption that changes in the concentration field (Figure 3) will not affect the flow field appreciably.

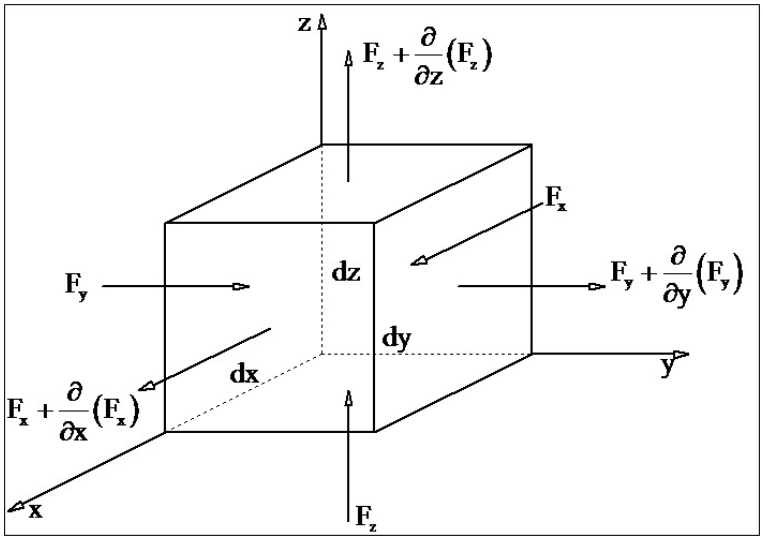

Figure 3. The balance of tracer of elementary space

The partial differential equation describing the fate and transport of chemical components or contaminants of the species k in a three-dimensional space in transient groundwater flow systems can be written as follows:

$$\frac{\partial\left(\phi C^k\right)}{\partial t} = \frac{\partial}{\partial x_i}\left(\phi D_{ij}\frac{\partial C^k}{\partial x_j}\right) - \frac{\partial}{\partial x_i}\left(\phi v_i C^k\right) + q_s C_s^k + \sum R_n$$

where ϕ means porosity of the aquifer, dimensionless, (fraction), C_k is the dissolved concentration of species k, (M/L^3), t is time (T), $x_{i,j}$ is distance along the respective Cartesian coordinate axis (L), $D_{i,j}$ is the hydrodynamic dispersion coefficient tensor (L^2/T),

v_i is the seepage or linear pore water velocity based on the Darcy equation (L/T), q_s is the volumetric flow rate per unit volume of aquifer representing fluid sources and sinks (1/T), C_s^k is the concentration of the source or sink flux for species k (M/L^3), and $\sum R_n$ is the chemical reaction term ($M/L^3/T$).

Figure 4. Water sampling for tritium measurement

3. Results

Water samples were collected on the test site close to Kecskemét in 2012 (Figure 4). The model of Kecskemét shows the same results as the model of Méntelek. We obtained a tritium profile from the transport model (Figure 5). The red line was constructed from data of 2001, when the wells were drilled, and the groundwater was sampled during drilling. From these drillings the largest TU value was established at 9.5 m. The figure simulates 2 peaks, which is an interesting thing: the researches started in 1971 on this site, during 10 years of sewage disposal, when the splashed water had a TU value, which was 0 TU (the deep groundwater has 0 TU tritium content). After the research work the tritium content of the precipitation appeared in the shallow groundwater, this look likes the second peak at 13.6 m below the surface. The blue line shows the calculated values. These model values need to be clarified and calibrated, as the obtained line is an adducing result. However it can be seen that the model works in an acceptable manner, and it shows the character of the red curve.

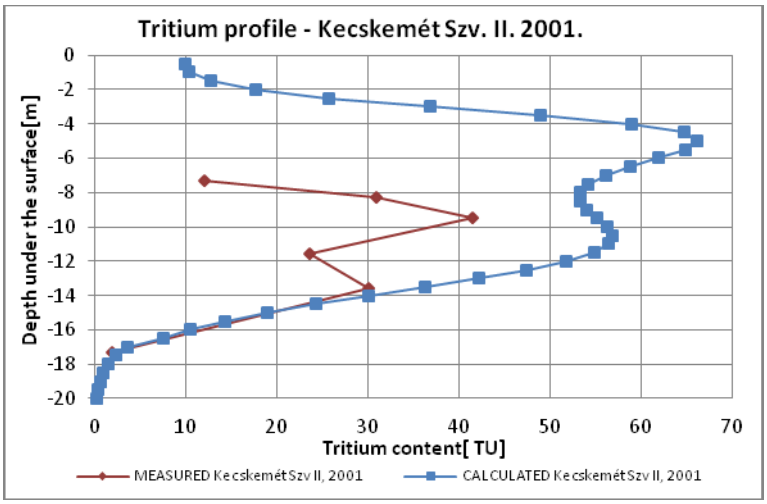

Figure 5. The tritium profiles of Kecskemét

4. Conclusion

Nowadays isotopes are very important tools for hydrogeology. Numerical transport modeling is also a useable tool for defining some problems in earth science and engineering. In this case study we determined that isotope hydrology and transport modeling applied together is a possible tool for investigating the natural recharge from precipitation.

Acknowledgements

The described work was carried out as part of the TÁMOP-4.2.2/B-10/1-2010-0001 project in the framework of the New Hungarian Development Plan. The realization of this project is supported by the European Union, and co-financed by the European Social Fund.

References

[1] Kompár, L.–Szűcs. P.–Palcsu, L.–Deák, J.: A természetes utánpótlódás meghatározása trícium izotóppal. Műszaki Tudomány az Észak-kelet Magyarországi Régióban 2012. Debreceni Akadémiai Bizottság Műszaki Szakbizottsága, Debrecen, 2012.
[2] Tóth, L.: A kecskeméti kommunális szennyvízelhelyező- és hasznosító rendszer üzemeltetésének tapasztalatai. Kecskemét, 1979.
[3] Vízgazdálkodási Tudományos Kutató Részvénytársaság (VITUKI Rt.): Felszín alatti víz vizsgálatok kijelölt mintaterületeken (2001. évi zárójelentés). Témaszám: 712/1/5127-01. Budapest, 2001.
[4] McDodald, M. G.–HARBAUGH, A. W.: *The History of MODFLOW*. Ground Water, 2003, 41 (2), pp. 280–283.

Geosciences and Engineering, Vol. 1, No. 2 (2012), pp. 105–110.

REMARKS ON THE PROBLEM OF OUR FUTURE ENERGY SOURCES

MOLNÁR, JÓZSEF
Associate professor, University of Miskolc (Hungary),
Institution of Mining and Geotechnical Engineering,
H-3515 Miskolc-Egyetemváros, bgtmj@uni-miskolc.hu

1. Introduction

Renewable energy sources, such as biomass produced as agricultural and forest waste, have become very fashionable energy sources throughout the world and in Hungary as well. In contrast, coal is generally considered an old-fashioned fuel, and coal mining is accordingly not fashionable. This opinion is usually explained by the emission produced by burning coal, especially carbon-dioxide emission. It is not only supposed but generally accepted that the emission rate produced by burning biomass cannot be higher than the amount of carbon-dioxide that the plant captured during its whole life. Although this opinion is arguable, regulations are based on it. So coal-fired power plants are forced to use biomass too, produced mostly by agriculture and forestry. Thesises of a short objective comparison of emission rates of mineral and biomass fuels furthermore, some essential technical and economic aspect of their utilization are discussed in the paper.
Keywords: fuels, biomass, coal, power generation emission rate, CO_2 emission

2. Emission rates resulted by burning fuels

2.1. Energy consumption of Hungary. Despite certain expectations neither the energy nor electric energy consumption decreased in Hungary since 1990, according to the 22 years official historical data published by the Hungarian Central Statistical Office. Unfortunately domestic production of mineral fuels decreased during almost the whole period in question with the exception of a slight increase in the last years. So the country has become strongly dependent on fuel (mostly hydrocarbons and uranium) imports [6, 12, 21].

2.2. An order of magnitude of fuel sources of the country. Hungary is considered poor in mineral reserves including fuel sources. This is not quite true, as its explored industrial lignite, brown coal and hard coal reserves could provide a significant rate of its fuel demand for centuries using even the recent extraction technologies. More than 1900 million tons of hard coal with a significant methane content could be extracted from underground and approximately 4300 million tons of lignite with opencast method, according to the Hungarian Office for Mining and Geology (source: *http://www.mbfh.hu/*). Continuous opencast mining method is economic and efficient in lignite production. Recent underground mining methods probably do not enable mechanized and efficient extraction of deep hard coal seams due to their unfavourable geological characteristics. Certain results of underground coal gasification experiments can be encouraging if some essential problems, such as stable maintenance and regulation of the pyrolysis process, resulting gas of high heat content could be solved. It would be interesting to make an objective analysis

of this and the conventional mining methods, comparing basic parameters, e.g. mine development, stability of cavities, surface subsidence, mine output, etc.

A further question should be the extraction method of coalbed methane content. Although a remarkable quantity of methane is contained in the coal seams, the rather low permeability of the coal seams and certain experiences obtained in the Mecsek and other coalfields do not support optimistic expectations.

2.3. Emission rate of burning different fuels. Numerous combustible chemical compounds, many samples of biomass such as straw, corn-stalk and different kinds of firewood, etc., and furthermore chemical composition of coal samples from every coal basin of Hungary [1, 5, 8, 20] were examined in a long-term research to estimate the expected specific composition of the flue gas produced by burning the materials in question containing exactly 1 MJ of heat. The estimation method was basically stoichiometric. Results obtained by the analysis [14, 17–19] perfectly match the values contained in the Hungarian regulation. Consequently, regulation is based on stoichiometric calculations. The basic results can be summarized as follows.

The carbon-dioxide emission rate per heat content of the fuel is nearly the same for burning different kinds of coal (0.091–0.118 $MJ \cdot kg^{-1}$), according to the great amount of Hungarian coal samples. Emission from coal combustion is only slightly higher than from burning liquid hydrocarbon products and biomass, and *theoretically* 1.5–2 times higher than that of methane (0.55 $MJ \cdot kg^{-1}$), the basic component of natural gas. It is very important to emphasize, that if the influence of long-distance transportation (e.g. volumetric losses and energy consumption of the transportation, etc.) and the carbon-dioxide content of the gas is taken into account in the emission calculations, this result can be significantly unfavourable. Methane loss results greenhouse effect in the atmosphere to a 21-times greater extent than carbon-dioxide of the same quantity.

Although the greenhouse effect of vapour cannot be neglected, this factor is not limited by Hungarian regulations. The vapour emission rate of coal is significantly, 2–3 times lower than that of natural gas and biomass.

Sulphur-dioxide emission is significant if a great quantity of coal is used as source of heat. This is why flue gas desulfurization units should be operated in coal-fired power plants resulting extra costs. Utilizing natural gas and biomass does not result a high sulfur-oxide emission rate. The ash content of coal is the highest of all examined fuels. Although coal ash and flue gas desulfurization (FGD) gypsum are industrial wastes, but can be useful raw materials at the same time [13, 15].

2.4. Greenhouse equivalent of the emission from biomass. The greenhouse equivalent of the gas emitted by the biomass in question is not equal to but higher than the quantity of emitted carbon-dioxide by the plants in question. The mass of the methane produced by the decay of the parts of the plant during its whole life and after it must be taken into consideration as well. As the greenhouse effect of methane is 21 times higher than of the carbon-dioxide, the greenhouse effect of the biomass is worse that of coal of low methane content. Unfortunately this fact was totally ignored when contributing the appropriate regulation which enables not to take into account the carbon-dioxide emission from biomass.

3. Technical and economic aspects of utilizing biomass and coal

3.1. Annual quantity of straw and corn-stalk. Some 9 million tons of straw and corn-stalk are produced in Hungary annually. This quantity of biomass is called a by-product in recent common usage. Crop yields calculated for dry materials are rather low at the first sight: approximately 1.6 $m^2 \cdot kg^{-1} \cdot year^{-1}$ for corn and corn-stalk together, 1.0 $m^2 \cdot kg^{-1} \cdot year^{-1}$ for corn-stalk and straw, 0.6 $m^2 \cdot kg^{-1} \cdot year^{-1}$ for firewood from energy forests or other kinds of energy plantations, and 0.2 $m^2 \cdot kg^{-1} \cdot year^{-1}$ for firewood from conventional forests. The average lower heat content of the dry fuel is about 17.5 $MJ \cdot kg^{-1}$ [2–4, 22].

3.2. Value of a field in agriculture and mining. Even for average 20–30 m thick sand and gravel deposits of approximately 250 years and the best soils are needed to produce agricultural products of the same value as the sand and gravel which can be found below the same area [11].

3.3. Heat content of the agricultural and forest biomass. The approximate heat content of 9 million tons of dry biomass of 17.5 $MJ \cdot kg^{-1}$ (lower) heating value amounts 157.5 $PJ \cdot year^{-1}$. The total amount of energy from other agricultural wastes can be estimated at a similar value [16, 18]. Some 4991 MW of power could be obtained from burning all straw and corn-stalk reserves annually without any heat losses. For a 30% efficiency in converting energy from heat to electricity a remarkable 1497 MW electric output could be obtained, 1996 MW for 40%, 2495 MW for 50% and 2994 MW for 60%.

3.4. Area required for producing such a quantity of biomass. If 1.0 $m^2 \cdot kg^{-1} \cdot year^{-1}$ crop yield is taken into account for corn-stalk and straw, a 9000 km^2 area is required to produce fuel for power generation, described in the previous paragraph [2, 10, 16, 18]. Beside harvesting corn and grain corn-stalk and straw must be collected from the same area, too. Unfortunately, while this area is continuous, it consists of fragmented fields of numerous owners, which make acquisition and transportation rather difficult. Areas of the three largest Hungarian counties can facilitate to imagine the real size of the area in question: Bács-Kiskun 8445 km^2, Borsod-Abaúj-Zemplén 7242 km^2 and Pest 6393 km^2 (1 January, 2004).

The area of Hungary per capita is 9300 m^2. If the total energy demand would be satisfied by domestic agricultural biomass production, a 6400 m^2 area would be necessary or 3000 m^2 if only electrical power generation is considered. [9, 16, 18]

3.5. Capability of soils to grow biomass for energy purposes. Approximately 1700 to 17000 years are needed fo 1 m^2 area of good soil of Hungary to be able to produce the same quantity of heat in the form of biomass as could be extracted from the same area of a 2–2.5 m thick brown coal or a 7–10 m thick lignite deposit. So if the same quantity of heat is to be produced as agricultural or forest biomass instead of mining coal, a significantly (a thousand to ten thousand times) larger area of land of the country is required [16, 18]. Consequently, the area occupied by mining operations is significantly less than the agricultural and forest area that could provide the same quality of energy. And even this smaller area is reclaimed. The use of agricultural and forest lands is not restricted by

Hungarian regulations. But several sales and purchases as well as changes in land registry must forego use of the same land for mining purposes.

3.6. Biomass storage facilities. Straw and corn-stalk produced for energy purposes can be harvested once a year in the Hungarian climate. The duration of the harvest in question does not exceed a quarter year. Furthermore running out of the fuel reserve gathered in the previous year cannot be allowed for strategic reasons. Consequently storage facilities should be built for the biomass, whose total capacity must be equal to or more than the annual quantity of the fuel. Special precautions are needed to avoid risks (e.g. fire hazards etc.) resulted by the concentrated storage of the total amount of the biomass.
The capacity of the transportation system, including the roads, must be sufficient for the haulage of the harvested biomass to the storage facilities or the power plants within a 3-months-period. Once ingathering is ready, equipment cannot be used for this purpose during the following 9 months.

3.7. Safety of fuel supply. Any power plant should be supplied with fuel of the appropriate quality and quantity during its whole lifetime. Sometimes certain properties of quality can be significantly different from those of coal. To guarantee safe supply, biomass must not be allowed to be sold for other purposes even if temporary prosperity would offer more profitable possibilities. So long-term contracts are probably necessary for fuel supply as is quite usual in the market of mineral fuels, such as coal, hydrocarbons and nuclear fuel.

3.8. Biomass fuels are not free. Production of agricultural and forest biomass is not free and usually requires human assistance, except if it is considered waste and only *in situ*. Utilization of biomass is costly, too, sometimes even for wastes. It should be emphasized that unexplored mineral reserves are free as well *in situ* as no human assistance was needed for their genesis. Furthermore coal reserves are renewed over geological ages too.

3.9. Area required for producing such quantity of biomass. The price of fuels is determined by marginal costs regardless of whether the fuel is mineral, agricultural or forest in origin. So the price of products obtained by the processing of biomass, such as biomass pellets, biodiesel oil, bioethanol, etc., must not exceed the prices of other fuels for similar purposes made of coal or hydrocarbons. Consequently, usually either governmental subventions are needed and paid or taxes or other duties are introduced in order to eliminate the difference and maintain this activity. No matter which solution is selected, higher energy prices would be the result.

One of the main arguments against underground mining was its need for financial support [7]. This support, enabled by temporary regulation of the European Union, never exceeded an annual 8–10 billion HUF or 50 million US dollars during the past 6–7 years for a Hungarian underground coal mine of 1–1.5 million tons output per annum. As a result of this approach, almost all proposals concerning the coal industry are excluded from different funding possibilities, financed by the administration.

3.10. Energy biomass cannot be used for other purposes. Straw, corn-stalk, sugar cane, sugar beet and other similar products cannot be utilized in the different branches of agriculture once used as a source of energy. Nor can the land which was occupied for

production. A cleared forest cannot capture any carbon-dioxide from the atmosphere. On the other hand a living forest can not only stabilize the climate and reduce some environmental risks but finally is able to capture the carbon-dioxide from the atmosphere emitted by power plants, cement plants and waste incinerators.

3.11. Size of regions providing biomass fuel for a power plant. A simple model was introduced to estimate the size of regions which can provide sufficient fuel for a power plant of P electric output and of $0.3 \le \eta \le 0.6$ efficiency of converting heat to electricity. The region is circular of R radius. A concentric circle of R_0 radius is reserved for the power plant and the storage facility. A $q = 1$ $m^2 \cdot kg^{-1} \cdot year^{-1}$ average crop yield and $H = 17.5$ $MJ \cdot kg^{-1}$ lower heating value for biomass are taken into consideration. The radius of the region, mass of the fuel to be stored annually (m) and radial component of the freight ton kilometres (S_{rad}) were determined as follows, the results can be read in Table 1:

$$R = \sqrt{R_0^{\,2} + \frac{P}{\pi \cdot \eta \cdot q \cdot H}}\,,\quad m = \frac{P}{\eta \cdot q} \text{ and } S_{rad} = \int_{(A)} r \cdot q \, dA = \frac{2\pi}{3} \cdot q \cdot \left(R^3 - R_0^{\,3}\right)$$

Table 1

Estimated parameters of biomass fuel supply of power generation($0.3 \le \eta \le 0.6$)

Electric output, P (MW)	**Mass of the fuel, m (10^3 tons/year)**	**Radius of the region, R (km)**	**Radial component of freight ton kilometres, S_{rad} (10^3 tkm/year)**
5	15–30	1.73–2.45	2.2–6.2
50	150–300	6.9–9.8	700–2000
800	2400–4800	22–30	44000–125000

4. Conclusions

Numerous aspects were reviewed in this short study concerning the application of coal and biomass as fuel for power generation. Finally the question arises: can biomass be considered as an alternative fuel in power generation? Sophisticated equipment is available for the economic utilization of biomass in certain situations. However, considering emission, haulage and storage, coal seems to be more economic for higher outputs.

Acknowledgements

This work was carried out as part of the TÁMOP - 4.2.1.B - 10/2/KONV - 2010 - 0001 project in the framework of the New Hungarian Development Plan. The realization of this project is supported by the European Union, co - financed by the European Social Fund.

References

[1] Balassa, G.: Égés áramlásban. Tankönyvkiadó, Budapest, 1986. p. 19.
[2] Büki, G.: Energetika. Műegyetemi Kiadó, Budapest, 1997.
[3] Büki, G.: A földhő energetikai hasznosításának hatékonysága (I). Mérnök Újság, 2008. október. Loaded from the http://www.mernokujsag.hu/index.php?tkod=4323&tcim=A%20f%

F6ldh%F5%20energetikai%20hasznos%EDt%E1s%E1nak%20hat%E9konys%E1ga%20(I)&ev=2008&szam=9&honap=OKT%F3BER&n=90, January 21st, 2009

[4] Büki, G.: A földhő energetikai hasznosításának hatékonysága (II). Mérnök Újság, 2008. november. Loaded from the http://www.mernokujsag.hu/index.php?tkod=4360&tcim=A%20f%F6ldh%F5%20energetikai%20hasznos%EDt%E1s%E1nak%20hat%E9konys%E1ga%20(II)&ev=2008&szam=10&honap=NOVEMBER&n=90, January 21st, 2009

[5] Ebbing, D. D.–Wrighton, M. S.: General Chemistry. Hugton Mifflin, Boston, 1987. p. 165–167.

[6] Energiamérleg. A Központi Statisztikai Hivatal StatADAT táblája. Loaded from the http://portal. ksh. hu/pls/ksh/docs/hun/xstadat/xstadat_eves/tabl3_08_01i.html homepage, October 14th, 2008.

[7] Evaluation of State aid for the coal industry. A report by Europe Economics and Fraunhofer ISI with BSR Sustainability and the Krakow Institute for Sustainable Energy. Europe Economics, Chancery House, 53–54 Chancery Lane, London, WC2A 1QU. 20 October, 2006.

[8] Farkas, O.: Ipari kemencék tüzeléstani számításai. Tankönyvkiadó, Budapest, 1990. p. 70.

[9] Farkas, O.–Szemmelweisz, T.: Gondolatok a biomassza hazai hasznosításáról. Északkelet-Magyarország. Gazdaság-kultúra-tudomány. 2008. 2. szám, p. 21–26.

[10] Hicks, T. G. (editor): Power Plant Evaluation and Design Reference Guide. McGraw-Hill Engineering Reference Guide Series, McGraw-Hill Book Company, 1986.

[11] Horányi, I.: A föld méhének kincse – az állam vagyona. Jó gazda az állam? Bányászati és Kohászati Lapok, Bányászat, 135. évfolyam (2002.) 5. szám, p. 29–32.

[12] Kovács, F.: A primer energiahordozók aránya a villamosenergia-termelésben. Bányászati és Kohászati Lapok, Bányászat, 137. évf. 1. szám, p. 4–8.

[13] Kovács, F.–Molnár, J.–Valaska, J.: Chemical and Mechanical Characteristics of Byproduct Gypsum Produced in a Hungarian Lignite-Fired Power Plant. Proceedings of the 19th World Mining Congress, Mining in the 21st Century. Quo Vadis? 1–5. November, 2003, New Delhi (India). Volume 2. pp. 1305–1311. Oxford and IBH Publishing Co.Pvt. Ltd. New Delhi.

[14] Molnár, J.: Magyarországi szenek és más fosszilis tüzelőanyagok energetikai alkalmazásakor várható emisszió. A Miskolci Egyetem Közleményei, A sorozat, Bányászat, 75. kötet, Egyetemi Kiadó, Miskolc, 2008, pp. 121–130.

[15] Molnár, J.: Composite construction materials made of the byproducts of generating electrical energy, produced in a Hungarian coal-fired power plant. *In* Proceedings of the 20th World Mining Congress, Mining and Sustainable Development, Teheran (Iran), 7–11 November, 2005. Geological Survey of Iran and National Geoscience Database of Iran, 2005, pp. 157–160.

[16] Molnár, J.: Alternatívája-e ma a növényi biomassza a szénnek a villamos energia termelésben? Bányászat és Geotechnika. A Miskolci Egyetem Közleménye, *A* sorozat, Bányászat, 79. kötet, Miskolc, Egyetemi Kiadó, 2010. pp. 53–61.

[17] Molnár, J.. Remarks to the Carbon-dioxide Emission from Lignite-Fired Power Generation in Hungary. *In* Proceedings of 10th International Symposium Continuous Surface Mining, Technische Universitat Bergakademie Freiberg, Freiberg, Freiberg (Germany). 13–15 September, 2010, pp. 353–357.

[18] Molnár, J.– Debreczeni, Á.: Comparison of Emission Rates of Power Generation Using Coal or Biomass as Fuel. *In* 22nd World Mining Congress&Expo, 11–16. September, 2011, İstanbul (Turkey). In: Sinasi Eskikaya (editor): Proceedings of 22nd World Mining Congress. Turkish National Committee. Volume III, pp. 103–109.

[19] Molnár, J.: Magyarországi szenek energetikai alkalmazásakor várható emisszió. X. Bányászati, Kohászati és Földtani Konferencia. Nagyszeben, 2008. április 3–6., p. 76–78.

[20] Pecznik, P.: Biomassza: a régi-új energiaforrás. III. rész. FVMMI, Gödöllő. Agrárágazat. Loaded from the http://www.agraroldal.hu/biomassza_cikk.html homepage, October 14th, 2008

[21] Villamosenergia-mérleg. A Központi Statisztikai Hivatal StatADAT táblája. Loaded from the http://portal.ksh.hu/pls/ksh/docs/hun/xstadat/xstadat_eves/tabl3_08_02i.html, Oct. 14th, 2008

[22] Zvolenszki, I.: Atomenergia helyett ésszerű mezőgazdasági melléktermék-hasznosítás. Északkelet-Magyarország. Gazdaság-kultúra-tudomány. 2008. 1. szám, pp. 15–20.

Geosciences and Engineering, Vol. 1, No. 2 (2012), pp. 111–116.

PYRITE OXIDATION UNDER CIRCUMNEUTRAL pH CONDITIONS

FERENC MÓRICZ[1]–FERENC MÁDAI[2]–INGAR F. WALDER[3]
[1]Institute of Mineralogy and Geology, University of Miskolc, Hungary;
moriczferi@gmail.com
[2]Institute of Mineralogy and Geology, University of Miskolc, Hungary;
askmf@uni-miskolc.hu
[3]Kjeøy Research and Education Center, Norway;
ifwalder@kjeoy.no

1. Introduction

In the last two decades the effect of Acid Rock Drainage (ARD) has become the leading environmental problem in the mining of sulphidic type ores. In sulphidic mine wastes a principal weathering process is the sulphide oxidation, resulting in low pH and mobilizing heavy metal contamination.

Usually the extracted sulphidic ores consist of different metal sulphides with various oxidation rates. The most common, iron-bearing sulphides – pyrite, pyrrhotite – usually became part of the mining waste and are stored in mine waste facilities where these minerals are exposed to atmospheric water and oxygen that results in quick oxidation processes. However if neutralizing minerals are available, they can buffer the acid production and hence reduce the heavy metal mobilization.

From a mining waste management point of view, a crucial question is whether there are enough available buffering minerals that can consume acidity. Regulations require that the neutralisation potential should exceed by 3–4 times the acid producing potential to consider the waste material safe from ARD production. However, this does not mean that pyrite oxidation stops even under these conditions. In the porous waste rock material in presence of water and oxygen, pyrite grain surfaces start oxidizing, thus creating an acidic micro-environment. Calcite, as a quick neutralizing mineral, is able to maintain a pH range. The net chemical reaction does not show acid production, but sulphide oxidation with possible metal leaching takes place.

Neutral rock drainage (NRD) was detected at some mining waste facilities (e.g. mines in the Kola Peninsula, Russia (high-F), the Schwaz and Brixlegg Mines, Austria (high-Sb), the Endako Mine, BC, Canada (high-Mo)), where weathering and consequent metal leaching takes place under circumneutral conditions [1].

The focus of the current work is to prove whether the ARD effects and pyrite oxidation could happen in the zone of neutral pH and to estimate the oxidation rate. Moreover, the authors would like to emphasize the importance of proper waste management and planning of mining waste facilities. This research work was completed to prove whether Equation (1) takes place, to demonstrate the presence of the oxidation process, even if the discharging pH is not acidic.

$$2FeS_{2(s)} + 3CaCO_{3(s)} + 9H_2O_{(aq)} + 8O_{2(g)} \rightarrow \quad (1/a)$$

$$\rightarrow 2Fe(OH)_{3(s)} + 3CaSO_4 * 2H_2O_{(s)} + SO_{4(aq)}^{2-} + 3CO_{2(g)} \quad (1/b)$$

Based on Eq. (1), the sulphide oxidation can be indicated by the following: an iron-hydroxide crust on the surface of the fresh pyrite grains, gypsum coating on the surface of the calcite, detection of the sulphate concentration in the seepage, the appearance of released carbon-dioxide and increasing oxygen gas consumption.

In the experiment, a kinetic test (column test) was done on a sulphidic mine waste sample from Recsk to speed up the sulphide oxidation and therefore mimic the long-term geochemical behaviour of the sulphidic mining waste material.

2. Theoretical background

The most abundant sulphide minerals in most sulphidic waste facilities are pyrite (FeS_2) and pyrrhotite ($Fe_{(1-x)}S$). Only iron-bearing sulphides produce acid during their oxidation. Iron release itself is not so toxic, but the acidification promotes toxic element release from other sulphides such as sphalerite (ZnS), chalcopyrite ($CuFeS_2$), galena (PbS) and arsenopyrite (FeAsS) [2].

Detailed investigation of the sulphide oxidation began a few decades ago. One of the basic equations for pyrite oxidation, Eq. (2). was created by Nordstrom [3], who assumed the process to be an abiotic system, thus the oxidizer agent is the oxygen:

$$FeS_{2(s)} + H_2O_{(aq)} + \frac{7}{2}O_{2(g)} \rightarrow 2SO^{2-}_{4(aq)} + Fe^{2+}_{(aq)} + 2H^{+}_{(aq)} \tag{2}$$

The Fe^{2+} – released by pyrite oxidation – may be further oxidized (3) to Fe^{3+}, decreasing the acidity by consuming a proton:

$$Fe^{2+}_{(aq)} + \frac{1}{2}O_{2(g)} + H^{+}_{(aq)} \rightarrow Fe^{3+}_{(aq)} + \frac{1}{2}H_2O_{(aq)} \tag{3}$$

The resulting Fe^{3+} is a stronger oxidizer agent than the oxygen itself, thus it can lead to the oxidation of pyrite even in an oxygen free environment (4). Moreover, the transport of the gas is limited by slow diffusion processes, but the Fe^{3+} as a dissolved ion can move easily by seepage or water flows.

$$FeS_{2(s)} + 14Fe^{3+}_{(aq)} + 8H_2O_{(aq)} \rightarrow 15Fe^{2+}_{(aq)} + 2SO^{2-}_{4(aq)} + 16H^{+}_{(aq)} \tag{4}$$

Reaction (2) can occur both abiotically or biotically. Reaction (3) is a slow reaction that requires biotic catalysis, but reaction (4) occurs quickly [4]. Reactions (2) and (3) can occur only in low pH, because the Fe^{2+}-Fe^{3+} oxidation is effective only under pH 2, catalyzed by *Acidobacillus ferrooxidans*, which can maintain such a condition.

If the pH is above 4, the Fe^{3+} can be hydrolyzed and precipitate (5) as Fe^{3+}-hydrite, decreasing the amount of the oxidizer agent in the aqueous solution. Although ferrihydrite is commonly assumed to be the product of sulphide oxidation, goethite (6) is much more commonly observed and is abundant in sulphidic wastes [5].

$$Fe^{3+}_{(aq)} + 3H_2O_{(aq)} \rightarrow Fe(OH)_{3(s)} + 3H^{+}_{(aq)} \tag{5}$$

$$Fe^{3+}_{(aq)} + 2H_2O_{(aq)} \rightarrow FeOOH_{(s)} + 3H^{+}_{(aq)} \tag{6}$$

On the other hand the reverse of the equation (5) and (6) can be occur as well, if the acidity goes under a limit (approximately pH 3.5) which is acidic enough to dissolve back the already precipitated solid mineral phases. The leading oxidizer agent–oxygen or Fe^{3+}– depends on the pH value. Singer and Stumm suggested that Fe^{3+} is the dominant oxidant under low pH conditions [6].

If there are neutralizing minerals in the system, they consume the acidity directly, slowing the oxidation rate and stopping the metal release by precipitation. The neutralizing reaction is written in Equation (7), which shows how calcite can dissolve back, and thus can neutralize the acidity. Figure 1 summarizes the above-listed reactions.

$$CaCO_{3(s)} + 2H^{+}_{(aq)} \rightarrow Ca^{2+}_{(aq)} + H_2O_{(aq)} + CO_{2(g)} \quad (7)$$

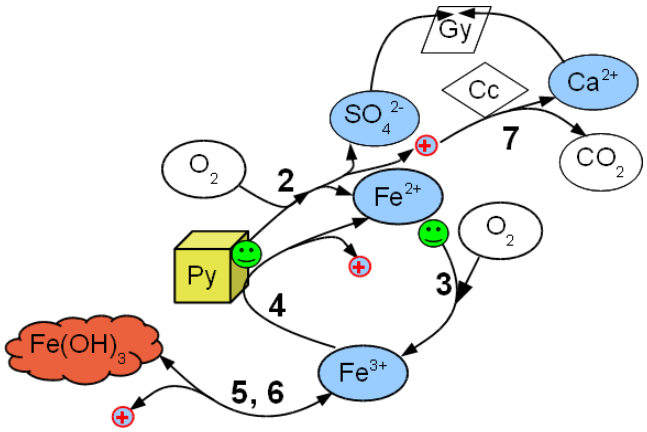

Figure 1. Schematic representation of reactions 2, 3, 4, 5, 6 and 7. Abbreviations and symbols: Py: pyrite, Cc: calcite, Gy: gypsum, ☺: bacteria, +: H^{+} ion.

3. Analysis and results

A sulphidic sample was collected from the waste dump of the Recsk deep level (East Mátra Mts., NE Hungary) from the level–900. The ore body is a copper porphyry and skarn copper deposit. The sample was taken from the extracted material of the "Western 3" ore exploration adit, from the contact of the exoskarn and the carbonates. The waste dump on the surface – approximately 300–350 tonnes – makes up only a small part of the original amount, because most of it has already been transported to other waste dumps. For the experiments bouldersof 10–20 cm diameter were selected from the waste material. After the removal of the secondary mineralization from the boulders, they were crushed to under 2 mm. This crushing gave us a fresh, non-oxidized surface for the kinetic test analysis.

The major minerals of the investigated sample are about 40% quartz, 40% pyrite, 12% calcite, and 3% chalcopyrite. There is some galena, sphalerite and dolomite as well.

3.1. Column test

Three kg of this freshly crushed sample was investigated by column test at Kjeøy Research and Education Centre, Norway, to mimic the long-term behaviour of the sulphidic mine wastes. The column test was done for 119 days (17 weeks). On 3 kg of the sample, with a grain size of 1–2 mm, continuously humid air was pumped through to provide the oxygen and humidity that speeds up and maintains the pyrite oxidation. Once a week the sample was rinsed through with 1000 ml distilled water and the seepage was analyzed for basic chemical parameters (pH, alkalinity), anion and cation content.

The pH curve (Figure 2) clearly indicates that after 2 weeks the system has already stabilized. The circumneutral pH (around 7.2) shows that the presenting calcite buffers the acidity and can balance the system. The instability of the first 2 weeks and the initial lower pH was caused by the effect of the "first flush": some easily soluble secondary sulphates remained on the grain surfaces, which dissolve back, resulting in lower pH.

The same effect is visible in the sulphate concentration curve (Figure 2). The gradually decreasing sulphate release after the first 2 weeks shows that there was some available fine-grained – therefore quickly oxidizing – pyrite in the sample. As the fine-grained pyrite is consumed, the sulphate release gradually stabilizes.

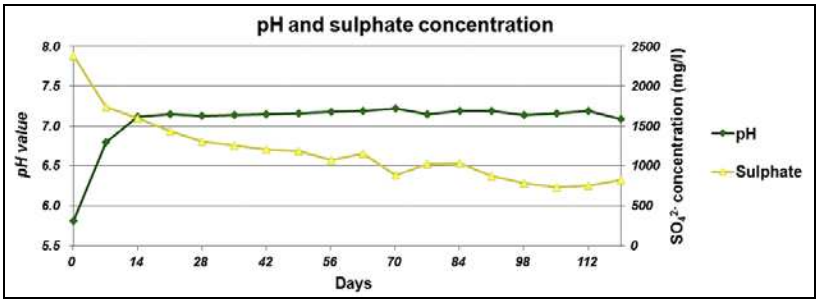

Figure 2. pH value and sulphate content in the seepage of the column test

At the end of the test period, the column was sealed to air for a week to measure the oxygen consumption and carbon dioxide release by the oxidation [Eq. (2)] and neutralizing [Eq. (7)] process. Figure 3 shows clearly that carbon dioxide content increased continuously, which shows the dissolution and efficient neutralizing effect of calcite, while the decreasing oxygen content shows the presence of the oxidation process.

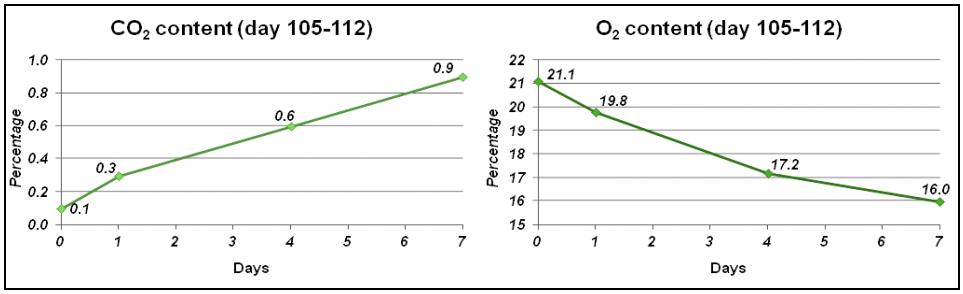

Figure 3. CO_2 release and O_2 consumption in the column

3.2. Mineralogical changes

Equation (1) tells us that if pyrite is oxidizing and calcite is present, a secondary iron mineral crust should form on the surface of the pyrite grains. Moreover, taking into consideration Eqs. (4) or (5), gypsum coating needs to appear on the surface of the calcite. Backscattered SEM images were taken from the sample surface. Figure 4 shows the non-altered pyrite surface with brighter colour and the secondary iron phases – caused by alteration of pyrite – with darker grey colour. The iron oxide phases appear as tiny plates and cover the pyrite surface.

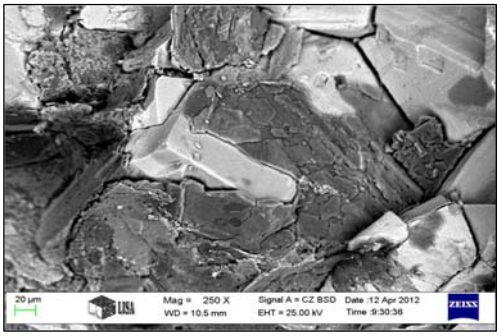

Figure 4. Secondary iron oxide–hydroxide mineral coating on pyrite surface.

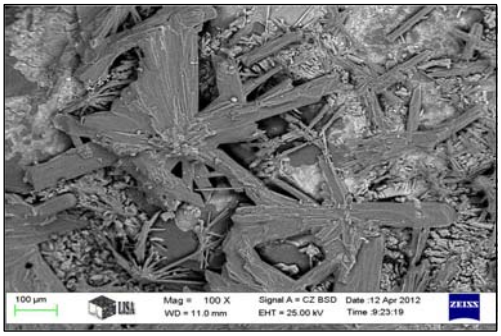

Figure 5. Gypsum needles on calcite grains. Backscattered SEM images

Close to the appearance of secondary iron minerals, tabular crystals of gypsum were also found as a stable end-product after the alteration of pyrite. Figure 5 shows that on the eroded surface of the calcite – appearing with bright colour – tiny, darker gypsum needles are present. This feature means also that the gypsum has already started to cover, thus encapsulate the calcite grains. This phenomena shows that the still effective neutralizing capacity will decrease in the future, due to the decreasing free reactive surface of calcite.

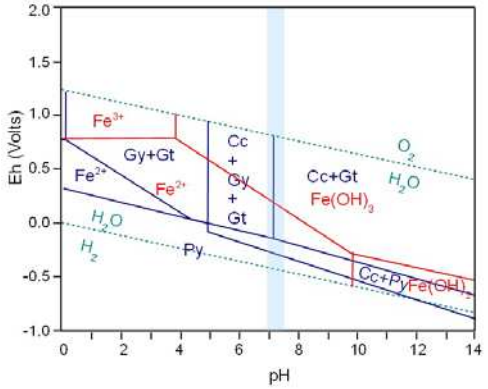

Figure 6. Eh-pH diagrams of C-Ca-Fe-S-H_2O (blue) and Fe-O_2-H_2O (red) systems at standard conditions (calculated by HSC Chemistry). Vertical blue strip: measured stable pH range of the seepage water

4. Conclusion

Pyrite oxidation of the copper-porphyry and skarn mining waste material was detected in experiments by the sulphate concentration (Figure 2) in the seepage, the appearance of carbon-dioxide and decrease of oxygen gas in the air-tightly closed sample holder (Figure 3) and by the detected secondary iron mineral crust on the surface of the fresh pyrite grains (Figure 4), as well as by a gypsum coating on the surface of the calcite (Figure 5). Conversely, no acidity appears, because of efficient neutralization by the calcite (Eq. (7)).

Although the Eh-pH diagram in Figure 6 shows standard conditions, it shows that the Eh-independent stability: calcite + goethite ↔ calcite + gypsum + goethite occurs at pH 7.2 –7.3. The measured and rather constant pH of the seepage was around 7.3, which indicates that the system is upper-limited at this pH by the calcite dissolution. The diagram indicates that in less oxidative micro-environments, dissolved Fe^{2+} can appear within the porous waste rock, which is favourable for pyrite oxidation.

As the amount of the pyrite in the sample is over double the amount of calcite, ARD can be predicted ahead in an uncertain time. Kinetic test results show that the rate of oxidation in the pyritic system is continuous and stable, until the point where the neutralizing capacity is higher than or at least equal to the acid production. After that the oxidation will increase exponentially, because the pyrite oxidation works as a chain reaction, and there will be no available buffering silicates in the waste rock. Without appropriate waste management the increased pyrite oxidation will lead to acidification accompanied by toxic element mobilization from other presenting sulphides such as calcopyrite or galena, although the waste rock heap currently does not show any sign of environmental risk.

Acknowledgement

The work described was carried out as part of the TÁMOP-4.2.1.B-10/2/KONV-2010-0001 project in the framework of the New Hungarian Development Plan. The realization of this project is supported by the European Union, co-financed by the European Social Fund. Mecsek Öko Ltd. has kindly permitted the collection of the samples for the tests.

References

[1] Nordstrom, D. Kirk.: Various origins of circumneutral mine drainage problems with classification. U.S. Geological Survey, 2010, GSA Denver Annual Meeting (31 October–3 November 2010)

[2] Blowes, D. W.–Ptacek, C. J.–Jurjovec, J.: Mill tailings: hydrogeology and geochemistry. In: Blowes, D. W.–Jambor, J.L.–Ritchie, A. I. M. (Eds.):The Environmental Geochemistry of Sulfide Mine-Wastes, Short Course Handbook, 2003, Volume 31, pp. 95–116.

[3] Nordstrom, D. K.: Aqueous pyrite oxidation and the consequent formation of secondary iron minerals. In: Kittrick, J. A.–Fanning, D. S.–Hossner, L. R. (eds.): Acid Sulfate Weathering. Soil Sci. Soc. Am., 1982, pp. 37–56.

[4] Stumm, W.–Morgan, J. J.: Aquatic chemistry–An introduction emphasizing chemical equilibria in natural waters. New York, John Wiley & Sons Inc., 1981, p. 470.

[5] Jambor, J. L.: Mineralogy of sulfide-rich tailings and their oxidation products. In: Environmental Geochemistry of Sulfide Mine-Wastes. Mineralogical Association of Canada, Short Course Handbook, 1994, Volume 22, pp. 59–102.

[6] Singer, P. C.–Stumm, W.: Acid mine drainage: The rate determining step. Science, 1970, Vol. 167, pp. 1121–1123.

Geosciences and Engineering, Vol. 1, No. 2 (2012), pp. 117–122.

CALCULATION OF UNCONFORMITY RELATED ERODED STRATAL THICKNESSES ALONG THE MID-HUNGARIAN MOBILE BELT IN THE DANUBE-TISZA INTERFLUVE AREA, HUNGARY

NAGY ZSOLT[1]–POGÁCSÁS GYÖRGY[1–2]–JUHÁSZ GYÖRGYI[2]–HATALYÁK PÉTER[2]–MILOTA KATALIN[2]–CSIZMEG JÁNOS[1]–LAUKÓ ÁGNES[2]–GOMBOS CSABA[2]

[1]Eötvös Loránd University, H-1117 Budapest. Pázmány Péter sétány. 1/C, e-mail: zsolt.nagy.1989@gmail.com
[2]Hungarian Oil Co. (MOL NyRt.), H-1117 Budapest. Október huszonharmadika u. 18, e-mail: gypoga@mol.hu

1. Introduction

The Neogene Pannonian Basin is underlain and surrounded by tectonic units of the Alpine-Carpathian-Dinaridic system of orogens. Many tectonic units of the orogen systems underwent significant shortening during the Mesozoic to Cenozoic period. The Pannonian basin fill is regarded as post-tectonic, as it rest unconformably on large parts of the Alpine-Carpathian-Dinaridic tectonic units. These sediments were later deformed in several places by deformations related to basin formation and inversion. Stratigraphic and tectonic evolution of the basin fill is fairly well understood [1, 6, 10, 11], but location of tectonic boundaries is still rather uncertain.

Results of detailed seismic surveys and deep drilling indicate that potential hydrocarbon-bearing formations can be assigned to three tectono-stratigraphic mega-sequences [8]. The Upper Miocene-Quaternary mega-sequence, of 4–6 km maximum thickness, is represented by molasse formations deposited during the early Late Miocene. The Paleogene-Middle Miocene mega-sequence, consists of 3–4 km maximum thickness infill wrench basins, rifts, half grabens and flexural basins. The Mesozoic mega-sequence includes a rather heterogeneous group of tectonic units. The Mid-Hungarian Mobile Belt (MHMB) is situated above the Szolnok-Sava belt and above it shares boundaries with the ALCAPA and Tisza mega-unites [10]. It is the most significant neotectonic zone of the Pannonian Basin [9]. The faults of the Mid-Hungarian Mobile Belt were active through the complete Neogene period. MHMB recorded multiple deformations during Miocene-Quaternary, witnessing an inherited weakness zone [3, 5, 11].

2. Sedimentation and tectonic settings

The ALCAPA mega-unit, constituting the basement of the north-western part of the Neogene Pannonian Basin, consists of different continental and oceanic fragments which were welded together during the complex Late Jurassic-Cretaceous-Paleogene evolution [2].

The south-eastern part of the Pannonian Basin is underlain by the Tisza-Dacia mega-unit [4]. This mega-unit implies a series of nappes consisting of basement and its Mesozoic cover (Figure 1). The pre-Triassic basement of the Tisza-Dacia mega-unit consists of various Variscan high-grade metamorphic rocks. The Alpine nappe pile that forms the Tisza-Dacia mega-unit includes, from NW to SE, the Mecsek, Bihar and Codru nappe

systems [4]. In principle, nappe emplacement direction is toward the NNW and consists of northward propagating sequence of Cretaceous thrusting events [12].

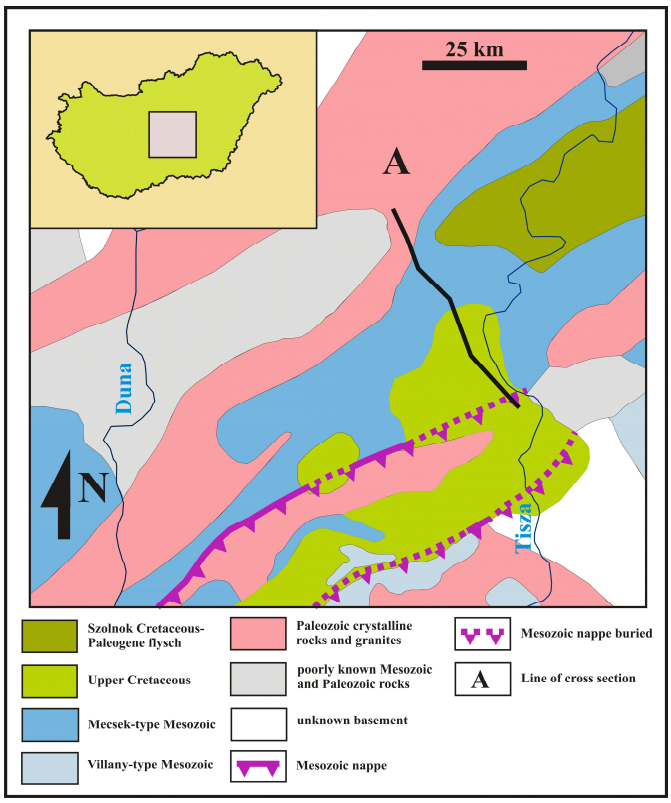

Figure 1. Simplified pre-Tertiary geological map of the Danube-Tisza Interfluve part of the Pannonian Basin with boundary of the nappes and the location of the different type of Mesozoic rocks modified after [13]

The basal members of the overlying Permian-Mesozoic succession are generally Late Permian continental red beds covered by Muschelkalk-type facies which grades into more massive Mid-Triassic carbonate build-ups overlain by Keuper facies. The Mecsek nappe system is characterised by Early Jurassic coal measures. Substantial Late Jurassic and Early Cretaceous facies variations were related to the different facies zones of the Tisza-Dacia mega-unit (Figure 2). Valanginian to Barremian volcanic activity in the Mecsek Mountains coincided with the opening of the Valais-Magura Ocean and with the departure of the Tisza microcontinent from the European continent. The Bihar nappe system is characterised by Lower Cretaceous reefal limestones. The most internal and structurally highest units, the Codru nappe system, generally contain Jurassic to Lower Cretaceous pelagic red limestones, dark shales and turbidites.

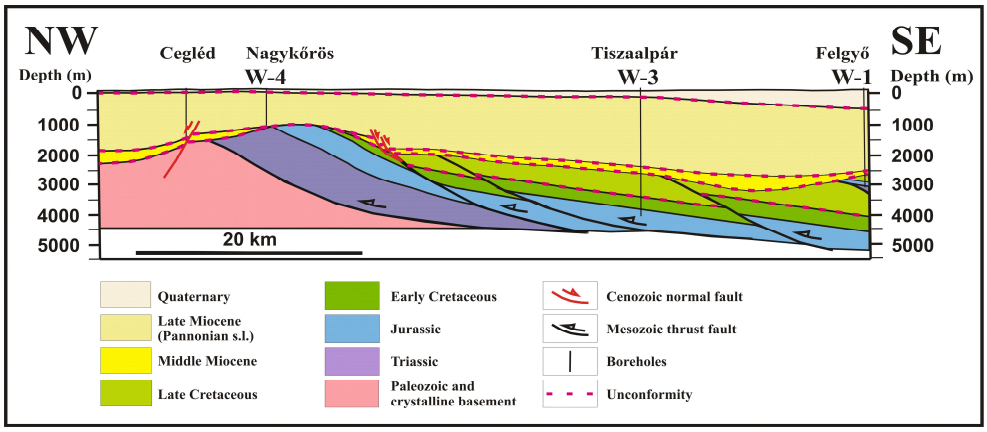

Figure 2. Idealized NW-SE profile through the Danube-Tisza Interfluve with thrust, normal faults and erosional horizons; for location, see Figure 1

The second, early Late Cretaceous deformation episode peaked during the Turonian. Structures are typically sealed by an erosional unconformity of Late Turonian to Coniacian age overlain by Upper Cretaceous foredeep deposits. The second Cretaceous compressional thrusting event, according to Haas [4], can be distinguished from the first one rather well in the area of the Tisza-Dacia mega-units. The early Late Cretaceous unconformity can be overlain by Late Cretaceous or Paleogene sediments. No Paleogene compressive events are known from the Tisza-Dacia mega-units.

The complex tectonic history of the Danube-Tisza Interfluve part of the "Mid Hungarian Line" as revealed by [1], includes intra-Oligocene–Early Miocene thrusting, Middle Miocene extension, local Late Miocene inversion, Late Miocene–Pliocene normal faulting and left-lateral wrenching.

In the Late Neogene sedimentary succession three tectonically driven unconformities were identified by Pogacsas et al. [10] in the central part of the Danube-Tisza Interfluve Area as follows: 1) Base Late Miocene Unconformity 2) Top Late Miocene Unconformity, 3) Late Pliocene Unconformity. Age dating of horizons younger than 5.9 Ma is more uncertain because of the poor seismic resolution of the near-surface part of the sedimentary basin fill. Juhasz et al. [6] identified similar unconformities based on sedimentological analysis of the Kaskantyú-2 well. Here the expected duration of the hiatuses were from 6.2 Ma to 3.9 Ma in the case of the Top Late Miocene Unconformity and from 3.2 Ma to 1.8 Ma in the case of the Late Pliocene Unconformity. The succession bounded by the Top Late Miocene Unconformity and the Late Pliocene Unconformity was affected by nearly vertical wrench fault zones [7, 10].

3. Eroded strata thickness

Out of several unconformities related erosional events we chose two and calculated the eroded stratal thicknesses along these unconformities in the Danube-Tisza Interfluve Area. Reconstruction of eroded stratal thicknesses with graphic method was based on Ro%-depth

data, and the scenarios were tested with 1D subsidence history analysis applying PetroMod software.

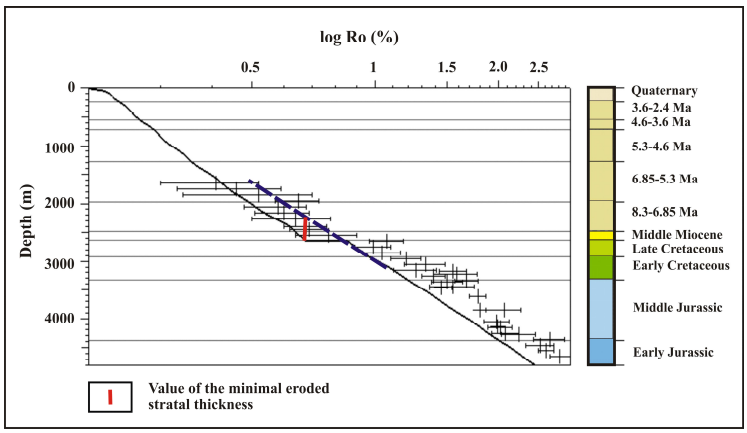

Figure 3.Thickness of stratigraphic units in the W-2 well, measured and calculated vitrinite reflection (R_0)

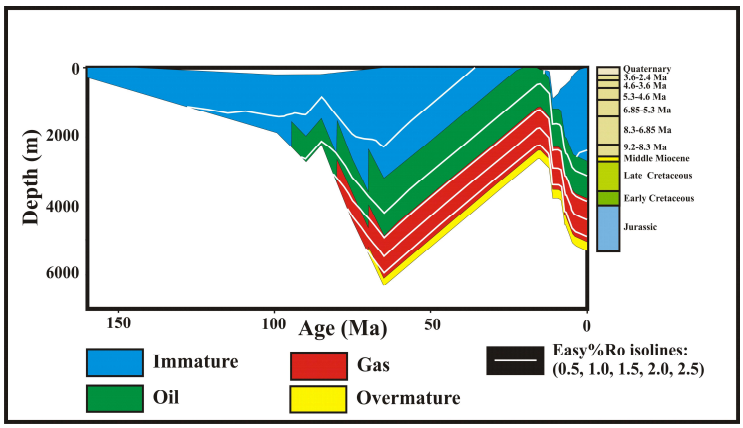

Figure 4. Time-space evolution of the W-3 well. The eroded stratal thickness value can be obtained directly from the depth versus time diagram.

3.1. Late Cretaceous to Miocene erosional event. The estimation of unconformity related eroded sediment thickness value was based on vitrinite reflection–depth profile with graphic method (Figures 3 and 4). A contour map was compiled on the basis of the eroded thickness value of nine wells. The magnitude of the erosion fluctuates within a wide range. The minimum and the maximum values were 1,000 and 3,800 metres (Figure 5).

3.2. Middle Miocene to Late Miocene erosional event. The magnitude of this erosional event was smaller than in the Late Cretaceous to Miocene. Because of that, it did not have as definite an impact on the thermal maturity as the Late Cretaceous to Miocene event had.

According to our preliminary results, the magnitude of the Middle Miocene to Late Miocene erosion was between 50 and 300 metres in the study area (Figure 6). The range of the erosion decreased from north-east to south-west.

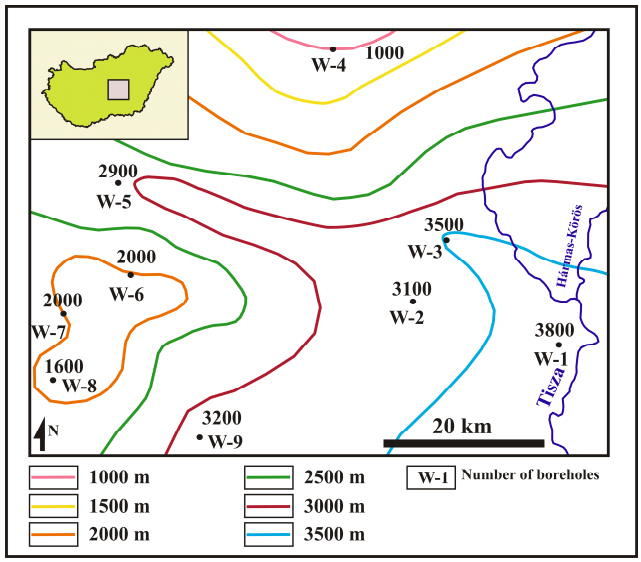

Figure 5. Contour map of the eroded sediment thicknesses (Latest Cretaceous-Middle Miocene) in the studied part of the Danube-Tisza Interfluve

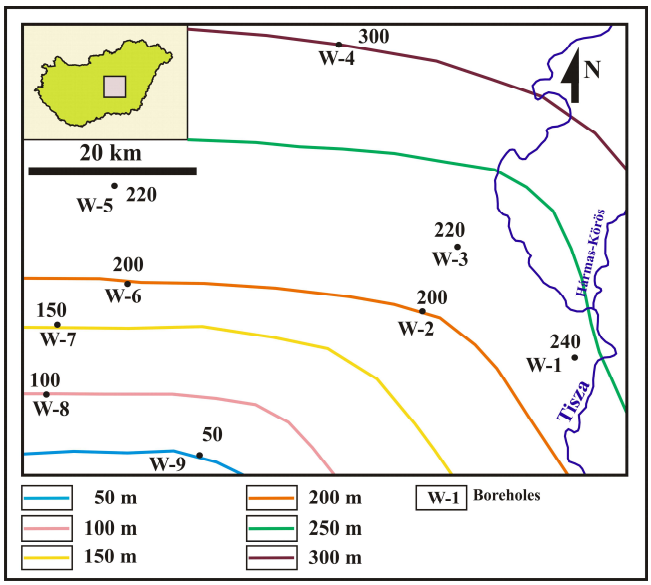

Figure 6. The contour map of the eroded sediment thicknesses (Early and Middle Miocene-Late Miocene) in the studied part of the Danube-Tisza Interfluve

4. Conclusion

The distribution and magnitudes of eroded thickness values are different in the case of the Late Cretaceous to Miocene and the Late Miocene to Pliocene-Quaternary erosional events. The Late Cretaceous to Miocene unconformity significantly affected the thermal maturity while the impact of the Middle Miocene to Late Miocene event was much weaker.

Acknowledgements

Supports of OTKA # 6086 grant are gratefully acknowledged. Eötvös Loránd University acknowledges support of this research by Schlumberger via the PetroMod University Grant Program.

6. References

[1] Csontos, L.–Nagymarosy A.: The Mid-Hungarian line: a zone of repeated tectonic inversions. Tectonophysics, 1998, 297, pp. 51–71.
[2] Csontos, L.–Vörös A.: Mesozoic plate tectonic reconstruction of the Carpathian region. Paleogeography Paleoclimatology Paleoecology, 2004, 210, pp. 1–56.
[3] Fodor, L.–Bada, G.–Csillag, G.–Horvath, E.–Ruszkiczay-Rüdiger, Z.–Palotás, K.–Síkhegyi, F.–Timár, G.–Cloetingh, S.–Horváth, F.: An outline of neotectonic structures and morphotectonics of the western and central Pannonian Basin. Tectonophysics, 2005, 410, pp. 15–41.
[4] Haas, J.: Geology of Hungary; Mesozoic (in Hungarian: Magyarország Földtana, Mezozoikum) school book of Eötvös Loránd University, 1994, pp. 119.
[5] Jarosinski, M.–Beekman, F.–Matenco, L.–Cloetingh, S.: Mechanics of basin inversion: Finite element modelling of the Pannonian Basin System. Tectonophysics, 2011, 502, pp. 121–145.
[6] Juhász, Gy.–Ó. Kovács, L.–Müller, P.–Tóth-Makk, Á.–Phillips, L.–Tóth-Makk–Lantos, M.: Climatically driven sedimentary cycles in the late Miocene sediments of the Pannonian Basin, Hungary. Tectonophisics, 1997, 282, pp. 257–276.
[7] Juhász, Gy.–Pogácsás, Gy.–Magyar, I.–Hatalyák, P. (in rev.): The Alpar canyon system in the Pannonian Basin, Hungary – its morphology, infill and developement. Submitted to Global and Planetary Change.
[8] Kókai, J.–Pogácsás Gy.: Hydrocarbon plays of Mezozoic Nappes, Tertiary Wrench Basins and Interior Sags in the Pannonian Basin. First Break, 1991, 9. 7, pp. 315–334.
[9] Lőrincz, K. D.–Horváth, F.–Detzky, G.: Neotectonics and its relation to the Mid-Hungarian Mobile Belt. In: Neotectonics and surface processes: the Pannonian Basin and Alpine/Carpathian System (S. A. P. L. Cloetingh–F. Horváth–G. Bada–A. C. Lankrejier, Eds.). European Geosciences Union Stephan Mueller Special Publication Series, 2002, 3, pp. 247–266.
[10] Pogácsás Gy.–Juhász Gy.–Dudás Á.–Csizmeg J.: Wrench Tectonics Control on Neogene-Quaternary Sedimentation and Hydrocarbon Accumulation along the Mid-Hungarian Mobile Belt. AAPG Search and Discovery Article, 2012, #10388.
[11] Pogácsás, Gy.–Juhász, Gy.–Németh, N.–Dudás, Á.–Csizmeg, J.: Shortening features in the late Miocene-Pliocene sediments along the central part of the Mid Hungarian Mobile Belt. Travaux Géophysiques, 2011, XL, pp. 62–63.
[12] Schmid, S. M.–Bernoulli, D.–Fugenschuh, B.–Matenco, L.–Schaefer, S.–Schuster, R.–Tischler, M.–Ustaszewski, K.: The Alps–Carpathians–Dinarides-connection: a compilation of tectonic units. Swiss J. Geosci, 2008, 101, pp. 139–183.
[13] Tari, G.–Horvát, F.: Alpine Evolution and Hydrocarbon Geology of the Pannonian Basin: An Overview. AAPG Memoir, 2006, 84, pp. 605–618.

Geosciences and Engineering, Vol. 1, No. 2 (2012), pp. 123–128.

TRAVELTIME DIFFERENCES IN SEISMIC REFRACTION INVERSION

TAMÁS ORMOS[1]–ANIKÓ NOÉMI PARIPÁS[2]
[1] associate professor, University of Miskolc,
3515 Miskolc-Egyetemváros, gformos@uni-miskolc.hu
[2] research fellow/PhD student, University of Miskolc,
3515 Miskolc-Egyetemváros, gfpan@uni-miskolc.hu

1. Introduction

The application of seismic refraction methods is very widespread in near-surface geological investigations for e.g. hydrogeological, geophysical engineering and geotechnical purposes [1, 2]. In a surface seismic measurement various source types can be used, related to which trigger error may occur during field measurements. If elastic waves are generated by explosion, an approx. 1–4 ms triggering error can occur due to the error of the geophysical blasting cap. Generating the waves with weight dropping or hammer strike, a piezoelectric ceramic or a geophone serves the trigger signal – cycle skipping may occur. These triggering errors can cause problems in the interpretation of measured data and the estimation of the parameters, especially in shallow explorations as the accuracy or the errors of the trigger time have greater importance there compared to that of deeper explorations.

This problem was examined earlier in the inversion of three-component seismic VSP surveys in a coal mine using the traveltime differences between the upper and lower geophone-triplet [3]; and in shallow seismic reflection exploration, estimating the shot distortion on each common shot gather and eliminating them by shifting all the traces [4].

In this paper the idea of double-trace data is applied to refraction traveltime data, a concept that was developed by Dobróka et al. [5] for tomographic interpretation. The modified conjugate gradient and SIRT algorithms proved to be effective for solving the problem described above. With this theory the problem of the inaccurate trigger time is attempted to be solved in the field of seismic refraction.

2. Traveltime differences in the forward problem

In the evaluation process of seismic measurements it is usually a problem that the measured traveltime dataset has some amount of triggering error originating from the inaccuracy of the source time. This problem mainly arises in seismological aspects where the measurement is continuous and the exact time of the wave generation is unknown [6]. However the inaccurate trigger time also causes problems in the near-surface exploration of geological structures (seismic refraction methods) as in these cases relatively small traveltimes are measured that are comparable to the amount of triggering error occurring. Therefore all traveltime data related to the same source point have the same amount of trigger error, i.e. a certain value of time shift presents on the traveltime curves. In Figure 1 the problem of inaccurate source time is presented with an exact dataset and a dataset with

trigger errors, in addition to the results of simple traveltime inversion and traveltime difference inversion.

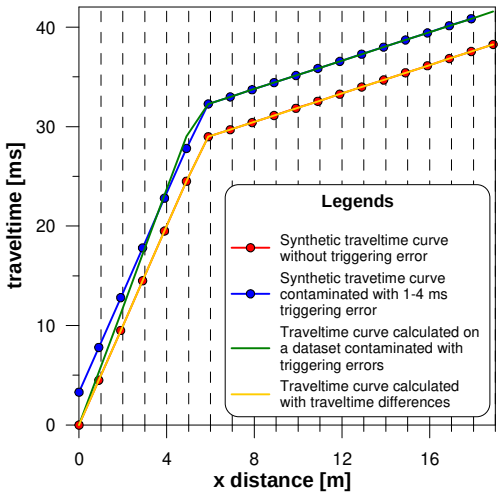

Figure 1. The representation of the evaluation problems of triggering errors in the traveltime dataset

To avoid the effects of this (1–4 ms) error, the interpretation of the data can be performed with traveltime differences instead of exact traveltime data. This idea was used formerly by Dobróka et al. [5] for tomographic interpretation with double-trace data. For solving the problem they used the modified conjugate gradient and SIRT algorithms.

The same concept is used in this paper for the interpretation of refraction traveltime data; therefore a certain receiver is chosen as a reference and traveltime differences (Δt) are calculated from all the other traveltime data related to the same source point:

$$\Delta t_{i,s}^{(meas)} = t_{i,s}^{(meas)} - t_{r,s}^{(meas)} \tag{1}$$

where $t_{i,s}$ indicates the traveltime data of a wave generated from the s-th source point and received by the i-th receiver (geophone); $t_{r,s}$ means the traveltime data detected by the reference geophone. Firstly a traveltime difference dataset has to be generated from the measured dataset and in the evaluation procedure there are several approaches to solve the inverse problem.

2. Inversion theory

Once a traveltime difference dataset is generated from the measured dataset the occurring inverse problem can be solved either for the original traveltime dataset or for traveltime differences. In this paper a solution is presented where traveltime differences are applied in the inversion procedure using the difference of the Jacobian matrices ($J_{i,s}$) calculated for the reference traveltimes ($G_{r,s}$) and the whole traveltime dataset ($G_{i,s}$). The idea is described in Eq. (2) with the same notations as in Eq. (1):

$$J_{i,s} = G_{i,s} - G_{r,s} \tag{2}$$

The inversion method uses this newly calculated Jacobian matrix in the algorithm based on the damped least squares method:

$$\mathbf{m} = \left(\mathbf{J}^T\mathbf{J} + \varepsilon^2\mathbf{I}\right)^{-1}\mathbf{J}^T\Delta\mathbf{t}^{(meas)} \tag{3}$$

where **m** means the model vector, $\Delta\mathbf{t}^{(meas)}$ means the measured traveltime difference data, **J** means the difference Jacobian matrix of the partial derivatives of the traveltime data and **I** is an identity matrix multiplied by the scalar damping factor ε^2. Applying simple ray tracing, only the first arrivals are taken into consideration in the inversion procedure and a two- or three-layered 1D structure can be interpreted. It had been proved that 1D inversion can be used to provide acceptable estimations when contoured cross-sections of 2D structures are constructed [7] and that local 1D forward modelling can be used for the investigation of 2D structures in the inversion of DC geoelectric data [8].

3. Synthetic Studies

In this paper an experimental study is presented to solve the problem of inaccurate trigger time (triggering errors) that occurs in seismic field measurements. As the method is under development, in this paper our investigations on 1D structure are shown.

A shallow (max. depth: 10 m), three-layered 1D geological structure was studied in an early step of this theoretical approach. A 'measured' dataset was generated on the exact synthetic model with FD-Vidale type ray tracing [9]. Thus a difference exists between the forward problem solution of data generation and our inversion algorithm. We contaminated this synthetic dataset (131 data) with 1% of synthetic noise of normal distribution (Gaussian noise) and a triggering error of 3–8 ms (a relatively huge amount of triggering error, differing for each source point). Therefore a highly erroneous dataset was created.

The traveltime dataset was 'measured' with a total of 41 receivers and the waves were generated from 5 source points. The same dataset was tested with the normal traveltime inversion method and with the method using traveltime differences. The results can be seen in Table 1, where *D* means the data misfit (the relative distance between the measured erroneous and the estimated datasets), and *d* means the model misfit (calculated for the whole section) [10].

In Table I the values of *D* are somewhat misleading, as in general people tend to think that the data misfit has to be minimal at the best result of the inversion. In this case – as the 'measured' dataset is highly erroneous – the data misfit has less significance. In traveltime difference inversion the procedure is based on the minimization of the traveltime difference data misfit; results are shown in the second row of Table 1 (D_{td}).

However the value of model misfit has a huge significance in this consideration, as it can tell us the real usability and efficiency of our inversion algorithm. In this value a number nearly 30 times smaller than that of the normal traveltime inversion can be seen as a result of traveltime difference inversion (Table 1). This declares the usability and reliability of an inversion method calculating with traveltime differences for a three-layered 1D geological situation.

Table 1

Results of the two inversion methods – tested on a highly erroneous synthetic dataset (contaminated with Gaussian noise and triggering errors)

	Results of **Normal Traveltime Inversion** Method	Results of **Traveltime Difference Inversion** Method
D [%] Fit in Data Space	40.1	102.9
D_{td} [%]calculated with traveltime differences	40.1	5.06
d [%] Fit in Model Space	**28.49**	**1.01**

Besides the values of data misfit, the fit of traveltime curves is also meaningful. In Figure 2 the fit of the erroneous dataset (red symbols) and the normal traveltime inversion results (blue lines) can be seen; and also the traveltimes calculated on the exact model (black rings). The misfits are eye-catching, especially if we consider the fact that the misfit has to be seen for traveltimes related to the same geophone (vertically). In Figure 3 the fit of the same erroneous dataset (green symbols) and the traveltime difference inversion results (orange lines) can be observed. In this figure, moreover, the poor fit of the exact dataset (black rings) and the inversion results can be noticed.

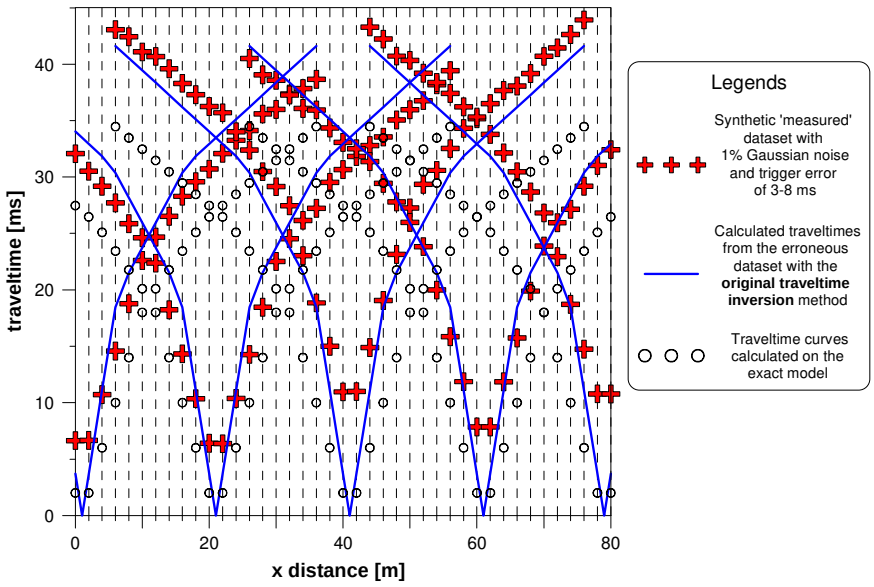

Figure 2. Results of the normal traveltime inversion method: D = 40.1% (data misfit) from the measured erroneous dataset, and d = 28.5% (model misfit) from the exact model

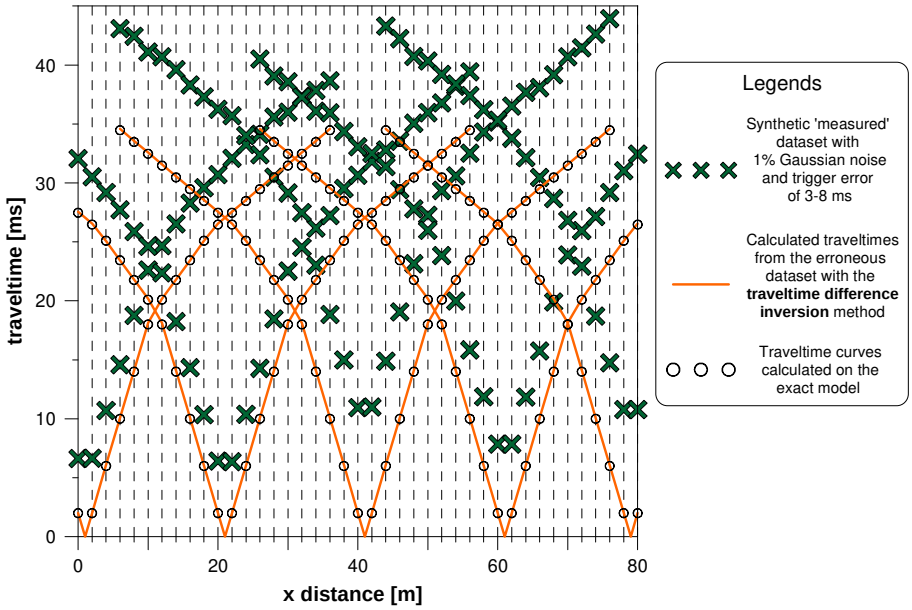

Figure 3. Results of the traveltime difference inversion method: data misfit of D = 5.1% from the measured erroneous dataset and a model misfit of 1.0% from the exact model.

4. Field studies

Besides synthetic studies a new method has to prove its usability on field datasets as well. The field measurements presented below were carried out in Izsófalva, in the North-Eastern part of Hungary. The elastic waves were generated with hammer strikes and detected by SM7 type 30 Hz geophones with 2 m spacing. Although the source time was triggered with a 10 Hz geophone installed directly adjacent to the source, a triggering error of approximately 1–3 ms occurred during the measurements.

The seismograms were processed with 10–200 Hz band-pass filter and an AGC gain using 70 ms window. The length of the evaluated sub-section is 34 m with 5 sources and 18 geophones, altogether 90 measured data (the field dataset has the same order of magnitude as the synthetic one above). According to our previous knowledge the investigated near-surface structure is nearly one-dimensional, with a gravely and a shaley layer, therefore the measured dataset was interpreted as a two-layered 1D structure (3 definable parameters) with both the inversion using normal traveltime data and that using traveltime differences.

A better fit was obtained using traveltime differences (calculated for traveltime differences). For traveltime differences D_{td} = *11.9%*, while using simple traveltime data *D=17.6%*. The relatively higher fitting error can be explained by the fact that structures in nature are hardly 1D; besides measurement errors, modelling error was also presented in these values of relative data distances.

5. Conclusion

Defining the accurate trigger time is usually a problem in refraction field investigations of near surface structures. However by using a method that calculates with traveltime differences the error of source time could be highly reduced; therefore, the reliability of the results can be significantly better than that of the measured data. Assuming even 3–8 ms of triggering error in the synthetic case, the effects of the inaccurate source time disappeared. The method was tested on field data as well (measured above a nearly 1D, 2-layered medium). The results prove the usability of the new inversion method even in the case of in-line offset sources. The method will be further developed for 2D geological structures and its implementation is planned in the series expansion based multilayer inversion method [11, 12] developed formerly in the Department of Geophysics (University of Miskolc).

Acknowledgements

The described work was carried out as part of the TÁMOP-4.2.1.B–10/2/KONV–2010–0001 project in the framework of the New Hungary Development Plan. The realisation of this project is supported by the European Union, co-financed by the European Social Fund.

References

[1] Palmer, D.: Are refraction attributes more useful than refraction tomography? First Break, 2010, Vol. 28, pp. 43–52.
[2] Paripás, A. N.–Ormos, T.: Resolution and ambiguity studies for a series expansion based multilayer refraction inversion method. Acta Geod. et Geoph. Hung., 2012, 47(2), pp. 197–209.
[3] Breitzke, M.–Dresen, L.–Csókás, J.–Gyulai, Á.–Ormos, T.: Parameter estimation and fault detection by three-component seismic and geoelectrical surveys in a coal mine. Geoph. Prosp., 1987, Vol. 35, pp. 832–863.
[4] Sun, R.: Trigger Time Synchronization in Shallow Seismic Exploration. TAO, 2000, Vol. 11(2), pp. 381–392.
[5] Dobróka, M.–Dresen, L.–Gelbke, C.–Rüter, H.: Tomographic inversion of normalized data: double-trace tomography algorithms. Geophysical Prospecting, 1992, Vol. 40, pp. 1–14.
[6] Martino, S.–Scarascia Mugnozza, G.: The role of the seismic trigger in the Calitri landslide (Italy): historical reconstruction and dynamic analysis. Soil Dynamics and Earthquake Engineering, 2005, Vol. 25, pp. 933–950.
[7] Beard, L. P.–Morgan, F. D.: Assessment of 2-D structures using 1-D inversion. Geophysics, 1991, Vol. 56, pp. 874–883.
[8] Gyulai, Á.–Ormos, T.: A new procedure for the interpretation of VES data: 1.5-D simultaneous inversion method. Journal of Applied Geophysics, 1999, Vol. 41, pp. 1–17.
[9] Vidale, J.: Finite-difference calculation of travel times. Bulletin of the Seismological Society of America, 1988, Vol. 78(6), pp. 2060–2076.
[10] Paripás, A. N.–Ormos, T.: Inversion of First Breaks on Multilayered Media. 6th Congress of the Balkan Geophysical Society. 2012, Extended Abstracts, A21. pp. 1–5.
[11] Dobróka, M.: On the absorption-dispersion of Love waves propagating in inhomogeneous seismic waveguide of varying thickness; the inversion of absorption-dispersion properties. Doctor of Science Thesis (Hungarian Academy of Science), 1994, Miskolc, Hungary.
[12] Ormos, T.: Inversion of refracted travel-times for near-surface investigation. EAGE 64th Conference and Exhibition, 2002, Extended Abstract, D025. pp. 1–5.

Geosciences and Engineering, Vol. 1, No. 2 (2012), pp. 129–136.

GEOLOGICAL APPLICATIONS OF THE VLF METHOD

GÁBOR PETHŐ
Associate research professor,
H-3515 Miskolc, University of Miskolc, Dept. of Geophysics,
gfpg@uni-miskolc.hu

1. Introduction

Just like in the case of any electromagnetic (EM) method, the electrical properties of the ground affect the behaviour of radio waves as well. The first EM measurement using radio frequencies applied wave-tilt techniques and was made at relatively high frequencies with shallow penetration depth [1]. The earliest EM measurement with radio waves of 3–30 kHz was carried out in 1963 with the aim of ore prospecting [2]. In the late sixties commercially available ground very low frequency (VLF) instruments were introduced into near-surface exploration. These instruments can be used to observe either the magnetic field and/or to determine the terrain's apparent resistivity. Over 1D half-space the magnetic field at the surface is linearly polarized. However in the presence of a lateral conductivity inhomogeneity – situated between the surface and skin depth – the total magnetic field at the surface will be elliptically polarized due to the induced magnetic field. Usually the induced vertical magnetic field component is small compared with the primary azimuthal magnetic field component. In this case the ellipticity of the magnetic polarization ellipse is approximately equal to the quadrature component of the ratio of the vertical and the azimuthal magnetic component, and the tilt angle of the ellipse approximately equals the real component of the same ratio [3]. If the radial electric field and the azimuthal magnetic field component are known the apparent resistivity at the VLF frequencies can be derived.

Takács was the first in Hungary to develop the radiokip method with instruments to apply the EM fields of distant LF transmitters for near-surface geological explorations [4]. The VLF method was introduced and intensively used in Transdanubian Central Range bauxite exploration by ELGI [5]. In the frame of this work Farkas developed the VLF invariant resistivity method based on the concept of the magnetotelluric impedance tensor [6]. The VLF method utilizes the frequency range of 10 kHz–30 kHz, providing poor depth resolution. To overcome this resolution problem this frequency range was extended and in addition to the VLF carrier waves the low frequency (LF) signals from civilian radiotransmitters are also utilized by the RMT (Radiomagnetotelluric) method. Takács carried out and interpreted the first RMT soundings in Hungary in the range of 18.3 kHz and 630 kHz. He measured both the electric and magnetic field components and MT 1D inversion was applied [7]. The radiofrequency resistivity (RF-R) device measuring in the range of 12 kHz–240 kHz was successfully applied to delineate karst structures [8]. In 1973 Tilsley applied a portable VLF transmitter as a supplementary source to the regular VLF transmitters [9]. To cope with the interpretation problem arising from the mutual position between transmitter and structural strike direction or to overcome the poor coupling with the target the use of a portable transmitter can be recommended. For the determination of

sufficient distance between the portable VLF transmitter and VLF profiles numerical modelling is also needed [10].

2. VLF resistivity response over layered half-space

If the VLF wave impedance – which is the ratio of the radial electric and the horizontal azimuthal magnetic field component – is independent of the transmitter direction, the geology can be considered as 1D down to the penetration depth. The apparent resistivity of the inhomogeneous ground (ρ_a) can be defined as:

$$\rho_a = \frac{1}{2\pi f_{VLF}\mu_0}\left|\frac{E_r}{H_\phi}\right|^2 \tag{1}$$

In equation (1) f_{VLF} stands for the frequency, μ_0 denotes the absolute permeability of a vacuum. In the carrier wave transmitted into the homogeneous ground the horizontal radial electric field component leads the horizontal magnetic field perpendicular to the transmitter bearing in phase by 45°. The phase difference between E_r and H_ϕ can furnish information about the changes of conductivity in a vertical sense till approximately the penetration depth. Assuming a horizontally stratified half-space with a lower layer more resistive compared with the upper one, the phase angle $\Phi(E_r, H_\phi)$ will be less than 45°, and it is greater than 45° if there is an increase in conductivity with depth. In practice a 1D assumption can be applied to geology with slow variations in geometry. Locally 1D approximation proved to be successful in the exploration of covered communal waste (in Nyékládháza) and fault localization (in the Csanyik Valley of the Bükk Mountains). For the interpretation the 1D inversion method given by [11] was applied.

3. VLF method for elongated conductivity structures

Although one encounters 3D conductivity structure with anisotropy in general, locally 2D approximation without anisotropy can frequently be applied. First the theoretical background is presented.

3.1. Basic equations for E and H polarization

Maxwell's first equation states that an electric field is induced by the time-varying magnetic field and this electric field is proportional to the negative rate of change of magnetic flux. This can be written in a cylindrical coordinate system as:

$$\frac{1}{r}\frac{\partial E_z}{\partial \phi} - \frac{\partial E_\phi}{\partial z} = -\frac{\partial B_r}{\partial t} \tag{2}$$

$$\frac{\partial E_r}{\partial z} - \frac{\partial E_z}{\partial r} = -\frac{\partial B_\phi}{\partial t} \tag{3}$$

$$\frac{1}{r}\frac{\partial}{\partial r}(rE_\phi) - \frac{1}{r}\frac{\partial E_r}{\partial \phi} = -\frac{\partial B_z}{\partial t} \tag{4}$$

Maxwell's second equation expresses that every current flow produces a magnetic field and it is proportional to the total current flow, i.e. the sum of the conduction and displacement current. It has the following form:

$$\frac{1}{r}\frac{\partial H_z}{\partial \phi} - \frac{\partial H_\phi}{\partial z} = j_r + \frac{\partial D_r}{\partial t} \tag{5}$$

$$\frac{\partial H_r}{\partial z} - \frac{\partial H_z}{\partial r} = j_\phi + \frac{\partial D_\phi}{\partial t} \tag{6}$$

$$\frac{1}{r}\frac{\partial}{\partial r}(rH_\phi) - \frac{1}{r}\frac{\partial H_r}{\partial \phi} = j_z + \frac{\partial D_z}{\partial t} \tag{7}$$

If we assume that r coincides with the structural strike and there is an $e^{i\omega t}$ time dependent EM field variation, furthermore we neglect the effect of the displacement current, we shall get simpler component equations, mainly because all partial derivatives with respect to r can be approximated by zero. Actually at greater distances from the transmitter constant EM fields can be observed along profiles parallel to the transmitter bearing. Note that these statements are valid only for elongated (at least locally 2D conductivity) structures. Taking into account the constitutive relations between magnetic induction and magnetic field intensity, and between electric current density and electric field for homogeneous, isotropic earth, instead of (2)–(4) we can write:

$$\frac{1}{r}\frac{\partial E_z}{\partial \phi} - \frac{\partial E_\phi}{\partial z} = -i\omega\mu H_r \tag{8}$$

$$\frac{\partial E_r}{\partial z} = -i\omega\mu H_\phi \tag{9}$$

$$\frac{1}{r}\frac{\partial E_r}{\partial \phi} = i\omega\mu H_z \tag{10}$$

Similarly, instead of the Maxwell's second equations:

$$\frac{1}{r}\frac{\partial H_z}{\partial \phi} - \frac{\partial H_\phi}{\partial z} = \sigma E_r \tag{11}$$

$$\frac{\partial H_r}{\partial z} = \sigma E_\phi \tag{12}$$

$$-\frac{1}{r}\frac{\partial H_r}{\partial \phi} = \sigma E_z \tag{13}$$

If equations (8), (12), (13) are taken into one set of equations, it contains only H_r, E_ϕ, E_z components and similarly, in the set of equations consisting of (9), (10), (11) the three remaining components – E_r, H_ϕ, H_z – can be found. In order to get the simplest partial differential equation to be solved in the first case, the values of the electric field components from (12) and (13) into (8) have to be substituted.

After some operations:

$$\frac{\partial^2 H_r}{(r\partial\phi)^2} + \frac{\partial^2 H_r}{\partial z^2} = i\omega\mu\sigma H_r \tag{14}$$

In the second set of equations the values of the magnetic field components have to be substituted from (9) and (10) into (11) and we can obtain:

$$\frac{\partial^2 E_r}{(r\partial\phi)^2} + \frac{\partial^2 E_r}{\partial z^2} = i\omega\mu\sigma E_r \tag{15}$$

Equation (14) describes the H-polarization and (15) corresponds to the E-polarization case. The physical-mathematical significance of this is that independently of the angle of the incident plane wave the EM field can be divided into two parts which can be treated separately. An additional conclusion is that – depending on the mutual position of the transmitter bearing and strike direction – we can encounter pure E- and H-polarization cases. The basic equations derived here can be finite differenced and depending on the boundary conditions different linear equation systems will have to be solved.

3.2. VLF measurements over elongated geological structures

The VLF method is a useful tool in geological mapping [12] and it may even have geothermal, environmental and geophysical engineering applications as well. Here special emphasis is put on elongated conductivity structures, where locally 2D approximation can be applied. When restricted to 2D conductivity inhomogeneities there are two modes. This classification is based upon the angle between the transmitter bearing and the structural strike. If they coincide with each other, then the term of E polarization or TE mode is used. In this mode current channelling in the conductive part can be experienced. In the case of elongated conductive targets with finite geometry the magnetic field perpendicular to the strike induces closed-loop eddy currents in the targets and their magnetic fields are added to that of the galvanic current flow. If the structural strike is perpendicular to the transmitter bearing, the case is called H polarization or TM mode. In TM mode a galvanic effect can be observed. As a result a secondary electric field of the oscillating electrical charge accumulation on the interfaces perpendicular to the primary electric field can be measured. For this reason both modes can be effective tools to locate near-surface vertical or nearly vertical contacts and embedded conductivity inhomogeneities. In a poor 2D situation an induced vertical magnetic field can be measured only in E polarization.

Several attempts were made to locate caves in the Bükk Mountains and in Esztromos Hill [13]. VLF measurements made over known caves and numerical modelling proved that cave localization is possible if the cave is situated within the skin-depth range. Instead of the cave, sometimes the fault along which the cave was forming could be detected, because it was closer to the surface and it suppressed the EM response due to the cave. By means of VLF measurements we also managed to assess the limestone from a mining point of view.

Owing to the geographical position of the Bükk Mountains and taking into account the dominant strike direction, the VLF EM field due to GBR transmitter approximately meets the H polarization condition in the Bükk Mountains. The geological surroundings of a spring were investigated with apparent resistivity and its phase measurements.

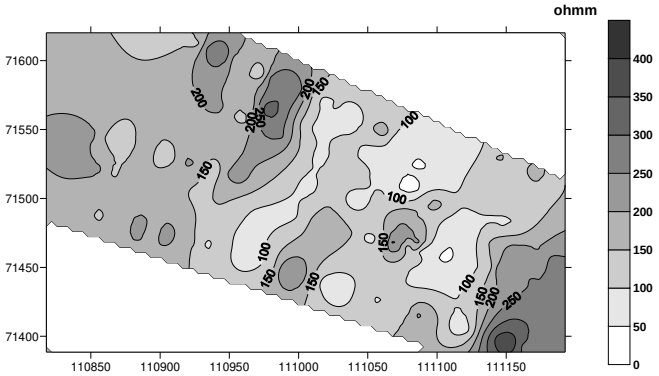

Figure 1. VLF apparent resistivity map due to GBR at Köpüs Spring

The resistivity (in Figure 1) and phase (in Figure 2) anomalies show similarities for the neighbouring profiles parallel to the transmitter bearing. This correlation is more pronounced in the case of the phase map, because apparent resistivity is disturbed by thin surface inhomogenities, while phase is hardly influenced by it. The interpretation can be considered as an underestimated problem because the number of unknowns is greater than the measured data available (there are three geological formations characteristic of the surroundings of Köpüs Spring). For TM mode we applied finite difference grids using rectangular elements with 39 columns and 49 rows [14]. A classical trial-and-error method was used: the parameters were changed until the best fit between the measured data and computed data was reached along all profiles. The geology for the southern-most profile is presented in Figure 3. The impermeable mudstone behaves like a "barrier" and determines the position of the spring.

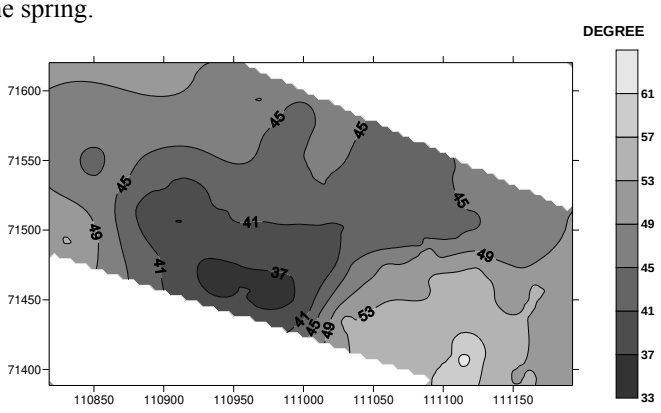

Figure 2. VLF apparent resistivity phase map due to GBR at Köpüs Spring

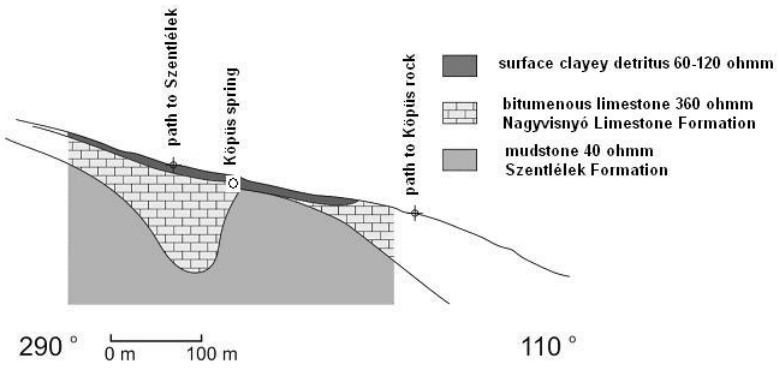

Figure 3. Interpretation based on resistivity and phase at Köpüs Spring

With a FUX 18.3 kHz transmitter at Szögszéktető (also in the Bükk Mountains) the approximate position of a metavolcanic rock hosted in Triassic limestone was determined. Due to the mutual position of the strike of the conductive body and the French VLF transmitter the situation could be approximated by E-polarization and a simplified inversion was applied for interpretation. It is based on the fact that the secondary vertical magnetic field is generated by discrete, stationary current lines inside the targets [15].

4. Conclusions

VLF method can be an effective tool in near-surface exploration. The interpretation of the elongated structures is relatively easy if the structural strike coincides with the transmitter direction or they are perpendicular to each other. If there is no distant transmitter meeting this condition, the use of a portable VLF transmitter is recommended.

Acknowledgement:

The described work was carried out as part of the TÁMOP-4.2.1.B-10/2/KONV-2010-0001 project in the framework of the New Hungary Development Plan. The realization of this project is supported by the European Union, co-financed by the European Social Fund.

References

[1] Barfield, R. H.: Some measurements of the electrical constants of the ground at short wavelengths by the wave method. Proc. Inst. Electr. Electron. Eng., 1934, 75, pp. 215–220.
[2] Paal, G.: Ore prospecting based on VLF-radio signals. Geoexploration, 1965, 3, pp. 139–147.
[3] Smith, B. R.–Ward, S. H.: On the computation of polarization ellipse parameters. Geophysics, 1974, 39, pp. 867–869.
[4] Takács, E.: On the application of radiokip method (in Hungarian). Magyar Geofizika, 1971, XII, pp. 148–160.

[5] Kakas, K.–Nyitrai, T.–Rezessy, G.–Simon, A.–Szabadváry, L.: Complex geophysical exploration of the Transdanubian Central Range (in Hungarian). Annual Report for 1975 of the Hungarian Geophysical Institute "Roland Eötvös", 1976, pp. 11–22.
[6] Farkas, I.: VLF invariant resistivity method (in Hungarian). Internal Report of the Hungarian Geophysical Institute "Roland Eötvös", 1978.
[7] Csókás, J.–Dobróka, M.–Gyulai, Á.–Hursán, L.–Ferenczy, L.–Ormos, T.–Pethő, G.–Steiner, F.–Szűcs, P.–Takács, E.–Turai, E.: Development of geophysical methods aiming at environmental protection (in the frame of 1553-93 TEMPUS JEP, in Hungarian), 1993, Vol. 1., pp.1–49.
[8] Bosch, F. P.–Müller, I.: Continuous gradient VLF measurements: a new possibility for high resolution mapping of karst structures. First Break, 2001, 19, pp. 343–350.
[9] Tilsley, J. E.: A portable VLF-EM source for the use in geological mapping of veins and fault structures and conventional prospecting. David S. Robertson and Associates Report, Toronto, 1973.
[10] Pethő, G.–Ficsór, L.–Szabó, I.: Comparision of 2-D VLF and 2.5-D HED's far field regime EM fields. MicroCAD 2006, Geoinformatics-Spatial Informatics, Section B, 2006, pp. 35–40.
[11] Grissemann, C.–Reitmayr, G.: VLF Magnetotellurics in Ore Exploration and Structural Geology. 48th SEG Meeting in San Francisco, 1978.
[12] McNeill, J. D.–Labson, V.: Geological mapping using VLF radio fields. In: Electromagnetic methods in applied geophysics, Vol. 2, SEG, pp. 521–640.
[13] Ficsór, L.–Majoros, Zs.–Pethő, G.: VLF method for surveying caves. 10th International Congress of Speleology, 1989, Proceedings I, pp. 127–129.
[14] Németh, N.–Pethő, G.:Geological mapping by geobotanical and geophysical means: a case study from the Bükk Mountains (NE Hungary). Central European Journal of Geosciences, Versita, 2009, Vol. 1 (1) pp. 84–94.
[15] Takács, E.–Pethő, G.– Szabó, I.: Comparative investigations about the applicability of current density pseudosections in the interpretation of 2D VLF vertical magnetic anomalies. Acta Geod. Geoph. Hung., 2005, Vol. 40 (2) pp. 127–146.

Geosciences and Engineering, Vol. 1, No. 2. (2012), pp. 137–142.

COAL EXPLORATION FOR UNDERGROUND GASIFICATION (UCG) – IT'S ALL ABOUT PLANNING

ANDRIES DU PLOOY[1]–PÉTER MAJOROS[2]–DÓRA PAPRIKA[3]–
JOHAN BRAND[4]–PETER VAN VUUREN[5]
[1]UCG Exploration Manager, Wildhorse Energy, driesd@wildhorse.com.au
[2]Senior Geologist, Wildhorse UCG Kft., pmajoros@wildhorse.hu
[3]Geologist, Wildhorse UCG Kft., dpaprika@wildhorse.hu
[4]Technical Director, Wildhorse Energy, johanb@wildhorse.com.au
[5]UCG Technology Manager, Wildhorse Energy, peterv@wildhorse.com.au

1. Introduction

The unconventional use of coal to supplement Natural Gas (NG) in the power and chemical industry makes Underground Coal Gasification (UCG) an important technology in economically producing unconventional gas. Present day exploration and production technologies pave the way "*from a potential to actual production*".

A 3D seismic survey has been applied in Southern Hungary for the site selection of UCG resource blocks, as well as in the design of the most optimal exploration drilling program. The latter exploration techniques directional drilled injection and production wells are planned in the coal seams to sustain the burning front.

Wildhorse UCG Kft is a pioneer in the design and introduction of environmentally friendly coal-based syngas for electric power generation in East-Central European countries. Additionally the syngas can be utilised to supplement national gas supplies as an alternative fuel gas. In this paper the role of 3D seismic measurements is discussed in defining the "Mecseknádasd UCG project".

Wildhorse UCG Kft completed 3D seismic measurements in April and May of 2011 in the Mecseknádasd UCG project area. The goal of the seismic measurements is to image and clarify the structural conditions and to reveal faults and other discontinuities in the coal formation explored previously by historic deep drilling in the area.

1. Mecsek Hills Project

The Mecsek Coalfield is located in south-west Hungary approximately 220 km from Budapest on the northern edge of Pécs. This city is a regional centre at the coalfield's south-west corner. A number of smaller towns are also located around the coalfield's periphery. The region is well connected to other parts of Hungary and surrounding countries by national road and rail networks.

The project covers an area known as the Mecsek Coalfield, a Mesozoic coal complex which is a remnant block of pre-Tertiary rocks within the Tertiary Pannonian basin. The area has seen significant historic coal production over a period which ended in 2004 and yielded approximately 300 Mt. However government data suggest that significant coal deposits remain below the limit of underground mining.

2. Regional and local geology

The coalfield forms a regional topographical feature rising above the surrounding hilly plains to over 600 m above sea level. There is a general radial drainage pattern with gentle valley sides with mostly re-growth and mature forest with some farmed areas.

The regional tectonic history is complex and four major extensional and compressional deformation phases have been identified between the Late Permian to Late Tertiary periods [1]. Structurally, the field comprises an easterly plunging complex faulted anticline/ syncline fold system comprising Triassic, Jurassic and Cretaceous age rocks overlain unconformably by Tertiary age sediments and volcanics. There was a period of igneous activity from the Early Cretaceous to the Miocene with injection of sills and dykes into the sedimentary sequence, which in places intrude into the coal seams. Normal and reverse faults are common in the Mecsek Coalfield and have divided it into a series of discrete fault blocks (see Figure 1).

The MCF was formed during the Upper Triassic Rhaetian stage and the Lower Liassic Hettangian and Lower Sinemurian stages. It is a 120–1200 m thick, limnic and paralic sequence comprising inter-bedded coal, siltstone, sandstone and limestone. The coal does outcrop in the south-western part of the tenement package (Pécs-Vasas), where it has been partially exploited by open cast mining [2].

The MCF is underlain by the Late Triassic age Karolinavölgy Sandstone Formation, a 500–600 m thick deltaic sequence. The overlying Cretaceous sediments cover only small areas and were generally formed in pelagic depositional environments. The Jurassic and Triassic stratigraphy of the MCF is shown in Figure 1.

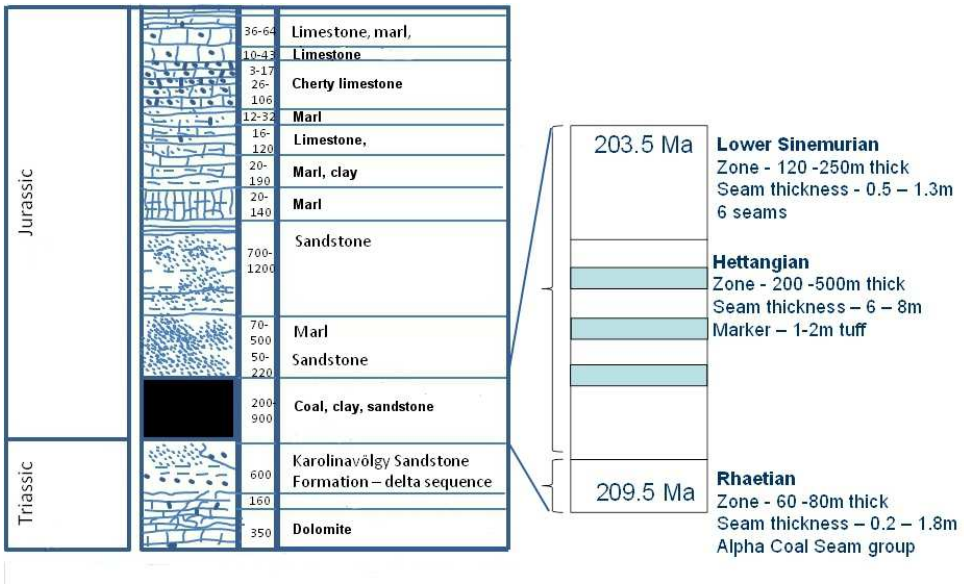

Figure 1. Mecsek coal formation [3]

On the basis of lithology and sedimentary facies the formation is divided into three members that can be traced across the entire Mecsek area (see Figure 1):

1. The Upper Member (Sinemurian lower part), a marine facies which developed as the basin was inundated.
2. The Middle Member (Hettangian), a fluvial flood plain facies with some brackish marine facies in the upper parts.
3. The Lower Member (Rhaetian), a lacustrine and alluvial freshwater sequence.

These three coal bearing members contain between 10 and 42 individual seams with greater than 0.5 m thickness with seam dips ranging from 20º-80º depending on their structural position in the basin. The Middle Member contains the thickest seams. The coal formation occurred in a half graben or monoclinal basin with thickest coal accumulation occurring in the south [4].

The Middle Member is 200-500 m thick and contains the seams of main UCG interest. Seams are of greatest thickness and lateral extent in this member, although seam correlation across the entire basin is difficult due to complex geological structure. Further exploration focused on this seam package.

3. Váralja exploration target

This area is on the northern margin of the Mecsek Coalfield (see Figure 2) and has the basin's largest known unexploited coal deposits.

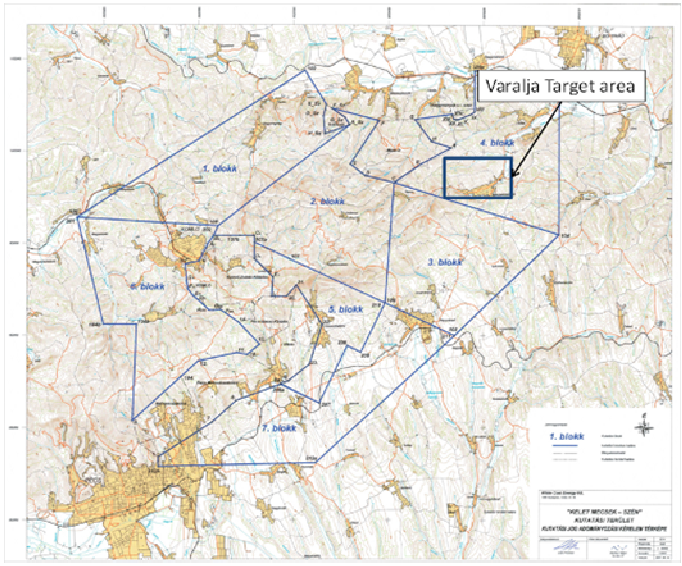

Figure 2. Location of the Varalja exploration target

The area is the most structurally complex in the coalfield. There are three main fault types; basin margin normal growth faults; a series of reverse faults resulting from compressional events; and a series of late stage thrust faults associated with Miocene compressional events.

The area of greatest complexity occurs in the adjacent exploration block (Calamites KFT area), where the faulting and thrusting are the most intense. Moving eastward into Wildhorse Coal Block 4 the structural complexity is reduced. The coal deposits occur as a series of large, relatively uncomplicated thrust blocks.

The target area is within the Wildhorse Coal Block 4, where extensive historical drilling has demonstrated the presence of large coal deposits. This was conducted on grid lines spaced at ~600 m with hole spacing along lines at ~500 m. The drilling indicates that substantial deposits suitable for UCG may be present at depths from 800–1200 m.

4. 3D seismic survey

A 3D seismic survey is complementary to a well-planned drilling program in exploration areas and gives more detail on the structural regime and thus the continuity of the seams.

Figure 3 indicates that the structural complexity due to extensional and compressional tectonics of the Mecsek Coalfield is the principal risk to the project. For a clearly defined UCG Project, an understanding of the distribution of the major faults is essential.

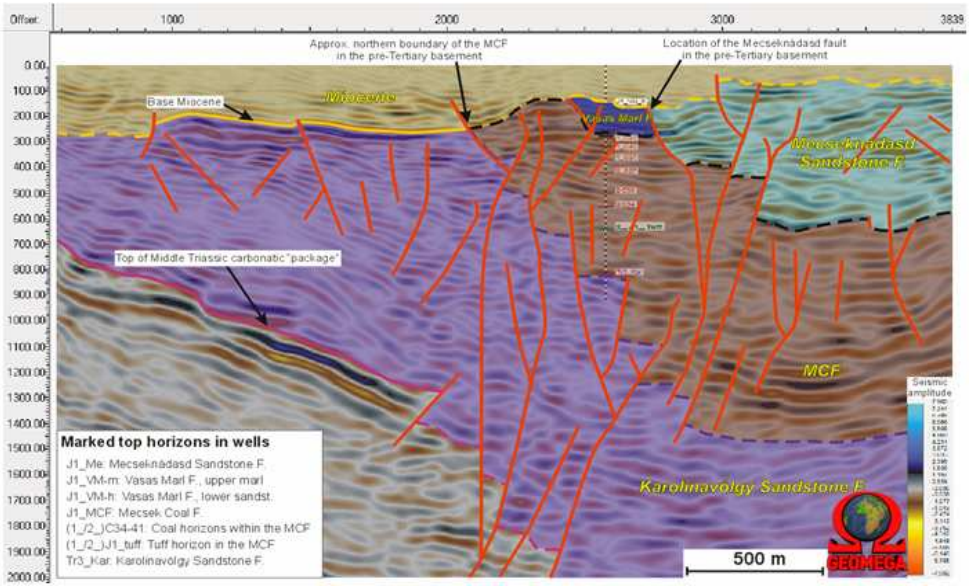

Figure 3. Seismic section - Interpreted Inline from the 3D seismics

Wildhorse contracted Geomega Ltd. to perform an integrated geological and geophysical evaluation of the Váralja South coal exploration area (Eastern Mecsek Mts., South Hungary). The aim of the study, which has been primarily focused around the newly

acquired and processed 3D seismic survey shot beginning 2011, was to provide geological-tectonic support for this project as well as for its future drilling programs.

5. Conclusions

The work conducted concerning the Eastern Mecsek coal exploration block can be summarized in the following:

- a complete geological-geophysical evaluation of the area was covered by the 3D seismic survey
- this was performed using the integrated geological and geophysical database loaded into SMT Kingdom project evaluation software
- seismoctectonic block characterization: 20 seismoctectonic blocks were identified within the Mecsek Coal Formation, which seem not to be affected internally by significant faulting, at least in the scale of the seismic resolution. The boundaries of these blocks are usually tectonic. These blocks are recommended to be the primary focus of further exploration work (Figures 4 and 5).

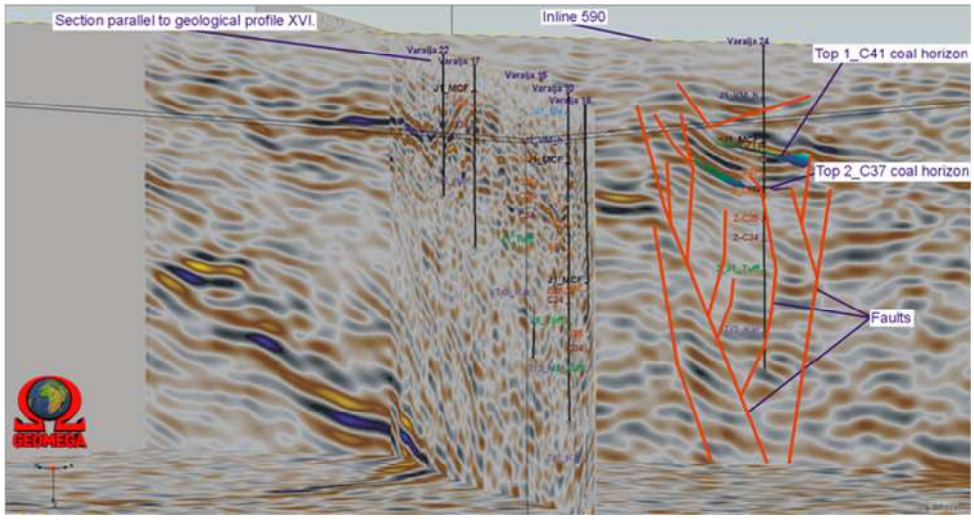

Figure 4. 3D section of an identified perspective block with the bounding faults

The quality of the seismic surveys is much better than expected considering the mountainous terrain. North of the area coherent and continuous reflectors can be identified, which are in agreement with geological sections inferred from earlier exploration wells. In the main target zone of the survey, however, the seismic image indicates that the sedimentary succession (including the coal-bearing sequence) is heavily tectonised. Comparison of the main tectonic zones seen in the seismic survey with the tectonised character of certain boreholes shows very good spatial agreement. This integrated analysis allowed us to construct a large-scale tectonic model of the area. This model implies that a

regionally important strike-slip shear zone runs across the study area, which can be held responsible for the heavily tectonised nature of the coal-bearing sequence.

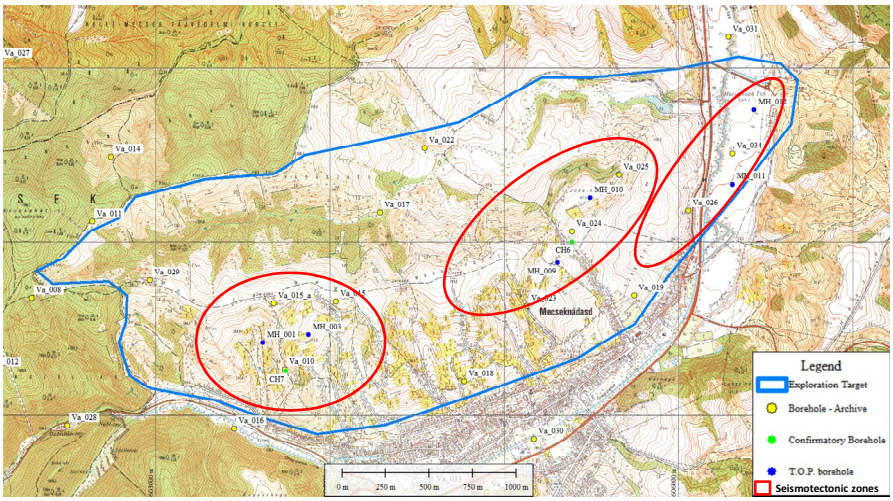

Figure 5. Contours of seismotectonic blocks within three zones

The new tectonic model and the heavily tectonised nature of the MCF in the Váralja South area is of utmost importance for the future planning of the UCG project, which relies on the presence of continuous and undisturbed coal bodies.

The above-mentioned data and model was taken into account during project implementation strategy (planning of directional boreholes and infrastructure) and to cross-check all future well locations against the seismic survey to reduce the technical and geological risk of the operations. It also assisted the focus of the indicated and measured drilling programs and substantially reduced exploration costs and complexity.

References

[1] Tari, G. C.–Horváth, F.: Alpine evolution and hydrocarbon geology of the Pannonian Basin: an overview. The Carpathians and their Foreland: Geology and Hydrocarbon Resources, Memoir 84. AAPG, 2006, pp. 605–618.
[2] Némedi-Varga, Z. (ed.): A mecseki feketekőszén kutatása és bányaföldtana, 1995.
[3] Wein, Gy.: A Mája-déli feketekőszénterület (Mecsek-hegység) földtani felépítése. Bányászati Lapok, 1962, 10, pp. 655–662.
[4] Hámorné Vidó, M.: Coal seam correlation and data compilation for coal resources calculation following the JORC Code requirements in the Mecsek-K exploration area. 2009, ELGI, Unpublished report for White Coal Energy Ltd.

Geosciences and Engineering, Vol. 1, No. 2 (2012), pp. 143–148.

FROM THE "PALÓC KARST" TO THE FISSURE WATER OF VOLCANIC ROCKS – SELECTIONS FROM HYDROGEOLOGY OF NÓGRÁD COUNTY, HUNGARY

PÉTER PRAKFALVI
Geologist, Hungarian Office for Mining and Geology,
1145 Budapest, Columbus u. 17–23.,
peter.prakfalvi@mbfh.hu

1. Introduction

Nógrád County is generally considered as an area poor in groundwater and thermal water. This summary statement is only partially acceptable. Significant amounts of cold water and slightly thermal water are available; however compared to the area of good conditions in the country this county is characterized by lower temperatures of both groundwater and thermal water. This is because there are no large karstic areas on the surface and no subsurface providing intensive water fluxes into the deeper sections. Among pre-Quaternary rocks, the siliciclastic (sandstone) and volcanic rocks play the most important role in watercatchment due to their largest surface coverage; however the effect of subordinated limestone should not be ignored. This paper presents the geological hydrogeological characteristics of the three hydrogeological units.

2. Limestone

In the area under study two different types of limestone can be distinguished according to their geological ages as well as their karstic development. Triassic limestone occurs only in block spots on the left bank of the Danube – all in all a few km^2 area on the surface, but this still has a relatively significant role in the thermal water regime. There are no karst springs in the county's rock because the karst water level is below the actual erosion base (the karst water level is approx. 110 m bsl), and therefore this water is known only from boreholes. Two of them are introduced in Tables 1 and 2.

Triassic limestone can be found approximately 15 km away from the Bér 1 borehole (in the vicinity of Nézsa), in a relative small area, so it is likely that this thermal water originated from a SW to NE directional upflow which can be identified as a part of the general Transdanubian convective upward flow. However, the possibility cannot be excluded that that the recharge area is the andesite from Cserhát Mountain and the flow is driven from NE to SW. Such a decision requires the analysis of the area in detail.

Triassic limestone can be found on the surface about 5 km distance SE from the Berkenye borehole, which could be a recharge area, although the andesite of Börzsöny as recharge formation cannot be excluded.

The Miocene types of limestone that are generally deposited on the volcanic formations of Cserhát Mountain are also considered as good aquifers.

Table 1

Berkenye (core boring in sections)

No.	**Z (bsl)**	**Bottom level (m)**	**Filtered depth interval (m)**	**Rocks in filtered or opened section**
K-1	206.07	482	321.7–459.8 (5 sections)	Eocene marl, Triassic limestone, Miocene andesite (not aquifer)
Initial water table (m)	Operating level (m)	Discharge (l/min)	Discharged water temperature (°C)	karstic water level (bsl)
–88.2	–98.0	85	31	118.5

Table 2

Bér, borehole (core boring in sections)[1]

No. #	**Z (bsl)**	**bottom level (m)**	**Filtered depth interval (m)**	**Rocks in filtered or opened section**
Bér 1	202.78	1395.6	1208.6–1336.6	Eocene marl, Triassic limestone
Initial water table (m)	Operating level (m)	Discharge (l/min)	Discharged water temperature (°C)	karstic water level (bsl)
–96.6	?	190	52	106.18

From the area of "mini karsts" around Mátraverebély, both downflow-cold (Szentkúti source group) and upstream-warm (Hot Well, 16–17 °C) springs originate. Based on investigations of higher discharges (30–60 l/min) the karstic water can be separated quite well from the fissure water of the andesite formations (5–20 l/min).

3. Sandstone

The so-called "Glauconitic Sandstone" formation has the highest surface coverage in the county. Due to its double porosity (pores+cracks) it is considered as a moderate aquifer [2]. Surprisingly, this rock was called "Palóc Karst" by Noszky [3], a geologist who was familiar with the area, especially because of its denudation. Beyond denudation further study of other features of the karst were also confirmed by their very distant relationships,

such as the outgoing sources of edges, but mostly the deposited travertine terraces. During the water cycle as an effect of CO_2 absorbed from the soil and air the 15% carbonated cement material is dissolved from sandstone and deposited as travertine entering into the surface. Discharges of drilled holes in this rock are near to 100 to 200 l/min at some 10 metres drawdown. Thermal waters are not included because of their blocked distribution of tectonics and the cold effect of downstream water.

The downflow is proved by the data of a deep and thoroughly investigated drilled well (Salgótarján, Vv–1 = K–3), given in Table 3.

Table 3

Salgótarján, Vv–1 = K–3

Depth interval (m)	**Rocks**	**Initial water table (m)**
117.0–303.9	"Glauconitic Sandstone"	–9.3
317.2–410.6	"Glauconitic Sandstone"	–15.56
410.6–456.9	"Glauconitic Sandstone"	–21.2

Due to the effect of filtration resistance the distinct vertical hydrogeological units are loaded from top to bottom, and not from the bottom of an upward flow [4]. This is partly supported by the extremely high geothermal gradient of the well (15-22 m/°C) compared to the Hungarian average of 30.73 m/°C.

Some borehole data from the area of upward flow (Bátonyterenye-Kisterenye, Ke–1 = K–8) are given in Table 4 [5].

Table 4

Bátonyterenye–Kisterenye, Ke–1 = K–8

Depth interval (m)	**Rocks**	**Initial water table (m)**
93.24–101.6	"bedrock sand of coal II."	+1.7
235.6–239.6	"foot gravel"	+7.6
247.14–256.2	"foot gravel"	+15
258.5–270.7	"foot gravel"	+16.2
287.3–373.0	"Glauconitic Sandstone"	+17.7

The upward flow is confirmed by the initial water table levels increasingly changing with the depths and also by the smaller (anomalous) geothermal gradient (19.63 m/°C). The flow regime is presented in Figure 1, where the water of the downflow system was recovered by a borehole.

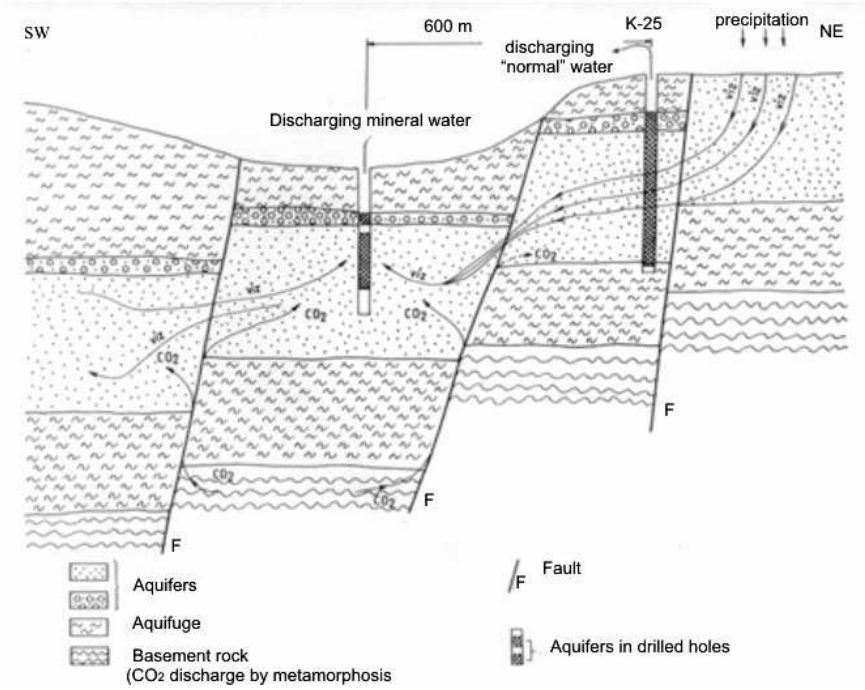

Figure 1. Hydrogeological profile of two boreholes. where the downflow and upflow zones were observed (Edited by P. Prakfalvi P. drawn by J. Kakuk)

4. Volcanic rocks

The volcanic rocks of mountains esentially have a similar role in the water cycle as other karst areas have. as these areas can also recharge. but their conductivity is less than that of the karst [6]. Frequently slightly thermal water can be obtained from the springs. sometimes discharging by reservoir energy at the wells on the shoulders of the volcanic mountains. The amounts of discharging water are considerably smaller than from karstic rocks, which are associated with the material of volcanic rocks. Due to their much higher filtration resistance in cracked or fissured volcanic rocks than in karst,. the ratio of water infiltration is less percentable. Nevertheless, the low temperature requires some explanation. One reason is surely based on the location of volcanic rocks characterized by superficial expansion (a large area for infiltration), in addition to a narrow and thin volcanic root zone (i.e. volcanic vent). The root zone does not provide sufficiently for the penetration of water into the greater depths. According to wells drilled in the root zone of the karst area. the root zone of the karstic areas is greater than their extension on the surface.

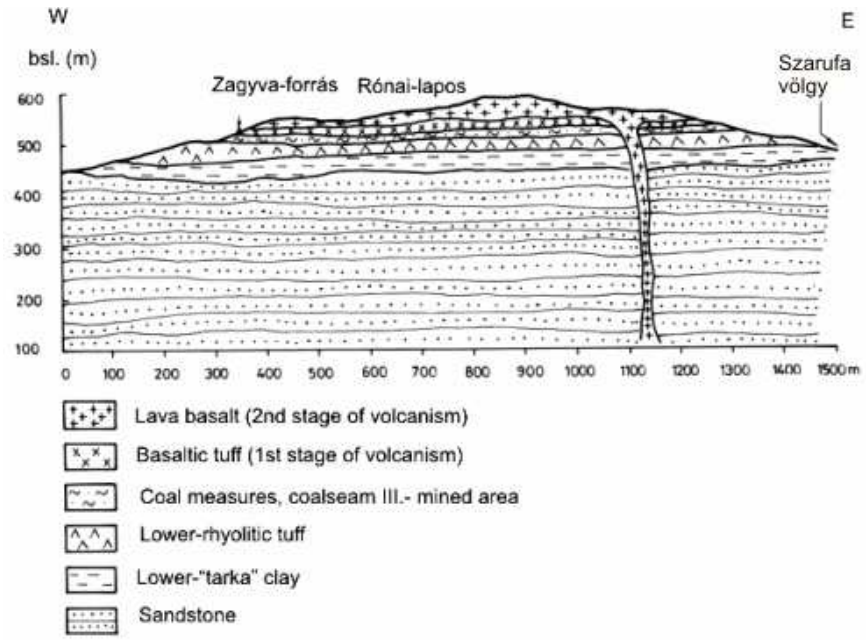

Figure 2. Distribution of basalt rock on the surface is incomparably greater than the area of horizontal section of volcanic breakthroughs
(Edited by P. Prakfalvi, drawn by J. Kakuk)

According to the mining experiences of Nógrád Coal Mine Co., it is known that the volcanic breakthroughs are usually much smaller than the surface distribution of the volcanic area, since the volcanic vents were exploited around by the coal mining procedures. For example, under the almost 13-km^2 Medves basaltic layer just a few breakthroughs – some 100 m^2 vents – have been identified (Figure 2).

The flow regime of an andesite mass (Ecseg, Bézma) and its outbreaks on the surface are shown in Figure 3. Due to the above-mentioned reasons the gravity drainage of precipitation is restricted by the depth; only lukewarm water flows out both from the thermal spring (20–60 l/min. 17.6 °C) and from the borehole (1–2 l/min).

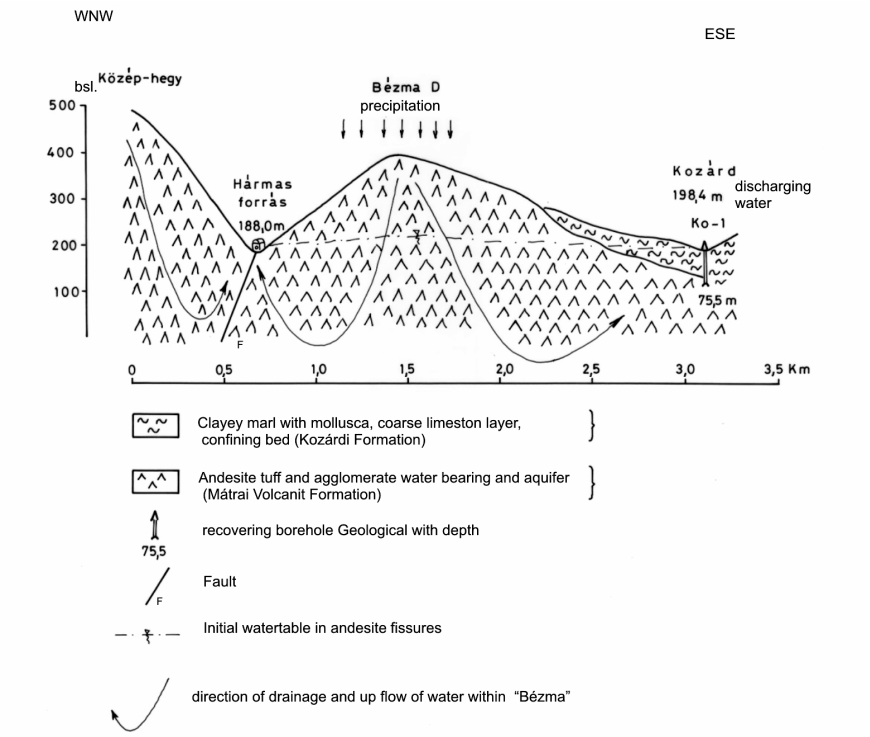

Figure 3. Hydrogeological profile through Bézma hill
(Edited by P. Prakfalvi, .drawn by J. Kakuk)

References

[1] Balogh, J. et al.: Final report of Bér-1 hydrocarbon prospecting drilling. MBFH Adattár, 2004.
[2] Hámor, G.: Geological conditions of Nógrád-Cserhát study area. Geologica Hungarica series Geologica Tomus 22. Budapest, 1985, p. 307.
[3] Lorberer, Á.: Investigation on hydrogeological and factual water resources balance of municipal water supply of Salgótarján, Vízügyi Közlemények, 1976. 1. pp. 84–110.
[4] Noszky, J. Sr.: Rovings on "palócföld". Manuscript. Országos Földtani Szakkönyvtár, Budapest, 1940, p. 164.
[5] Vitális, S.: New hydrogeological data on Salgótarján and its vicinity. Hidrológiai Közlöny, 1939. 19. pp. 47–61.
[6] Vitális, S.: New medicinal water in Kisterenye. Hidrológiai Közlöny, 1939. 19. pp. 62–74.

Geosciences and Engineering, Vol. 1, No. 2 (2012), pp. 149–154.

NATIONAL RADIOACTIVE WASTE REPOSITORY 2011-2012: CONSTRUCTION OF THE FIRST TWO DISPOSAL GALLERIES

GÉZA SZEBÉNYI[1]–JÓZSEF BERTA[2]–GÁBOR HÁMOS[3]–
JÓZSEF CSICSÁK[4]–RICHÁRD SZABÓ [5]
[1]Leader geologist of assessment,
Mecsekére Zrt., Esztergár L. út 19., Pécs 7633 (Hungary)
szebenyigeza@mecsekerc.hu;
[2]head of mining department, bertajozsef@mecsekerc.hu;
[3]head of geological department, hamosgabor@mecsekerc.hu;
[4]project director, csicsakjozsef@mecsekerc.hu;
[5]modeling geologist, szaborichard@mecsekerc.hu

1. Introduction

The Bataapáti site was selected for the storage of the low and intermediate level radioactive waste on the basis of a multilateral consideration. The site and its sorroundings geographically belong to the Geresd Hills and geologically to the Mórágy Granite Pluton. In the northwest part it spreads over the East Mecsek. The site is located in the centre of this region.

The surface exploration phase was completed in 2003 [1]. On the basis of the results the specialised authority agreed on geological suitability within the boundaries of the polygon appointed in the exploration area. The construction of the inclined shafts (serving as access tunnels) meant the subsurface exploration phase, which, in accordance with the approved plan, was launched in late 2004 and was completed in mid-2008 [2].

The final report of the underground exploration program [2] was prepared during the excavation of the last section of the inclined shafts. It confirmed that the subsurface exploration had achieved its task objective and proved that the natural conditions of the Bátaapáti site are suitable for a low and intermediate level radioactive waste repository [3].

Phase I (the so-called "small loop" tunnel system) of the construction of the National Radioactive Waste Repository (NRWR) in Bátaapáti was carried out between 2008 and 2009 [9]. The first and second stages (construction of the "large loop" tunnel system and the subsurface areas of final water treatment system) of Phase II were basically completed in June 2010 [17]. The operating systems of the NRWR and the first two disposal galleries of the No. 1 chamber field (I-K1 and I-K2) were constructed (completed by the end of September, 2011) within the third stage of the second phase [18], [21–22].

After the completion of the small-loop tunnel system a summarising geological evaluation was prepared [15]. An expert summary [13] was made in 2010 with consideration of the data available as of 31 May 2010. These reports were followed by the disposal gallery preliminary design [16] in May, 2011 and the recently prepared geological summary [19], which are based on data collected before the date of 24 April 2012. The Pécs District Mines Inspectorate received the geological summary [20] about the construction phases of the NRWR between 2008 and 2012 in early June 2012. Zoltán Balla was responsible for the small-scale geological modeling [4], [5], [6] and Gyula Maros mainly for the structural-tectonic synthesis [11–12].

1. Geological setting

The Bátaapáti site has been established in the 338-million-year-old rocks [10], [8] of the Mórágy Granite Pluton at the southeastern edge of the East Mecsek, south of the Mecsekalja Dislocation Zone, which consists of paleozoic metamorphic rocks. The Mórágy Granite consists dominantly of granitic, less dioritic intrusive rocks. It also contains acidic dykes, which are genetically attached to them. The subvolcanic alkali basalt dykes characterised by diverse composition and classified among the Lower-Cretaceous Rozsdásserpenyői stratigraphic unit are a rare type of rocks, but in connection with the repository are very significant (due to their correlation with high transmissivity). In the granitic rocks of the Mórágy Granite the dioritic rocks compose downward-widening, dominantly steeply dipping lens-like, NE-SW trending bands, which are parallel to the strike of the Mecsekalja Dislocation Zone. Between the rocks characterized by different chemical composition, transitional, hybrid rock-types were formed [2].

The tectonic evolution of the above-mentioned rocks formed diverse structures, showing a series of multiple renewal characterized by variable filling, usually along its strike too. The structure has significantly higher impact on the hydrogeological and geotechnical conditions than does the mineralogical composition [15]. The distributional principles of the most significant structures determine the tectonic and hydrogeological feature of the site.

The presence of strike-slip type, braided-sigmoidal structures whose sizes range from macro to micro-scale is the most basic feature of the tectonic character of this area. These form a complex conductive channel system because of their inner structure.

The site is divided into hydrogeological blocks by E-W striking non-conductive and NE-SW, NNW-SSE striking conductive structures. The structures which are parallel to the strike of the Mecsekalja Dislocation Zone are significant both hydrogeologically and geotechnically, as the highest transmissivity values and the thickest weakened zones are associated with this direction.

Despite the favourable lithological composition, significant base-metal, radioactive ore indications or regional hydrothermal alteration accompanied with ore mineralization have not been exposed during the performed work [14].

In the scale of the subsurface geological the hydro-geological modeling is based on a pattern consisting of the combination of geological bands and hydro-geological stripes, which is divided into units (blocks) by non-conductive zones [7].

2. Characterisation of the No.1 chamber field

The No. 1 chamber field is located in the tectonic/hydro-geological unit which is delineated by the “Péter” and “Zoltán” fault, as non-conductive zones. This area is traversed by the “Patrik” fault. Well conductive strips run along both its northern and southern margin while at its eastern and western side so-called hydro-geological boundary structures – zones – can be traced [7].

In the area of the No. 1 chamber field the most important geological feature is the banded geological structure and the stripe-zone-like hydrogeological character, which is the result of NE-SW and NNW-SSE striking tectonics (Figure 1). We have distinguished three NE-SW bands on the basis of their lithology: the northern, middle and southern bands.

The *northern monzonitic band* comprises of dioritic rocks (monzonite, hybrid monzonite) and a NE-SW striking alkali basalt dyke which intersects the dioritic rocks. This dyke has average dip direction of 318º/72º and is 0.60–1.90 m thick. It is intersected by NE-SW and NW-SE striking faults and fractures, along which the offset can be several meters. Sometimes the dyke along these faults and fractures can be brecciated and shows argillitization of varying degrees. The main plane of the dyke is uneven tectonically segmented. The monzonitic rocks of the northern band are mostly intact, slightly jointed and have favourable geotechnical features. The occasional highly conductive 20-NE-SW structure runs along the alkali–dyke, but open fractures of the monzonitic rocks are also characterized by high transmissivity.

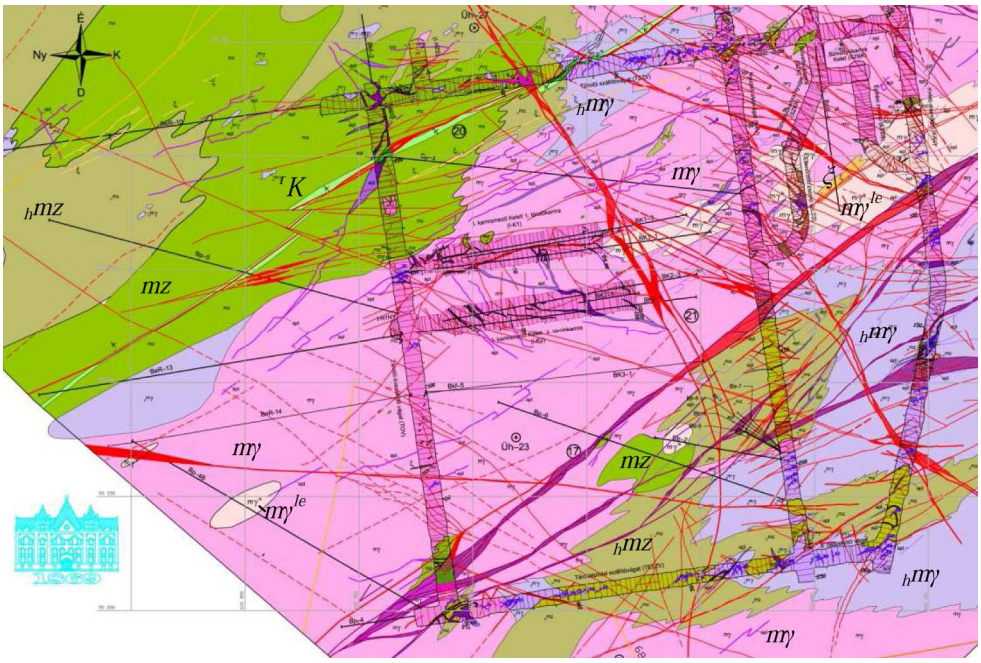

Figure 1. Geological map of the No. 1 chamber field (from [20], by MÁFI [12])
Legend: mγ – monzogranite, $m\gamma^{le}$ – leucocratic monzogranite, $_h m\gamma$ – hybride monzogranite, $_h mz$ – hybride monzonite, mz – monzonite, ξ – syenite, $^r K$ – alkali basalt

The northern band is gradually connected to the *middle monzogranitic band*, mostly built up by monzogranite with some minor leucocratic monzogranites. The middle band appears in the NW part, with gradual transitions from the monzonites through hybrid rock types (hybrid monzonite, hybrid monzogranite). Elongated syenite bodies with thickness of a few meters are also characteristic to these transition zones. The Patrik fault forms the southeastern limit of the middle band. The southeastern part of the middle band is homogenous, dry, while to the northwest the fracturation increases gradually, and seepage appears. The geotechnical characteristics of the "TOV" drift near the Patrik fault gradually improve from the south. Between 50 and 120 meters of the drift the geotechnical features

are favourable. The fractured middle quality (category III) rock masses are become more frequent approaching the northwestern limit of the band. The geotechnical characteristics are similar in the "NAV" drift around the Patrik fault, but with a much wider transition zone. The first two repository chambers are located in the middle, monzogranitic lithological unit (band).

The *Patrik fault (17-NE-SW)* separates the middle band from the southern band. This is a fault zone of primary importance: it is 10–15 m wide with variable internal structure. It has a braided-sigmoidal morphology, and it is built up from carbonatized monzogranite boudins and several-meter-wide clayey core zones. The core zones mostly have a flaky, lentil or brecciated structure with clayey, carbonatic, polimictic breccia filling. The Patrik fault has NE-SW strike, and a steep dip to the SE, but planes dipping to NW can also occur. In its internal structure loose, brecciated, open, SW dipping, and NW-SE striking structures are found. The Patrik fault (17-NE-SW) is by far the most dominant geotechnical element of the "large-loop" drift system. The Patrik fault is traversed by the "NAV" and "TOV" drifts exposed (category V) rocks of 15 m length, with a clay bearing fault zone more than 10 meters thick.

The *southern hybrid lithological band* is made up of various types of rocks, from monzogranite in the NW through hybrid monzogranite, hybrid monzonite intruded by leucoratic monzogranite (based on the Btr-2 hole) to the SE direction. Because none of the occurring lithology types could be considered dominant, petrologically the rocks were labeled hybrid. The geotechnical characteristics of these rocks are usually favourable, but they frequently contain open fractures with very good water conductivity properties. This band contains several important high water conductivity, NE-SW striking structures, from which those with higher water influx were given individual names (18-NE-SW, 19-NE-SW). From the observations derived from the "Btr" holes tests, the water conducting channel system is variable. The good water conductivity channels are frequently connected to monzonite bodies.

The 21-NNW-SSE significant structure stretches in the eastern wing of the chamber field, while the 22-NNW-SSE structure is in the western flank. The latter was defined mostly by hydro-geological data.

3. Conclusions

The Bátaapáti repository is intended for the final disposal of low and intermediate level radioactive wastes (L/ILW).

Surface-based geological investigations of the Bátaapáti L/ILW repository site were conducted between 1997 and 2003. Underground investigations were carried out during the excavation of the access tunnels (2005–2008). The forming of the 1st and 2nd repository chambers and the installation of the operational systems were carried out in 2011–2012, within the construction of the II/3 construction phase of the National Radioactive Waste Repository. Geological, hydro-geological and geotechnical investigations were performed within the investigation programme of the National Radioactive Waste Repository in Bátaapáti and were financed by the Hungarian Agency for Radioactive Waste Management (PURAM).

The host rock of the repository is monzonite and monzogranite of the Mórágy Granite Formation of Early Carboniferous age. Crystalline rocks are intersected by Lower

Cretaceous alkali volcanic dykes. Hydro-geological and geotechnical properties are strongly influenced by large-scale tectonic zones with complex inner structure and extensive development of fault gouge and breccia. The first two repository chambers are located in the middle, monzogranitic litological unit (band). This unit offers the most favourable properties for the further chamber construction.

Acknowledgements

We would like to express our thanks to Patrik Török and Eduárd András, who have willingly helped in the preparation of this publication. We would also like to express our thanks to MÁFI, Golder Zrt., Kőmérő Kft., and Geo-Log Kft employees, who played an important role in the professional work. We would like to acknowledge the approval of this paper by RHK Kft, who ordered and executed these projects.

References

[1] Balla Z.–Albert G.–Chikán G.–Dudko A.–Fodor L.–Forián-Szabó M.–Földvári M.–Gyalog L.–Havas G.–Horváth I.–Jámbor Á.–Kaiser M.–Koloszár L.–Koroknai B.–Kovács-Pálfy P.–Maros Gy.–Marsi I.–Palotás K.–Peregi Zs.–Rálisch L.-né–Rotárné Szalkai Á.–Szőcs T.–Tóth Gy.–Turczi G. (MÁFI); Prónay Zs.–Vértesy L.–Zilahi-Sebess L. (ELGI); Galsa A.–Szongoth G. (Geo-Log); Mező Gy.–Molnár P. (Golder); Székely F. (Hygecon); Hámos G.–Szűcs I.–Turger Z. (Mecsekérc); Balogh G.–Jakab G.–Szalai Z. (MTA FKI) Az atomerőművi kis és közepes aktivitású radioaktív hulladékok végleges elhelyezésére irányuló program. A felszíni földtani kutatás zárójelentése, Bátaapáti (Üveghuta), 2002–2003, I–III. kötet. Kézirat, Országos Földtani és Geofizikai Adattár: T:20914; Magyar Állami Földtani Intézet, Budapest, 2003, Tekt. 1102; Bátatom Kft., Budapest, BA-03-156.

[2] Balla Z.–Császár G.–Földvári M. –Gulácsi Z. –Gyalog L.–Horváth I. –Kaiser M. –Király E. –Koloszár L.–Koroknai B.–Magyari Á.–Maros Gy.–Marsi I.–Musitz B.–Rálisch E.–Rotárné Szalkai Á.–Szőcs T.–Tóth Gy.–Berta J.–Csapó Á.–Csurgó G.–Gorjánácz Z.–Hámos G.–Hogyor Z.–Jakab A.–Molnos I.–Ország J.–Simoncsics G.–Szamos I.–Szebényi G.–Szűcs I.–Turger Z.–Várhegyi A.–Benedek K.–Molnár P.–Szegő I.–Tungli Gy.–Madarasi A.–Mártonné Szalay E.–Prónay Zs.–Tildy P.–Szongoth G.–Gacsályi M.–Moskó K.–Kovács L.–Mónus P.–Vásárhelyi B. Bátaapáti hulladéktároló felszín alatti létesítményeinek előkészítési munkái 2004–2007. A felszín alatti földtani kutatás zárójelentése. Kézirat, Mecsekérc Zrt., Budapest, 2008., RHK Kft. Irattára, Paks, RHK–K–082/08

[3] Balla, Z.: Értékelő jelentés a létesítési engedély földtani megalapozásához. Kézirat, 2008. január. Magyar Állami Földtani Intézet, Budapest. RHK Kft. Irattár, Paks, RHK–K–028/08

[4] Balla, Z.: Földtani-tektonikai modell. Közreműködés 3D modellezésben. Jelentés a 2008V-214. számú, Üh-186/2008. kódjelű szerződés FA80801 kódszámú tételének teljesítéséről. – Kézirat, Magyar Állami Földtani Intézet, 2009, Tekt. 1466; RHK Kft. Irattár, Paks, RHK-K-070/09.

[5] Balla, Z. 2010A: Geológiai-tektonikai modell 2. 3D/4D modellek aktualizálása. Jelentés az Üh-82/2009. számú szerződés T80670 kódszámú tételének teljesítéséről. – Kézirat, Magyar Állami Földtani Intézet, Tekt. 1475; RHK Kft. Irattár, Paks, RHK-K-036/10.

[6] Balla, Z. 2010B: Geológiai-tektonikai modell 3. 3D/4D modellek aktualizálása. az Üh-82/2009. számú szerződés T80670 kódszámú tételének teljesítéséről. Kézirat, Magyar Állami Földtani Intézet, Tekt. 1477; RHK Kft. Irattár, Paks, RHK-K-095/10.

[7] Benedek, K. (2010: Az első két kamra paramétereit származtató vízföldtani modell. Kézirat. 2010. február. RHK Kft., Paks, RHK-K-159/09, p. 16., 18.

[8] Gerdes, A.: Report on the LA-ICP-MS U-Pb dating of four borehole samples from the Mecsek Mountain granitoids. Kézirat, Magyar Állami Földtani Intézet, Budapest, 2006, Tekt. 1304.

[9] Jakab A.–Deák F.–Kovács L.–Maracsik Z.–Máté K.–Németh L.–Rátkai O.–András E.–Szamos I.–Szebényi G.–Török P.–Gyalog L.–Borsody J.–Füri J.–Gulácsi Z.–Király E.–Maros Gy.–Rálisch E., Szabadosné Sallay E. A Bátaapáti Nemzeti Radioaktívhulladék-tároló feltáró vágatai térkiképzése 1. ütem. Vágatdokumentációs jelentés „kishurok". Kézirat, 2009. június, Kőmérő Kft. – Mecsekérc Zrt. – Magyar Állami Földtani Intézet, Pécs–Budapest. RHK Kft. Irattára, Paks, RHK–K–040/09

[10] Klötzli, U. S.–Buda Gy.–Skiold, T.: Zircon typology, geochronology and whole rock Sr-Nd isotope systematics of the Mecsek Mountain granitoids in the Tisia Terrane (Hungary). — Mineralogy and Petrology, 2004, 81 (1–2), pp. 113–134.

[11] Maros Gy.–Koroknai B.–Palotás K.–Musitz B.–Füri J.–Borsody J.–Kovács-Pálffy P.–Kónya P.–Viczián I.–Balogh K.–Pécskay Z.: Brittle Fault Zones in the Mórágy Granite: New Structural and K–Ar Data (Törészónák a Mórágyi Gránitban: új szerkezeti és K–Ar-adatok). – A MÁFI Évi Jelentése 2009, pp. 91–112.

[12] Maros Gy.–Borsody J.–Füri J.–Koroknai B.–Palotás K.–Rálischné Felgenhauer E.: A Mórágyi-rög ÉK-i részének szerkezetföldtani értékelése a töréses szerkezetekre. Kézirat, 2012. február 28., Magyar Állami Földtani Intézet, Budapest.

[13] Molnár P.–Szebényi G.–Kovács L.: Előzetes földtani értékelés az MTD 2. módosításához. Kézirat, 2010, Mecsekérc Zrt., Pécs, RHK Kft. Adattár, Paks: RHK-K-108/10

[14] Szebényi G.–Hámos G.–András E.–Török P.–Barabás A. 2009a: Ásványi Nyersanyagkutatás összefoglaló zárójelentése. Kézirat, Mecsekérc Zrt., Pécs. RHK Kft. Irattára, Paks. RHK–K–046/09

[15] Szebényi G.–Hámos G.–András E.–Török P.–Majoros Gy.–Szamos I.–Molnár P.–Benedek K.–Kovács L. 2009B: Összefoglaló értékelő jelentés a felszín alatti létesítés tervezése és a biztonsági jelentés számára. Kézirat, Mecsekérc Zrt., Pécs, 2009. december, RHK Kft. Irattár, Paks, RHK-K-181/08

[16] Szebényi G.–Molnár P.–Kovács L.–András E. 2011A: Kamraprognózis (I-K1 és I-K2 kamra). Kézirat, 2011. május 31., Mecsekérc Zrt., Pécs. RHK Kft., Paks. RHK-K-147/10

[17] Szebényi G.–Török P.–András E.–Szamos I.–Kovács L.–Deák F.–Jakab A.–Máté K.–Rátkai O.–Gyalog L.–Borsody, J.–Füri J.–Gulácsi Z.–Maros Gy.–Rálisch E.–Molnár P. 2011B: A Bátaapáti Nemzeti Radioaktívhulladék-tároló feltáró vágatai térkiképzése II. ütem 1-2. szakasz. Vágatdokumentációs jelentés – „nagyhurok". Kézirat. Mecsekérc Zrt. – Kőmérő Kft – MÁFI – Golder, Pécs–Budapest, 2011. december. RHK Kft. Irattár, Paks, RHK-K-048/10M01

[18] Szebényi G.–Török P.–András E.–Szamos I. (Mecsekérc Zrt.), Gyalog L.–Borsody J.–Füri J.–Gulácsi Z.–Maros Gy. (MÁFI) Deák F.–Jakab A.–Kovács L.–Máté K. (Kőmérő Kft.) 2012A: Az NRHT I-K1 és I-K2 tárolókamra vágatdokumentációs jelentése. Kézirat, Mecsekérc Zrt., Pécs, 2012. február. RHK Kft. Irattár, Paks: RHK–K–075/11M01

[19] Szebényi G.–Török P.–András E. (Mecsekérc Zrt.), Korpai F. (Golder), Kovács L. (Kőmérő Kft.) 2012B: Az I. kamramező kamratelepítési viszonyai (előterjesztés). Kézirat. 2012. május, Mecsekérc Zrt., Pécs. RHK Kft. Irattár, Paks: RHK-K-047/12M01

[20] Szebényi G.–Török P.–Hámos G.–András E.–Szamos I.–Miskolczi R.–Gulácsi Z.–Maros Gy. (MÁFI), Mező Gy.–Korpai F. (Golder), Kovács L. (Kőmérő) 2012D: Földtani összefoglaló jelentés. NRHT létesítés 2008–2012. Kézirat. 2012. június, Pécs–Budapest, RHK Kft. Irattár, Paks, RHK-K-020/12.

[21] Török P.–Berta J.–Szebényi G.–Sütő R.–Szamos I. (Mecsekérc Zrt.); Rátkai O.–Kovács L. (Kőmérő Kft.) 2012A: Az I-K1 tárolókamra műszaki kivitelezési és vizsgálati dokumentációs jelentése. Kézirat. 2012. május. Mecsekérc Zrt., Pécs. RHK Kft. Irattár, Paks: RHK-K-006/12M01

[22] Török P.–Berta J.–Szebényi G.–Sütő R.–Szamos I. (Mecsekérc Zrt.); Rátkai O.–Kovács L. (Kőmérő Kft.) 2012B: Az I-K2 tárolókamra műszaki kivitelezési és vizsgálati dokumentációs jelentése. Kézirat. 2012. május, Mecsekérc Zrt., Pécs. RHK Kft. Irattár, Paks: RHK-K-013/12M01.

Geosciences and Engineering, Vol. 1, No. 2 (2012), pp. 155–160.

SEISMIC TOMOGRAPHY MEASUREMENTS IN THE RADIOACTIVE WASTE DISPOSAL SITE IN BÁTAAPÁTI

PÉTER TILDY[1]–ZSOLT PRÓNAY[1]–ENDRE TÖRÖS[1]
[1]Geological and Geophysical Institute of Hungary
Stefánia út 14, Budapest, Hungary, 1143
tildy.peter@mfgi.hu; pronay.zsolt@mfgi.hu; toros.endre@mfgi.hu

1. Introduction

As a part of the underground investigations of intermediate and low-level radioactive waste disposal site in Bátaapáti, seismic and DC tomographic measurements were carried out to obtain a better understanding of the geological setting and structure and of the hydrogeological situation of the rock mass. The measurements were conducted in an underground space fully surrounded by galleries, which means almost optimal survey geometry. The large number of other investigations carried out in the tunnels made it possible to compare the tomography map with the widely used rock mass qualification parameters (Rock Quality Designation – RQD [1], and Quality of the rock mass – Q-value [2]), and the hydrogeological properties of the rock.

2. Data acquisition and processing

Due to the physical dimensions of the investigated rock mass we had to carry out the field work in 5 stages, using 24 2-component mining geophones, and 120–125 source points (9 kg sledgehammer) at each [Figure 1. a)].

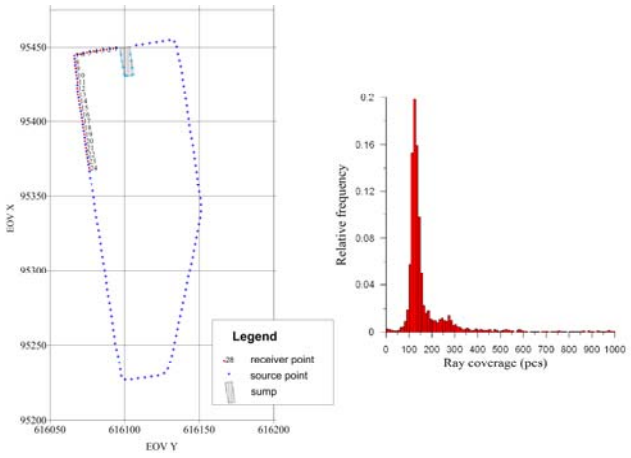

Figure 1 a) Measurement layout of the 5 measurement steps; b) ray coverage frequency of the tomography processing

The survey was designed to achieve the best possible image taking into consideration the characteristic wavelength (about 10 m for the 4000–5500 m/s P-wave velocity and 400 Hz dominant frequency). Based on these properties the source and receiver spacing was 4.5 m. The relative frequency of ray coverage (the number of ray paths crossing the unit cell) can be seen in Figure 1b.

The tomography reconstruction technique applied was the simultaneous iterative reconstruction technique (SIRT) [3]; wave propagation was modelled by the "expanding time field" algorithm [4].

3. Tomography maps and geology

Generally seismic velocities are a function of the rock type, the fracturing, the fluid or gas content and the rock stresses. Based on laboratory measurements carried out on rock samples from the area of investigation, the geomechanical properties of different igneous and volcanic rocks – i.e. the matrix properties – are similar. However seismic velocities of different rock types show differences (Figure 2). The main cause of these differences is the different background fracture system of the different rock bodies.

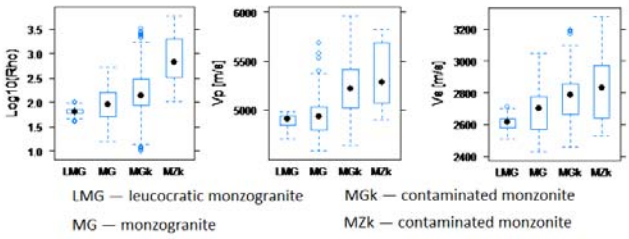

Figure 2. Physical properties of different rock types

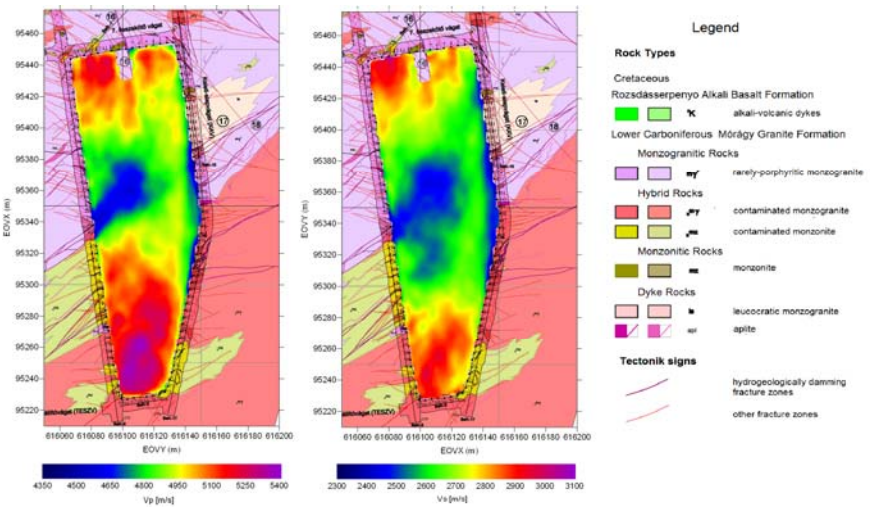

Figure 3. P- and S-wave tomography map inserted in the geologic map

The main fracture zone penetrating the investigated area (indicated by the red arrow) can be clearly seen in Figure 3. The most interesting feature of its tomographic image is the strong horizontal variability. Notwithstanding that this zone can be identified in both shafts, this kind of variability along the strike is definitely new information, and should be taken into account for any future activity here.

4. Comparison of seismic and rock mass properties

Rock mass properties are used for various engineering design and stability analysis. The classification is usually based on empirical parameters like a RQD parameter or a set of them, as in case of rock quality (Q-value). RQD is a rough measure of the degree of jointing in a rock mass, measured as a percentage of the drill core in lengths of 10 cm or more. High-quality rock has an RQD of more than 75%, low quality of less than 50%. The Q-value is based on RQD, but the shear strength and stress environment of the rock are also involved in the determination of the value. It can range between 0.00006 (for an exceptionally poor rock mass) and 2666 (exceptionally good).

The special location made it possible to compare the seismic velocity tomography maps with the rock mass property data obtained from the tunnels – i.e. from the perimeter of the investigated area. However these comparisons have some limitations from various aspects.

General limitations:

- Offset: rock mass was observed on the tunnel wall during tunnel construction, while seismic parameters originate from the internal area behind the wall.
- Time gap: seismic measurements were carried out several months after the tunnelling. The aquifer system was disturbed and weak zones were injected.
- Limitations related to seismic tomography:
- Limited resolution. The resolution is determined by the velocity and the frequency of seismic waves in the rocks (wavelength).
- Errors are swept out to the boundaries by tomographic algorithms where the ray coverage is uneven and less than average.
- Smoothing/averaging effect of long ray-paths. Seismic arrival times are integrated over long distances.
- Geotechnical data related limitations:
- Estimated and discrete values expressed in one scale to calculate RMR and Q-value, direction and scale dependence of parameters.

The cell-by-cell correlation of the successive values in the galleries is shown in Table 1.

Table 1

Correlations between velocities and rock mass properties (rock mass properties are obtained from [5])

	RQD	**RMR**	**LOG(Q)**	**$RQD_{smoothed}$**	**$RMR_{smoothed}$**	**$LOG(Q)_{smoothed}$**
Vs	78.4%	74.0%	58.1%			
Vp	63.8%	60.8%	42.1%			
$Vs_{smoothed}$				91.1%	89.6%	87.8%
$Vp_{smoothed}$				76.9%	76.4%	80.0%

The similar character of RQD and V_s can be seen in Figure 4 for real (black) and smoothed (red) data sets. This means that the trend of RQD can be forecast from seismic velocities with an accuracy of around 90%.

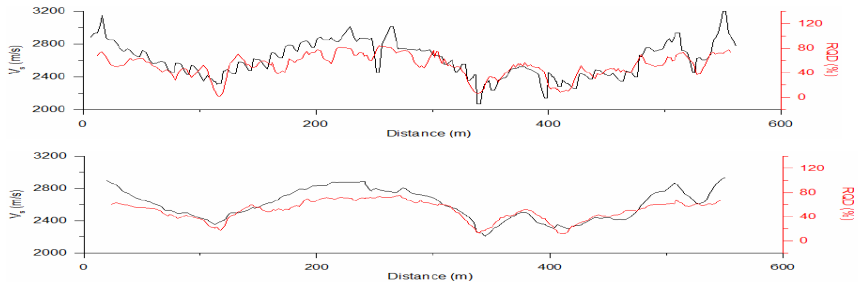

Figure 4. Comparison of RQD values and S-wave velocity alongside the perimeter of galleries: plots of real (above) and smoothed (below) data sets

5. Estimation of support categories from seismic velocities

The support requirements of underground excavations are generally determined from the rock mass classification parameters, especially from RMR or Q-value. The connection between the seismic velocity distribution along the tunnels and the support categories applied to these sections was also investigated. The results show that the estimation of support categories from the S–wave velocities is no less reliable than that from any other current method.

Based on the above comparison, the seismic velocity values can be scaled and transformed to rock mass properties, or directly to support categories (Table 2, Figure 5).

Table 2

Support categories in Vs ranges

Support Category	**$V_{s,\,min}$ (m/s)**	**$V_{s,\,max}$ (m/s)**
II	2550	2750
III	2400	2550
IV	2000	2400
V		2000

The similarity of the applied and calculated support categories is excellent along the tunnels (Figure 5a), but of course the estimation for the rock mass is limited by the accuracy of the tomographic image reconstruction (non-uniqueness problems, resolution limits, etc.) so the most straightforward evaluation of the results can be comparison of the data set for the sumps which were driven after the measurements (Figure 5b). However comparison of the data sets for the stumps is even more complicated than for the tunnels, because of the greater distance (the sumps are located at greater depth, outside the plane of the head tunnels), and the different (more strict) principles of support category selection due to the more complicated excavation geometry. The latter problem can be handled by a

small modification: the calculated support categories should be compared with the categories determined from the rock mass classification parameter (Q value), yetrather than the applied support.

Calculated and Q-value based support categories at the sumps are less similar than those at the head tunnels, but taking into account that the differences increase with greater offset (the deeper location of stumps) and, that the size of the fracture zone which penetrate the sumps is limited, one can conclude that the differences can be caused by the vertical changes of geomechanical properties of the rock mass.

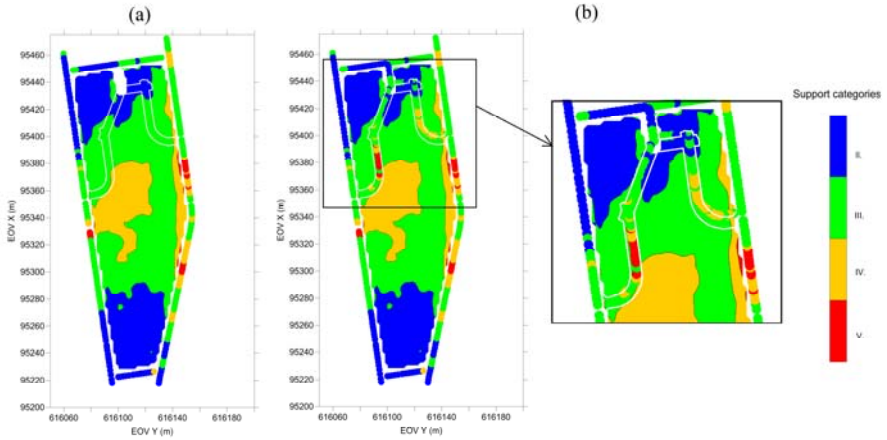

Figure 5. Calculated and applied support categories at the head tunnels (a) and sumps (b)

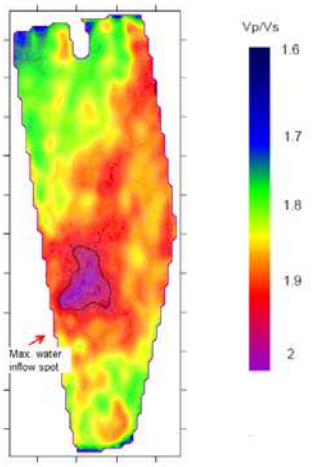

Figure 6. V_p/V_s and the hydrogeological connections (red arrow shows max. water inflow)

6. Vp/Vs – estimation of hydrogeological properties of rock mass

The investigated rocks can be considered as fractured reservoirs, so it was expected that the propagation of P-waves and S-waves would be different, since the latter does not propagate in liquid. The ratio of S- to P-wave velocities is sensitive to lithology and interstitial fluid – i.e. to the hydraulic properties of the rock on the perimeter of the transmitted area. This expectation was confirmed (Figure 6). The strong Vp/Vs anomalies correlate well with the great water inflows.

7. Conclusions

The patterns of P- and S-wave velocity maps show the strong vertical and lateral variability of the tectonic and lithological elements and help us to understand the structure of the investigated fractured rock mass. P-wave and especially S-wave velocities are in good correlation with RQD, RMR and Q-value, since their values are influenced by similar effects. The transversal velocities correlate better with rock mass classification than had been expected. Furthermore the hydrogeological correspondence of rock masses could be predicted by Vs/Vp ratios.

Acknowledgements

The authors would like to thank the Public Limited Company for Radioactive Waste Management (PURAM) for providing the necessary conditions for our study, and also all of the experts who were involved in the geological-hydrogeological-geotechnical investigations and who have helped our work.

References

[1] Deere, D. U. Deere, D. W.: The RQD index in practice. In: Rock classification systems for engineering purposes, (L. Kirkaldie, ed.), ASTM Special Technical Publications 984, Philadelphia, 1988, pp. 91–101.

[2] Barton, N. R.: Rock Mass Classification and Tunnel Reinforcement Selection using the Q-system". In: Rock classification systems for engineering purposes, (L. Kirkaldie, ed.), ASTM Special Technical Publications 984, Philadelphia, 1988, pp. 59–88.

[3] Vidale, J.: Finite Difference Calculation of Travel Times. Bulletin of Seismological Society of America, 1988, Vol. 78, pp. 2062–2076.

[4] McMechan, G. A.–Harris, J. M.–Anderson, L. M.: Cross-hole tomography for strongly variable media. Bulletin of Seismological Society of America, 1987, Vol. 77, pp. 1945–1960.

[5] Jakab, A.–Deák, F.–Kovács, L.–Maracsik, Z.–Máté, K.–Németh, L.–Rátkai, O.–András, E.–Szamos, I.–Szebényi, G.–Török, P.–Gyalog, L.–Borsody, J.– Füri, J.–Gulácsi, Z.– Király, E.–Maros, Gy.–Rálisch, E.–Szabadosné, Sallay, E.: Tunnel interior design and construction of access tunnels of National Radioactive Waste Repository at Bátaapáti 1st stage. Geotechnical documentation of tunnels — "Small Loop", RHK-K040/09, Mecsekérc Zrt. Pécs, 2009.

Geosciences and Engineering, Vol. 1, No. 2 (2012), pp. 161–166.

APPLICATION POSSIBILITIES OF IP METHOD IN THE FIELDS OF ENVIRONMENTAL PROTECTION, ORE- AND DIRECT HYDROCARBON EXPLORATION

ENDRE TURAI
Associate professor, University of Miskolc,
Department of Geophysics, H-3515 Miskolc-Egyetemváros
gfturai@gold.uni-miskolc.hu

1. Introduction

From the 1950s the induced polarization (IP) method became well known as an effective geophysical method of ore exploration in the geophysical literature [1–3]. It was applied successfully in ore exploration both in time-domain (TDIP) and frequency-domain (FDIP) measurements, because the metallic polarization phenomenon can occur on the surface of ore showing conductive (free electronic) electric conduction – in a dissociated ionic environment. This type of polarization causes measurable IP anomalies.

On the other hand, the metallic content is not the only factor resulting in polarizability of the medium: filtration- and membrane effects as well as electrochemical (redox) properties can also lead to similar phenomena. Due to recognition of this, nowadays the IP method has turned into one of the most efficient geophysical methods for environmental investigations. In electromagnetic geophysical practice [4], however, it is also known that pyrite chimneys may be formed in the roof of productive (containing crude oil, or natural gas) hydrocarbon reservoirs, which causes metal polarization. The ring-like IP anomaly over hydrocarbon reservoirs may be an important feature of productivity in direct hydrocarbon explorations.

Time constant analysis means a novel opportunity of application in all three areas (environmental protection, ore- and direct hydrocarbon exploration). The time constant spectrum of the IP signal can be calculated with TAU-transformation [5]. Anomalies appearing in the interval of the short time constants (smaller than 1 sec) can be bound to less dangerous environmental effects (filtration and membrane), while the larger (higher then 1 sec) time constants connected to dangerous polarizations (redox and electrode) indicate chemical and metallic contamination. Analysis of the interval of high time constants makes it possible to define the types of ores and the pyrite chimney above the borders of productive hydrocarbon reservoirs.

2. TAU-tansformation of time-domain IP data

The strictly monotonously decreasing function $\eta_a(t)$ can generally be written as an integral transform of $w(\tau)$ function

$$\eta_a(t) = \int_0^\infty w(\tau) e^{-\frac{t}{\tau}} d\tau \tag{1}$$

where t is the time and τ is the time-constant.

In equation (1) the function w(τ) is called the spectrum of time-constants of the IP measurement. It represents all the important spectral information of the polarization. Let us define the TAU-transformation as a procedure generating the spectrum of time-constants from the polarizability curves:

$$w(\tau) = TAU[\eta_a(t)] \tag{2}$$

The time-constant spectrum represents all the important information (regarding the medium) of the time-domain IP data. After introducing the concept of the TAU-transform, some approximate solutions [5] and a general inversion solution [6] were developed for continuous time-constant spectra and also for the case of line spectra.

3. Interpretation methods for estimation of type and level of soil and rock contaminations

The TAU-transform method was applied first in a TEMPUS project [7] and was tested above several contaminated areas in Hungary (Nyékládháza – 1997–2008; Ráckeve – 1997; Kecskemét – 1997; Győröcske – 1999; Pásztó – 2000; Tokaj – 2001; Balmazújváros –, 2002; Szerencs – 2004; Tiszapalkonya – 2004; Berekböszörmény – 2007; Nagytárkány – 2008; Darvastó – 2008; Miskolc–Hejőpart – 2008; Tiszavasvári – 2008; Nagytétény – 2008; Miskolc–Bedő-hegy – 2009; Telkibánya – 2010; Miskolc–Salakbánya – 2010; Miskolc, Gózon L. út – 2010 and Miskolctapolca–Várhegy – 2010). In Felsőtelekes the Háromkő Company measured IP data for the examination of the state of the refuse dump site in 2011.

Based on our field experiences two ways were introduced for the estimation of the type and the amount of soil contamination. According to the first approach the calculation of contamination type comes from the time constant value of the time constant spectra ($w(\tau)$). The estimation of the level of soil contamination is based on the Weighted Amplitude Value (WAV) of the time constant spectra. The second approach estimates the corrected apparent conductivity of the contaminated material (σ_{corr}) as a product of WAV parameter and measured apparent conductivity.

Taking the IP curve $\mu_a(t)$ measured in the field into account we can compute the time constant spectrum based on equation (2) and qualify the main types of polarization mechanisms by the τ_n time-constant values [8].

The main components of the contaminating material in a contaminated site are connected to the main types of polarizations (Table 1); thus, we can emphasize the redox and metallic effects with time constants higher than 1 second (connected to dangerous components – chemical and metallic) and similarly we can reduce the lower time constant filtration and membrane effects (connected to non-dangerous components – water and disperse clay) using a simple weighting procedure [8]:

$$WAV(\tau) = \frac{\tau\, w(\tau)}{[1\ sec]} \tag{3}$$

Table 1

Geological sources of polarization

Type of polarization	Source of polarization
filtration	porous soil and rocks with conductive fluid
membrane	porous soil and rocks with disperse clay and water
electrochemical or redox	chemical agent with high reactivity for oxidation or reduction
metallic	metallic components in porous rocks with conductive fluid

The WAV (Weighted Amplitude Value) section shows the region of the more dangerous components, thus we can estimate the level of the soil contamination using the following practical scale of the Weighted Amplitude Value (WAV) of time-constant spectra (Table 2). In ore and refuse dump exploration this scale is useful for the estimation of polarizable metallic ore concentration.

Table 2

Levels of soil contamination

Contamination level or polarizable ore concentration level	WAV
very high (vh)	0.2 (20%) <
high (h)	0.1 (10%) - 0.2 (20%)
medium (m)	0.05 (5%) - 0.1 (10%)
small (s)	0.02 (2%) - 0.05 (5%)
clean (c)	< 0.02 (2%)

Let us define the time constant dependent corrected apparent conductivity of the media ($\sigma_{corr}(\tau)$) as a product of the WAV parameter and apparent conductivity ($\sigma_a = 1/\rho_a$):

$$\boldsymbol{\sigma_{corr}(\tau) = 1000\,\sigma_a\, WAV(\tau)\left[\frac{mS}{m}\right]} \tag{4}$$

The contamination level of the soil can be estimated based on equation (4) by using the corrected apparent conductivity. If the σ_{corr} value is approximately 50–100 milli-Siemens/meter (mS/m) the soil has a medium contamination level.

4. Field results of time-domain IP data measured above contaminated areas

This section presents some field results of IP data measured above the Felsőtelekes refuse dump.

Figure 1 shows the vertical WAV section calculated on the measured profile in the Felsőtelekes area. As can be seen, there are WA values over ten percent, indicating high and very high contaminated areas under the surface caused by metallic (Figure 2) and redox

polarization effects. When the ore concentration of the waste rock body is relatively high there are high WA values, too.

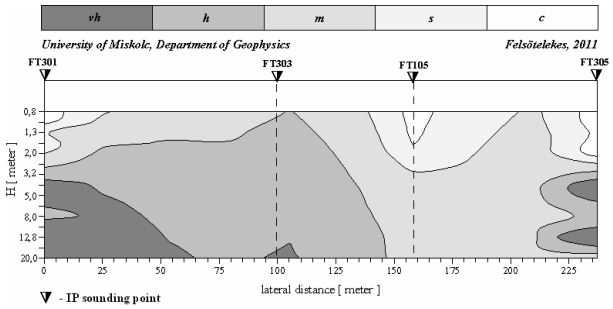

Figure 1. Vertical WAV section

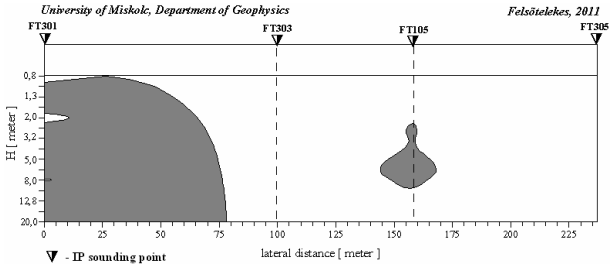

Figure 2. Vertical section of metallic effect (1 sec < τ)

The corrected apparent conductivity vertical section is presented in Figure 3. The thick black contour line shows the points of the section where the corrected conductivity value is the critical 100 mS/m.

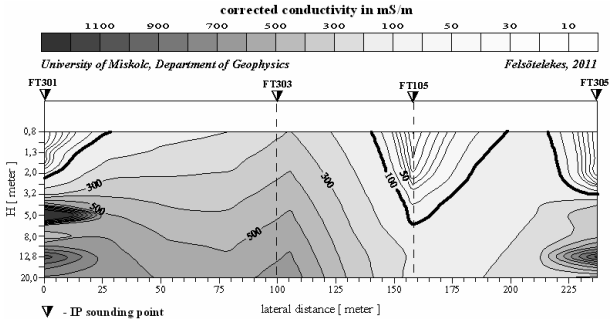

Figure 3. Vertical section of the corrected apparent conductivity

Finally, let us see the WAV map (Figure 4) and the area of metallic polarization (Figure 5) calculated at a 10 m reference depth. These maps inform us about the lateral distribution of the polarizable ore concentration in the Felsőtelekes waste rock body.

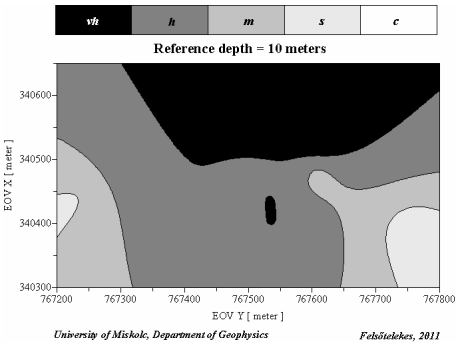

Figure 4. WAV map at 10 m depth

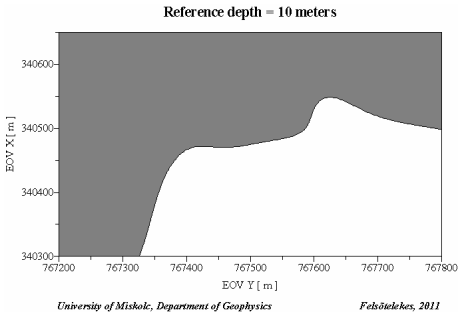

Figure 5. Area of metallic polarization

5. Application possibility of IP method for direct surveying hydrocarbon reservoirs

High IP values have been measured over several oil reservoirs [4]. Near the reservoirs the methane (CH_4) and hydrogen sulphide (H_2S) contents can cause the chemical processes visible in Fig 6. The product of this process is an ore mineral (FeS_2–pyrite).

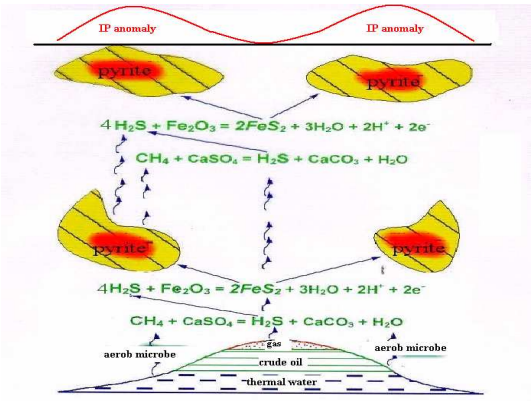

Figure 6. Chemical processes in the roof of hydrocarbon reservoir

The pyrite causes a characteristic metallic polarization, which gives IP values with high time constants. These high time constant values (over 1 sec) show the lateral boundaries of hydrocarbon reservoirs on the surface of measurement. This ring-like IP anomaly correlates well with the lateral boundary of the hydrocarbon reservoir determined from the interpretation of 3D seismic measurements [Figure 7. a)], but there are no measured IP anomalies over a reservoir containing only thermal water [Figure 7. b)].

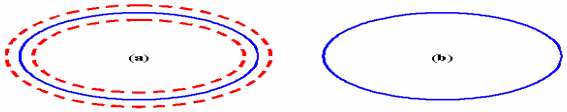

Figure 7. a) Lateral boundary of hydrocarbon reservoir with ring-like IP anomaly b) Lateral boundary of thermal water reservoir

6. Conclusions

Two methods were introduced for the estimation of the type and the level of soil contamination and polarizable ore concentration. These methods are useful for identifying ore, assessing possible contamination from refuse dumps, and of course for direct hydrocarbon exploration.

It was shown that the TAU-transformation of time-domain IP data clearly detected polarizable ore content of the refuse dump near Felsőtelekes. The analysis of the IP data shows that there are some very highly contaminated parts in the waste-rock body. The types of the polarization were mainly metallic and redox.

Pyrite causes a characteristic metallic polarization, which gives IP values with high time constants. This ring-like IP anomaly correlates well with the lateral boundaries of hydrocarbon reservoirs.

Acknowledgements

The described work was carried out as part of the TÁMOP - 4.2.1.B - 10/2/KONV - 2010 - 0001 project in the framework of the New Hungarian Development Plan. The realization of this project is supported by the European Union, co−financed by the European Social Fund.

References

[1] Wait, J.R.: Overvoltage Research and Geophysical Applications. London, Pergamon Press, 1959.
[2] Keller, G. W., Frischknecht, F. C.: Electrical Methods in Geophysical Prospecting. Oxford, Pergamon Press, 1966.
[3] Sumner, J. S.: Principles of Induced Polarization for Geophysical Exploration. Amsterdam, Elsevier Scientific Publishing Company, 1976.
[4] Nagy, Z.: Geophysical Stratigraphy (in Hung.). Miskolc, University of Miskolc (manuscript), 1990.
[5] Turai, E.: TAU-Transformation of Time-Domain IP Curves. ANNALES Univ. Scien. Budapestinensis de Rolando Eötvös Nom., Sectio Geophysica et Meteorologica, Tomus I-II., 1985, pp. 182–189.
[6] Turai, E., Dobróka, M.: A New Method for the Interpretation of Induced Polarization Data – the TAU-Transform Approach. 63rd EAGE Conference, Extended Abstracts, 2001, pp. 049/1-049/4.
[7] Turai, E., Elsen, R., Limbročk, K.: Analysis of IP Time-Domain Data Measured above a Waste Site Near Offheim using TAU-Transformation of IP Chargeability Curves. TEMPUS project report, JEP 1553-92, DMT-Bochum, 1992.
[8] Turai, E.: IP Data processing results from using TAU-transformation to determine time-constant spectra. Geophysical Transactions, vol. 44 (3-4), 2004, pp. 301–312.

Geosciences and Engineering, Vol. 1, No. 2 (2012), pp. 167–172.

SOME FIELD MEASUREMENT RESULTS OF IP METHOD

ENDRE TURAI
Associate professor, University of Miskolc, Department of Geophysics
H-3515 Miskolc-Egyetemváros, gfturai@gold.uni-miskolc.hu

1.Introduction

This paper presents some interpretation results of induced polarization (IP) data using TAU-transformation of time-domain IP curves measured in the field [1]. Two methods for the estimation of type and level of soil contamination and of polarizable ore concentration have been introduced using time constant analysis.

The theoretical basis of TAU-transformation and the contamination estimation [2–3] are presented in the current volume of this journal [4]. The TAU-transform method was applied first in a TEMPUS project [5] and it has also been tested above several contaminated areas within Hungary ([4], also Rudabánya – 2011, Felsőtelekes – 2011 and Ózd – 2012). This paper presents interpretation results from the Nagytétény, Tiszavasvári and Ózd areas.

2. Soil contamination interpretation results of IP data collected above Nagytétény waste site

IP time-domain data were measured in a Schlumberger electrode array above the Nagytétény communal waste site. At each IP sounding point 16 discrete current electrode spacing points were used, and the array parameters were MN = 1 m, AB_{min} = 3.2 m and AB_{max} = 100 m, where MN was the potential electrode spacing and AB was the current electrode spacing.

In Figure 1 the vertical WAV (Weighted Amplitude Values) section of the first profile measured from IP data indicates a very high level of contamination [1]. Making a complex time-constant analysis [1], our results show that there is mainly metallic (Figure 2) and redox (Figure 3) polarization in the Nagytétény waste site. Where WA values are high there are redox (electrochemical) and metallic polarizations. Membrane polarization (Figure 4) was correlated with a low contamination level appearing on the WAV section (Figure 1).

The vertical section of corrected conductivity over Nagytétény is presented in Figure 5, where the lighter contour lines show the corrected conductivity value of 50 milliSiemens/meter (mS/m), indicating a medium level of contamination.

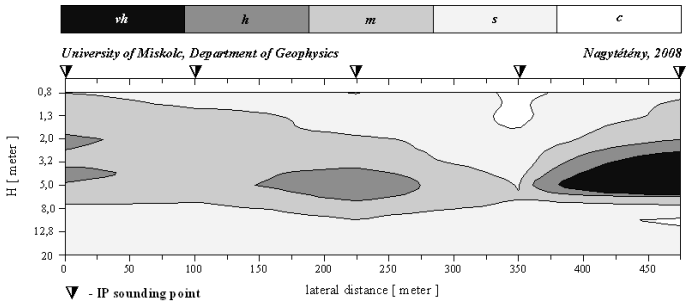

Figure 1. Vertical WAV section (WAV levels: > 0.2 – very high; 0.1-0.2 – high; 0.05-0.1 – medium; 0.02–0.05 – small; < 0.02 – clean)

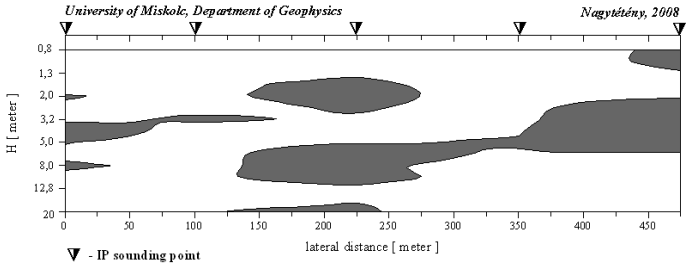

Figure 2. Vertical section of metallic effect (1 sec < τ)

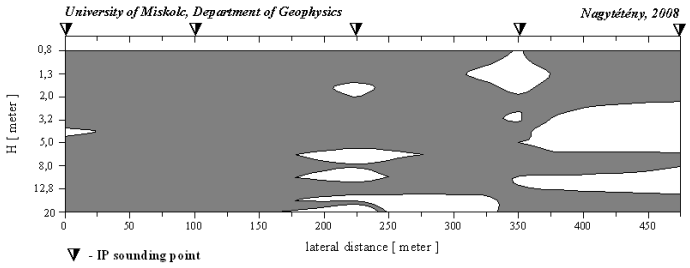

Figure 3. Vertical section of redox effect (0.6 sec < τ < 1.2 sec)

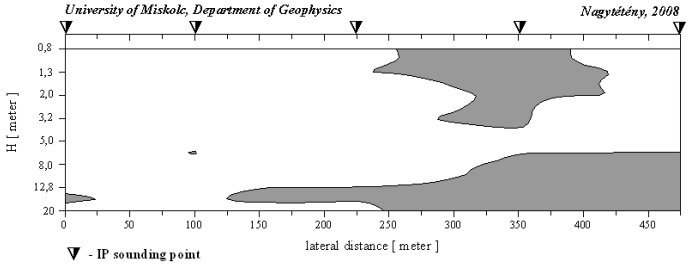

Figure 4. Vertical section of membrane effect (0.2 sec < τ < 0.8 sec)

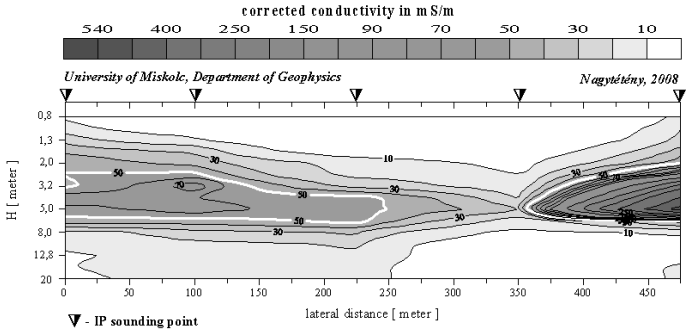

Figure 5. Vertical section of the corrected apparent conductivity

3. Time constant analysis of Time-Domain IP data measured over Tiszapalkonya ash slag

Figure 6 shows the vertical WAV section calculated over the Tiszapalkonya ash slag site. (Also in this measurement Schlumberger electrode array was used for IP soundings). As can be seen, there are only small and medium WA values, indicating some dangerous regions under the surface caused by redox (Figure 7) and membrane polarization effects.

Sometimes the membrane effect appears with either low apparent resistivity (ρ_a) or high apparent polarizability, therefore let us determine the corrected conductivity (σ_{corr}) [1] section. The corrected conductivity vertical section is presented in Figure 8. The lighter contour line shows the points of the section where the corrected conductivity value reaches the critical 100 mS/m.

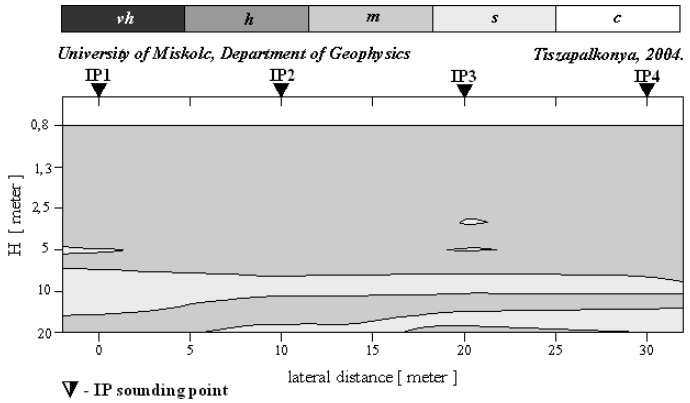

Figure 6. Vertical WAV section at Tiszapalkonya (WAV levels: > 0.2 – very high; 0.1–0.2 – high; 0.05–0.1 – medium; 0.02–0.05 – small; < 0.02 – clean)

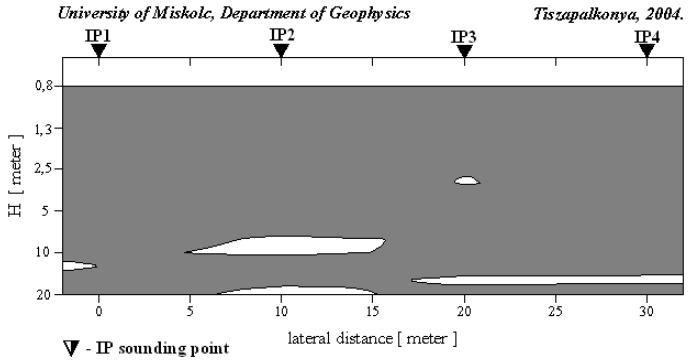

Figure 7. Vertical section of redox effect (0.6 sec < τ < 1.2 sec)

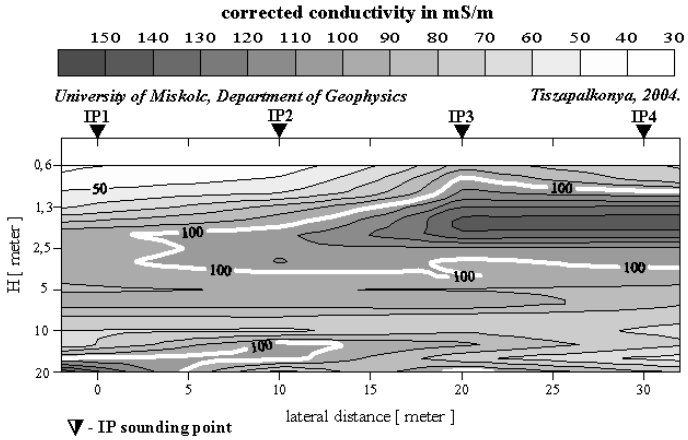

Figure 8. Vertical section of the corrected apparent conductivity

4. Soil contamination interpretation results above Ózd inert waste site

In 2012 the Háromkő Company measured IP data over the Ózd inert waste site. This section presents the calculated contamination levels of the inert waste site using the TAU transformation of IP curves. The following figures compare the two parameters (WAV and corrected apparent conductivity) introduced in [1] for the estimation of soil contamination levels on three reference depths.

Figures 9 and 10 show the WAV and corrected conductivity maps at a reference depth of 2 m. Only small soil contamination appears at this depth level on the northern part of the investigated area. It can be seen clearly that the lower boundary of the small contamination level correlates well with the thick black 50 mS/m contour line on Figure 10.

The soil contamination level is the highest at the 4 m depth level (Figure 11); however it reaches only the medium value.

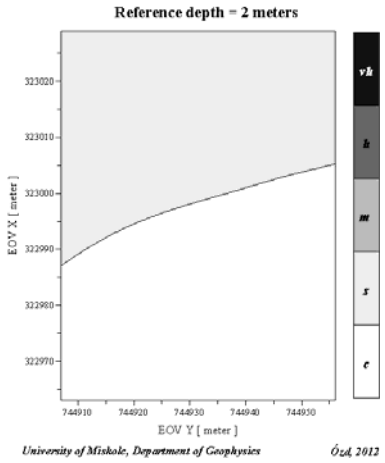

Figure 9. WAV map at 2 m depth

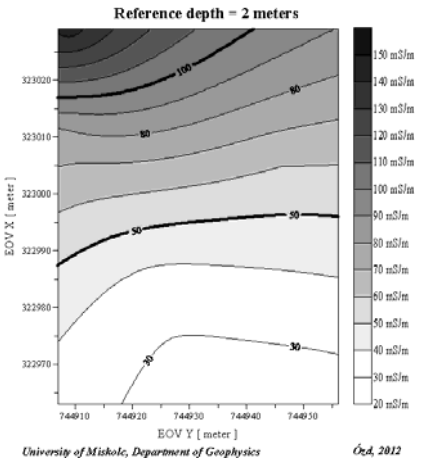

Figure 10. σ_{corr} map at 2 m depth

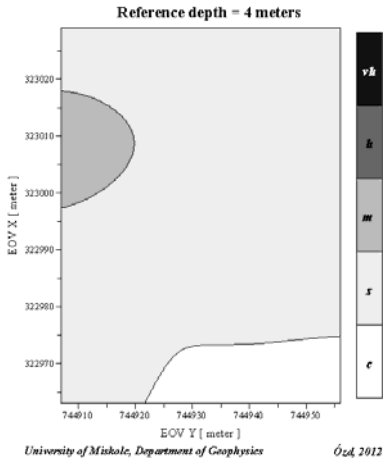

Figure 11. WAV map at 4 m depth

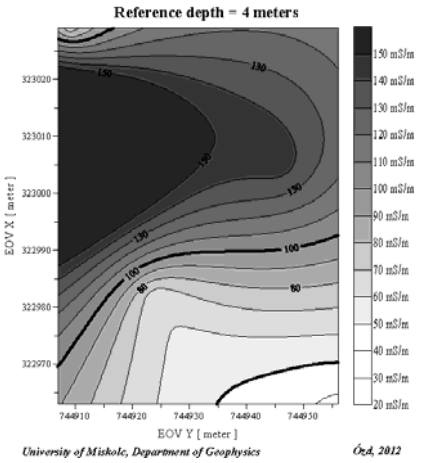

Figure 12. σ_{corr} map at 4 m depth

The soil contamination levels are low and medium on the western part of the area at a 10-metre depth (Figure 13). It is clearly visible that on all three depth levels the thick black 50 mS/m valued corrected conductivity contour line (Figure 10, Figure 12 and Figure 14) correlates with the lower limit of the low contamination very well.

Finally we can conclude that the Ózd inert waste site has no serious environmental problem, because mainly clean and low levels of contamination can be detected there.

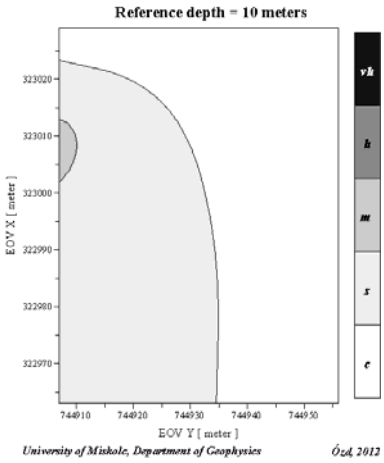

Figure 13. WAV map at 10 m depth

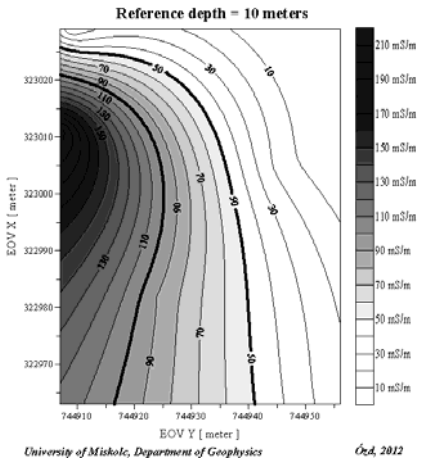

Figure 14. σ_{corr} map at 10 m depth

5. Conclusions

The time constant analysis [1] based on TAU transformation of IP data was applied successfully to all three presented exploration areas for the characterization of soil contamination. A strong correlation has been observed between the WAV and the corrected conductivity maps in all cases.

Acknowledgements

The described work was carried out as part of the TÁMOP-4.2.1.B-10/2/KONV-2010-0001 project in the framework of the New Hungarian Development Plan. The realization of this project is supported by the European Union, co-financed by the European Social Fund.

References

[1] Turai, E.: TAU-Transformation of Time-Domain IP Curves. ANNALES Univ. Scien. Budapestinensis de Rolando Eötvös Nom., 1985, Sectio Geophysica et Meteorologica, Tomus I–II., pp. 182–189.

[2] Turai, E.–Dobróka, M.: A New Method for the Interpretation of Induced Polarization Data – the TAU-Transform Approach. 63rd EAGE Conference, Extended Abstracts, 2001, pp. 049/1–049/4.

[3] Turai, E.: IP Data processing results from using TAU-transformation to determine time-constant spectra. Geophysical Transactions, 2004, Vol. 44 (3–4), pp. 301–312.

[4] Turai, E.: Application possibilities of IP method in the fields of environmental protection, ore- and direct hydrocarbon exploration. Journal of Geoscience and Engineering, University of Miskolc, 2012 (See in the same volume of this journal)

[5] Turai, E.–Elsen, R.–Limbročk, K.: Analysis of IP Time-Domain Data Measured above a Waste Site Near Offheim using TAU-Transformation of IP Chargeability Curves. TEMPUS project report, JEP 1553-92, DMT-Bochum, 1992.

Geosciences and Engineering, Vol. 1, No. 2 (2012), pp. 173–178.

NEUTRON WELL-LOGGING PROFILES IN SLOPED THIN LAYER FORMATIONS SIMULATED BY MONTE CARLO METHOD

URSZULA WOŹNICKA[1]–DOMINIK DWORAK[1]–URSZULA WIĄCEK[1]–
TOMASZ ZORSKI[2]
[1]Henryk Niewodniczanski Institute of Nuclear Physics,
Radzikowskiego 152 str., PL-31-342 Kraków, Poland.
Urszula.Woznicka@ifj.edu.pl, Dominik.Dworak@ifj.edu.pl, Urszula.Wiacek@ifj.edu.pl
[2]AGH University of Science and Technology, Faculty of Geology,
Geophysics and Environment Protection, Dept. of Geophysics,
Al. A. Mickiewicza 39, PL-30-059 Kraków, Poland.
zorski@geol.agh.edu.pl

1. Introduction

Neutron well-logging is one of the basic methods of well logging for porosity and lithology determination. A neutron source, placed in a borehole tool, creates a neutron field in the nearest environment – around the borehole. A neutron detector placed in the same tool at some distance from the source registers neutrons coming from that field. It gives information on some of the petrophysical parameters of rocks surrounding the borehole.

Descriptions of neutron fields and properties of neutron transport in matter have been strongly developed in reactor physics, both in the field of analytical and numerical methods. The same rules of neutron transport physics in various environments and the same mathematical methods can be used also for the description of neutron fields in geophysical applications.

Analytical description of the neutron fields can be done only for simple geometries, e.g. for the neutron field created by a point neutron source located in an infinite cylindrical borehole – surrounded by infinite and homogeneous rock medium. However, many interesting analytical solutions that are useful in the interpretation of neutron well-logging have been designed and applied in practice [1, 2]. More complex geometries – as, for instance, dipped thin layer formations crosscut by the cylindrical borehole – are not suitable for the analytical considerations.

Monte Carlo (MC) methods are continuously developed in the neutron transport domain. It is possible to reproduce, with very good accuracy, the real neutronic experiment, for example the neutron profiling in almost realistic measurement conditions. Monte Carlo simulations are a powerful tool supporting interpretation of neutron measurements in case of complex borehole geometries.

Advanced numerical software which can be implemented for a simulation of neutron well logging is the MCNP^{TM} code [3]. The program performs simulation of neutron transport in matter with the use of the Monte Carlo method. That possibility stems from the stochastic nature of neutron transport. Physical phenomena like neutron slowing down, scattering, and absorption processes are sampled from their probabilities and the whole history of the individual neutron transported from the source up to the final absorption can be followed. An advantage of this type of simulation is that all parameters such as porosity, elemental composition of rocks, tool construction, borehole filling and its diameter, etc. are

known in advance, because they make up the input data for the numerical calculations. This gives the possibility to examine the influence of each parameter of the medium individually on the response of the well-logging tool. An applicability of the MCNP code for nuclear geophysics is not limited to neutron well-logging tools. Very interesting results and solutions can be also obtained for neutron-gamma and gamma-gamma methods [4, 5].

The paper includes results of numerical calculations of neutron fields around the borehole and the corresponding response of the neutron-neutron well-logging tool on an example of the selected neutron well-logging tool (NNTE). Many neutron borehole profiles have been simulated for a wide range of asymmetric borehole–thin-layer geometries. The general model consists of an infinite rock, intersected by an infinite long borehole. A thin, flat rock layer of different lithology crosses that infinite rock under a certain angle to the borehole. To be close to reality the rock lithologies similar to those of the North-West Poland formations (shale sands) were chosen for the calculations. Numerous combinations of parameters – various porosities and thermal neutron absorption cross sections of the rocks as well as different layer thicknesses and slope angles – have been considered. The main goal of the research is to present the influence of an angle between a thin-layer and a borehole axis on the response of a neutron well-logging tool. Results are instantly useful for elaboration of the well-logging interpretation procedures for directional drillings, where the rock layers are usually sloped, or even highly inclined to the borehole axis.

2. Numerical model of the thin layer formation and borehole

The geometry of the problem is presented in Figure 1. The geological formation consists of a thin flat rock layer of thickness 5 cm $\geq H \geq$ 50 cm surrounded by an infinite, other rock medium. These two different rock spaces (called further simply the "layer" and "surroundings") are represented in the calculations by two different rock models. All our rock models consist of the same rock matrix, and they can differ only in porosities, ϕ, and/or in thermal neutron absorption cross sections, Σ_a, as is explained below. The rock matrix, same for each rock model, has density equal to 2.63 g/cm^3 and its chemical composition is as follows:

	SiO_2	Al_2O_3	Fe_2O_3	CaO	K_2O	H_20	CO_2
mass %	72.5	7.0	2.0	7.5	1.8	1.2	8.0

This is the characteristic composition of the Carpathian Miocene formation in Poland. To define the particular rock models, the three different porosity values of that rock matrix were chosen: ϕ = 7.5, 20 or 45%, where the pores are completely filled with fresh water. It was further assumed that the Σ_a of the pure rock matrix may be equal to 15 c.u. or 40 c.u. To reach such Σ_a values a little amount of ^{10}B isotope (correspondingly 0.00163 % and 0.00663% by mass) was added to the rock matrix (at the SiO_2 expense). That small artificial supplement of the strong neutron absorber, ^{10}B, has an influence only on thermal neutron capture and does not change major remaining parameters of the formation. However, the effective Σ_{aeff} of each rock model of given porosity differs from the matrix Σ_a because of the presence of water filling the pore space. The Σ_{aeff} have been calculated applying $\Sigma_a(H_2O)$ = 22.24 c.u. Six different rock models, summarized in Table I, were built on the basis of the above assumptions. Each of these models can play a double role in the calculations – it can work as the thin layer or as the surroundings.

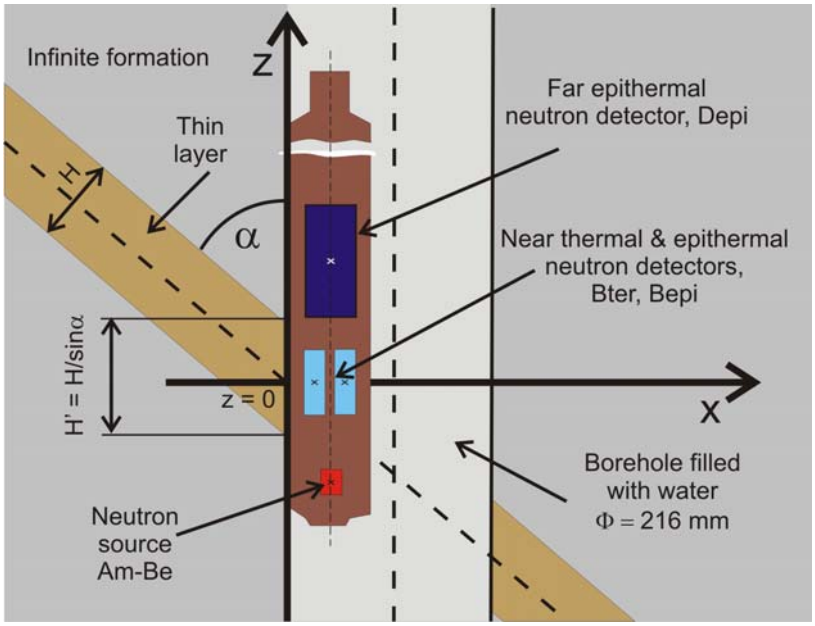

Figure 1. Formation – borehole geometry for MC modeling

The borehole of diameter 216 mm, filled with the fresh water, intersects the whole formation - under an angle $15° \geq \alpha \geq 90°$ to the thin layer. In this way, our general model as shown in Figure 1 has seven changeable parameters: four of them describe the physical properties of the "thin layer and its surrounding medium" (two different ϕ and Σ_a), two others describe the "layer geometry" (H, α), and the last one (depth "z") gives the actual position of the NNTE tool relative to the thin layer.

Table 1

Parameters of rock models used in MC calculations

Rock model	**ϕ [%]**	**Σ_a [c.u.]**	**$\Sigma_{a\,eff}$ [c.u.]**	**ρ_{vol} g/cm^3]**
Miocen-1 (M-1)	7.5	15	15.54	2.508
Miocen-2 (M-2)	7.5	40	38.67	2.508
Miocen-3 (M-3)	20.0	15	16.45	2.304
Miocen-4 (M-4)	20.0	40	36.45	2.304
Miocen-5 (M-5)	45.0	15	18.26	1.897
Miocen-6 (M-6)	45.0	40	32.01	1.897

The NNTE well-logging tool (Neutron–Neutron–Thermal–Epithermal) is a neutron tool equipped with an Am-Be neutron source and a set of three detectors: two near detectors (thermal, Bter, and epithermal, Bepi) and one remote detector (epithermal, Depi). The two epithermal detectors create a compensate dual-detector tool which is low sensitive to the borehole impact and to the neutron absorption properties of the medium. The near Bter detector is sensitive to hydrogen content and the Σ_{aeff} of the environment. The detailed

numerical model of the NNTE tool has been created and validated in benchmark experiments [6].

3. The MCNP calculations and results.

A detailed description of the MCNP simulations is included in [8]. The responses of each detector have been calculated for the infinite homogeneous media – corresponding to the rock models from M-1 to M-6. The results are included in Table II. The original MCNP results give an average number of neutrons absorbed in a unit of the detector volume, per one neutron emitted from the source. Using the calibration procedure for the NNTE tool [6], these raw data have been recalculated to clearer units [count/s]. The detector responses obtained for the infinite media show the wide range of variability. Some of trends in the profile curves can also be visible. Let us consider the thin layer of the M-6 model surrounded by the infinite medium M-1: the Bter detector counts ~944 count/s when the neutron tool goes through the M-1 rock model and next the negative anomaly is created (with the minimum value ~400 count/s) when it goes through the M-6 layer. The actual shape and size of the anomaly depends mainly on the thickness H of the thin layer, angle α, porosity ϕ, and $\Sigma_{a\ eff}$. In some cases the size of the anomaly does not reach the count rate of the respective infinite medium (see e.g. Figure 2, Detector Bepi, H = 15 cm).

Table 2

Numerical results of the detector responses in infinite rock models

Rock model	Bter [count/s]	σ(Bter) [count/s]	Bepi [count/s]	σ(Bepi) [count/s]	Depi [count/s]	σ(Depi) [count/s]
M-1	943.99	2.55	298.60	0.90	169.17	1.05
M-2	741.82	2.08	297.39	0.89	164.43	1.04
M-3	719.61	2.23	224.36	0.79	95.55	0.84
M-4	560.44	1.91	224.14	0.78	93.52	0.83
M-5	484.04	1.89	166.81	0.70	60.72	0.76
M-6	400.20	1.68	166.69	0.70	59.94	0.76

The examples of calculated profiles are presented in Figure 2. The thin layer (M-2 rock model: low porosity and high $\Sigma_{a\ eff}$) is surrounded by the rock model M-5 (high porosity and low $\Sigma_{a\ eff}$). The profiles registered by near detectors are presented: on the left for thickness of the thin layer H = 15 cm, and on the right for H = 50 cm. The slope angle α varies from 90° up to 30° (H = 50 cm) and 15° (H = 15 cm). The zero value on the depth axis marks the point when the centre of the detector is situated opposite the intersection of borehole and layer symmetry lines. The anomalies registered by the remote Depi detector has a similar course as for the near Bepi detector. The straight vertical lines mark the responses of the detectors in infinite rock models M-2 and M-5, respectively.

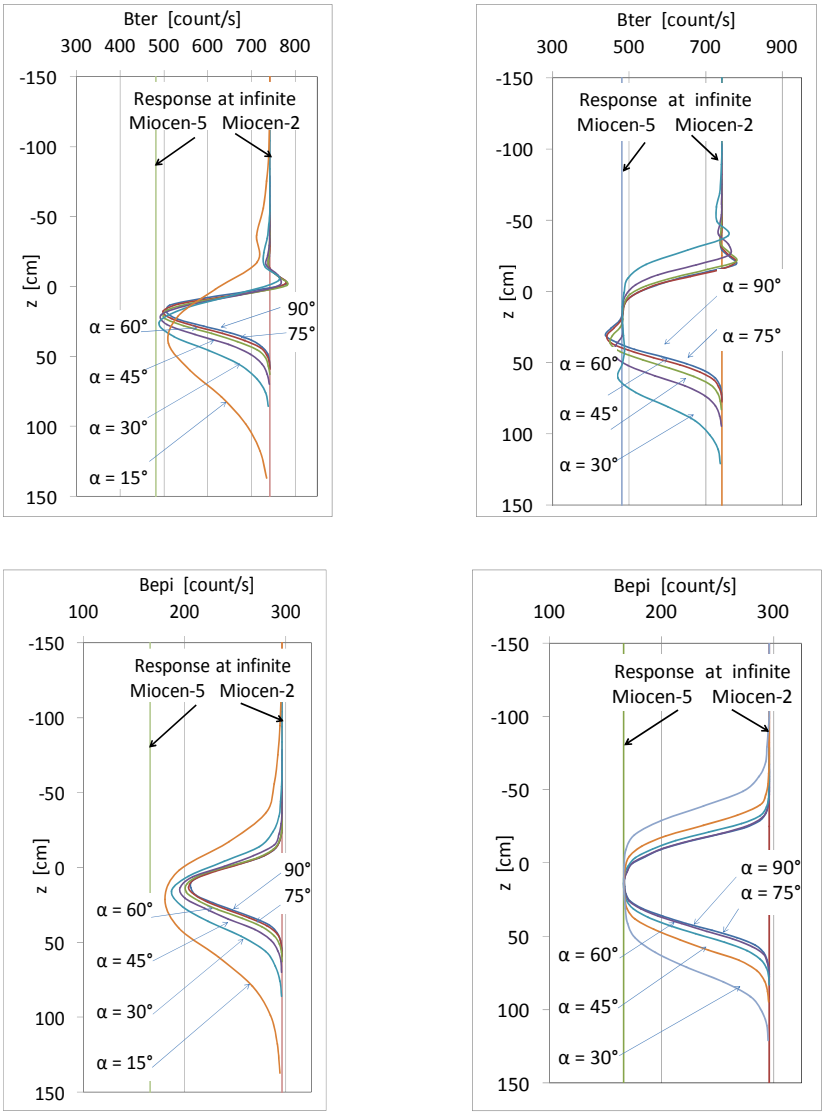

Figure 2. Neutron profiles modeled by m-c simulations for Bter and Bepi detectors for different slope angles, α, for Miocen-5 thin layer: left: H = 15 cm, right: H = 50 cm thickness. The layer is surrounded by Miocen-2 rock model. Description of the z axis – as in Figure 1

The change in the slope angle α causes changes in the shape of anomalies; the width is growing and the slope of the anomalies decreases. The slope of the anomaly becomes asymmetric for the Bter response. This results both from the strong asymmetry of the formation-layer geometry and from the presence of tool asymmetry (location of the source-

detector system in relation to the rock formation). The strong differences between the neutronic properties of both rock models (M-2 and M-5) can create disturbances on the boundary layer.

4. Conclusions

The presented selected results of the MC simulations of the neutron tool in the complex borehole–thin layer formation geometry show the capabilities of numerical modeling of neutron transport processes. The announced series of profiles are used as the input data to the next considerations associated with the elaboration of the new interpretation procedures of well logging profiles in sloped thin layer formations. As is shown in *Figure 2*, starting from the $\alpha \leq 45°$ the obtained well logging profiles require different interpretation procedures than the simple, symmetrical borehole–formation geometry, that means geometry with $\alpha = 90°$.

The numerical simulation method as presented above can be also useful for optimization of the construction of neutron well logging tools, e.g. optimization of source–detector distances as well as the design of proper shielding layers protecting detectors from the direct source radiation and from scattered radiation originated from the borehole fluids.

Acknowledgements

Work performed within the research project was realised at the Institute of Nuclear Physics (IFJ PAN) financed by the Ministry of Science and High Education (MNiSW) No. N N525 337238 during the period 22.03.2010–21.09.2012.

References

[1] Czubek, J. A.: Scaling Neutron Fields in Well Logging, Nucl. Geophys., Vol. 6, 1992, 445–486.
[2] Czubek, J. A., Woźnicka, U.: Neutron Flux and Axial Moments in Three-region Cylindrical Geometry Applied for Neutron Log Calibration. Part I: Theoretical Description, Acta Geoph. Pol., XLVI, No. 4, 1998, 427–447.
[3] MCNP – A General Monte Carlo N-Particle Transport Code, Version 5, X-5 Monte Carlo Team, Diagnostics Applications Group, Los Alamos National Laboratory, "MCNP Homepage", http://mcnp-green.lanl.gov/index.html
[4] Dworak, D.–Woźnicka, U.–Zorski, T.–Wiącek, U.: Numerical modeling of the gamma–gamma density tool responses in horizontal wells with an axial asymmetry. Appl. Rad. Isotopes, 69, 2011, 268–274.
[5] Cywicka-Jakiel, T.–Zorski, T.: Improvement of the MCNP simulated n-gamma spectrometer response function using the new ENDF/B-VI evaluations for thermal neutron capture. Nucl. Instr. Meth. A, 580, 2007, 94–97.
[6] Drabina, A.–Zorski, T.: Applications of MCNP programme for NNTE neutron tool response simulation (in Polish), Int. Sci.-Tech. Conf. GEOPETROL 2006, Zakopane 18-21.09.2006, Prace Instytutu Nafty i Gazu, 137, 2006, 509–515.
[7] Woźnicka, U.–Dworak, D.–Wiącek, U.–Zorski, T.: Numerical response of NNTE neutron logging tool in dipped thin-layer formations. Assumptions and preliminary results of Monte Carlo calculations. (in Polish), IFJ Report, 2050/AP 2011; www.ifj.edu.pl/publ/reports/2011.